



**Frontiers of
Characterization
and Metrology for
Nanoelectronics
2015**

**April 14-16, 2015
Dresden, Germany**

**Editors:
E.M. Secula
D.G. Seiler**

www.nist.gov/pml/div683/conference/

Committee Co-Chairs



David Seiler

National Institute of
Standards and Technology



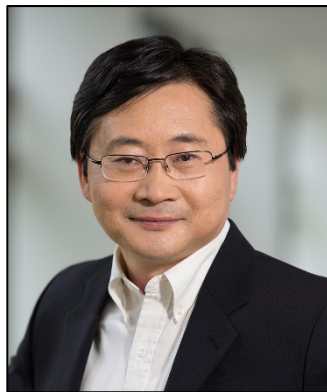
Ehrenfried Zschech

Fraunhofer Institute for Ceramic
Technologies and Systems



Bob McDonald

Formerly of Intel
(Treasurer)



Zhiyong Ma

Intel



Alain Diebold

CNSE, SUNY Albany

Committee Members

- Amal Chabli, CEA-Leti
- Luigi Colombo, TI
- Michael Current, Current Scientific
- Ajey Jacob, Global Foundries
- Toshihiko Kanayama, AIST
- Shifeng Lu, Micron
- Ulrich Mantz, Zeiss
- Lori S. Nye, Brewer Science, Inc.
- Yaw Obeng, NIST
- Lothar Pfitzner, Fraunhofer IISB
- Sesh Ramaswami, Applied Materials
- Erik Secula, NIST
- George Thompson, Intel
- Sandip Tiwari, Cornell University
- Victor Vartanian, ISMI
- Wilfried Vandervorst, IMEC
- Usha Varshney, NSF

Cover Caption: Simulated colorized SEM image, based on Monte Carlo modeling and simulation. The particles are silicon, with the smallest one being 5 nm in size. These simulated structures are used for the calibration/evaluation of various 3D measurement methods.

2015 International Conference on Frontiers of Characterization and Metrology for Nanoelectronics

Welcome to the 2015 International Conference on Frontiers of Characterization and Metrology for Nanoelectronics (FCMN)! Our goal is to bring together scientists and engineers interested in all aspects of the characterization technology needed for nanoelectronic materials and device research, development, and manufacturing. All approaches are covered in this conference: chemical, physical, electrical, magnetic, optical, in-situ, and real-time control and monitoring. The conference summarizes major issues and provides critical reviews of important semiconductor techniques needed as the semiconductor industry moves to silicon nanoelectronics and beyond. It is hoped that the invited talks, contributed posters, and informal discussions will be a stimulus to provide practical perspectives, breakthrough ideas for research and development, and a chance to explore collaborations and interactions on a world-wide basis.

We are pleased to have Nobel Prize winner Klaus von Klitzing, Max-Planck-Institut FKF; Suresh Venkatesan, Senior Vice President, Technology Development, Global Foundries; and Hubert Lakner, Executive Director, Fraunhofer Institute for Photonic Microsystems, as keynote speakers for the event! Thirty other invited talks will offer overviews in the sessions that follow. Posters will supplement these overviews with the latest metrology-based research results. These posters represent significant contributions to the latest developments in characterization and metrology technology, especially at the nanoscale.

The 2015 FCMN is the 10th in the series of conferences devoted to metrology frontiers for the semiconductor industry. It emphasizes the latest advances in characterization and metrology that will help shape the future of the nanoelectronics revolution. The proceedings for most of the previous conferences in the series were published as hard-cover volumes by the American Institute of Physics, New York. All but the 1995 and 2011 proceedings are available to view for free on-line at www.nist.gov/pml/div683/conference/archives.

This year, the committee is excited to bring the FCMN to Dresden, Germany, for the first time! While a city of notable art treasure, architectural sights, and a charming landscape, Dresden also has largest hub of microelectronics in Europe. Dresden is a center of materials science and engineering (more than 2000 materials scientists and engineers at TU Dresden and in several institutes). We hope you will enjoy this beautiful location!

It is our sincere hope that you find this conference stimulating and enjoyable!

With best wishes from the Committee Co-Chairs,

David Seiler, NIST;

Ehrenfried Zschech, Fraunhofer Institute for Ceramic Technologies and Systems;

Bob McDonald, formerly of Intel (Treasurer);

Zhiyong Ma, Intel; and

Alain Diebold, CNSE, SUNY Albany

Purpose and Goals

The FCMN brings together scientists and engineers interested in all aspects of the characterization technology needed for nanoelectronic materials and device research, development, and manufacturing. All approaches are welcome: chemical, physical, electrical, magnetic, optical, in-situ, and real-time control and monitoring. The conference summarizes major issues and provides critical reviews of important semiconductor techniques needed as the semiconductor industry moves to silicon nanoelectronics and beyond.

Contributed Posters

One of the major emphases of this conference is on the contributed posters. These extended poster abstracts selected by the committee represent significant contributions to the frontier, state-of-the-art materials, and device characterization and metrology.

Poster authors are responsible for setting up their displays, being present for the poster session on Tuesday afternoon, and removing their displays at the end of the conference.

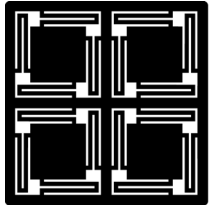
Poster Session

The poster session with complimentary wine and cheese is scheduled for the end of Tuesday at the Dresden Hilton.

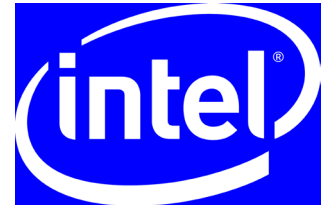
Banquet

A dinner banquet will be held on Wednesday, Apr. 15th, at Pulverturm, which is located just around the corner from the Dresden Hilton.

Platinum Sponsors



HYSITRON®



Gold Sponsor



GLOBALFOUNDRIES®

Sponsor

- American Elements

Exhibitors

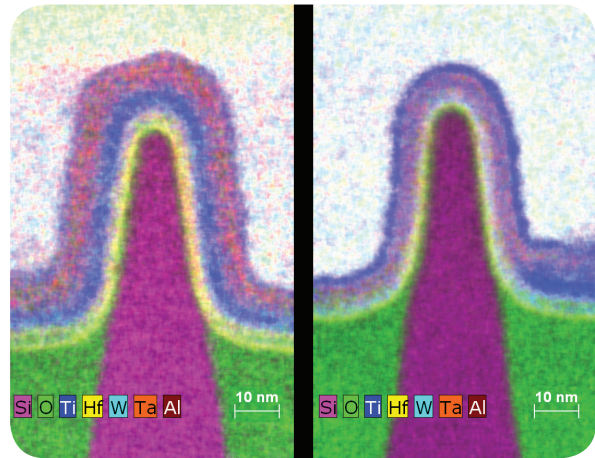
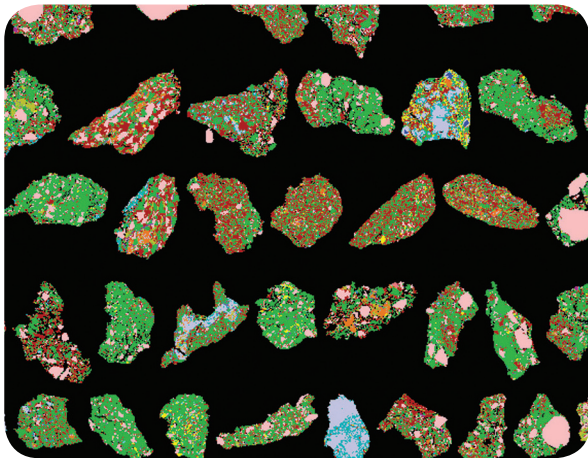
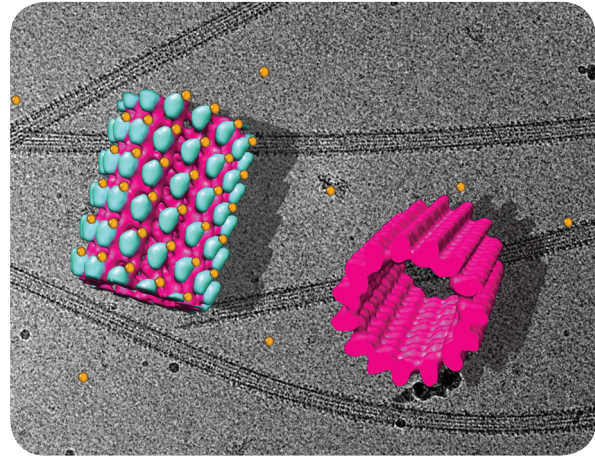
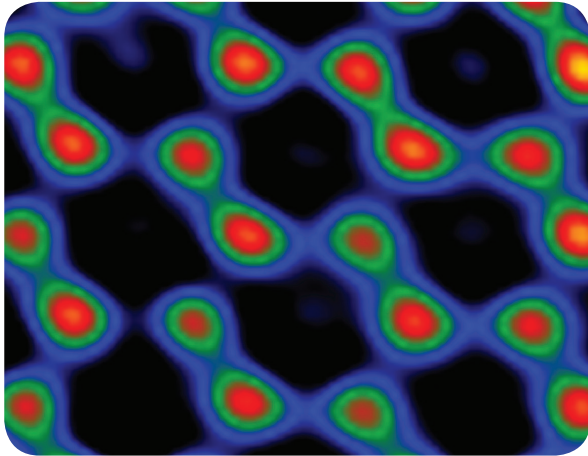
- CAMECA
- Dresden Fraunhofer Cluster Nanoanalysis
- Metryx

Supporting Organizations

- National Science Foundation (NSF)
- American Vacuum Society (AVS)

Cooperation Partners

- Dresden Fraunhofer Cluster Nanoanalysis
- Fraunhofer IKTS Dresden
- Technische Universität Dresden – Dresden Center for Nanoanalysis (DCN) and Center for Advanced Electronics Dresden (cfaed)
- National Institute of Standards and Technology



(Top left) Atomic resolution phase image of graphene. Sample courtesy of N. Alem and A. Zettl, University of California, Berkeley. Images Joerg Jinschek and Emrah Yucelen, FEI, Hector Calderon, IPN, Mexico, and C. Kisielowski, NCEM, USA. Exit wave reconstruction by Joerg Jinschek. **(Top right)** Helical reconstruction of microtubules decorated by an Eg5-metallothionein-gold complex. Image: Cedric Bouchet-Marquis. **(Bottom left)** Drill cuttings from a CO₂ injection well. Image: CO2CRC, Australia. **(Bottom right)** 22 nm PMOS transistor structure. Image: FEI NanoPort.

FEI customers find answers that change the world.

Every day, FEI customers prove that deeper understanding of the microscopic world advances health, standards of living, safety, and productivity in our world. We share their passion and their dedication, and we focus all of our capabilities and commitment on one thing. **Their success.**

Learn more at FEI.com



HYSITRON'S NANOMECHANICAL METROLOGY + R&D TOOLS

• TSV | 3D-IC | LOW-K | PACKAGING •



REDEFINING WHAT'S POSSIBLE FOR RESEARCH & PROCESS CONTROL

Cutting-edge technology requires redefined tools to study the material properties for research and process control. Hysitron provides innovative solutions to industry's most challenging mechanical reliability problems with our fully automated, ultra-precise suite of Nanomechanical Metrology Tools (NMT), platform systems, and in-situ (SEM and TEM) instruments.

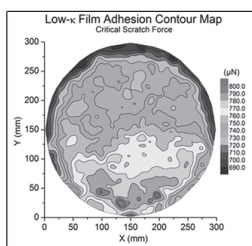
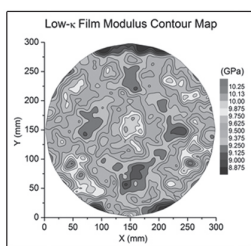
- **NMT Series** – Developed specifically for near-line process control in a 24/7 production environment, the NMT Series provides quantitative nanoscale hardness, modulus, and interfacial adhesion measurements on 200 and 300mm wafers with precision and accuracy.
- **TI Series** – Platform instrument for failure analysis and lab settings.
- **PI Series** – A full line of SEM and TEM in-situ tools for most SEM's and TEM's.

Thin Film Adhesion & Uniformity | Thin Film Mechanical Properties | Bond Pad Hardness & Uniformity | 3D-IC Wafer Bonding
TSV Thermal Cycling | Leadframe Durability | Surface Morphology | Solder Strength & Thermal Stability | And More...

Thin Films

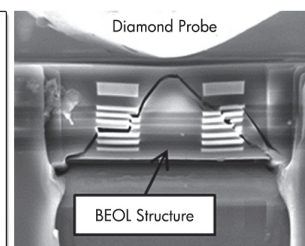
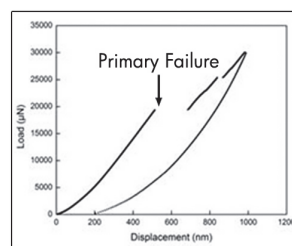
Modulus Mapping: An array of nanoindentation tests performed across the surface of a 200nm thick ULK film on a 300mm wafer reveals local variations in modulus.

Adhesion Mapping: Localized adhesion testing to beyond the wafer edge.

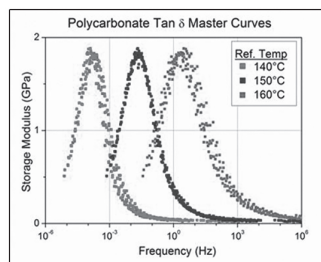


In-Situ Characterization

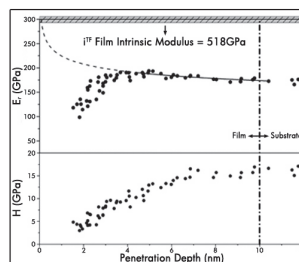
Locate features and directly observe tests using SEM imaging. Synchronized video and data enables cohesive/adhesive failure identification within BEOL structures.



Dynamic Mechanical Analysis



Ultra-Thin Film Modulus



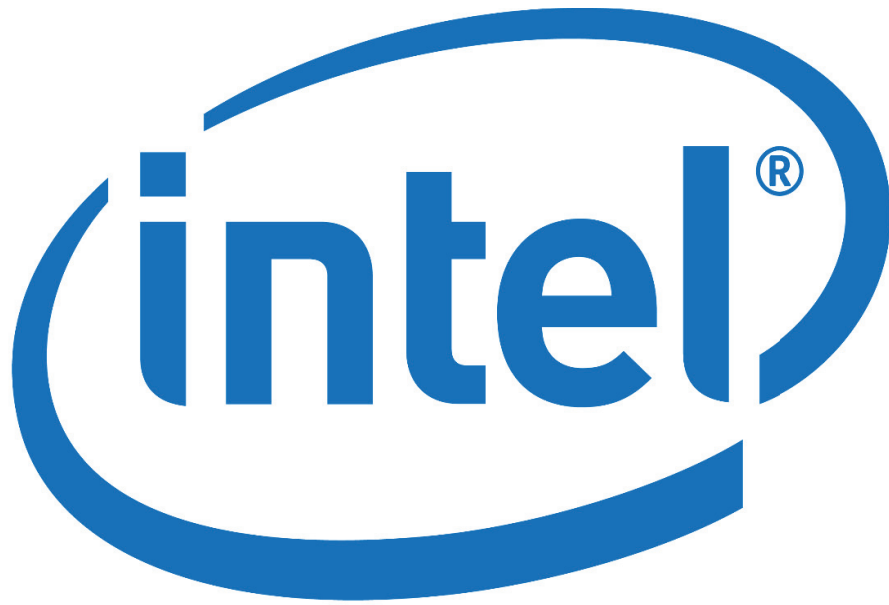
10.1nm TiN
Si
Intrinsic Modulus = 518GPa



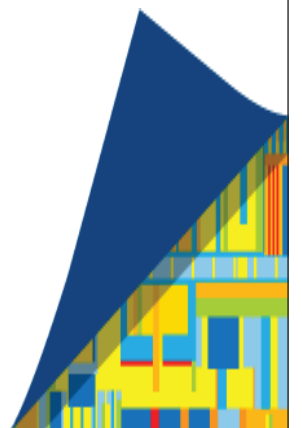
HYSITRON®

Contact us today for more information on Hysitron's Nanomechanical Metrology Tools!

+1-952-835-6366 | info@hysitron.com | www.hysitron.com



Look Inside.™



A world leader in data storage

The Thin-Film Magnetic Head Division of Western Digital is pleased to serve as a corporate sponsor for FCMN 2015

We are grateful for 35 years of support from the metrology community.



wd.com

Your Field Emission SEMs for High Contrast,
Low Voltage Images From Any Sample
ZEISS GeminiSEM Family



The ZEISS GeminiSEM family stands for effortless imaging with sub-nanometer resolution and high detection efficiency, even in variable pressure mode. With the GeminiSEM family you get a flexible and reliable field emission SEM for your research, industrial lab or imaging facility. You always acquire excellent images from any real world sample.



www.zeiss.com/geminiSEM



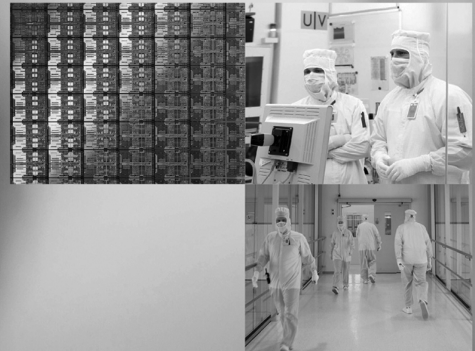
We make it visible.

GLOBALFOUNDRIES is collaborating with the best companies in the world to build the things everyone loves.

Great things don't happen by accident.

They happen when great companies collaborate.

GLOBALFOUNDRIES brings innovative ideas to some of the finest companies in the world. Then works with them to build the next greatest thing.



GLOBALFOUNDRIES®



Supporting semiconductor R&D and mass production with unique tools to measure, image and monitor composition and thickness of advanced materials.



LEAP® 5000

New, high efficiency, high yield Atom Probe for 3D nanoscale analysis of complex structures.

EX-300 Shallow Probe

In-line, contactless, composition & thickness metrology on blanket & patterned wafers: accelerates the time to market of advanced logic & memory devices.



IMS Wf

Fully automated SIMS tool with benchmark ULE depth profiling performance. Highest sensitivity on thin films and implants.

www.cameca.com • cameca.info@ametek.com

Metryx

A Lam Research Company

Providing Process Control with Mass Metrology

Innovative Mass Metrology for Product Wafer Monitoring

- **On Product Wafers**
- **Cost Effective**
- **Fast Response**
- **Improves Productivity**
- **Reduces Risk**

www.metryx.net | info@metryx.net



Dresden Fraunhofer Cluster Nanoanalysis

Ten Fraunhofer Institutes together with TU Dresden and the Helmholtz-Zentrum Berlin have established a joint center as a recognized partner for industry. The Dresden Fraunhofer Cluster Nanoanalysis conducts applied research and development discovering suitable technical and conceptual solutions for advancement of analysis methods, development of components and systems, development of application strategies, and consultation and services.

Applications areas include micro-, nano-, and optoelectronics, renewable energy sources, lightweight construction, and functional materials. Key competencies cover electron and ion microscopy, scanning probe microscopy, spectroscopic, and optical techniques, x-ray analysis, nanomechanical techniques, characterization of nanoparticles, inline metrology, and system integration.

Contact: Tatjana Heller, Phone +49 (0) 351 88 815-609
Tatjana.heller@ikts-md.fraunhofer.de

Address: c/o Fraunhofer IKTS-MD Dresden, Maria-Reiche-Straße 2, 01109 Dresden, Germany

www.nanoanalytik.fraunhofer.de/english/index.html

PROGRAM AT A GLANCE

	Morning	AM Sessions	PM Sessions	Evening
Tuesday Apr. 14 th	7:30 Registration / Attendee Check-in	8:30 Conference Opening 9:00 Keynote Talks 11:45 General	13:45 Microscopy Metrology 15:45 Elec. Char. Metrology for New Memories	16:45 Poster Session
Wednesday Apr. 15 th	8:00 Registration / Attendee Check-in	8:30 Advanced and Novel Characterization Techniques 11:00 Next Generation Defect Inspection	13:30 Characterization for 1D and 2D Electronics 15:30 Metrology for Patterning	19:00 Banquet
Thursday Apr. 16 th	8:30 Registration / Attendee Check-in	9:00 Metrology for CMOS and Beyond 11:00 Nanoscale Thermal and Mechanical Characterization	12:00 3D IC Analysis / Metrology	

Tuesday, April 14

Registration

7:30 – 8:30

Conference Opening

8:30

Conference Opening and Overview

Ehrenfried Zschech (Fraunhofer) and David Seiler (NIST)

Keynote Talks

Session Chair: David Seiler, NIST

9:00

Characterization Challenges In The 28 nm Technology Node 25

Hubert Lakner, Executive Director, Fraunhofer Institute for Photonic Microsystems

9:45

Techno-Economics Pressure In Semiconductor Value Chain May Impact Consumers
And Global Economy – What Is Our Solution? 28

Suresh Venkatesan, Senior Vice President, Technology Development, Global Foundries

10:30

Coffee Break and Poster Viewing

11:00

Nanoelectronics for Metrology 29

Klaus von Klitzing, Max-Planck-Institut FKF

General

Session Chair: Ehrenfried Zschech, Fraunhofer

11:45

Material Requirements for 3D IC and Packaging 31

Bill Bottoms, Chair of Packaging ITRS

12:15

Paradigm Shift in Metrology for Probing 3D-Structures and Confined Volumes . . . 34

Wilfried Vandervorst, Imec

12:45

Lunch and Poster Viewing

Microscopy Metrology

Session Chair: Zhiyong Ma, Intel

13:45

Probing Optical and Electronic Properties of Defects Through Scanning
Transmission Electron Microscopy and First-Principles Theory 35
Steve Pennycook, University of Tennessee

14:15

Strain Characterization at Nanoscale Using Electron Beam Based Techniques . . . 38
Jean-Luc Rouviere, CEA-Leti

14:45

High-resolution X-ray Diffraction of Epitaxial Thin-Films
and Patterned Nanostructures. 41
Matthew Wormington, Jordan Valley Semiconductors Ltd.

15:15

Coffee Break and Poster Viewing

Electrical Characterization Metrology for New Memories

Session Chair: Luigi Colombo, TI

15:45

Characterization of Magnetic Nanostructures for STT-RAM Applications
by Use of Macro- and Micro-Scale Ferromagnetic Resonance 44
Tom Silva, NIST

16:15 – 18:45

Poster Session (with Wine and Cheese)

Wednesday, April 15

Registration

8:00 – 8:30

Advanced and Novel Characterization Techniques

Session Chair: UshaVarshney, NSF

8:30

XRD/TEM/EELS Studies on Memory Device Structures 47
Santosh Kurinec, Rochester Institute of Technology

9:00

Positron Annihilation Spectroscopy Measurements for Porosimetry
Determination of Micro-and Meso-porous Systems 50
Reiner Krause-Rehberg, Martin Luther University Halle, Germany

9:30

Imaging Electron Motion in Nanostructures 53
Bob Westervelt, Harvard

10:00

Advances in Atom Probe Metrology 56
Karen Henry (Intel) and Thomas Kelly (Cameca)

10:30

Coffee Break and Poster Viewing

Next Generation Defect Inspection

Session Chair: Shifeng Lu, Micron

11:00

Scatterfield Microscopy, Including the Fundamental Limits
of Optical Defect Metrology 59
Rick Silver, NIST

11:30

Defect Inspection for Advanced Technology Nodes 63
Tuyen Tran, Intel

12:00

Advances in Multi-Beam SEM Technology for High Throughput
Defect Inspection 66
Gregor Dellemann, Carl Zeiss Microscopy GmbH

12:30

Lunch and Poster Viewing

Characterization for 1D and 2D Electronics

Session Chair: Amal Chabli, CEA-Leti

13:30

Silicidation and Strain Analysis in Si Nanowires 69

Walter Weber and Markus Löffler, Technical University Dresden, Germany

14:00

2D Materials Beyond Graphene for Future Electronics 72

Frank Schwierz, TU-Ilmenau, Germany

14:30

Raman Spectroscopy in Graphene 76

Andrea Ferrari, Univ. of Cambridge

15:00

Coffee Break and Poster Viewing

Metrology for Patterning

Session Chair: Stefan Zollner, NMSU

15:30

Metrology Challenges Towards N7. 77

Philippe Leray, Imec

16:00

Current Status of CDSAXS: Is it Fab-Ready? 79

Joe Kline, NIST

19:00

Banquet

Thursday, April 16

Registration

8:30 – 9:00

Metrology for CMOS and Beyond

Session Chair: Wilfried Vandervorst, Imec

9:00

CMOS Characterization/Metrology Challenges for the Lab to the Fab 82

Paul van der Heide, Global Foundries

9:30

Recent Progress in Advanced in-line Metrology for High-Mobility
Semiconductors 85

Andreas Schulze, Imec

10:00

Thermal Wave Analysis of Implanted Layers in Semiconductors:
Measurement Performance vs. Process Requirements 88

Nicolas Siedl, Infineon

10:30

Coffee Break and Poster Viewing

Nanoscale Thermal and Mechanical Characterization

Session Chair: Scott List, Intel

11:00

Combined Nanoindentation and AFAM for Mechanical Characterization
of Ultra Low-k Thin Films 92

Andre Clausner, Fraunhofer IKTS Dresden, Germany

11:30

Phase Change Properties and Strain Engineering in 2D Materials 95

Evan Reed, Stanford University

3D IC Analysis/Metrology

Session Chair: Martin Gall, Fraunhofer

12:00

Thermo-Mechanical Reliability of TSVs 98

Paul Ho, UT Austin

12:30

Lunch and Poster Viewing

13:30

Challenges and Solutions for Chip-Package Interaction 101
Kris Vanstreels, Imec

14:00

DFM and DFR Requirements for 3D Stacked Systems to Materials Data
and Characterization Techniques 104
Valeriy Sukharev, Mentor Graphics

14:30

Process and Materials Characterization: Perspectives from Wafer Level
Processing for Packaging 107
Sesh Ramaswami, Applied Materials

15:00

X-ray Tomography for Process Development and Failure Analysis 108
Jürgen Gluch, TU Dresden/Fraunhofer IKTS

15:30

New Scanning Acoustic Microscopy Technologies Applied
to 3D Integration Applications 110
Peter Czurratis, PVA Tepla

16:00

Conference End

Poster Presentations

- 1. Optical Constants of Ni_{1-x}Pt_x and Ni_{1-x}Pt_xSi for In-Line Contact Metrology. 112**
Lina S. Abdallah^{1,}, Stefan Zollner¹, Mark Raymond², Ahmet S. Ozcan³, and Christian Lavoie⁴*
¹Department of Physics, New Mexico State University, MSC 3D, Las Cruces, NM, USA
²GLOBALFOUNDRIES, Albany, NY, USA
³IBM, 850 rue Jean Monnet, 38926 Crolles, France
⁴IBM Research Division, Yorktown Heights, NY, USA
^{*}Now at: Intel Corporation, 2501 Northwest 229th Avenue, Hillsboro, OR, 97124, USA
- 2. Metallic Contamination Analysis of 450 mm Wafers Using VPD-DC-ICPMS and LPD-ICPMS 115**
C. Agraffeil¹, H. Fontaine¹, T. Lardin¹, V. Enyedi¹, D. Noventa¹, B. Charlet¹, G. Delpu², and T. Brillouet²
¹Univ. Grenoble Alpes, F-38000 Grenoble, France - CEA, LETI, MINATEC Campus, F-38054 Grenoble, France
²RECIF Technologies, 9 Rue des briquetiers, 31703 Blagnac, France
- 3. Positron Annihilation Spectroscopy: an Emerging Technique for Characterization of Oxygen Vacancies in Hf-based-high-k Materials? 118**
M. Alemany^{1,4,3}, P. Desgardin⁴, A. Chabli², F. Bertin³, M. Gros-Jean¹, M.-F. Barthe⁴
¹STMicroelectronics, 850 rue Jean Monnet, 38926 Crolles, France
²Univ. Grenoble Alpes, INES, F-73375 Le Bourget du Lac, France, CEA, LITEN, Department of Solar Technologies, F-73375 Le Bourget du Lac, France
³Univ. Grenoble Alpes, F-38000 Grenoble, France, CEA, LETI, MINATEC Campus, F-38054 Grenoble, France
⁴CNRS, CEMHTI UPR3079, Univ. Orléans, F-45071 Orléans, France
- 4. Further Development of Electron Tomography 122**
M. Birke, D. Utess, E. Langer, and H.-J. Engelmann
GLOBALFOUNDRIES Module One LLC & Co. KG, Center for Complex Analysis, MS E23-MA, D-01109 Dresden, Germany
- 5. Development and Characterisation of Scatterometry Reference Standards 125**
Bernd Bodermann¹, Bernd Loechele², Frank Scholze¹, Johannes Endres¹, Juergen Probst², Matthias Wurm¹, Max Schoengen², Michael Krumrey¹, Sven Burger³, and Victor Soltwisch¹
¹Physikalisch-Technische Bundesanstalt, Bundesallee 100, 38116 Braunschweig and Abbestraße 2-12, 10587 Berlin, Germany
²Helmholtz-Zentrum Berlin für Materialien und Energie GmbH, Albert-Einstein-Str. 15, D-12489 Berlin, Germany
³JCMwave GmbH, Bolivarallee 22, D-14050 Berlin, Germany
- 6. Non-conventional Structural and Chemical Characterisations for the Industry of Nano-electronics 128**
E. Capria^{1,8}, J. Beaucourt², I. Bertrand⁶, N. Bicaïs³, E. Boller¹, C. Curfs^{4,5}, G. Chahine¹, A. Fitch¹, R. Kluender^{4,5}, T.A. Lafford¹, Y.M. Le-Vaillant⁶, F. Lorut³, J.S. Micha^{4,7}, E. Mitchell¹, O. Robach^{4,7}, J.C. Royer^{4,5}, T.U. Schüllj¹, and J. Segura-Ruiz^{2,8}
¹European Synchrotron Radiation Facility, Grenoble, France
²Institute Laue-Langevin, Grenoble, France
³ST Microelectronics, France
⁴Univ. Grenoble Alpes, F-38000 Grenoble, France
⁵CEA LETI, MINATEC Campus, F-38054 Grenoble, France
⁶SOITEC, France
⁷CEA/INAC and CNRS, Grenoble, F-38054, France
⁸IRT NanoElec Advanced Characterisation Platform, Grenoble, France
- 7. Nanostructure Imaging on Plasmonic Gratings by Epi-fluorescence Microscopy 130**
Biyen Chen¹, Sangho Bok¹, Samiullah Pathan¹, Suresh Dhananjay², Anandhi Upendran³, Raghuraman Kannan⁴, Cherian Mathai¹, Keshab Gangopadhyay^{1,5}, and Shubhra Gangopadhyay¹
¹Dept of Elec. and Comp. Eng., Univ. of Missouri, Columbia, MO, USA
²Department of Bioengineering, University of Missouri, Columbia, MO 65211, USA
³School of Medicine, University of Missouri, Columbia, MO 65211, USA
⁴Department of Radiology and Biological Engineering, University of Missouri, Columbia, MO 65211, USA
⁵Nanos Technologies LLC, 8650 Westlake Road, Columbia, MO 65202, USA

8. Quantifying Ellipsometric Precision for Multichannel Rotating-Element Spectroscopic Ellipsometers	133
<i>Yong Jai Cho, Won Chegal, Jeong Pyo Lee, and Hyun Mo Cho</i>	
Division of Industrial Metrology, Korea Research Institute of Standards and Science, 267 Gajeong-ro, Yuseong-gu, Daejeon 305-340, Republic of Korea	
9. Sub-10 nm-thick-carbon Nanotube Tip for AFM.	136
<i>J. Choi^{1,2}, K. Y. Jung³, S. K. Kanth^{1,4}, B. C. Park¹, H. S. Kim⁴, and L. Joon²</i>	
¹ Korea Research Institute of Standards and Science, Daejeon 305-340, South Korea	
² Chungnam National University, Daejeon 305-764, South Korea	
³ Nanofocus Inc., Seoul 152-050, South Korea	
⁴ Sunmoon University, Asan 336-708, South Korea	
10. 300 mm and 450 mm Standard Calibration Wafers – A Standard Tool for Semiconductor Metrology Calibration and Matching	139
<i>Rand Cottle¹, Menachem Shoval², Yuval Agami², Frank Tolic³, Stephen Bennett³, and Martin Rodgers³</i>	
¹ Global 450mm Consortium, CNSE at SUNY Polytechnic Institute, Albany, NY	
² Metro450 Consortium, Office of Chief Science, MAGNET program, Tel Aviv, Israel	
³ CNSE, Colleges of Nanoscale Science and Engineering at SUNY Polytechnic Institute, Albany NY	
11. Non-Destructive Compositional Metrology of NAND Memory and Emerging Non-Volatile Memories	141
<i>Olivier Dulac, Anna Meura, Anne-Sophie Robbes, Mona Moret and David J. Larson</i>	
CAMECA, 29 quai des Grésillons, 92 622 Gennevilliers, France	
12. Liquid-metal-jet X-ray Tube Technology for Nanoelectronics Characterization and Metrology	144
<i>E. Espes, B. A. M. Hansson, O. Hemberg, G. Johansson, M. Otendal, T. Tuohimaa, and P. Takman</i>	
Excillum AB, Torshamnsgatan 35, 164 40 Kista, Sweden	
13. Breakthrough of STEM and FIB Automation in Critical Dimension Metrology of Wafer Manufacturing	147
<i>Jianxin Fang, Wei Hong, Jose Garjado, Juanita Castillo, Zhipeng Li, and Haifeng Wang</i>	
Western Digital Corporation, 44100 Osgood Road, Fremont, CA 94539, USA	
14. Electron Energy-Loss Spectroscopy (EELS) Analysis on MoS₂ Layers Transferred on Silicon	149
<i>Karine Florent¹, David MacMahon², Andrea Brothers², and Santosh Kurinec¹</i>	
¹ Microelectronic Engineering, Rochester Institute of Technology, Rochester NY, USA	
² Micron Technology Inc., Manassas, VA, USA	
15. Characterization of Near- to Far-Field Transformers by Interferometric Fourier-Scatterometry	151
<i>K. Frenner, V. Ferreras-Paz, and W. Osten</i>	
Institut für Technische Optik (ITO), Universität Stuttgart, Pfaffenwaldring 9, D-70569 Stuttgart	
16. Transmitted Small Angle X-Ray Scattering Intensity Enhancement with a Designed Grating	154
<i>Wei-En Fu, Yen-Song Chen, Yun-San Chien, and Wen-Li Wu</i>	
Center for Measurement Standards, Industrial Technology Research Institute, 321 KuangFu Rd Sect 2, Hsinchu, Taiwan, ROC	
17. Potential of the EsB Detector in the Low Voltage Scanning Electron Microscopy (LVSEM): Application in Microelectronics.	157
<i>Aránzazu Garitagoitia Cid^{1,2}, Rüdiger Rosenkranz¹, Martin Gall¹, and Ehrenfried Zschech^{1,2}</i>	
¹ Fraunhofer Institute for Ceramic Technologies and Systems - Materials Diagnostics (IKTS-MD), Maria-Reiche-Str. 2, 01109 Dresden, Germany	
² Dresden Center for Nanoanalysis (DCN), TU Dresden, 01062 Dresden, Germany	

- 18. Correlative Atom Probe and STEM-HAADF Tomography of Nanodevices 159**
A.Grenier¹, S.Duguay², R.Serra¹, J.P. Barnes¹, G Audoit¹, D Cooper¹, D. Blavette², N. Rolland², and F. Vurpillot²
¹Univ. Grenoble Alpes, F-38000 Grenoble, France, CEA, LETI, MINATEC Campus, F-38054 Grenoble, France
²Groupe de Physique des Matériaux, UMR 6634 CNRS – Université de Rouen, BP 12, 76801 Saint Etienne du Rouvray Cedex, France
- 19. Impact of Line Edge Roughness Patterns on the Reconstructed Critical Dimensions in Scatterometry 162**
H. Gross¹, S. Heidenreich¹, M.-A. Henn¹, F. Scholze¹, G. Dai¹, A. Rathsfeld², and M. Bär¹
¹Physikalisch-Technische Bundesanstalt, Braunschweig and Berlin, Germany
²Weierstrass Institute for Applied Analysis and Stochastics, Berlin, Germany
- 20. Electron Tomography of Advanced Transistor Architectures 164**
Andrew A. Herzing¹ and Jiong Zhang²
¹Material Measurement Laboratory, National Institute of Standards and Technology, Gaithersburg, MD 20899 USA
²Intel Corp., 2501 NW 229th Ave, Hillsboro, OR, 97124 USA
- 21. Reference-free, Depth-dependent Characterization of Nanoscaled Materials Using a Combined Grazing Incidence X-ray Fluorescence and X-ray Reflectometry Approach . . 167**
Philipp Hönicke¹, Blanka Detlefs², Claudia Fleischmann³, Matthias Müller¹, Emmanuel Nolot², Helen Grampeix², and Burkhard Beckhoff¹
¹Physikalisch-Technische Bundesanstalt (PTB), Abbestr. 2-12, 10587 Berlin, Germany
²CEA-LETI, 17 rue des Martyrs, 38054 Grenoble, France
³imec, Kapeldreef 75, BE-3001 Leuven, Belgium
- 22. Extreme Ultraviolet Nanometrology for Imaging of New Dynamics in NanoSystems. . . . 170**
Kathleen Hoogeboom-Pot¹, Jorge Hernandez-Charpak¹, Dennis Gardner¹, Matthew Seaberg¹, Bosheng Zhang¹, Travis Frazer¹, Elisabeth Shanblatt¹, Christina Porter¹, Robert Karl¹, Erik Anderson², Weilun Chao², Justin Shaw³, Margaret Murnane¹, Henry Kapteyn¹, Daniel Adams¹, and Damiano Nardi¹
¹JILA, 440 UCB, University of Colorado, Boulder CO 80309
²Center for X-Ray Optics, Lawrence Berkeley National Laboratory, Berkeley, CA 94720
³Electromagnetics Division, NIST, Boulder, CO 80305
- 23. Simulation of Ga Ion Induced Amorphization in Si During FIB Using TRIDYN Simulation . 173**
Jin Huang¹, Markus Loeffler¹, Wolfhard Moeller² and Ehrenfried Zschech^{1,3}
¹Technische Universität Dresden, Dresden Center for Nanoanalysis (DCN), Helmholtzstrasse 18, 01187 Dresden, Germany
²Institute of Ion Beam Physics and Materials Research, Helmholtz-Zentrum Dresden-Rossendorf, Bautzner Landstr. 400, 01328 Dresden, Germany
³Fraunhofer Institute for Ceramic Technologies and Systems (IKTS), Maria-Reiche-Strasse 2, 01109 Dresden, Germany
- 24. Characterization of Cross-Sectional Profile of Resist Pattern Using Grazing-Incidence Small Angle X-Ray Scattering. 176**
Yoshiyasu Ito, Akifusa Higuchi, and Kazuhiko Omote
Rigaku Corporation, 3-9-12 Matsubara-cho, Akishima, Tokyo, Japan 190-8666
- 25. Metamorphic Growth-Related Defects and Electrical Properties in III-Sb Materials for High-Mobility p-MOSFETs 179**
A. P. Jacob¹, S. Madiseti², S. Sasaki², V. Tokranov², M. Yakimov², M. Hirayama², S. Bentley¹, and S. Oktyabrsky²
¹GLOBALFOUNDRIES at Albany NanoTech, Albany, NY 12203, USA
²SUNY College of Nanoscale Science and Engineering, Albany NY 12203, USA
- 26. Analysis of Defects in SiGe and Ge 183**
Abhijeet Joshi and James Ewan
Active Layer Parameterics, Inc., Los Angeles, CA 90024

- 27. In-Situ Real-Time Monitoring and Control of Kinetic Processes in Atomic Layer Depositions by Spectroscopic Ellipsometry with 1.25 Hz Sampling Rate 186**
Marcel Junige¹, Varun Sharma¹, Ralf Tanner¹, Daniel Schmidt², Greg Pribil³, Matthias Albert¹, Mathias Schubert², and Johann W. Bartha¹
¹Technische Universität Dresden, Institute of Semiconductors and Microsystems, 01062 Dresden, Germany
²Singapore Synchrotron Light Source, National University of Singapore, Singapore 117603, Singapore
³J. A. Woollam Co. Inc., 645 M Street, Suite 102, Lincoln, Nebraska 68508-2243, USA
⁴Department of Electrical Engineering, University of Nebraska-Lincoln, Lincoln, Nebraska 68588-0511, USA
- 28. Characterization of Plasma Process Induced Damage Near SiN/SiO₂/Si Interface by Room Temperature Photoluminescence 189**
Jung Geun Kim¹, Ho Jin Cho¹, Sung Ki Park¹, Seok-Hee Lee¹, Byoung Gon Choi², Jea Young An², Young Il Cheon², Young Ho Jeon², Toshikazu Ishigaki³, Kitaek Kang³, and Woo Sik Yoo³
¹SK hynix, Icheon, Gyeonggi-do, 467-701, Korea
²SK hynix, Cheongju, Chungcheongbuk-do, 361-480, Korea
³WaferMasters, Inc., San Jose, California, 95112, USA
- 29. Application of Raman Spectroscopy for Local Stress Methodology and Characterization of Amorphous Carbon and SiGe Films in Semiconductor Process Development. 192**
Jae Hyun Kim^{1,2}, Chang Hwan Lee², Koon Ho Bae², and Seung Min Han¹
¹Graduate School of EEWS, Korea Advanced Institute of Science and Technology, 291 Daehak-ro, Yuseong-gu, Daejeon 305-701, Korea
²SK Hynix, 2091, Gyeongchung-daero, Bubal-eub, Icheon-si, Gyeonggi-do, South Korea
- 30. Positron Annihilation Lifetime Spectroscopy (PALS) on Advanced, Self-assembled Porous Organosilicate Glasses 195**
M. Kraatz¹, A. Clausner¹, M. Gall¹, E. Zschech¹, M. Butterling², W. Anwand³, A. Wagner³, R. Krause-Rehberg², and K. Pakbaz⁴
¹Fraunhofer Institute for Ceramic Technologies and Systems – Materials Diagnostics, Maria-Reiche-Str. 2, 01109 Dresden, Germany
²Department of Physics, Martin Luther University Halle-Wittenberg, Von-Danckelmann-Platz 3, 06120 Halle Germany
³Institute of Radiation Physics, Helmholtz-Zentrum, Dresden-Rossendorf, P.O. Box 510119, 01314, Dresden, Germany
⁴SBA Materials, Inc., Albuquerque, 9430-H San Mateo Blvd. NE, New Mexico 87113, USA
- 31. Terahertz Time-Domain Spectroscopy for Characterization of Doping Profiles in Semiconductors. 198**
Santosh Kurinec¹, Chih Yu Jen¹, Gaurav Tulsyan², and Christiaan Richer³
¹Microsystems Engineering, Rochester Institute of Technology, Rochester, NY 14623, USA
²Materials Science & Engineering, Rochester Institute of Technology, Rochester, NY 14623, USA
³Department of Chemical Engineering, Rochester Institute of Technology, Rochester, NY 14623, USA
- 32. Real-Time Monitoring of Thin-Films Using Temperature-Controlled Ellipsometry for Nanotechnology Applications 201**
C. Licitra, F. Piegas Luce, F. Mazen, P. Noé, J. El-Sabagy, V. Jousseau, E. Beche, and L. Vignoud
Univ. Grenoble Alpes, F-38000 Grenoble, France
CEA, LETI, MINATEC Campus, F-38054 Grenoble, France
- 33. High Precision X-Ray Multilayer Mirrors for Customized Solutions 204**
S. Niese¹, M. Krämer¹, T. Holz¹, P. Krüger², S. Braun³, E. Zschech², and R. Dietsch¹
¹AXO DRESDEN GmbH, Gasanstaltstr. 8b, 01237 Dresden, Germany
²Fraunhofer IKTS-MD, Maria-Reiche-Str. 2, 01109 Dresden, Germany
³Fraunhofer IWS Dresden, Winterbergstr. 28, 01277 Dresden, Germany

- 34. Analysis of Surfaces for Immobilization of Biomolecules Using Soft X-Ray Spectrometry 206**
*A. Nutsch¹, C. Streeck¹, J. Weser¹, B. Beckhoff¹, D. Grötzsch², W. Malzer², P. Dietrich³, T. Fischer³,
C. Nietzold³, K. Rurack³, and W. Unger³*
¹Physikalisch-Technische Bundesanstalt (PTB), Abbe Strasse 2-12, 10587 Berlin, Germany
²Technische Universität Berlin, Hardenbergstr. 3610623 Berlin, Germany
³Bundesanstalt für Materialforschung und -prüfung (BAM), Unter den Eichen 87, 12205 Berlin, Germany
- 35. Application of Helium Ion Microscopy to Direct Nano-patterning of Graphene. 209**
Shinichi Ogawa and Yuichi Naito
Nanoelectronics Research Institute, National Institute of Advanced Industrial Science and Technology (AIST) West 7A, 16-1 Onogawa, Tsukuba, Ibaraki 305-8569 Japan
- 36. Sensitive Nanomaterials Detection and Analysis in Solution 211**
Janahan Ramanan¹, Basil G. Eleftheriades¹, Bhagrava Ravoori², Marie Tripp², Tuyen K. Tran², and Amr S. Helmy¹
¹Department of Electrical and Computer Engineering, University of Toronto, Toronto M5S 3G4, Canada
²Intel Corporation, Hillsboro, OR, USA
- 37. In-Die High Resolution Nanotopography Data, Impact in the CMP Process Monitoring for Advanced Nodes 214**
N. Ruiz¹, F.Dettoni², M. Rivoire^{1,2}, V.Balan¹, and C. Beitia¹
¹Univ.Grenoble Alpes, F-38000 Grenoble France, CEA, LETI, MINATEC Campus, F-38054 Grenoble, France
²STMicroelectronics, 850 rue Jean Monnet, 38926 Crolles, France
- 38. High Resolution X-ray Diffraction for in-line Monitoring of Ge MOSFET Devices. 217**
Paul Ryan¹, Matthew Wormington², Jianwu Sun^{3,4}, Andriy Hikavyi³, Yosuke Shimura^{3,5,6}, Liesbeth Witters³, Hilde Tielens³, and Roger Loo³
¹Jordan Valley Semiconductors UK Ltd, Belmont Business Park, Belmont Durham, DH1 1TW, UK
²Jordan Valley Semiconductors Inc., 3913 Todd Lane, Suite 106, Austin, TX 78744, USA
³IMEC, Kapeldreef 75, B – 3001 Leuven, Belgium
⁴Currently at the Department of Physics, Chemistry and Biology (IFM), Linköping University, Linköping 58183, Sweden
⁵Instituut voor Kern- en Stralingsfysica, KU Leuven, 3001 Leuven, Belgium
⁶FWO Pegasus Marie Curie Fellow
- 39. Advanced Metrology for Beyond Silicon Semiconductor Device Structures 220**
Andreas Schulze¹, Roger Loo¹, Johan Meersschaut¹, Dennis van Dorp¹, David Gachet², Jean Berney², Wilfried Vandervorst^{1,3}, and Matty Caymax¹
¹imec, Kapeldreef 75, 3001 Leuven, Belgium
²Attolight AG, EPFL Innovation Park Building D, 1015 Lausanne, Switzerland
³KU Leuven, Dept. of Physics and Astronomy, Celestijnenlaan 200D, 3001 Leuven, Belgium
- 40. Advanced Broadband Optical Inspection on Complex Logic Structures Using NanoPoint at 28nm Design Nodes. 224**
Robert Teagle¹, Hoang Nguyen¹, Ralf Buengener¹, Peter Lin¹, Ankit Jain², Sumanth Kini², Rahul Lakhawat², and Ravi Sanapala²
¹GLOBALFOUNDRIES, 400 StoneBreak Road Extension, Malta, NY 12020
²KLA-Tencor, 2 Bayberry Drive, Malta, NY 12020
- 41. Conductive Diamond Probes for Advanced Atomic Force Microscopy 226**
V. Usov^{1,2,3}, N. O'Hara^{2,3}, Z. Xiapu^{1,2}, D. Scanlan^{2,3}, A. Potie^{1,2}, J. Boland^{1,2}, and G.L.W. Cross^{1,2,3}
¹School of Physics, Trinity College, Dublin 2, Ireland
²Advanced Materials and BioEngineering Research Centre (AMBER), Trinity College, Dublin 2, Ireland
³Adama Innovations Ltd., CRANN, Trinity College Dublin, Dublin 2. Ireland
- 42. Sub 20 nm Particle Inspection on EUV Mask Blanks 228**
Peter Bussink, Jean-Baptiste Volatier, Peter van der Walle, Erik Fritz, and Jacques van der Donck
TNO, P.O. Box 155, 2600 AD, Delft, The Netherlands

43. Three-Dimensional SEM Metrology for Nanoelectronics	231
<i>András E. Vladár and John S. Villarrubia</i>	
National Institute of Standards and Technology, Semiconductor and Dimensional Metrology Division, Physical Measurements Laboratory, Gaithersburg, MD 20899 USA	
44. Grazing Incidence X-ray Fluorescence (GI-XRF) for Thin Film and Ultra-thin Film Thickness Metrology.	234
<i>Charles C Wang, Nimoal Sun, Jiang Lu, Weifeng Ye, Chi Ching, and Yuri Uritsky</i>	
Applied Materials, Inc., M/S 0203, 3100 Bowers Ave, Santa Clara, CA 95054	
45. Robust Optical Modeling of SiGe Layers.	237
<i>Martin Weisheit¹, Robert Melzer¹, Henry Bernhardt¹, and Adam Urbanowicz²</i>	
¹ GLOBALFOUNDRIES Module 1 LLC & Co. KG, Wilschdorfer Landstraße 101, D-01109 Dresden	
² now at Nova Measuring Instruments	
46. Effects of Image Processing on Electron Diffraction Patterns Used for Nanobeam Diffraction Strain Measurements	240
<i>Mark Williamson¹, Piet van Dooren¹, and John Flanagan²</i>	
¹ FEI Company, Achtseweg Noord 5, 5651 GG Eindhoven, The Netherlands	
² FEI Company, 5350 NE Dawson Creek Drive, Hillsboro, OR 97124	
47. Measurement Range Induced Electron Density Perturbations in X-Ray Reflectometry . . .	243
<i>Donald Windover</i>	
Materials Measurement Science Division, Materials Measurement Laboratory, National Institute of Standards and Technology, Gaithersburg, MD 20899, USA	
48. 2D and 3D Nanoscale Measurements of Electric and Magnetic Fields in Functional Materials with Electron Holography.	246
<i>Daniel Wolf, Felix Börrnert, Jonas Krehl, Andreas Lenk, Hannes Lichte, Axel Lubk, Falk Röder, Jan Sickmann, Sebastian Sturm, and Karin Vogel</i>	
Triebenberglaboratory, Institute of Structure Physics, Technische Universität Dresden, 01062 Dresden, Germany	
49. Barrier Modification of Metal-contact on Silicon by Sub-2 nm Platinum Nanoparticle . . .	249
<i>H. Zheng¹, S.C. Su¹, S. Mukherjee¹, K. Gangopadhyay^{1,2}, and S. Gangopadhyay¹</i>	
¹ Department of Electrical and Computer Engineering, University of Missouri Columbia, Missouri 65201, U.S.A.	
² Nanos Technologies LLC, Columbia, Missouri 65203	

Characterization Challenges in the 28 nm Technology Node

H. Lakner, R. Liske, E. Reich, M. Drescher

*Fraunhofer IPMS - Center Nanoelectronic Technologies (CNT),
Königsbrücker Straße 178, 01099 Dresden, Germany*

Corresponding author: phone +49 351 8823 111, hubert.lakner@ipms.fraunhofer.de

Nanoelectronic devices consist of many different materials covering the whole range of electronic properties, e.g. metals, insulators and semiconductors. Each material is tuned for highest performance, while the amount of material needed for one electronic device rapidly decreases according to the device scaling.

Due to the ever smaller dimensions the effort to characterize materials on a nanometer scale increases tremendously. With the ongoing development of aberration corrected high resolution (S)TEM and 3D atom probe tomography suitable characterization methods exist to measure accurate film thickness and film composition on the nanoscale. However, the successful use of those techniques requires a challenging as well as time and cost consuming sample preparation which does not correspond with the speed of process optimization under industrial conditions. The combination of the need for speed and the not diminished expectation for high resolution imaging and spectroscopy is one major frontier in the characterization of nanoelectronics.

One of most engineered material stacks in the 28 nm technology node is the high-k metal gate stack. It substituted the formerly gate stack consisting of a silicon channel, a SiO₂ gate oxide and a poly-Si gate. In the 28 nm technology, new materials are introduced. Faster switching demands require a reduction in channel lengths and the leakage limitation constraints lead to the introduction of high-k materials. Then, optimizing the drain current involves the deposition of a metal gate possessing a higher electrical conductivity than poly-Si, and thus preventing poly-depletion and fermi-level pinning at the poly-Si/HfO₂ interface¹. To improve mobility and further adjust threshold voltage, SiGe is used as channel covered by an interfacial and a high-k oxide, followed by a metal gate and completed with poly-Si. Altogether, there are five different complex material-systems in a high-k metal gate stack on a thickness scale of 10 nm (Figure 1).

To characterize the film thicknesses and composition of the gate materials, conventional uncorrected brightfield HR-TEM is not sensitive enough. In this example the TEM resolution is insufficient to differentiate between thin and interfacial layers (Figure 2). A combination of imaging and EDX mapping already enhances the contrast to differentiate between channel, high-k oxide and metal gate in a reasonable time frame. The EDX resolution however is insufficient to detect impurities. Other electron microscopy techniques, such as aberration corrected STEM in combination with electron energy loss spectroscopy (EELS) is capable of resolving the gate stack layers and detecting impurities in the material. Although, sample preparation time and cost have to be taken into account in order to find a balance between the needs of the industry and the efforts which are put in the analysis.

Necessary 3D spatial information regarding impurities can be obtained using atom probe tomography. Here, surface atoms are evaporated from a very sharp sample tip by laser or HV pulsing. Measuring the mass over charge ratio, the X-Y position and the order of arrival of the ions on the detector allow reconstructing the composition and the original position of the atoms on the tip. The result is a 3D reconstruction of the film stack composition (Figure 1 right). For the high-k metal gate stack, atom probe tomography reveals that there is hardly any layered structure visible. Instead, the gate stack consists of overlapping interfaces.

At that stage of characterization, the most important question remains: Is the observed material intermixing real, e.g. does it originate from interdiffusion within the gate stack or is it an artefact from sample preparation, measurement conditions or the reconstruction process?

In order to answer that question there are two possibilities. Optimizing sample preparation as well as measurement conditions is one approach to reduce the risk of artefacts and consequently the risk of false data interpretation. But as stated before this is time and cost consuming.

Another elegant and rather fast approach is to combine these TEM and atom probe tomography results to other characterization methods. In production environment, electrical device characterization is very common for process optimization and performance characterization. The advantage of electrical measurements is their simplicity, velocity and degree of automation.

The complexity of analytical preparation and characterization methods seems to be one reason, why it is so difficult to predict the future of the device scaling. Although the 28 nm node is already commercialized and used especially in wearable devices, fundamental questions regarding material properties and interaction still remain open. However, understanding the 28 nm technology in much more detail is an important prerequisite for the nanoelectronic industry to further optimize their products with respect to power, performance and energy efficiency.

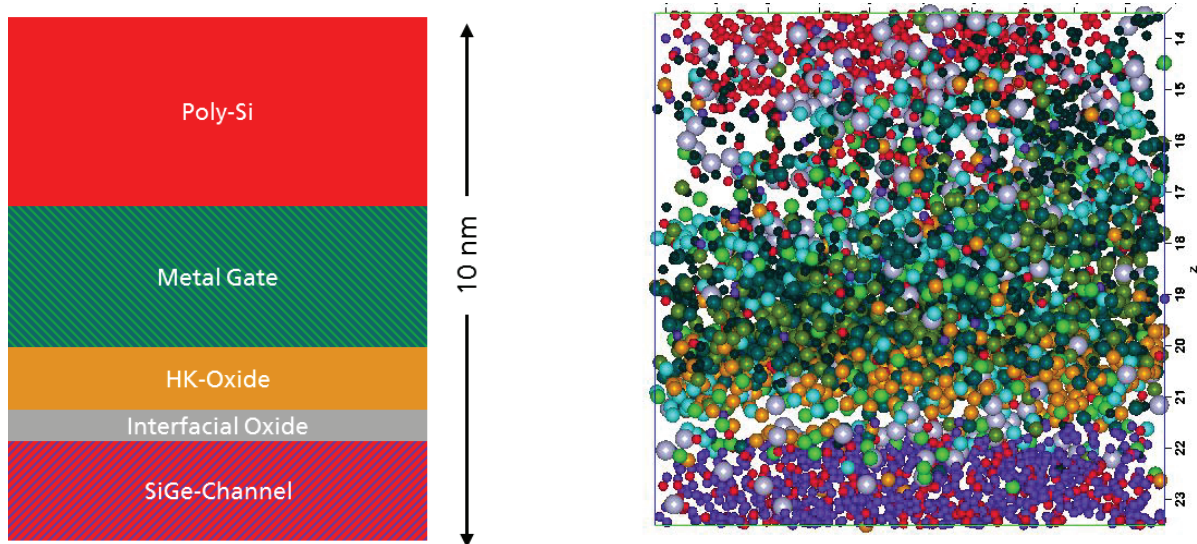


FIGURE 1. High-k metal gate film stack reconstructed by 3D atom probe.

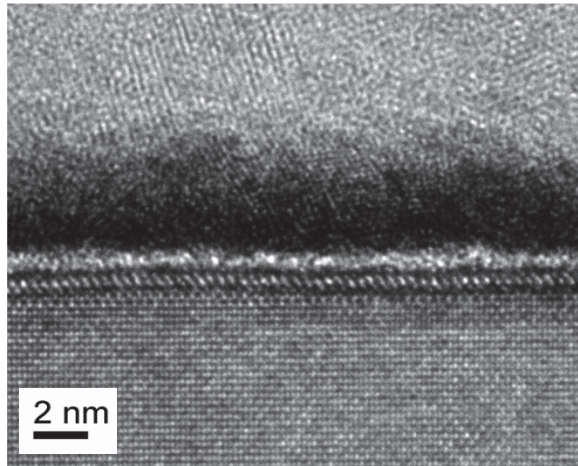


FIGURE 2. Brightfield TEM of a high-k metal gate stack.

REFERENCES

1. Hobbs, C.C., Fonseca, L. R. C.; Knizhnik, A., "Fermi-level pinning at the polysilicon/metal oxide interface-Part I". *Electron Devices, IEEE Transactions on (IEEE)* **51** (6): 971–977, 2004.

KEYWORDS

Characterization, nanoelectronics, sample preparation, high-k metal gate, TEM, atom probe tomography

Techno-Economics Pressure In Semiconductor Value Chain May Impact Consumers And Global Economy – What Is Our Solution?

Dr. Suresh Venkatesan, Sr. Vice President, Technology Development
GLOBALFOUNDRIES

INTRODUCTION

Semiconductors are only a fraction of Gross World Product, but a critical enabler of Global Economic Growth and Productivity. Cost effective technology innovations have kept Moore's law alive, although techno-economic challenges are mounting on each successive node. The cost of building a new advanced fab has reached \$6B. Process development and chip design costs are going up astronomically, while next generation SoCs in the IoT era are pushing cost-per-function to unprecedented levels. This Keynote will review the impact of cost pressure building up in the Semiconductor Value chain and possible Solutions to mitigate impact to Consumers and World economy.

Nanoelectronics For Metrology

Klaus von Klitzing

*Max Planck Institute for Solid State Research
Heisenbergstr.1
D-70569 Stuttgart
Germany*

INTRODUCTION

Metrology, the science of measurements, needs reliable measurement units. Starting with the “Meter Convention” in 1875, a worldwide agreement exists for standards and units which guarantee international uniformity. Today, seven base units are used (international system of units, SI units) which form the basis for all measurements. These fundamental units are: the second for time, the meter for length, the kilogram for mass, the kelvin for temperature, the ampere for electric current, the candela for luminous intensity, and the mole for the amount of substance. The General Conference on Weights and Measures, which meets in Paris since 1889 in roughly 4-year intervals, is responsible for the best definitions of base units in respect of accuracy and stability. In this way the meter definition changed during the last 100 years from a prototype (related to the one ten millionth part of the quarter of the terrestrial meridian) to a definition of 1,650,763.73 wavelengths of a special spectral line of the Krypton-Isotope ^{86}Kr to a fixed value of the velocity of light.

Since fundamental constants are the most stable quantities in our universe, the General Conference on Weights and Measures announced at his last meeting in November 2014 that a new SI system based on constants of nature may be recommended at the next meeting in 2018. Max Planck, who introduced two fundamental constants in his equation for the black body radiation (today known as Boltzmann constant k_B and Planck constant h), already mentioned in his most famous publication [1] that: “...with the help of fundamental constants we have the possibility of establishing units of length, time, mass, and temperature, which necessarily retain their significance for all cultures, even unearthly and nonhuman ones..”. Unfortunately, the Planck units cannot be reproduced experimentally with high accuracy so that an application in metrology was not possible. However breakthroughs in solid state physics, especially in nanoelectronics (quantum Hall effect, single electron transistor), opened the way for the envisioned introduction of a new SI system based on natural constants. In such a new system the electrical current will be based on a fixed value for the electrical charge e .

NANOELECTRONICS AND ELECTRICAL QUANTUM UNITS

Basic research on silicon field effect transistors with the goal to increase the electron mobility of these devices led to the discovery of the quantum Hall effect [2]. This quantum phenomenon can be observed for 2-dimensional electron systems. The two-dimensional behavior is best realized for graphene which consists of a monolayer of carbon. However, in general an electronic two-dimensional system exists, if the de-Broglie wavelength of electrons is comparable with the thickness of the electrically active layer which is true for quantum wells or inversion layers in MOSFET's. In addition to the quantization of the electron motion which leads to the two-dimensional behavior, a strong magnetic field has to be applied perpendicular to the layer. This magnetic field has to be strong enough to bend the electrons on closed orbits with quantized energies (Landau levels). The most important aspect of this modified energy spectrum effect with respect to applications in metrology is the fact that under the condition of fully occupied Landau levels an electrical resistance can be realized which depends exclusively on the fundamental constant $R_K = h/e^2$, called von-Klitzing constant [3]. High precision measurements of the quantized Hall resistance at 13 different national metrology institutes demonstrated, that accurate measurements of this quantized resistance are limited by the realization of an calibrated reference resistor within our international system of units. As a consequence a fixed value R_{K-90} for the fundamental quantized Hall

resistance was introduced in 1990 with a value of 25812,807 Ohms. This value of the conventional von-Klitzing constant is used worldwide for all resistance calibrations. Relative measurements between different quantum Hall devices (different wafers, different semiconductors like gallium arsenide [4], silicon [5] or graphene [6]) demonstrated that the value of the quantized Hall resistance is universal within the experimental accuracy of at least 10 digits. The same is true for the Josephson effect which allows the realization of a precise voltage standard based on the conventional Josephson constant $K_{J-90} = 483\,597.9 \times 10^9 \text{ Hz V}^{-1}$ [3]. These quantum units Ω_{90} and V_{90} for resistance and voltage are used outside the official system of units. They are more stable and reproducible than the corresponding units realized within the SI-System. All tests, including the realization of an "integrated quantized circuit" (IQC) with a single electron pump as a current generator [7] confirmed that the electrical quantum units depend exclusively on constants of nature. This means that a new SI system with fixed values for e and h will bring back the most accurate realizations of electric units into the international system of units.

ELECTRICAL QUANTUM UNITS AND THE UNIT OF MASS

The electrical quantum units based on the fundamental constants h and e are not only important for the new definition of the base unit ampere and the derived electrical units but even for a new realization of the unit of mass (kilogram) by comparing with the so called Watt balance the electrical force of a current in a magnetic field with the mechanical force of a mass. Combining this static experiment with a dynamical measurement (induced voltage if coil moves in a magnetic field) leads to a one-to-one correspondence between the Planck constant and the mass [8]. In a new SI system the base unit of mass will be replaced by a fixed value of the Planck constant. Such a redefinition will lead to a more stable definition of the mass since the prototype seems to change with time by about 50 μg over 100 years.

In summary, basic research on silicon field effect transistors with the discovery of the quantum Hall effect, were crucial for the development of a new system of units. Not only electrical units like electrical resistances and voltages can be related to fundamental constants but also the unit of mass, the kilogram, by comparing electrical with mechanical force.

REFERENCES

1. M. Planck. *Ann.Physik* **1**, 69-122 (1900)
2. K. v. Klitzing, G. Dorda, and M. Pepper, *Phys. Rev. Lett.* **45**, 494 (1980).
3. B. Taylor and T. Witt, *Metrologia* **26**, 47 (1989).
4. F. Schopfer and W. Poirier, *J. Appl. Phys.* **102** 054903 (2007).
5. A. Hartland, K. Jones, JM. Williams et al., *Phys.Rev. Lett.* **66**, 969 (1991).
6. T.J. Janssen, N.E. Fletcher, R. Goebel, JM. Williams et al., *New J. Phys.* **13**, 093026 (2011).
7. F. Hohls, A. Welker, Ch. Leicht et al., *Phys. Rev. Lett.* **109**, 056802 (2012).
8. M. Stock, *Metrologia*, **50** (1), R1-R16 (2013).

KEYWORDS

Quantum Hall effect, Watt balance, SI system

Material Requirements for 3D IC and Packaging

W. R. (Bill) Bottoms PhD

*Chairman, Third Millennium Test Solutions, Inc.
3101 Alexis Drive
Palo Alto, Ca. USA 94304*

INTRODUCTION

The electronics industry is nearing the end of Moore's Law scaling which has provided a roadmap enabling an orderly process to identify difficult challenges. This roadmap resulted in early focus on potential solutions so that, for almost 50 years, these challenges were met before they became "road blocks" that stopped the rate of progress. We are now experiencing reduced benefits from scaling as we near the fundamental limits of the physics. Much work has been done to identify a replacement for the CMOS switch and there are candidate technologies that look promising for some applications. However, even if a replacement is identified, it will be years before a viable replacement switch for CMOS will reach volume production for mainstream products. The only solution for maintaining the rate of progress in cost, power, performance and size is to use tools available to us today. These include use of the third dimension, heterogeneous integration, new packaging architectures, new production processes and new materials.

DIFFICULT CHALLENGES TO MAINTAIN PROGRESS

There are many difficult challenges associated with 3D integration and complex system in package (SiP) architectures. This includes thermal management, reliability, yield and test. These problems are relatively well understood and paths to solutions are available although many are too expensive to meet the cost requirements of a consumer dominated market. There are other problems that will inevitably present much more difficult challenges and they either arise due to new materials or new materials are required to resolve problems. The primary difference for these "other" problems is that they are not adequately understood and there is, as yet, no clear path to a solution. New metrology approaches will also be required to analyze the new package architectures and the new materials as they move into production.

The primary direction to maintain progress is to move system level components closer together in packaging and assembly to compensate for the limited future benefits of scaling transistors. The benefits are clear for power, performance, size and even cost. The difficult challenges that arise include thermal density, cross talk, increasing resistance of copper at nanoscale geometries and power integrity at near threshold operating voltage. At the same time we must deliver reliable systems that can survive the challenging environments for applications ranging from automotive to wearable devices. The ICs and the package substrates are increasing in area while the thickness is rapidly decreasing. This impacts yield and reliability associated with warpage and eventually will require flexibility in both ICs and packages. The materials and processes we use today cannot meet these challenges. During this decade 100 percent of the materials will change at the leading edge of complex, 3D SiP packaging to meet these challenges.

Materials Properties Required May Not Exist in Nature

Packaging for these devices must remain reliable in use cases with many thermal and mechanical stress cycles. The parameters that will determine reliability include modulus, interfacial adhesion, coefficient of thermal

expansion and fracture toughness in addition to the electrical properties of break down field strength, electromigration, leakage currents, resistance, loss tangent and dielectric constant. We understand these parameters for bulk materials in use today but many are reaching their limits and new materials are essential. Our “use case” for these new materials in most cases involves very thin layers of material where the interface dominates the properties. It is also true that many of the new materials will be nanomaterials or composites with nanomaterial components and we do not know the properties of the bulk materials let alone those of these interfaces.

The materials properties needed for conductors that not available today Include:

TABLE 1. New conductor properties required.

Material	Parameter	Current	Requirement
Conductors	CTE	$17 \times 10^{-6}/^{\circ}\text{C}$	$4 \times 10^{-6}/^{\circ}\text{C}$
	Electrical Conductivity (S/m)	6.02×10^7	$> 10 \times 10^7$ stable at nano-scale
	Contact resistance	minimal	minimal
	Thermal Conductivity W/(mk)	400	800

The carbon nanomaterials have properties that look promising for CTE, electrical conductivity and thermal conductivity as shown in Figure 1.

	Cu	CNT	GNR	
Max current density (A/cm ²)	$\sim 10^6$	$> 1 \times 10^8$	$> 1 \times 10^8$	$\times 10^2$
Melting Point (K)	1356	3800 (graphite)	3800 (graphite)	
Tensile Strength (GPa)	0.22	22.2	23.5	$\times 10^2$
Thermal Conductivity ($\times 10^3$ W/m-K)	0.385	1.75 <i>Hone, et al. Phys. Rev. B 1999</i>	3 - 5 <i>Balandin, et al. Nano Let., 2008</i>	$\times 10$
Temp. Coefficient of Resistance (10^{-3} /K)	4	< 1.1 <i>Kane, et al. Europhys. Lett., 1998</i>	-1.47 <i>Shao et al. Appl Phys. Lett., 2008</i>	
Mean Free Path @ room-T (nm)	40	> 1000 <i>McEuen, et al. Trans. Nano., 2002</i>	~ 1000 <i>Bolotin, et al. Phys. Rev. Let. 2008</i>	$\times 25$

FIGURE 1. Comparison of Copper with Carbon nano-materials

The electrical and thermal properties of the carbon nanomaterials exceed the future needs but they have limitations in contact resistance, ability to use these conductors for complex wiring traces and cost. Many questions must be answered before they can be considered as practical interconnect materials.

The table and figure above address only some examples for conductors. Similar unsatisfied requirements exist for insulators, dielectrics and polymers. The important parameters include:

- Breakdown field strength and leakage currents at high field strength
- Loss tangent at high frequency
- Fracture toughness at low modulus
- Interfacial adhesion
- Dielectric constant < 2 and > 40
- High thermal conductivity with electrical insulation

Candidate materials that provide a path to a solution for each one of these individual parameters are known. The challenge is that every application requires simultaneously satisfying all parameters key to that application. The

properties are highly coupled and there are no naturally occurring materials that can deliver satisfactory values for all parameters in most applications. This is illustrated in figure 2 below.

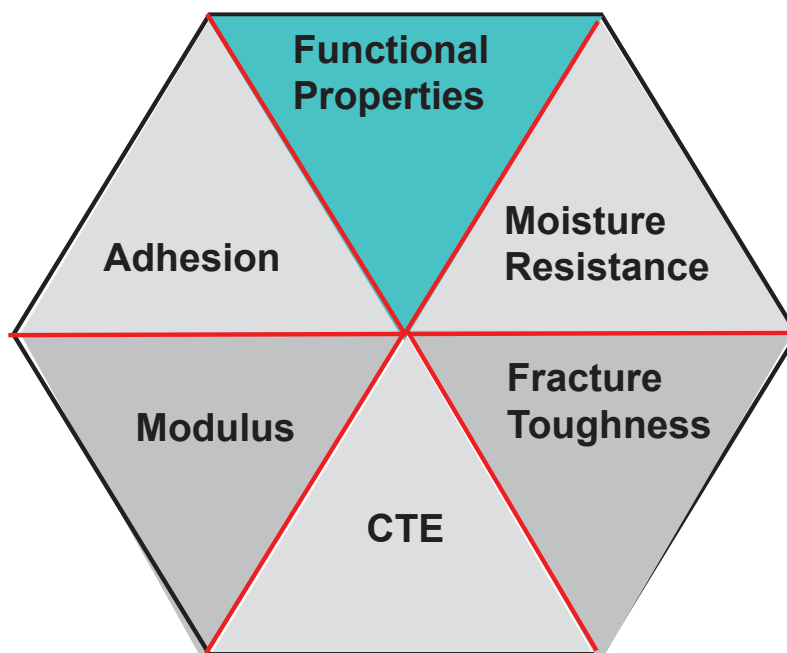


FIGURE 2. Coupled materials properties impact applications for all materials in a package

Composite Materials Can Only Be Optimized If Supported By Metrology

The materials properties must be optimized to achieve the best possible combination of properties for each application. One example is the use of polymers nano-composite materials in packaging. The applications are diverse and include thermal interface materials, mold compounds, underfill, adhesives (both conducting and insulating) and photonic wave guides. Each of these applications has unique properties that must be optimized while maintaining adequate values for all other parameters. This can only be done if we understand the materials and their interface properties.

Herein lies the most difficult metrology challenge. The bulk properties can be measured with metrology we have today. However, optimizing composite materials and interfacial adhesion between materials will require measurement of the bonding energy and stress at nanoscale dimensions. This will also require accurate measurements of the dispersion of nanomaterials inside in a host material that may be a metal, glass, ceramic or polymer. New, cost effective metrology tools will be essential for success.

Examples of promising work to date on new materials and processes such as electrographing, direct interconnect bonding, ultra-conducting copper, nano-solders and other new materials and processes will be discussed. The focus will be on potential solutions for new materials and processes to enable low cost production of reliable products using complex 3D SiP package architectures.

KEYWORDS

3D integration, composite materials, nanomaterials, packaging

Paradigm Shift in Metrology for Probing 3D-Structures and Confined Volumes

Wilfried Vandervorst

Imec

ABSTRACT NOT SUBMITTED AT TIME OF PRESS

Probing Optical and Electronic Properties of Individual Defects Through Scanning Transmission Electron Microscopy and First-Principles Theory

S. J. Pennycook¹, W. Zhou², M. P. Oxley^{2,3}, J. Lee⁴, J. Lin^{2,3}, J. C. Idrobo⁴, M. Kapetanakis^{2,3}, M. P. Prange⁵ and S. T. Pantelides^{3,2}

¹*Department of Materials Science and Engineering, National University of Singapore, Singapore*

²*Materials Science and Technology Division, Oak Ridge National Laboratory, Oak Ridge, TN, USA*

³*Department of Physics and Astronomy, Vanderbilt University, Nashville, TN, USA*

⁴*Center for Nanophase Materials Sciences, Oak Ridge National Laboratory, Oak Ridge, TN, USA.*

⁵*Fundamental and Computational Sciences Directorate, Pacific Northwest National Laboratory, Richland, WA, USA.*

INTRODUCTION

The successful correction of lens aberrations has greatly advanced the ability of the scanning transmission electron microscope (STEM) to provide direct, real space imaging at atomic resolution [1], both through improved spatial resolution and through enhanced signal to noise ratio. In monolayer materials such as BN, graphene or transition metal dichalcogenides, atom-by-atom characterization of atomic position is now a practical reality [2], even using accelerating voltages below the threshold for knock-on damage. Stable point defect complexes consisting of substitutional Si and N atoms lead to spatially localized enhancement of surface plasmon resonances at the sub-nanometer scale, acting as an atomic antenna in the petaHertz (10^{15} Hz) frequency range [3]. Contrary to expectations, images of such excitations obtained through electron energy loss spectroscopy (EELS) are highly localized, sometimes even exhibiting atomic resolution. EELS can also directly probe the nature of bonding at the single atom level [4]. Examples of such phenomena are presented below, together with a theoretical simulation of EELS images that includes both the formation of the STEM probe and solid state bonding effects for the first time [5]. This combined experimental/theoretical technique represents an atomic-resolution variant of optical absorption and promises to be a powerful probe of optical, electronic, and vibrational properties of individual defects in materials.

DIRECT DETERMINATION OF BONDING AT SINGLE POINT DEFECTS IN GRAPHENE

Figure 1 shows images from two Si point defects in monolayer graphene, in which the configurations can be directly seen to be either three- or four-fold Si-C coordination. EELS from the defects shows significant differences; the three-fold case shows structure at the Si L edge very similar to that of bulk sp^3 bonded materials, with a large peak just past the edge onset that is characteristic of empty d-states. In the case of the four-fold bonded Si atom, that peak is absent, indicating the d-states are no longer empty, i.e., they are participating in the bonding. This picture, determined directly from experiment, is fully confirmed through density functional calculations [4].

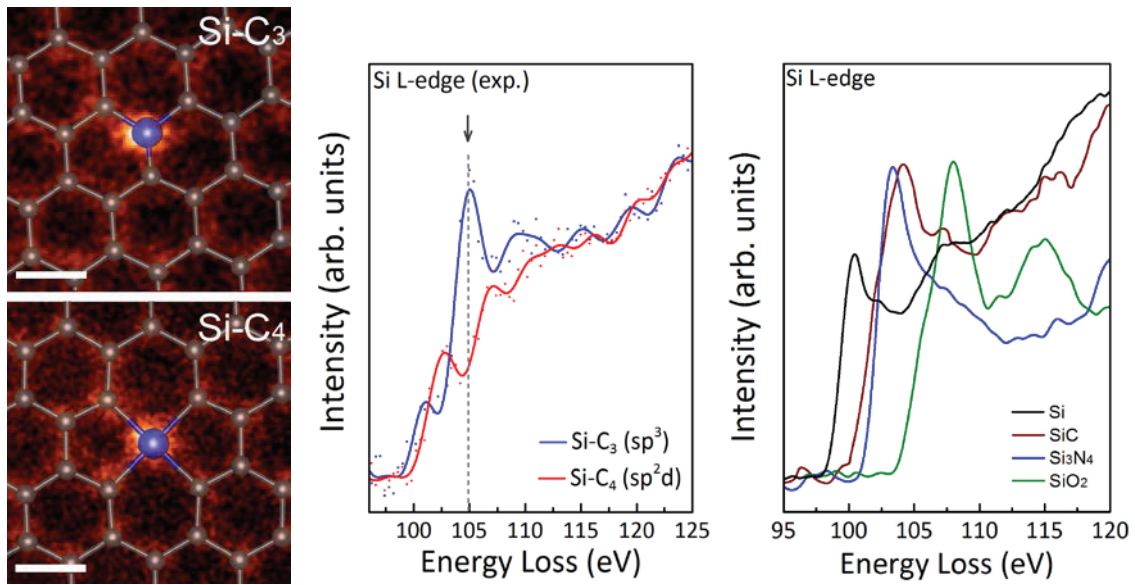


FIGURE 1. 3-fold and 4-fold coordinated Si impurities in graphene (left) with very different near edge structure (center). The arrowed peak in the 3-fold case is due to unoccupied *d*-states indicative of sp^3 bonding, as in bulk compounds (right). The absence of the peak in the 4-fold case indicates sp^2d bonding. Scale bars: 0.2 nm. Data obtained in a Nion UltraSTEM100 operating at 60 kV [4].

LOCALIZED “PLASMON” RESONANCES

Low loss EELS can also give information on optical properties, and Fig. 2 shows a surprisingly localized enhancement at the plasmon energy at the Si-N point defect shown in Fig. 1. The exponential decrease moving away from the two-layer region in the lower right of the image is consistent with the expected delocalization, however, the enhancement at the point defect is surprisingly localized, with a full-width-half-maximum of around 4 Å. The point defect complex is acting as an atomic-scale antenna in the petaHertz (10^{15} Hz) frequency range (11 eV is equivalent to a frequency in the order of 10^{15} Hz), and is the smallest resonant structure seen to date.

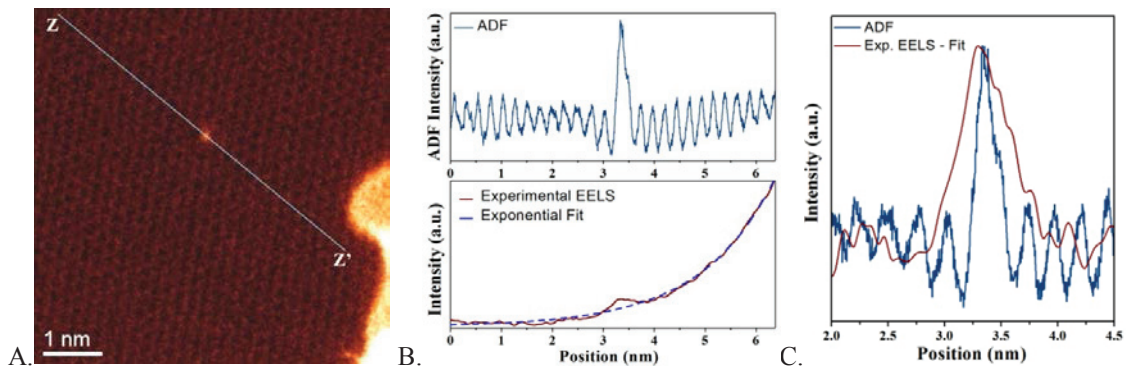


FIGURE 2. STEM-EELS line scan across a point defect in monolayer graphene. (A) Low-pass filtered ADF survey image. (B) Simultaneously collected ADF and integrated EELS signals from 11 to 18 eV (raw data) as a function of probe position along the line (*Z-Z'*) indicated in Figure A. (C) Comparison of the full-width-half-maximum between the ADF signal and the enhanced plasmon intensity from the substitutional Si atom. Reproduced from [4].

Detailed theoretical analysis shows that, although graphene shows peaks with shape and energy similar to the π and $\pi + \sigma$ peaks of graphite, they are not in fact plasmons, since the real part of the dielectric constant does not reach zero. They are in fact interband transitions [6].

ATOMIC RESOLUTION VALENCE EELS

Figure 3 shows an example of an atomic resolution image obtained in low loss EELS. It is not preservation of any elastic scattering mechanism, but indicates true atomic-level image of electronic transitions. To identify the transitions, the full theory combining dynamical electron diffraction with density functional theory [5] has been applied, and reproduces the images, as seen in Fig. 3. Analysis of the transitions responsible for the atomic resolution images shows that they arise from localized transitions between states of maximum atomic character.

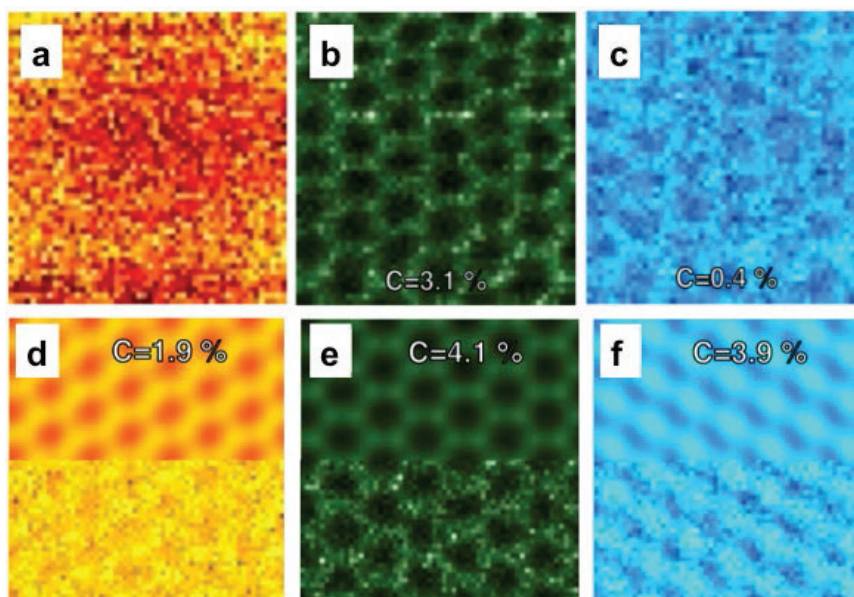


FIGURE 2. STEM-EELS images of monolayer graphene. (a-c) Experimental images using energy ranges of (a) 13-26 eV. (b) 26-42 eV. (c) 42-58 eV. Theoretical simulations (d-f) reproduce the contrast. Adding only 1% noise to the simulations (lower halves) shows how quickly the contrast can be obscured.

REFERENCES

1. S.J. Pennycook, in *Scanning Transmission Electron Microscopy*, eds. S. J. Pennycook and P. D. Nellist, New York: Springer, (2011) pp. 1-90.
2. O.L. Krivanek, M.F. Chisholm, V. Nicolosi, T.J. Pennycook, G.J. Corbin, N. Dellby, M.F. Murfitt, C.S. Own, Z.S. Szilagy, M.P. Oxley, S.T. Pantelides, and S.J. Pennycook, *Nature*, **464** 571-574 (2010).
3. Wu Zhou, Jaekwang Lee, Jagjit Nanda, Sokrates T. Pantelides, Stephen J. Pennycook, and Juan-Carlos Idrobo, *Nature Nanotechnology*, **7** 161-165 (2012).
4. W. Zhou, M. Kapetanakis, M. Prange, S. T. Pantelides, S. J. Pennycook, and J.-C. Idrobo, "Direct Determination of the Chemical Bonding of Individual Impurities in Graphene," *Phys Rev Lett*, **109** 206803 (2012).
5. M. P. Prange, M. P. Oxley, M. Varela, S. J. Pennycook, and S. T. Pantelides, *Phys Rev Lett*, **109**, 246101 (2012).
6. F. J. Nelson, J.-C. Idrobo, J. D. Fite, Z. L. Mišković, S. J. Pennycook, S. T. Pantelides, J. U. Lee, and A. C. Diebold, *Nano Lett*, **14**, 3827-3831 (2014).

KEYWORDS

Scanning transmission electron microscopy, electron energy loss spectroscopy, plasmonics, optical properties

Strain Characterisation at Nanoscale Using Transmission Electron Beam Based Techniques

J.L. Rouvière¹⁻², N. Bernier³, M. Vigouroux³, D. Cooper³

1 Univ. Grenoble Alpes, INAC-SP2M, F-38000 Grenoble, France

2 CEA, INAC-SP2M, F-38000 Grenoble, France

3 CEA, LETI, Minatec campus, 17 rue des Martyrs, 38054 Grenoble Cedex 9, France

INTRODUCTION

In the past decade, stimulated by the demand of the semiconductor industry, several new Transmission Electron Microscopy (TEM) based techniques have been proposed to measure strain. Presently, these TEM based techniques seem to be the only ones that can provide at the same time the high spatial resolution and the high precision required in nanoelectronics: resolution of about one nanometer and precision $\Delta a/a$ approaching $1e^{-4}$, where a is the lattice parameter. In a first part, a short overview of the TEM techniques for strain measurement is performed. In a second part, we present the solution that has our preference: Nanobeam Precession Electron Diffraction (N-PED).

OVERVIEW OF TEM TECHNIQUES FOR STRAIN MEASUREMENT

Since the built of the first TEM in Germany in 1931, TEM has greatly developed. TEMs are now quite complex instruments, but thanks to computers, their operations are becoming simpler when no software bugs happen. There are two main ways of working with a TEM: either a broad beam is made with the condenser lenses and a global image of the sample is performed (what we call "pure TEM" or shortly "TEM") or a tiny beam is made and scanned over the sample (this is Scanning TEM: STEM). Historically, STEM was harder to develop and lagged behind "TEM" for a long time. "TEM" provides nearly lived images and the image contrast can be easily enhanced by putting an aperture in the diffraction plane of the objective lens, method which is known as diffraction contrast imaging (DCI). In the last ten years, STEM has gained more and more interest thanks to important improvements and to our point of view seems more adapted for nanoelectronics applications¹.

As shown in table 1, there are many TEM techniques that can be used to measure strain. Here we cannot discuss on all these techniques and only some pros-and-cons are given in the last column of table 1. **The more effective way to measure strain in TEM is to measure directly the local lattice parameters** and there are 3 ways to do that. (i) Either the lattice planes are directly visualized and the variations of distances between the lattice planes i.e. strain, are directly measured. This happens in high resolution (HR) either **HR-TEM**²⁻³ or **Z-contrast HR-STEM**¹⁻³. Due to the necessity to have enough pixels between lattice planes and due to the limited number of pixels in the images, these techniques have generally a limited field of view and a limited precision. (ii) Or the lattice parameters are directly measured in the reciprocal space. This is what is achieved in all diffraction based techniques: **CBED**³⁻⁴ (Convergent Beam Electron Diffraction), **NBED**⁵ (Nanobeam Beam Electron Diffraction), **N-PED**⁶⁻⁷, and **EBSD**⁸ (Electron Back Scattering Diffraction). Although EBSD is a SEM (Scanning Electron Microscope) technique, we have put it in table 1 because it can provide maps of the 9 components of the deformation matrix (6 strain components and 3 rotation terms) and because a transmission mode is under development and should improve its spatial resolution. The diffraction based techniques have generally a good precision but the realization of maps can be time consuming. (iii) Or a "parameter" which is linked to the lattice parameters is measured. In holography based techniques (**DFEH**³⁻⁹ : Dark field Electron Holography or **DIH**¹⁰ : Dark Field In-line Holography) this is achieved by measuring the phase maps of some diffracted beams. The sample have to be tilted out-of a zone axis in order to enhance a given diffracted beam g and it is the phase of this diffracted beam which is very sensitive to the local lattice

parameters. In DCI¹¹, the "parameter" is the amplitude of a diffracted beam. Unfortunately the amplitude is not very sensitive to strain and also depends on sample thickness and sample composition. LACBED¹² (Large angle Convergent Beam Electron diffraction) is a mixture of diffraction and image. LACBED and DCI seem more adapted for having a global view of the sample. In the next part, we present the solution we have developed and adopted: N-PED⁶.

TABLE 1. Some characteristics of electron microscopy techniques (see text for meaning of abbreviations) that can visualize or measure strain field. Values in bold are a good point for the technique. Underline values means a weakness. 1D-strain (respectively 2D-strain and 3D-strain) means that only one component (respectively 4 and 9) of the deformation tensor are measured easily. FIB is Focus Ion Beam.

Technique	Precision	Spatial resolution	Field of view	Thickness	Comments
DCI ¹¹	<u>not quantitative</u>	2 nm	< 1 μm	10-400 nm	Just for seeing defects, quantification is difficult
HR-TEM ²⁻³	<u>0.2 %</u>	0.2 nm	100 nm	< 50 nm	Visualization of atomic columns, but need of very good TEM lamella (FIB is not good), poor precision
HR-STEM ¹⁻³	<u>0.1 %</u>	0.2 nm	400 nm	5 - 400 nm	Good for maps of large strain (> 1%)
Dfeh ³⁻⁹	0.02 %	2 nm	1 μm (map)	<u>\sim 100 nm</u>	Very good for 1D-strain but off-axis, need of a nearby reference, complexity for 2D-strain
DIH ¹⁰	0.01 %	1 nm	1 μm (map)	1 - 400 nm	No need of reference, very good for maps of 1D-strain but off-axis, image series
LACBED ¹²	<u>qualitative</u>	<u>\sim 3 nm (?)</u>	1 μm (map)	<u>> 100 nm</u>	Good for an overview of strained regions, poor resolution, quantification is difficult
CBED ³⁻⁴	0.02 %	0.5 nm	1 μm (scan)	<u>> 200 nm</u>	Precise but only for thick crystal, off-axis, complex, however 3D information and 3D-strain is possible
NBED ⁵	0.06 %	3 nm	1 μm (scan)	<u>< 200 nm</u>	On-axis, simple but not robust. good for profiles
N-PED ⁶⁻⁷	0.01 %	2 nm	1 μm (scan)	1 - 400 nm	Simple, robust and versatile (any thickness and orientation) for 2D-strain but maps require times
SFM ¹³	0.1 %	2 nm (?)	1 μm	5 - 400 nm	Just for 1D-strain, works on traditional devices
EBSD ⁸	0.01 %	<u>20 nm</u>	microns	surface	9 components of deformation , surface analysis, poor resolution, but a transmission mode is developed

NANOBEAM PRECESSION ELECTRON DIFFRACTION

N-PED is very similar to CBED and NBED: a small electron beam is made and diffraction patterns (DP) are acquired at different positions of this electron beam. One DP must be acquired in a region where no strain is assumed and this DP serves as a reference pattern, which can be acquired in a region far from the region of interest or in a different sample. The differences between N-PED, NBED and CBED are the diameter (d), the convergence angle (α) and the precession angle (α_p) of the beam. In fact there is a compromise between spot size and beam convergence: it is impossible to have a small parallel beam and the only way to reduce the beam size is to make it more convergent (see fig. 1). In classical CBED, diffraction spots are nearly tangent (i.e. $\alpha \sim 3$ mrad) and the probe size is quite small ($d \sim 0.5$ nm), but the diffraction disks do not have a uniform intensity (Fig. 1b). In NBED, as the disks are smaller this non-uniform intensity is less visible (Fig. 1a), but it is still present making the exact location of the diffraction maxima less precise and making NBED not a very robust technique (variations of intensity in the disks changes with thickness, orientation and composition and give noise in the profile of Fig. 1e). In N-PED the incident beam is rotated by a small angle around the observation direction, i.e. it is precessed, and a descan is applied after the sample in order to bring back the diffracted beams to their unprecessed positions. The advantages of the precession for strain measurement appear in Fig. 1. When precession is on, (i) more diffracted spots are visible, (ii) the uniformity of the spot intensity is improved and (iii) a better precision is obtained by locating the edges of the disks and (iii) a more convergent beam can be used leading to a smaller probe and a better location of edges (Fig. 1d). We implemented precession on two microscopes: a JEOL 2010 FEF microscope equipped with the Astar system from Nanomegas and a TITAN ultimate microscope with precession made by FEI. On the JEOL 2010FEF, mapping is rather fast (15 minutes for a map of 100x50 points) but the quality of the DPs are not as good as on the TITAN: on the Astar system, the bigger images are 512x512, DPs have some distortions, we got some issues with the stability of the alignments and we could not get probe smaller than 3 nm in the precession setting⁷. On the TITAN, we add to use our own scripts to acquire maps larger than 2 Gb with a 2Kx2K Gatan Ultrascan CCD camera and the precession speed is limited to 0.1s. The advantage of the TITAN setting is to be very stable and to be able to go back and forth between N-PED and

HR-STEM. Presently the drawbacks of N-PED are its speed and amount of data: for instance in fig. 2, 100x50 diffraction patterns of 1Kx1K pixels were acquired in about 90 minutes and occupy about 12 Gb on hard disk. As can be seen in Fig. 2, very smooth maps of the four components of the strain tensor can be obtained with N-PED. A compromise has to be found between precision, spatial resolution and diffraction size. By increasing slightly the probe size to 3 nm, a precision of $9e-5$ was obtained in the Si substrate with 2Kx2K patterns. However in most cases, patterns of 512x512 pixels should be sufficient. N-PED is a technique that is simple to use and very robust: thick or thin crystals can be analyzed; in the presentation, we will show how N-PED was successful for analyzing devices based on nanowires.

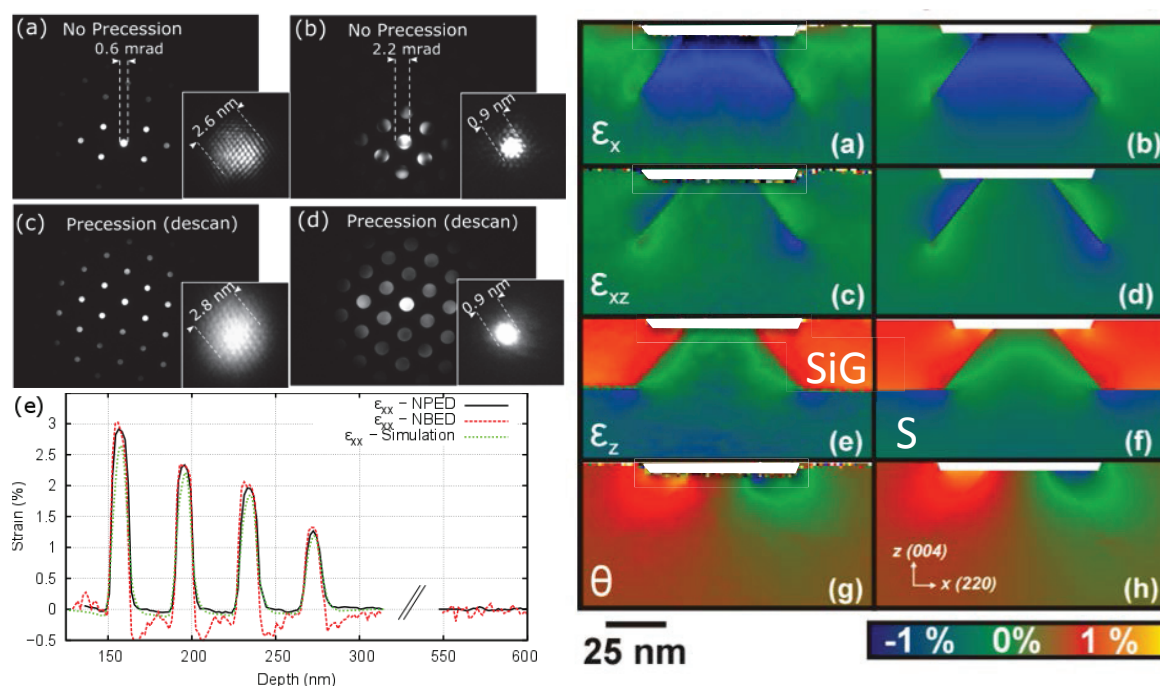


FIGURE 1. (left) (a-b-c-d) Diffraction patterns and the associated images of the electron being going through a perfect Si crystal observed along a $\langle 110 \rangle$ direction. (e) Three strain profiles (1 simulation and 2 experimental ones) taken along the growth [001] direction of 4 $\text{Si}_x\text{Ge}_{1-x}/\text{Si}$ layers ($x=0.2, 0.31, 0.38$ and 0.45) (see ⁶ for more details)

FIGURE 2. (right) Strain maps obtained in a device containing SiGe stressors and a Si_3N_4 layer above the SiO_2 layer (the whitened boxes) above the channel. (a-c-e-g) Experimental maps obtained from N-PED. (b-d-f-h) Maps obtained by Finite Element simulations: to reproduce experimental data, a -1.9 GPa stress was put in the amorphous Si_3N_4 layer.

REFERENCES

1. J. L. Rouviere, E. Prestat et al, *Journal of Physics: Conference Series* **471** 012001 (2013).
2. F. Hue, M. Hytch, H. Bender et al, *Phys. Rev. Lett.* **100** (15) 156602-4.3.(2008).
3. A. Béch , J.L. Rouviere , J.P. Barnes, D. Cooper *Ultramicroscopy* **131** 10-23 (2013).
4. A. Spessot, S. Frabboni, R. Balboni, A. Armigliato, *Journal Of Microscopy* **226** (2) 140–155 (2007).
5. A. B ch , J.L. Rouvi re, L. Clement, J.M. Hartmann, *Appl. Phys. Letters* **95**(12) 123114 (2009).
6. J. L. Rouviere, B ch  A et al., *Appl. Phys. Lett.* **103** 241913 (2013).
7. M. Vigouroux et al. *Appl.Phys. Lett.* **105** 191906 (2014).
8. S. Villert, C. Maurice et al., *Journal of Microscopy* **233** 290-301 (2009).
9. M. Hytch et al. *Transmission Electron Microscopy in Micro-nanoelectronic* John Wiley & Sons (2012).
10. C. T. Koch, V.B. zsd l and P. A. Van Aken *Appl. Phys. Lett.* **96** 091901 (2010).
11. D. D. Perovic, G. C. Weatherly and D. C. Houghton *Phil. Mag. A*, **64**:1, 1-28 (1991).
12. H. H. Liu, X.F. Duan, Q. X. Xu and B.-G. Liu, *Ultramicroscopy* **108** 816-820(2008).
13. S. Kim, S Lee, Y. Oshima et al., *Appl. Phys. Lett.* **102** 161604 (2013).

KEYWORDS

Strain, precession, nanobeam, electron diffraction, microscopy, transmission

High-Resolution X-ray Diffraction of Epitaxial Thin-Films and Patterned Nanostructures

Matthew Wormington

Jordan Valley Semiconductors, 3913 Todd Lane, Suite 106, Austin, TX 78744, USA

INTRODUCTION

For the past few generations of CMOS technology, the introduction of innovative materials and processes has been critical, in addition to lithographic scaling, for keeping the semiconductor industry following Moore's law. Strain engineering to increase the carrier mobility and hence drive current, as well as the introduction of high- k / metal gates to reduce leakage current, serve as notable examples of such innovation. Strain engineering through the selective epitaxial growth of SiGe(B) in the source/drain regions of transistors has been widely used by many logic manufacturers for some time. The epitaxial material creates compressive in-plane strain in the adjacent Si channel to improve the hole mobility in PMOS transistors. Recently, selective epitaxial growth of Si:C(P) or Si:P has been introduced by some manufacturers to create tensile in-plane strain in the channel of NMOS transistors to improve the electron mobility.

Innovations in transistor architecture are also well underway with the leading-edge manufacturers making the transition from planer (2D) to finFET (3D) transistors. Further innovation is expected at the sub-10 nm and below technology nodes that will be challenging both economically and technologically, since the innovations to make smaller and faster transistors will be more expensive than current processing methods. Economic issues aside, one of the most significant potential changes is the introduction of new channel materials with higher carrier mobility than silicon. Evolutionary options are SiGe and tensile Si, with the more revolutionary Ge and III-V options still being considered, for PMOS and NMOS transistors, respectively [1].

TABLE 1. Properties of selected high mobility semiconductor materials [2].

Material property	Si	Ge	GaAs	InAs	InP
Electron mobility ($\text{cm}^2 \text{V}^{-1} \text{s}^{-1}$)	1,400	3,900	8,500	40,000	5,400
Hole mobility ($\text{cm}^2 \text{V}^{-1} \text{s}^{-1}$)	450	1,900	400	500	200
Bandgap (eV)	1.12	0.66	1.42	0.35	1.34
Dielectric constant	11.7	16.2	12.9	15.2	12.5
Lattice parameter (\AA)	5.431	5.658	5.653	6.058	5.869
Lattice mismatch to Si (%)	0.0	4.2	4.1	11.5	8.1

There are many challenges associated with changes to the channel material. For example, the high-mobility materials have a large lattice mismatch to the Si lattice (see table 1) that would normally result in defect densities that are far too high for the channel of CMOS transistors. Integration schemes are being developed in order to significantly reduce defect densities and can broadly be classified into two categories depending on whether epitaxial growth of the channel material is done before or after the shallow trench isolation (STI).

High-resolution X-ray diffraction (HRXRD) is an important technique for the characterization and metrology of epitaxial materials and structures. In this presentation we will review the principles of the technique and how it has and can be applied to both the development and manufacturing of advanced CMOS technologies. We will review recent developments in hardware, software and methodologies and will use representative applications to illustrate what quantitative information is available from HRXRD analysis of epitaxial thin-films and arrays of patterned nanostructures both in the lab and fab. We will also present a brief overview of some recent measurements

performed using synchrotron sources that demonstrate the use of micro- and nano-beam XRD to study individual nanostructures.

HIGH-RESOLUTION X-RAY DIFFRACTION

HRXRD is a non-destructive, non-contacting technique that involves measuring the intensity of X-rays diffracted from single crystals, such as heteroepitaxial materials grown on substrates encountered in the compound and silicon semiconductor industries [3,4]. The principle of X-ray diffraction measurements is illustrated schematically in Figure 1. The technique provides strain measurements with high accuracy, precision and sensitivity with few assumptions using the crystal lattice of the sample as a “strain gauge”. In the most common setup, a highly collimated and monochromatic X-ray beam ($\text{Cu K}\alpha_1$ with $\lambda=1.54056 \text{ \AA}$) is incident on the sample. Beam sizes ranging from a few mm^2 for blanket wafer measurements down to $\sim 50 \mu\text{m}$ in diameter for measurement of metrology pads in the scribe-lines of product wafers are possible. The X-rays are diffracted from the periodic arrangement of atoms within the sample and the fine detail of the intensity distribution is measured as a function of angle using photon counting detector. The diffracted intensity distribution can be analyzed directly using the position, width and height of the diffraction peak(s) or by using a model based approach, where the intensity profile is simulated using a structural model whose parameters can be refined to give best agreement between calculated and experimental curves.

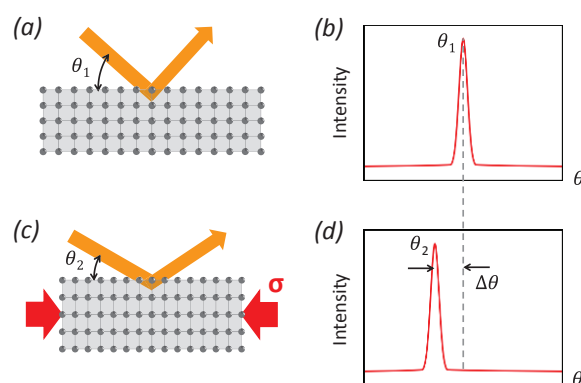


FIGURE 1: Schematic illustrating the principles of X-ray diffraction strain/stress measurements: (a) diffraction from a stress-free crystal slab, (b) the diffracted intensity as a function of angle from the stress-free crystal, (c) diffraction from a crystal slab with an applied uniaxial stress and associated strains (d) the diffracted intensity from the deformed crystal. A change in the diffraction angle results from the change in lattice spacing in the crystal.

HRXRD can give the composition, strain/stress and thickness of fully strained (pseudomorphic) epitaxial thin-film structures as well as providing information on defects such as dislocations that can lead to strain relaxation in epitaxial material above some critical thickness [3,4]. Until recently, the main use of HRXRD in fabs has been to qualify and monitor the chemical vapor deposition (CVD) chambers used to grow epitaxial materials. Most measurements have been performed on blanket wafers or solid metrology pads on product wafers. Additionally the technique has been used during development and process ramp it is accurate and comparatively straightforward compared to optical metrology, which requires a stable process in order to develop robust optical models. HRXRD has also been used as a reference metrology to help diagnose the root cause of problems when process excursions occur during manufacturing. There has also been some work done that demonstrates the unique capability of HRXRD to non-destructively monitor strain, and its evolution during processing, using arrays of features that better represent real devices than solid pads [5], but such use has been rather limited to date.

With the recent availability of high-performance linear (1D) detectors, measurements that were previously only possible in the lab are now available in the fab to support the development and control of the newer transistor architectures, such as finFETs, as well as development of sub-10 nm high mobility transistors [6]. The analytical power of reciprocal space maps (RSMs) can provide valuable and unique information on arrays of nanostructures including the volume average strain tensor components and assessment of defectivity. Additionally, RSMs can provide information on the size/shape of nanostructures, *e.g.* height and sidewall angle of fins, as well as their spatial arrangement, *i.e.* pitch and pitch-walking error from multiple patterning lithography [3,7].

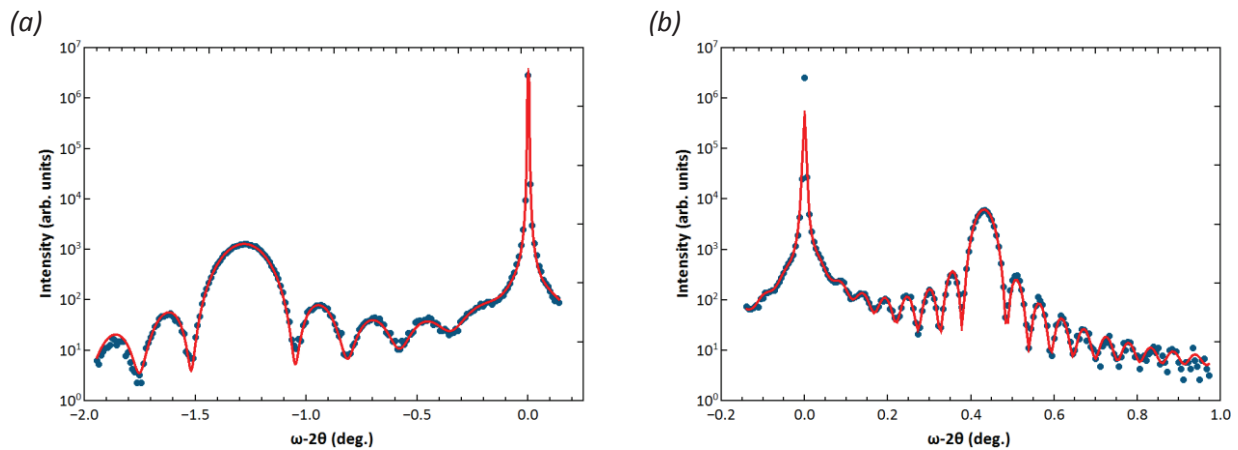


FIGURE 2 Measured (blue points) and best-fit simulation (red line) X-ray diffraction curves from fully strained epitaxial thin-films of (a) 22.5 nm $\text{Si}_{1-x}\text{Ge}_x$ with $x = 49.0\%$ and (b) 101.1 nm $\text{Si}_{1-x}\text{C}_x$ with $x = 1.4\%$ (incorporated) on Si(001) substrates (symmetric 004 reflection, $\text{Cu K}\alpha_1$ radiation).

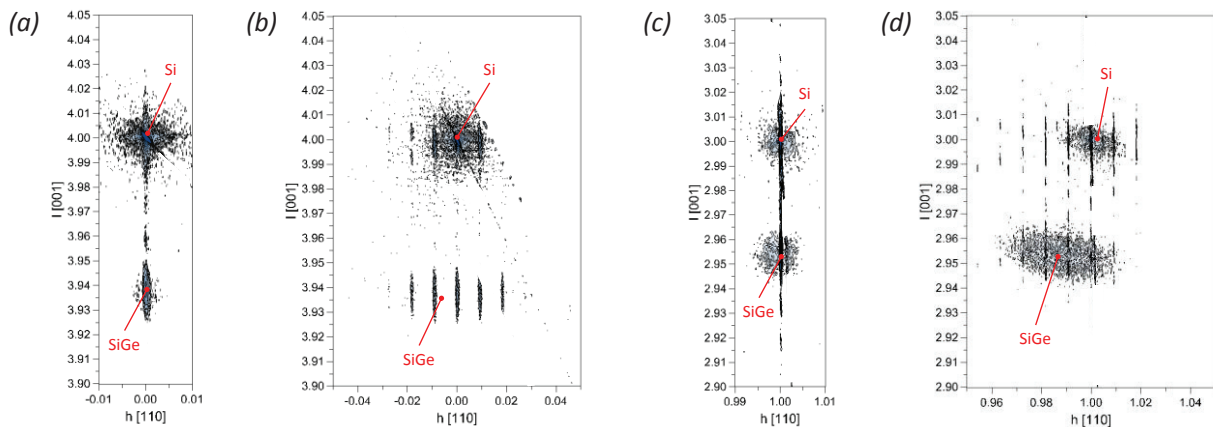


FIGURE 3: Measured RSMs from SiGe fins with 42 nm pitch on a Si(001) substrate. (a,b) Maps of the symmetric 004 reflection with the incident X-ray beam parallel and perpendicular to the fins, respectively. (c, d) Maps of the asymmetric 113 reflection with the incident X-ray beam parallel and perpendicular to the fins, respectively.

REFERENCES

1. M. LaPedus, *Semiconductor Engineering*, (January 22, 2015), Available online from: <http://semiengineering.com/industry-to-rethink-channel-materials/>
2. *Electronic Archive New Semiconductor Materials. Characteristics and Properties*, Available online from: <http://www.ioffe.ru/SVA/NSM/>
3. U. Pietsch, V. Holy and T. Baumbach, *High-Resolution X-ray Scattering: from Thin Films to Lateral Nanostructures*, 2nd Ed., Springer (2004).
4. D.K. Bowen and B.K. Tanner, *X-ray Metrology in Semiconductor Manufacturing*, CRC Press, (2006).
5. J.R. Holt et al., *J. Appl. Phys.* 114, 154502 (2013).
6. P. Ryan et al., *2015 International Conference on Frontiers of Characterization and Metrology for Nanoelectronics (FCMN)*, program/abstract book (April 14-16, 2015).
7. M. Medikonda et al., *J. Vac. Sci. Technol. B* 32, 021804 (2014).

KEYWORDS

Metrology, X-ray diffraction, thin-films, nanostructures, epitaxy, strain, stress

Characterization of Magnetic Nanostructures for ST-RAM Applications By Use Of Macro- and Micro-Scale Ferromagnetic Resonance

T. J. Silva, H. T. Nembach, and J. M. Shaw

*National Institute of Standards and Technology
325 Broadway
Boulder, CO 80301 USA*

BACKGROUND

Spin-torque memory is under consideration for high-speed, scalable, non-volatile memory applications. The storage medium is a magnetic layer with an intrinsic anisotropy that favors orientation of the magnetization in either of two directions perpendicular to the film plane. Read-out of the storage layer is based on spin-dependent tunneling from an adjacent magnetic reference layer, while the direct transfer of angular momentum in the form of electron spin is the driving mechanism for switching the magnetization in the storage layer.

In the write process for ST-RAM, the electron spin in the write-current exerts a torque on the magnetization that counters the intrinsic damping process. Once the write-current torque exceeds the damping, hysteretic switching occurs. Hence, damping is a critical parameter for the write-efficiency of spin-torque RAM. The zero-temperature critical current density J_{c0} is given by [1]

$$J_{c0} = \frac{ge\alpha\delta U_k}{\hbar p}, \quad (1)$$

where g , e , \hbar , are the spectroscopic splitting factor, electron charge, and reduced Planck's constant, respectively, U_k is the energy density of the switching barrier, δ is the storage layer thickness, p is the torque transfer efficiency, and α is the damping parameter. In the context of the standard Landau-Lifshitz phenomenology, the damping parameter describes the rate that the magnetization returns to equilibrium after an excitation:

$$\partial_t \hat{m}(\vec{r}) = -\gamma \mu_0 [1 + \alpha \gamma \mu_0 \hat{m}(\vec{r}) \times] (\hat{m}(\vec{r}) \times \vec{H}_{\text{eff}}(\vec{r})), \quad (2)$$

where $\gamma \doteq (g/2)(e/m_e)$ is the gyromagnetic ratio, m_e is the electron mass, μ_0 is the vacuum permeability, $\hat{m}(\vec{r})$ is the normalized magnetization vector, $\vec{H}_{\text{eff}}(\vec{r}) = -\vec{\nabla}U(\vec{r})/(\mu_0 M_s)$ is the net effective field, $U(\vec{r})$ is the free energy, and M_s is the saturation magnetization. Steady-state solution of eq. (2) in the limit of spatially uniform response for an ac magnetic field \vec{h} in the x - y plane, small amplitude motion, small variations of $U(\vec{r})$, and a saturating magnetic field \vec{H}_0 along the z -axis film-normal, leads to a linear response function $\hat{m} = \tilde{\chi} \vec{h}$, where $\tilde{\chi}$ is

$$\tilde{\chi}_{jk}(\omega) \equiv \left[(H_0 - M_{\text{eff}})^2 - \left(\frac{\omega}{\gamma \mu_0} \right)^2 - i \frac{2\alpha_{\text{eff}} \omega (H_0 - M_{\text{eff}})}{\gamma \mu_0} \right]^{-1} \left[\delta_{jk} (H_0 - M_{\text{eff}}) - i \varepsilon_{jk} \frac{\omega}{\gamma \mu_0} \right], \quad (3)$$

where $M_{\text{eff}} \doteq -2U_k/\mu_0 M_s$ is the effective magnetization that is in actuality the height of the energy barrier that prevents switching, and $\alpha_{\text{eff}} \doteq \alpha + (\gamma\mu_0\Delta H/(2\omega))$, where the inhomogeneous broadening ΔH is the rms variation of the resonance condition throughout the measured sample volume. The susceptibility has a resonance condition when $\omega = \gamma\mu_0(H_0 - M_{\text{eff}})$, also known as the ferromagnetic resonance (FMR). Hence, extraction of both the energy barrier (resonance position) and the damping (resonance linewidth) can be achieved by an FMR measurement of the ac permeability by use of a microwave circuit properly loaded with a candidate ST-RAM storage material.

MEASUREMENT METHODS

The method of VNA-FMR can be used to determine the microwave response of unpatterned blanket films of storage-layer candidate materials. The method uses a 70 GHz bandwidth vector-network-analyzer (VNA) to measure the transmission efficiency of a coplanar waveguide assembly loaded with the sample in near-field proximity to the waveguide. An electromagnet provides the saturating field of up to 2.2 T. For a given excitation frequency ω , H_0 is swept through the resonance condition. The resultant complex transmission spectra are then fitted to eq. (3). Measurement at a single frequency is inadequate for a unique determination of both α and ΔH_0 . Hence, the excitation frequencies are also varied. The frequency range is chosen to minimize the uncertainty in α .

Individual spectra are fitting to eq. (3). A sensitivity matrix is used to estimate the uncertainty in $M_{\text{eff}}(\omega)$ and $\alpha_{\text{eff}}(\omega)$ at measurement frequency ω . Linear regression is used to determine M_{eff} and α , with uncertainties determined by Monte Carlo methods. Details of the measurement method may be found in Ref. [2].

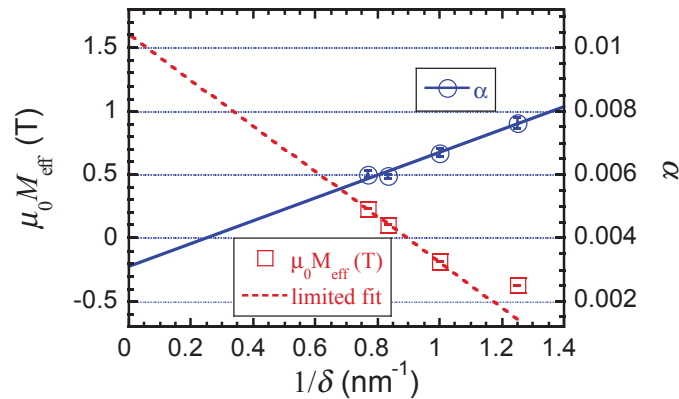


FIGURE 1. VNA-FMR data for effective magnetization and damping as a function of reciprocal storage layer thickness for a CoFeB sandwich structure. The anisotropy is oriented along the z -axis when $M_{\text{eff}} < 0$. The error bars are 1σ . They are estimated by use of the sensitivity matrix used for the fitting of the spectroscopic data to eq. (3). Linear fits to both the anisotropy and damping data are also shown, though the fit to M_{eff} is only for the samples with $\delta \geq 1$ nm. Both fits are extrapolated to the bulk limit ($1/\delta \rightarrow 0$). In both cases, the extrapolated values are in reasonable agreement with literature values for materials similar to $\text{Co}_{0.6}\text{Fe}_{0.2}\text{B}_{0.2}$.

We present in Fig. 1 an example of VNA-FMR data of M_{eff} and α for sputtered sandwich films MgO (2)/ $\text{Co}_{0.6}\text{Fe}_{0.2}\text{B}_{0.2}$ (δ)/ Ta (0.4)/ $\text{Co}_{0.6}\text{Fe}_{0.2}\text{B}_{0.2}$ (δ)/ MgO (2), where the parenthetic values are thicknesses in nm. The samples were all deposited on 100-mm CMOS-grade Si wafers, and were annealed after deposition at 300 C for 30 minutes. For this particular sample system, the observation of a linear dependence of M_{eff} and α on $1/\delta$ is evidence for interfacial contributions to both the anisotropy [3] and the damping [4]. We speculate that the deviation of the linear trend for M_{eff} at the smallest thickness is due to incomplete layer formation. The extrapolated values in the bulk limit of $\delta \rightarrow \infty$, $\alpha_{\text{bulk}} \cong 0.0031$ and $\mu_0 M_{\text{eff,bulk}} \cong 1.60$ T, are both in reasonable agreement with published values for similar materials [5][6]. Similar interfacial damping has been observed in a variety of other material systems, and is often ascribed to the spin-pumping mechanism, whereby magnon-electron scattering at ferromagnet/normal metal interfaces equilibrates the magnetic system [7].

Use of blanket-film measurements of α to obtain input parameters for micromagnetic simulations of ST-RAM performance is predicated on the assumption that damping is a purely local quantity, i.e. α does not depend on the magnetization distribution in neighboring regions. While this assumption appears valid at longer length scales, theory predicts that it will eventually breakdown at nanometer length scales [8][9].

To test these theoretical predictions, we developed a novel optical microscope with capabilities analogous to the VNA-FMR [10]. Because it is based on scanned optical microscopy methods, it has a spatial resolution as small as 0.3 μm when using diffraction limited optics. However, the dimensions of the structures of interest for STT-RAM are typically smaller than 50 nm. To measure structures that are well below the spatial resolution of the instrument, it is necessary to push the sensitivity to the fundamental limit. This was accomplished by use of optical heterodyne methods, whereby coherent mixing of cw lasers at differing frequencies can be used to both generate microwaves and detect ferromagnetic resonance via the magneto-optic Kerr effect. The heterodyne magneto-optic microwave microscope (H-MOMM) was developed at NIST, and remains the only instrument of its kind in the world. It has an unprecedented sensitivity that allows for the measurement of damping even when the magnetic excitations are as small as only a few 10's of nanometers.

And exemplary FMR spectrum for a single 100-nm-diameter nanomagnet of 10-nm-thick $\text{Ni}_{81}\text{Fe}_{19}$ is shown in Fig. 2. The magnetization is oriented in the plane of the substrate. By fitting the spectra to eq. (3), and then applying linear regression to the α_{eff} vs. ω data, we found that the damping is indeed non-local in character. In particular, there is a component of α proportional to $\nabla^2 m$ [10], as predicted in Refs. [8] and [9].

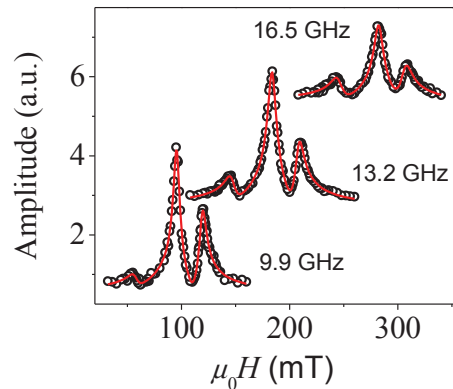


FIGURE 2. FMR spectra obtained by H-MOMM of a single, 100-nm-diameter nanomagnet patterned from a 10 nm $\text{Ni}_{81}\text{Fe}_{19}$ film. The data are the open circles, and the solid red lines are fits based on a superposition of eigenmodes, each of which follows eq. (3). The multiple modes are identified by comparison of the data with micromagnetic simulations. The low-field resonance is an eigenmode that spans the entire area of the nanomagnet, whereas the two high-field peaks are associated with localized modes that are proximate to the two ends of the nanomagnet along the applied field axis. It is assumed that subtle structural differences of the two ends split the end-mode into two peaks.

REFERENCES

- [1] S. Mangin, D. Ravelosona, J. A. Katine, M. J. Carey, B. D. Terris, and E. E. Fullerton, *Nat. Mater.* **5**, 210-215 (2006)
- [2] H. T. Nembach, *et al.*, *Phys. Rev. B* **84**, 054424 (2011).
- [3] G. H. O. Daalderop, P. J. Kelly, and F. J. A. den Broeder, *Phys. Rev. Lett.* **68**, 682 (1992).
- [4] S. Mizukami, Y. Ando, and T. Miyazaki, *J. Magn. Magn. Mater.* **226-230**, 1640 (2001).
- [5] J. M. Shaw, H. T. Nembach, and T. J. Silva, *Appl. Phys. Lett.* **99**, 012503 (2011).
- [6] J. M. Shaw, H. T. Nembach, and T. J. Silva, *Physical Review B* **85**, 054412 (2012).
- [7] C. T. Boone, H. T. Nembach, J. M. Shaw, and T. J. Silva, *J. Appl. Phys.* **113**, 153906 (2013).
- [8] V. G. Baryakhtar, *Sov. Phys. JETP* **60**, 863 (1984).
- [9] Y. Tserkovnyak, E. M. Hankiewicz, and G. Vignale, *Phys. Rev. B* **79**, 094415 (2009).
- [10] H. T. Nembach, J. M. Shaw, C. T. Boone, and T. J. Silva, *Phys. Rev. Lett.* **110**, 117201 (2013).

KEYWORDS

Spin torque, memory, switching, ferromagnetic resonance, damping, vector network analyzer, magneto-optics, microscope

XRD/TEM/EELS Studies on Memory Device Structures

¹Santosh K Kurinec, ²Sankha Mukherjee, ³Archana Devasia, ¹Surendra Gupta,
⁴Simone Raoux, ⁵Jean Jordan-Sweet, ⁶David MacMahon

¹*Microelectronic Engineering, Rochester Institute of Technology, Rochester NY 14623, USA*

²*Showa Denko HD Singapore, 2 Pioneer Crescent, Singapore, 628553.*

³*CRESST and NASA/GSFC, Greenbelt, MD 20771, USA*

⁴*Helmholtz-Zentrum Berlin für Materialien und Energie GmbH*

⁵*IBM T. J. Watson Research Center, Yorktown Heights, NY 10598, USA*

⁶*Micron Technology Inc., Manassas, VA 20110, USA*

INTRODUCTION

Over the past decade, numerous emerging memory technologies are being considered as contenders to displace either or both NAND flash and DRAM as scaling limitations of these conventional memories are perceived for applications in mobile devices. Some of these include Magnetic and Spin Transfer Torque Random Access Memory (MRAM, STTRAM), Phase Change RAM (PCRAM), Ferroelectric RAM and Resistive RAM memories. These technologies can be classified as relying on one of the movements: atomic, ionic, electron charge or spin in nanoscale thin films comprising of a variety of materials. The literature shows about 50 elements of the periodic table being investigated for these memory applications owing to their unique physical and chemical properties. Engineering memory devices requires nanoscale characterizations of film stacks for their chemical compositions and crystalline nature in addition to electronic properties such as resistance, magnetization and polarization depending upon the principle involved. This paper focuses on how x-ray diffraction (XRD), transmission electron microscopy (TEM) and electron energy loss spectroscopy (EELS) techniques have been employed to obtain insight into engineering magnetic tunnel junctions (MTJ) and PCM devices.

EXPERIMENTAL

The MTJ and PCRAM memory cells were fabricated using physical vapor deposition (PVD) of memory layers (MTJ at Veeco, PCRAM at Boise State University and IBM Watson Research Center) and subsequent design and fabrication at the RIT Microelectronic Engineering cleanroom facility. The time-resolved x-ray diffraction (TR XRD) analyses were performed at the National Synchrotron Light Source at Brookhaven National Laboratory. The incident beam wavelength was 1.797Å. XRD measurements were carried out while samples were heated at the rate of 1°C/s under flowing Helium to different temperatures. HRTEM and EELS analyses were performed at Micron Technology using Hitachi HD-2300 STEM fitted with a Gatan Enfina PEELS Spectrometer. 2D-XRD was performed at RIT using Bruker Dimension D8 system with GADDS detector.

MAGNETIC TUNNEL JUNCTION (MTJ)

A stack of CoFeB/MgO/CoFeB forms the core of the MRAM memory cell consisting of 10-12 layers comprising of top and bottom electrodes, pinning and barrier layers. For proper functioning of the MTJ, there must be band matching between CoFe and the tunneling barrier MgO which requires crystallization of these nanoscale thin layers. Amorphous CoFeB films are annealed with MgO as the template; however, boron diffusion needs to be investigated. While EELS can provide information on boron diffusion, XRD analysis in this thin film stack is not possible. Therefore, a multi layered (7 bi-layers) structure was designed for obtaining sufficient diffracted X-ray

signal while still maintaining structural resemblance to the single MTJ [1,2]. This enabled us to design suitable annealing conditions for crystallization of CoFeB and quantify boron diffusion in MgO as illustrated in Fig.1.

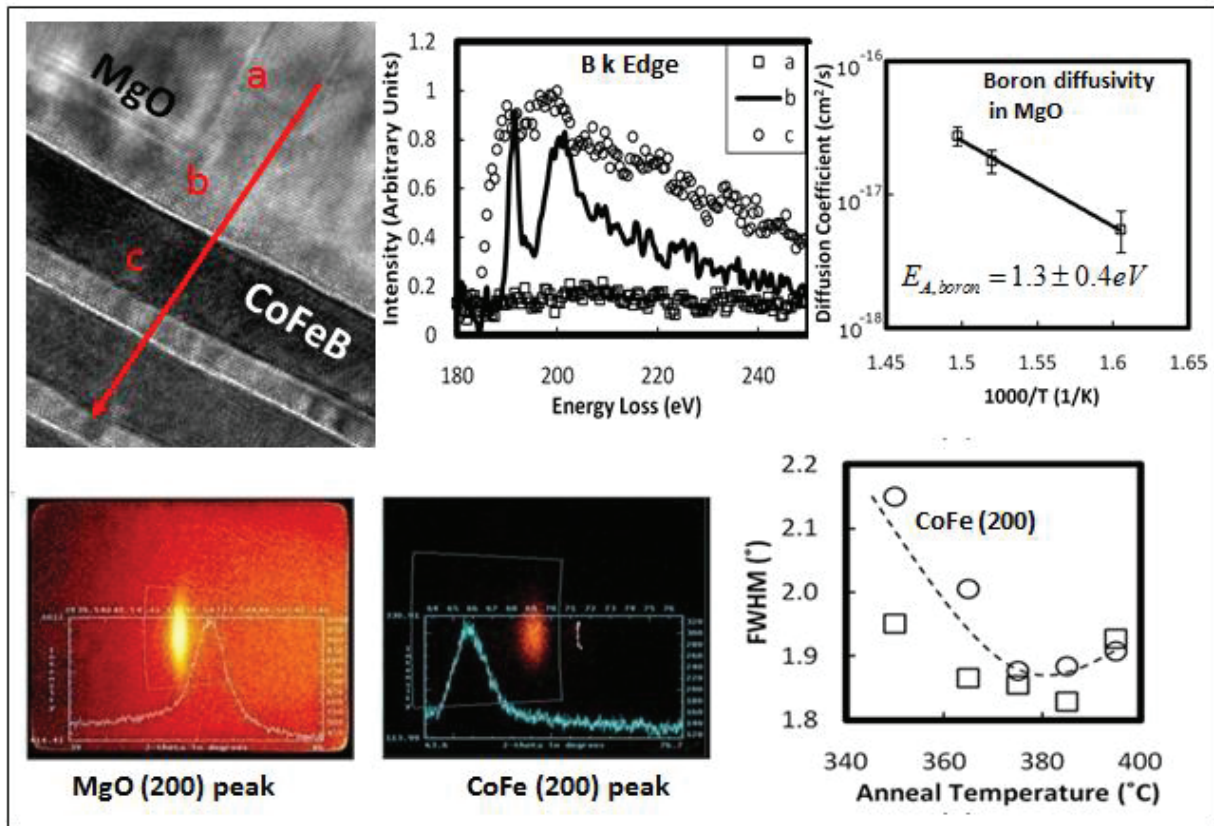


FIGURE 1. Top row: Boron EELS data acquired as a function of annealing at different locations to extract its diffusion coefficient in MgO; Bottom row: 2D-XRD of MgO and CoFe peaks to study crystallization and grain growth with annealing.

PHASE CHANGE MEMORY STRUCTURES

The phase change materials $\text{Ge}_2\text{Sb}_2\text{Te}_5$ (GST) and GeTe have been studied extensively for their application in re-writable optical storage and in PCRAM. Various configurations of GST and GeTe (bilayers and doped) have been investigated to design suitable memory cells for highly scaled devices. Bilayer chalcogenides composed of GeTe or Ge_2Se_3 and SnTe or SnSe are explored for these applications. Using TRXRD it has been demonstrated that stacked phase change memory films exhibit both structural and compositional dependency with annealing temperature. By the incorporation of a Sn layer the phase transition characteristics of Ge-chalcogenide thin films can be tuned. Clear evidence of thermally induced Ge, Sn and chalcogen inter-diffusion has been observed using HRTEM and PEELS. The study reveals the temperature limitations for each stack. It is observed that SnTe based devices exhibit lower threshold voltage, lower current at threshold, higher resistance margin and less variability in the SET state as compared to SnSe based devices [3]. Learning from the bilayer stacks, doped GST and GeTe, were investigated for the influence of various dopants on the crystallization behavior and electrical switching properties of GST and GeTe. The dopants included nitrogen, silicon, titanium, and aluminum oxide. TRXRD show that all GST samples (undoped and doped) first crystallized into the rocksalt crystal structure, and at higher temperature into the hexagonal phase [4]. The crystallization temperature increased with doping, and also the transition temperature from the rocksalt to the hexagonal crystal structure. For doped GeTe the crystal structure after heating was rhombohedral, similar to undoped GeTe, with slightly changed lattice constants. For GST nitrogen doping was most efficient in terms of increased crystallization temperature. Ti-doped GeTe material had the highest crystallization temperature of around 350 °C. The crystallization temperatures measured by XRD corresponded with the resistivity versus temperature measurements. It was observed that the doping can be used to tune the threshold field of the phase change material. In particular doping with aluminum oxide for GST and nitrogen doping for GeTe leads to a substantial increase in threshold field which is desirable for ultra-scaled

PCRAM devices. This work is being continued to study other RAM structures including ferroelectric tunnel junctions that will be presented at the conference.

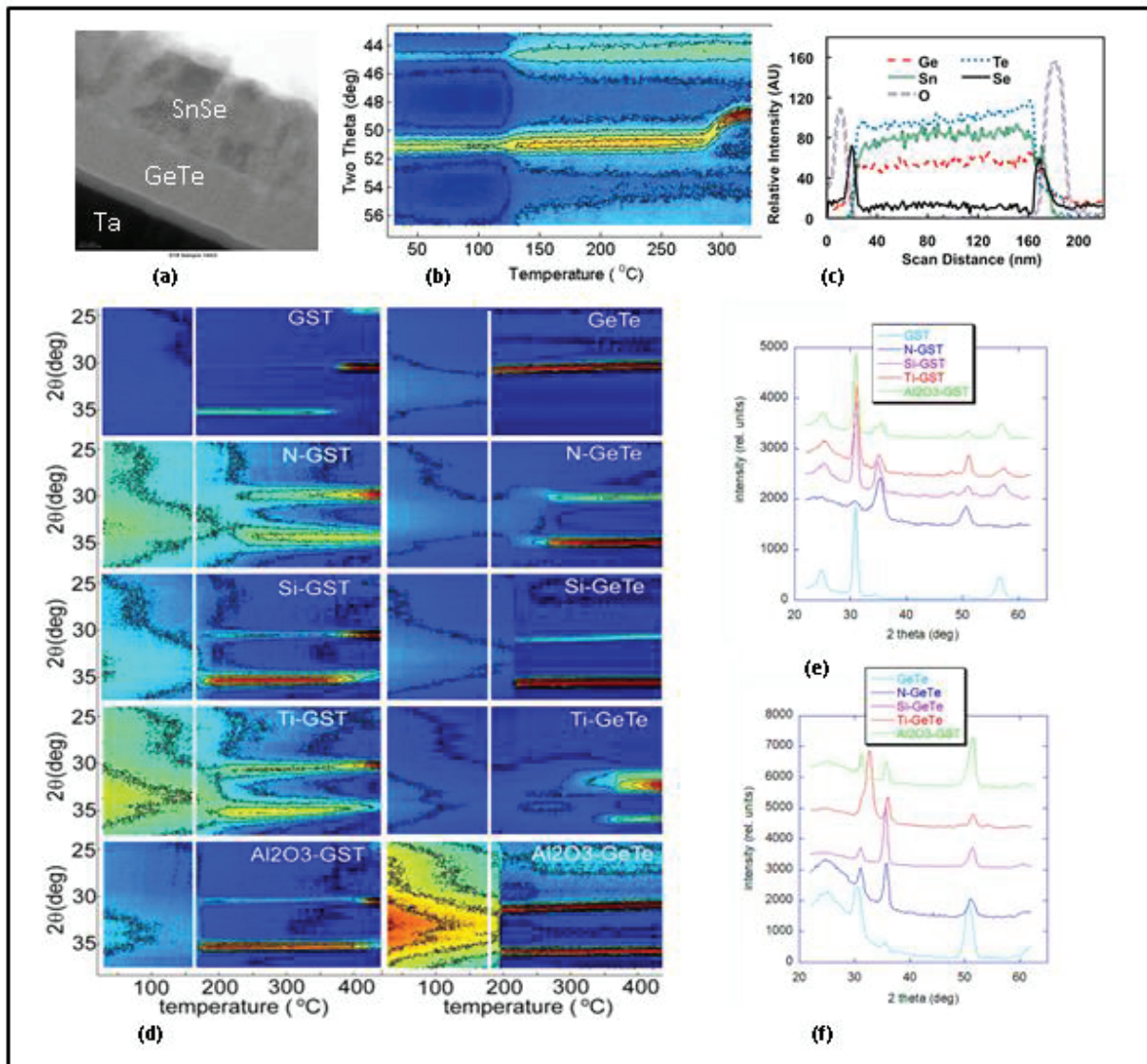


FIGURE 2. GeTe/SnSe stack (a) showing phase transition from rhombohedral to cubic structure of GeTe(Sn) phase ~ 300C (b); (c), PEEL elemental area scans for GeTe/SnSe sample as deposited and annealed to 340C; (d) TRXRD measurements on undoped and doped GST (left) and undoped and doped GeTe (right). Plotted is the intensity of diffracted XRD peaks as a function of temperature; (e, f) The θ - 2θ scans of undoped and doped GST and GeTe after a ramp to 450 °C [4].

REFERENCES

1. S. Mukherjee, D. MacMahon, F. Bai, C. -L Lee, S. K. Kurinec, Applied Physics Letters, 94, 082110, 2009.
2. S. Mukherjee, D. MacMahon, F. Bai, C. -L Lee, S. Gupta, and S. K. Kurinec, Journal of Applied Physics, Volume 106, Issue 3, pp. 033906-033906-7 (2009).
3. A. Devasia, S. Kurinec, K. Campbell and S. Raoux, Applied Physics Letters, 96/15, April 2010.
4. S. Raoux, D. Cabrera, A. Devasia, S. Kurinec, H. Cheng, Y. Zhu, C. Breslin and J. Jordan-Sweet, European Phase Change and Ovonic Symposium, September 2011, Zurich, Switzerland, pp. 76-83.

KEYWORDS

Time Resolved X-Ray Diffraction, Electron Energy Loss Spectroscopy, Magnetic Tunnel Junction, Phase Change Memory

Positron Annihilation Spectroscopy for Porosimetry of Micro- and Meso-porous Systems

R. Krause-Rehberg¹, W. Anwand², M. Butterling², M. Jungmann¹, A. Wagner²

1 Martin-Luther University Halle-Wittenberg, Inst. of Physics, 06099 Halle, Germany

2 HZDR, Inst. for Radiation Physics, PO-Box 510119, 01314 Dresden, Germany

INTRODUCTION

Positron annihilation has been used for decades to study the real and electronic structure of solids. Information on vacancy-type defects can be obtained. However, in dielectric media positrons can combine with an electron and form positronium (Ps) [1].

POSITRONIUM

Positronium as the lightest atom is formed in its singlet state as para-Ps (25%) and in the triplet state as ortho-Ps (75%). p-Ps has antiparallel spins and exhibit a very short lifetime of 125 ps which is not influenced by the host medium. It annihilates with two antiparallel gamma quanta of 511 keV each (m_0c^2). o-Ps has parallel spins and the lifetime in vacuum is 142 ns. It annihilates with three quanta summing up also to 1022 keV. In a medium, e.g. in a porous system o-Ps interacts with the pore walls and can exchange the electron to one with the opposite spin, i.e. forming p-Ps. This reduces the o-Ps lifetime distinctly. This process is called pick-off annihilation. In small pores the pick-off happens faster, i.e. the o-Ps lifetime becomes a unique function of the pore size.

This process can be described using quantum-mechanical models. The Tao-Eldrup model [2,3] takes into account only the ground state of Ps in a three-dimensional quantum well. It is valid to a pore size of 2 nm diameter. For larger pores, more sophisticated models include excited states of o-Ps and describe the whole size dependence up to a diameter of 100 nm where the vacuum lifetime of 142 ns is reached, e.g. [4].

POROSIMETRY USING O-PS

Fig. 1 shows the result of a calibration experiment where we studied controlled pore glass of a wide pore size range by positron annihilation [5]. The o-Ps lifetime τ_4 and the lifetime distribution σ_4 can be used to determine the pore size and the pore size distribution.

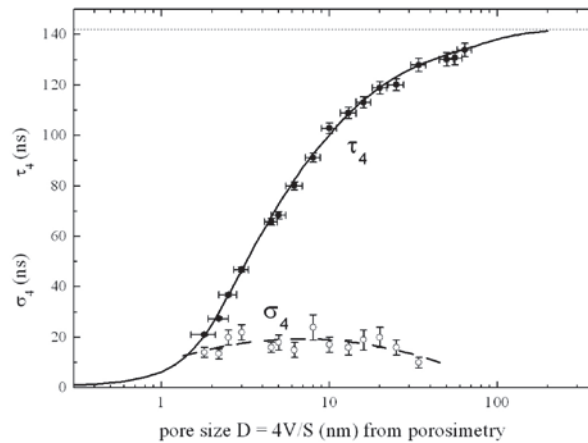


FIGURE 1. The o-Ps lifetime τ_4 and the lifetime distribution σ_4 obtained for controlled pore glass. The pore size was independently obtained by nitrogen absorption at 77K [5].

The pore size in Fig. 1 was obtained in parallel experiments using nitrogen adsorption at 77K. The sensitivity limit of positron annihilation ranges from micro- to mesopores, from about 0.3 nm to 40 nm pore diameter. In the talk, further examples of porosimetry in the field of low-k dielectric layers will be shown.

THE INTENSE SLOW POSITRON SOURCE MEPS AT HZDR

Positrons can be obtained from radioactive isotopes such as 22-Na. However, the source strength is limited and the β^+ spectrum exhibits a broad energy distribution up to the maximum energy of 540 keV. This leads to a deep penetration into porous samples up to 1 mm. Thus, thin layers cannot be studied. However, positrons can be moderated e.g. at W surfaces to obtain a slow, monoenergetic positron beam [6]. To obtain a high intensity source, positrons are better obtained by pair production in a reactor or using bremsstrahlung in a target of a high-energy electron beam. The MePS system (Mono-energetic Positron System) at the ELBE accelerator center at the Helmholtz-Center Dresden-Rossendorf (HZDR) utilizes a pulsed 40-MeV electron beam to obtain slow positron by pair production which can be re-accelerated to get depth profiles of porous layers [7].

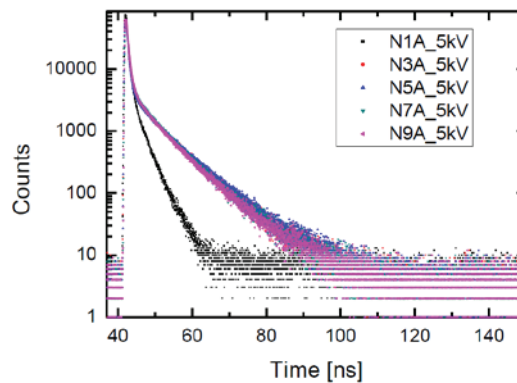


FIGURE 2. Positron lifetime spectra obtained using the MePS system at low-k layers at a depth of 450 nm.

Fig. 2 shows examples of positron lifetime spectra obtained for differently treated low-k dielectric layers of about 500 nm thickness at a positron energy of 5 keV corresponding to a mean penetration depth of 450 nm. From such data, the pore size distribution can be obtained as shown in Fig. 3.

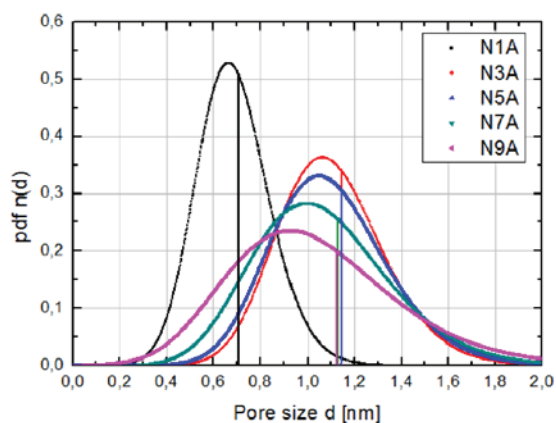


FIGURE 3. Pore size distribution obtained from positron lifetime spectra of Fig. 2.

REFERENCES

1. Y. C. Jean, D. M. Schrader and P. E. Mallon, *Principles and applications of positron & positronium chemistry*, New Jersey, London; World Scientific, 2003.
2. S. J. Tao. *J. Chem. Phys.*, **56**, 5499 (1972).
3. M. Eldrup, D. Lightbody, J. N. Sherwood. *Chem. Phys.*, **63**, 51 (1981).
4. T. Goworek, K. Ciesielski, B. Jasinska and J. Wawryszczuk. *Chem., Phys. Lett.*, **272**, 91 (1997).
5. S. Thraenert, E. M. Hassan, D. Enke, D. Fuerst and R. Krause-Rehberg, *phys. stat. sol. (c)* **4**, 3819 (2007)
6. P. J. Schultz and K. G. Lynn. *Rev. Mod. Phys.*, **60**, 701 (1988).
7. R. Krause-Rehberg, G. Brauer, M. Jungmann, A. Krille, A. Rogov and K. Noack, *Applied Surface Science* **255**, 22 (2008) .

KEYWORDS

porosimetry, micropores, mesopores, positron annihilation

Imaging Electron Motion in Nanostructures

Robert M. Westervelt^{*,†}

*Harvard University
School of Engineering and Applied Sciences
& Department of Physics
29 Oxford Street
Cambridge, MA 02138, USA*

QUANTUM MATERIALS AND DEVICES

Quantum materials and devices offer outstanding platforms for scientific discovery and the creation of new technologies - examples include semiconductor superlattices and heterostructures, and electrons in reduced dimensions - two-dimensional electron gas (2DEG), one-dimensional nanotubes and nanowires, and zero-dimensional quantum dots. Recently discovered quantum materials push toward the atomic scale - atomic-layer materials (including graphene and transition metal dichalcogenides) for devices that are only one atom or molecule thick, topological insulators (such as Bi_2Se_3) that carry data in edge states, and diamond nitrogen vacancy (NV) centers that store a qubit on a single atom, at room temperature. To create functional devices and systems for future electronics and photonics, we need to understand how electrons move through these nanostructures.

IMAGING THE MOTION OF ELECTRONS

This talk will describe techniques for imaging the motion of electronic charges and spins inside nanostructures that is needed to develop new devices and systems. We start with Imaging Electron Charge, then consider Imaging Electron Paths, and finally describe Imaging Magnetic Fields with a Diamond Nitrogen Vacancy (NV) Center.

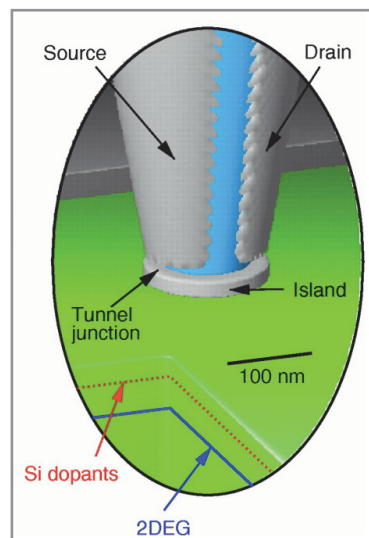


FIGURE 1. Single electron transistor (SET) tip for a scanned probe microscope (SPM) that acts as an ultrasensitive sensor to image the electronic charge in a nanostructure below.³

Imaging Electron Charge

A capacitive technique to probe a quantum dot was developed by Ashoori, who used this approach to measure the energy states of a dot using the Coulomb blockade spectroscopy.¹ He extended the method to image localized regions of a 2DEG in the quantum Hall regime, by attaching a sensitive charge amplifier to a metallic SPM tip held above the sample.² Ashoori used this approach to provide a spatial picture of the quantum Hall state.

Very high charge sensitivity was achieved by fabricating a single-electron transistor (SET) at the end of an SPM tip,³ as shown in Fig. 1. An SET can sense small fractions of an electron charge via the Coulomb blockade. An image of the charge density of a sample can be obtained by displaying the SET drain current as the tip is raster scanned above the surface. SET tips have been used to image the edge states of the quantum Hall effect⁴ and to image the electron-hole charge puddles in graphene,⁵ among other applications.

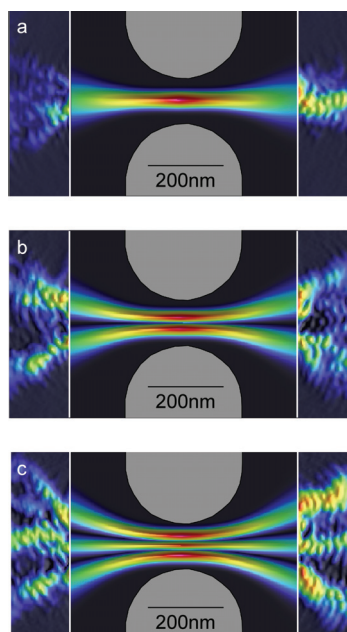


FIGURE 2. Scanned probe microscope images of the first three spatial modes of transmission through a quantum point contact in a two-dimensional electron gas. Interference fringes are spaced by half the Fermi wavelength.^{7,10}

Imaging Electron Paths

Electron paths through quantum devices are often ballistic, due to their small size and high electron mobility - examples are a GaAs 2DEG or a graphene layer. Westervelt's group developed a way to image electron flow by deflecting electrons with a capacitively coupled SPM tip.⁶⁻⁹ Images of the first three spatial modes of electrons traveling through a quantum point contact (QPC) can be obtained by backscattering electrons from a depleted 'divot' beneath the tip, as shown in Fig. 2 - the conductance change for the QPC is displayed as the SPM tip is raster scanned above the sample. Interference fringes for the electron waves are also observed, with spacing half the Fermi wavelength.^{7,10} In a related technique, the SPM tip is used as a movable gate to tune few-electron quantum dots.¹¹ Imaging experiments for electron flow through graphene devices have recently been carried out.

Image Magnetic Fields With A Diamond NV Center

The electron spins on a nitrogen vacancy (NV) center in diamond can store a qubit of information at room temperature, opening new paths to quantum information processing. In addition, a single NV center acts as a remarkably sensitive magnetosensor that can image magnetic field patterns with very high spatial resolution. Figure 3 shows a single NV center in a diamond nanowire at the end of a diamond cantilever.¹² The sensitivity at room temperature approaches the ability to image single electron spins.

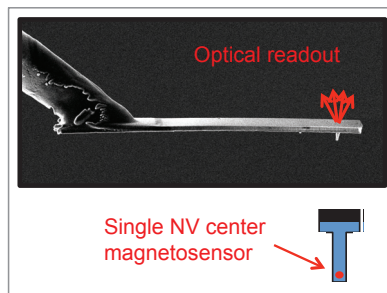


FIGURE 2. Nitrogen Vacancy (NV) center in a diamond nanowire at the end of a scanning probe microscope tip acts as an ultrasensitive, high spatial resolution sensor to image magnetic fields.¹²

REFERENCES

- * Director, Science & Technology Center for Integrated Quantum Materials (Harvard Univ., Howard Univ., MIT and Museum of Science, Boston), website <http://ciqm.harvard.edu>.
- † Supported by the NSF Science & Technology Center for Integrated Quantum Materials, grant DMR-1231319.
1. R.C. Ashoori, H.L. Stormer, J.S. Winder, L.N. Pfeiffer, J.J. Pearton, K.W. Baldwin and K.W. West, "Single-electron capacitance spectroscopy of discrete quantum levels," *Phys. Rev. Lett.* **68**, 3088 (1992).
 2. S.H. Tessmer, P.I. Glicofridis, R.C. Ashoori, L.S. Levitov and M.R. Melloch, "Subsurface charge accumulation imaging of a quantum Hall liquid," *Nature* **392**, 51-54 (1997).
 3. M.J. Yoo, T.A. Fulton, H.F. Hess, R.L. Willet, L.N. Dunkleberger, R.J. Chichester, L.M. Pfeiffer and K.W. West, "Scanning Single-Electron Transistor Microscopy: Imaging Individual Electron Charges," *Science* **276**, 579-582 (1997).
 4. A. Yacoby H.F. Hess, T.A. Fulton, L.N. Pfeiffer and K.W. West, "Electrical imaging of the quantum Hall state," *Solid State Commun.* **111**, 1-13 (1999).
 5. J. Martin, N. Akerman, G. Ulbricht, T. Lohmann, J.H. Smet, K. von Klitzing and A. Yacoby, "Observation of electron-hole puddles in graphene using a scanning single-electron transistor," *Nature Phys.* **4**, 144 (2008).
 6. M.A. Topinka, R.M. Westervelt and E.J. Heller, "Imaging Electron Flow", *Physics Today* **56**, 47 (2003).
 7. M.A. Topinka, B. LeRoy, S. Shaw, E. Heller, R.M. Westervelt, K.D. Maranowski and A.C. Gossard, "Imaging Coherent Electron Flow from a Quantum Point Contact", *Science* **289**, 2323 (2000).
 8. M.A. Topinka, B.J. LeRoy, R.M. Westervelt, S.E.J. Shaw, R. Fleischmann, E.J. Heller, K.D. Maranowski and A.C. Gossard, "Coherent Branched Flow in a Two-Dimensional Electron Gas", *Nature* **410**, 183 (2001).
 9. Katherine E. Aidala, Robert E. Parrott, Tobias Kramer, R. M. Westervelt, Eric J. Heller, Micah P. Hanson, Arthur C. Gossard, "Imaging Magnetic Focusing of Coherent Electron Waves", *Nature Physics* **3**, 464 (2007).
 10. B.J. LeRoy, A.C. Bleszynski, K.E. Aidala, R.M. Westervelt, A. Kalben, E.J. Heller, K.D. Maranowski and A.C. Gossard, "Imaging electron interferometer", *Phys. Rev. Lett.* **94**, 126801 (2005).
 11. P. Fallahi, A.C. Bleszynski, R.M. Westervelt, J. Huang, J. Walls, E.J. Heller, M. Hanson, A.C. Gossard, "Imaging a single-electron quantum dot", *Nano Lett.* **5**, 223 (2005).
 12. P. Maletinsky, S. Hong, M.S. Grinolds, B. Hausmann, M.D. Lukin, R.L. Walsworth, M. Loncar and A. Yacoby, "A robust scanning diamond sensor for nanoscale imaging with nitrogen-vacancy centres," *Nature Nano* **7**, 320-324 (2012).

KEYWORDS

Scanning probe microscope, image electron motion, image electron paths, image electron charge, image magnetic fields

Advances in Atom Probe Metrology

Thomas F. Kelly¹ and Karen T. Henry²

¹ *Cameca Instrument, Inc.*
5500 Nobel Drive, Madison, WI 5371, USA

² *Intel Corporation*
2501 NW 229th Avenue, Hillsboro, OR 97124, USA

INTRODUCTION

Semiconductor metrology is the measurement of physical dimensions or properties of semiconductor structures and devices. Atom probe tomography (APT) provides three-dimensional composition images of materials at the sub-100 nm scale and in this regard, may be utilized to measure local compositions, spatial relationships, and dimensions in structures. Thus, APT can be considered for semiconductor metrology. However, industrial metrology typically demands high performance in speed and precision. The needs of the industry span a wide range of throughput and precision and this presentation will discuss how APT might be used most effectively now and in the future to meet these challenges.

CURRENT STATUS

APT is a very capable analytical technique and like any technique, it has its strengths and limitations. It is worth reviewing these with regard to semiconductor applications to get a sense of how the technique can best be utilized. Table 1 lists the most important of these characteristics. The combination of high spatial resolution with high analytical sensitivity in a three-dimensional composition image is unique in analytical instrumentation. The accessible volumes are typically 100 nm by 100 nm by potentially greater than a micrometer in depth. This volume is well suited to semiconductor analyses, especially given the ability to locate features of interest to within approximately 10 nm. Additionally, recent improvements in detector engineering has made >80% detection efficiency commercially available. This is a very high efficiency by most analytical standards. However, in some applications like detection of small clusters and single-atom devices, every atom is important. As a metrology tool, compositional and spatial fidelity are crucial. The next section describes efforts to improve the technique.

ROADMAP FOR METROLOGY IMPROVEMENT

Semiconductor compositional metrology requires a challenging combination of high spatial resolution for very low concentration elements. Sometimes these elements are also challenging to analyze, like boron and carbon, because of their low atomic number. APT is well suited to address this type of challenge and currently is the only technique able to perform such measurements in three dimensions. Furthermore, there will continue to be improvements in the operational characteristics of the instrumentation. However, this is not the present question. Metrology thrives on precision and accuracy of measurement and we must address the question of whether and how the technique might be improved for semiconductor metrology. The most fundamental limitations of the technique

today, image distortion and compositional inaccuracy, are not constrained by physics but by technology. That is, there is no physical reason that these limitations cannot be eliminated: the technology to do so just has yet to be developed.

Table 1. Summary of the strengths and limitations of atom probe tomography as applies to semiconductor metrology.

Strengths of APT	Limitations of APT
Time to knowledge is acceptable (~1 day)	Not all materials will run well
Discrete 3-dimensional image	Limited field of view (<300 nm)
High analytical spatial resolution (0.3 nm)	Reconstruction distortions for heterogeneous materials
High analytical sensitivity (<10 appm)	High detection efficiency ~80% (but not 100%)
Specimen preparation is similar to TEM	Crystallographic information is limited
All atoms detected with equal efficiency	No chemical bonding information
High detection efficiency (>80%)	

Two major projects toward improved metrology are currently being pursued. For example, if the shape of the specimen apex is known during the entire atom probe experiment, we can then correctly back project the ion trajectories to the specimen. Kelly et al. [1] have considered what it will take to accomplish this formidable task and have concluded that combining an electron column with atom probe could succeed at this task. Other possibilities include field ion imaging of the specimen apex and self-contained iterative modeling of the specimen evaporation process to deduce the apex shape. Experiments are underway [2] to investigate electron imaging on a CAMECA LEAP for this purpose. The emphasis will be on determining the minimum amount of information needed from electron column hardware to reduce the distortions in atom probe images to negligible values.

There is more to be gained from the combination of scanning transmission electron microscopy (STEM) with APT than simply overcoming limitations. There are synergies that result from this particular combination. In fact, these two techniques are almost perfectly aligned synergistically, i.e., the limitations of TEM are a strength of APT and vice versa. For example, the high spatial fidelity, chemical sensitivity, and multiple imaging modalities of TEM offset limitations in APT and the high analytical sensitivity and three dimensionality of APT likewise offset limitations of TEM. So, it is a match that goes well beyond the value ascribed to resolving the distortions in APT images.

Compositional fidelity can be improved by detecting 100% of the evaporated ions and correctly identifying them. A program is underway at the University of Wisconsin [3] to develop a position-sensitive ion detector based on superconducting materials. The principal aim of this work is to achieve 100% detection of the ions. A secondary goal is to provide information about the kinetic energy of the arriving ions. This concept was put forward by Kelly [4] for atom probe tomography based on work of earlier investigators in other fields [5]. For an operating voltage of V , ions will arrive at the detector with neV of kinetic energy where n is the charge state and e is the fundamental charge constant. Modest kinetic energy resolving power will be sufficient to distinguish peak ambiguities based on charge state for the same mass-to-charge-state ratio. If these efforts are successful, most of the common peak ambiguities in atom probe tomography will be resolved.

These two independent developments, taken together, bring APT into the realm of atomic-scale tomography (AST). That is, with three dimensional images of very low distortion and 100% of the atoms correctly identified, AST would be able to tackle the most demanding analytical challenges that may be coming in the semiconductor industry. Graphene-based devices and single-atom transistors are being considered for the not-too-distant future of integrated

semiconductor structures. It will be essential that microscopies keep pace with these needs and be able to characterize every atom in the structures.

CONCLUSIONS

Characterization of semiconductor structures with atom probe tomography (APT) has proven to be effective even in the demanding environment of commercial semiconductor manufacturing. The principal limitation of APT, image distortions in multiphase materials, remains a concern. Future developments are aimed at eliminating these distortions as well as improving detector performance to reach 100% atomic detection efficiency. If these instrumental developments can be realized, APT can play a crucial role in the development of future nanoscale semiconductor devices.

REFERENCES

1. T.F. Kelly, M.K. Miller, K. Rajan, and S.P. Ringer, *Microsc. Microanal.* **19**, 652 (2013).
2. B.P. Gorman, D.R. Diercks, and T.F. Kelly, (2014).
3. R.F. McDermott, J.R. Suttle, and T.F. Kelly, (2014).
4. T.F. Kelly, *Microsc. Microanal.* **17**, 1 (2011).
5. G.C. Hilton, J.M. Martinis, D.A. Wollman, K.D. Irwin, L.L. Dulcie, D. Gerber, P.M. Gillevet, and D. Twerenbold, *Nature* **391**, 672 (1998).

KEYWORDS

atom probe tomography, semiconductor metrology, nanostructure analysis, atomic-scale tomography

Scatterfield Microscopy and the Fundamental Limits of Optical Defect Metrology

Richard M. Silver, Bryan M. Barnes, Martin Y. Sohn, and Hui Zhou

*Semiconductor and Dimensional Metrology Division, Physical Measurement Laboratory,
National Institute of Standards and Technology,
100 Bureau Dr. MS 8212, Gaithersburg, MD USA 20899-8212*

ABSTRACT

Defect inspection remains a critical manufacturing challenge due to the competing requirements between throughput and very high resolution. Currently only optical methods provide an acceptable solution, although there are a number of process layers and defect types that cannot be measured adequately. As a result there has been a continued drive to push optical methods to new levels of performance and sensitivity without compromising throughput. In this paper we describe several advanced optical engineering methods that improve resolution and extend optical techniques. Fourier control methods applied to both the illumination field and the imaged field offer the possibility to optimize sensitivity in a conventional or high angle optical system. This combined with polarization control is the current approach to extend conventional techniques. Recent advances that capture and use the full 3-D scattered field have recently been shown to improve detectability by up to nearly an order of magnitude. Although there are throughput costs to 3-D imaging, these costs may be mitigated if the 3-D data used to find best focus are also used in the volumetric analysis. Advances in wavelength scaling and coherence will also be contrast with existing methods.

INTRODUCTION

In leading-edge semiconductor manufacturing a limited number of wafers are fully inspected for defects, although critical portions of the exposure field may be monitored more frequently. And while details of the sampling schemes and strategies remain a largely proprietary aspect of process control, the pervasive tradeoff between resolution and throughput dominates defect inspection [1, 2]. Scanning electron microscopy (SEM) can provide adequate resolution for most inspection requirements, however, the magnification and field size needed to achieve the high resolution in an SEM implies that the usual slow scan mode used for high resolution imaging results in inadequate throughput. There have been advances in multi-beam systems that do promise to simultaneously solve the throughput resolution challenges, but technical challenges remain with respect to signal to noise ratios, beam homogeneity across the array, and extremely large data requirements [3]. There have also been advances in high-speed atomic force microscopy (AFM) for application in defect inspection, however, this approach is hampered by difficulty in measuring small trenches in dense layouts and also by the throughput versus resolution tradeoff.

The current emphasis is to use sophisticated optical engineering methods to extend what has been the method of choice [4]. In recent scatterfield microscopy work measuring finite and periodic targets, sub-nanometer sensitivity to changes in the feature dimensions has been demonstrated with nanometer scale accuracy [5]. This work combines polarization and Fourier control of the illumination combined with full three dimensional image acquisition. An example of the scatterfield data acquisition methods is shown in Fig. 1. Detailed rigorous modeling of the volumetric intensity data results in quantitative fits demonstrating nanometer scale accuracy.

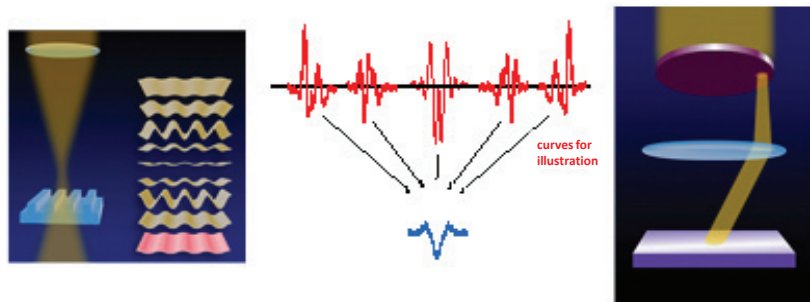


FIGURE 1. Schematics of the experimental methods for focus-resolved and angle-resolved data acquisition. Information about the target can be collected at various through-focus positions (center). Specific angles of light can be directed at the surface by engineering the CBF.

ANGLE-, FOCUS-, AND WAVELENGTH-RESOLVED DEFECT ANALYSIS

The most straight forward approach to adapt scatterfield microscopy to defect inspection is to implement elements of Fourier engineering of the illumination field or the collection path scattered field [6-8]. Polarization is also an important tool in this regime. The basic idea is to “tune” the illumination to the target of interest. With the pervasive use of unidimensional structures in leading edge optical lithography processes, these same layouts become more amenable to optical illumination field engineering, with spatial frequency content matched to the pitch, critical dimensions, and process stacks etc. being measured. Figure 2 shows an example of the potential gains from using tailored illumination including polarization optimization [9]. Optical engineering and optimization of the illumination field is accomplished using the optical configuration shown in Fig. 1.

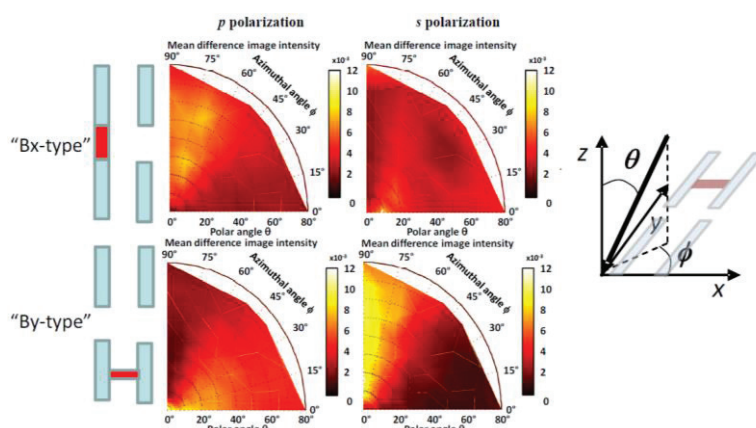


FIGURE 2. (left) Schematics of two types of highly directional bridge defects. (middle) Plots of a defect detection metric for the four possible combinations of p- and s-polarization and the two defect types shown at left. The plots show defect detectability based on a threshold as a function of polar and azimuthal illumination angle. (right) The polar and azimuthal illumination angles relative to the simulation layout. These simulations are for a 40 nm CD layout illuminated with $\lambda = 193$ nm light. Reprinted from Ref. 9.

The data in Figure 2 show that the optimum defect detectability for the “By”-type defect is obtained using linearly polarized light aligned with the defect but across the patterned lines and angle-resolved incident light with an incident plane along the lines and across the bridge. For the “Bx”-type defect, the detectability is best when illuminated using linearly polarized light aligned along the defect and the patterned lines with angle-resolved incident light having an incident plane along the lines and bridge. These methods for controlling the spatial frequency information of the illumination and scattered fields are now being implemented by the leading optical tool manufacturers. However, these techniques may be limited in their effectiveness for some types of defects at the 22 nm node and beyond.

An important advance which has been demonstrated to enhance sensitivity for targets at the 22 nm node and beyond is to use the full three dimensional scattered field [10, 11]. This technique goes beyond simple data

acquisition at best focus and uses the full three-dimensional scattered field in the defect analysis. A simulated example of volumetric data acquisition and analysis is shown in Figure 3. This figure shows the data acquisition sequence, the three-dimensional matrix formation, and subsequent creation of the volumetric differential image. This differential volumetric can be filtered in unique ways to obtain the identified defect shown in Figure 3d.

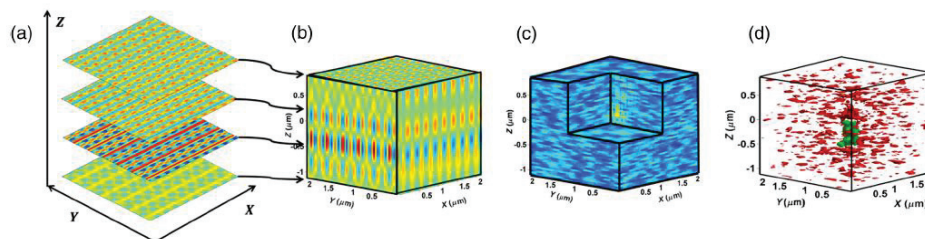


FIGURE 3. Schematic of three-dimensional volumetric processing. (a) Images from a defect are collected or simulated through focus. (b) These images can be transformed into a volume of intensity information. Likewise, a reference volume can also be obtained. (c) The defect and reference volumes are subtracted yielding a differential volume. A cut-out shows the defect within. (d) Intensity and spatial extent thresholding yields the large central sub-volume [green] in the center due to a defect, the remaining sub-volumes are noise [red]. Reprinted from Ref. 11.

This method improves detection because there is substantially more information used and improved filtering algorithms can be utilized. Algorithms that typically use continuity and areal threshold in two dimensions can be expanded to fully three dimensional applications. In recent published results, five-fold detection enhancements in experimental defect metrics have been demonstrated [10].

Since defect detection has many attributes in common with image based methodologies, wavelength scaling is also an important tool. Defects at the 22 nm node and beyond are deeply sub-wavelength. The optical response to defects at this scale means that the scattered information is well beyond the diffraction limit, although it is still contained in the scattered intensity. Even though this is a signal-based imaging measurement and not an edge-based imaging measurement, the results are strongly influenced by imaging wavelength. This is in part due to the strength of the scattering signal as the scattering sites approach 10 nm in size [12]. Figure 4 shows a comparison of angle resolved defect sensitivity plots for 193 nm and 266 nm wavelengths for a 22 nm wide defect. These data show that 193 nm has a strong influence on improving detection for both polarizations shown.

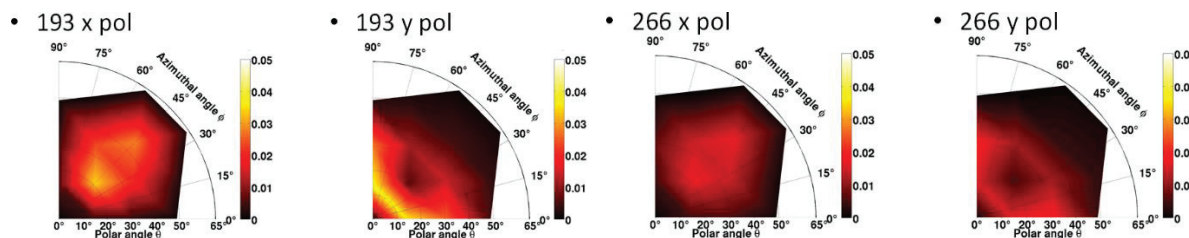


FIGURE 4. A comparison of defect sensitivity at 193 nm and 266 nm wavelengths using electromagnetic modeling. The plots show defect detectability based on a threshold as a function of polar and azimuthal illumination angle.

CONCLUSION

Fourier illumination path engineering, polarization optimization, and full use of the three-dimensional scattered field provide a path to extend the sensitivity and resolution of conventional optical methods while still achieving high throughput. An additional important attribute which can be used to optimize sensitivity and signal-to-noise ratio is Fourier filtering on the collection path. This allows the background or elements of the noise spectrum to be filtered out. Further gains may be achieved through additional wavelength scaling, although signal-to-noise challenges and low reflectivity will require careful thought in instrument design and optimization. The focus on optical methods of various wavelengths will continue due to the significant competition between high resolution and throughput. These goals are mutually incompatible and necessarily require compromise.

ACKNOWLEDGEMENTS

The authors wish to thank the SEMATECH Metrology Initiative for access to these intentional defect array wafers. We also thank András Vladár and Bin Ming for assistance in SEM measurements.

REFERENCES

1. International Technology Roadmap for Semiconductors, *2012 tables, Yield Enhancement*, <http://www.itrs.net/Links/2012ITRS/2012Tables/Yield_2012Tables.xlsx> (13 March 2014).
2. T. F. Crimmins, *Proc. SPIE* **7971**, 79710E (2012).
3. B. Thiel, M. Lercel, B. Bunday, and M. Malloy, *Proc. SPIE* **9236**, 92360E (2014).
4. R. M. Silver, B. Barnes, R. Attota, J. Jun, M. Stocker, E. Marx, and H. Patrick, *Appl. Opt.*, Vol. 46, 20, pp. 4248-4257 (2007).
5. J. Qin, R. M. Silver, B. M. Barnes, H. Zhou, and F. R. Goasmat, *Appl. Opt.*, **52**, 6512-6522 (2013).
6. R. M. Silver, B. M. Barnes, Y.-J. Sohn, R. Quintanilha, H. Zhou, C. Deeb, M. Johnson, M. Goodwin, and D. Patel, *Proc. SPIE* **7638**, 76380J (2010).
7. B. M. Barnes, R. Quintanilha, Y.-J. Sohn, H. Zhou, and R.M. Silver, *Proc. SPIE* **7971**, 79710D (2011).
8. Y.-J. Sohn, R. Quintanilha, B.M. Barnes, and R. M. Silver, *Proc. SPIE* **7405**, 74050R (2009).
9. B. M. Barnes, Y.-J. Sohn, F. Goasmat, H. Zhou, and R. M. Silver, *Proc. SPIE* **8324**, 83240F (2012).
10. B. M. Barnes, M. Y. Sohn, F. Goasmat, H. Zhou, A. E. Vladár, R. M. Silver, and A. Arceo, *Opt. Express* **21**, 26219-26226 (2013).
11. B. M. Barnes, F. Goasmat, M. Y. Sohn, H. Zhou, A. E. Vladár, and R. M. Silver, *J. Micro/Nanolith.* **14**, 014001 (2015).
12. T. F. Crimmins, *Proc. SPIE*. **7638**, 76380H (2010).

KEYWORDS

Defect metrology, defect sensitivity, defect detection, scatterfield microscopy, scatterfield optical microscopy, volumetric imaging

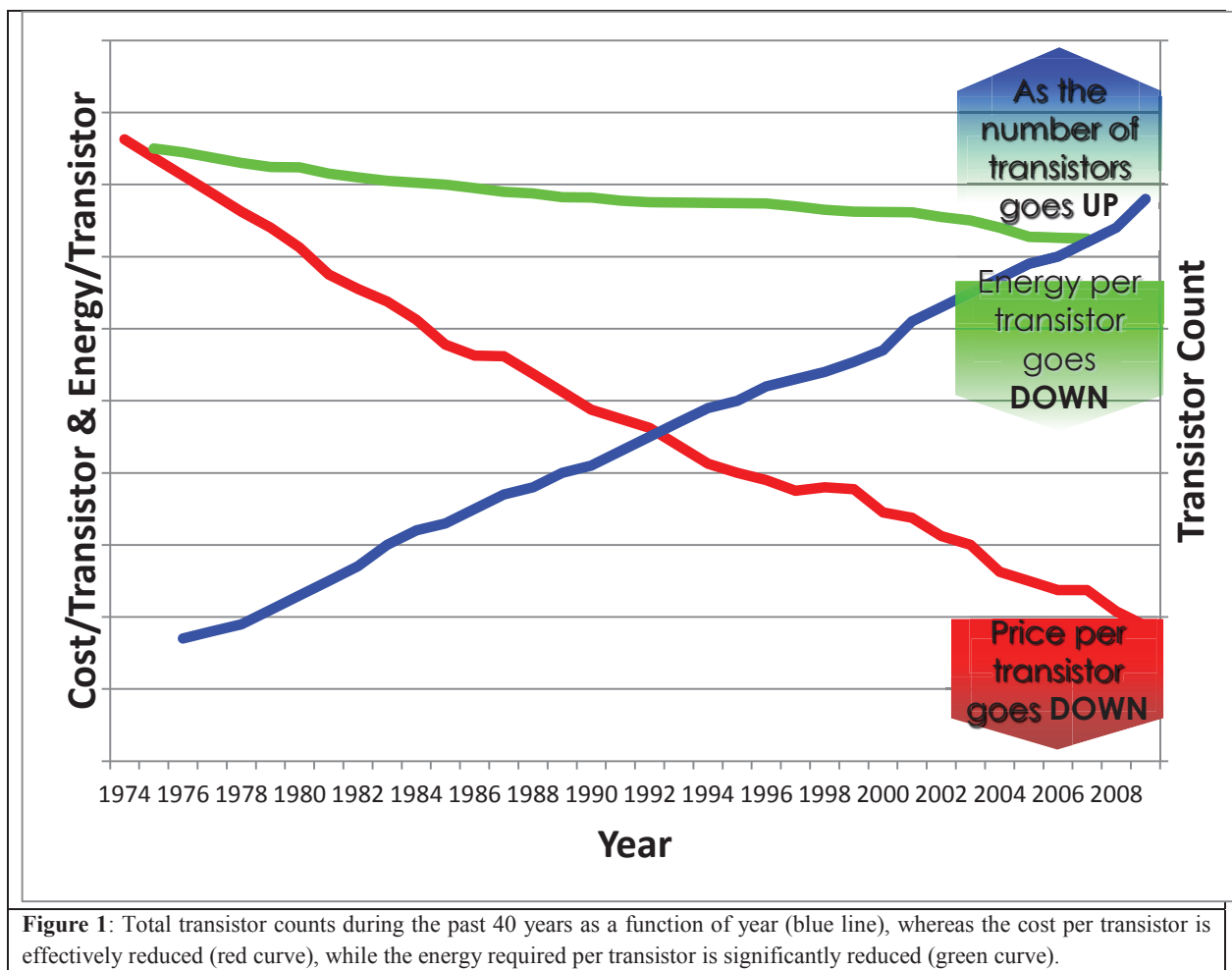
Defect Inspection for Advanced Technology Nodes

Tuyen Tran

*Portland Technology Development
Intel Corporation, 2501 NW 229th Ave., Hillsboro, OR 97124*

ABSTRACT

The Integrated Circuit (IC) as we know it since the early 60s has been continually incorporated into ever more large and small devices that actually impact people's lives. Yet the need for more IC is still insatiable. Around 1970 Gordon Moore observed that the number of integrated circuits in a device will be doubled every two year. This has since become known as Moore's law, and has been the basic driving force for advancement in the semiconductor industry for the past 30 years or so. In addition to 'doubling' the number of transistors roughly every 2 years, 'cost reduction' has become one of the biggest attractions of integrated electronics, and the cost advantage continues to increase as technology evolves toward the design and production of more powerful circuit functions on a single wafer substrate. What we have witnessed the last 40 years is that only in the semiconductor industry, the price per transistor actually goes down as the number of transistor goes up for any given device, as Figure 1 clearly illustrates. Furthermore, an additional benefit of Moore's law has been the energy efficiency enablement of devices from laptop to desktop to cell phone over the past 30+ years. This has been made possible due to a relentless effort to systematically reduce energy usage per transistor via either superior process efficacy and/or conscious design trade-off decisions.



In order to keep up with Moore's law while keeping the cost of high performance integrate circuit under control effectively, the minutiae details of a manufacturing process has to be optimized and controlled to an extend that was not possible before: Manufacturing devices and the processing equipments from which they are made of, need to be free of defects which affect yield, or devices need to be designed with a high level of built-in redundancy; Furthermore, lithographic linewidth and line edge roughness must be within ultra-tight control limits; film thickness and opto-mechanical properties have to be accurate, and uniform across the entire wafer area.

It has been known in general that the detection of particles on unpatterned substrates, and that of defects on patterned wafers is critical to Yield in the semiconductor industry. Unintended particulates left on surface of a wafer can result in Yield loss for that wafer, whereas unidentified sources of particulates from a semiconducting process equipment tool can easily render hundreds of wafers unusable. If the root cause of the particulates and the process equipment going out of control is not identified quickly, and fixes put in place, the resulting wafers processed will unlikely produce much yielding materials and will result in a loss of resources and more importantly, time. Hence, it is very important to fully identify the type (small, large, killer or non-killer defects, etc.) and characteristics (elemental make-up of defects, process step where defect originated from) of any defect in an integrated circuit process, so that the affected materials can be removed, and effective fixes for processing equipment's are in place before they can adversely affect Yield[1].

In the semiconducting industry, there are many techniques available to locate defects and contaminating particles on a surface of a semiconductor wafer. In general, these techniques fall into 2 categories: Spatially Filtered Bright Field imaging techniques, Low-angle Dark Field imaging technique[2]. Recently, electron beam inspection

technologies has been put to use at strategic part of the process and has emerged as a potential viable complement, if not near outright replacement of photon-based inspection tools. Additionally, there are certain proprietary techniques that could be used to identify killer or non-killer defects caused by OPC (optical proximity correction) marginality, or caused by a complex interaction between lithographic and etch processes.

In this paper, the most advanced defect inspection technologies encompassing Dark Field, Bright Field and Electron Beam capabilities will be reviewed and their effectiveness across different phases of a typical process node development at Intel will be discussed.

REFERENCES

1. T.K. Tran, *Advanced Metrology and Inspection*, Semicon KOREA, Seoul, Korea (2014).
2. van de Hulst, H.C., *Light Scattering by Small Particles*, Dover, New York (1957).

Advances in Multi-Beam SEM Technology for High Throughput Defect Inspection

Gregor Dellemann¹, Thomas Kemen¹, Anna Lena Eberle¹, Tomasz Garbowski¹,
Matt Malloy², Stefan Wurm², Benjamin D. Bunday², Brad Thiel³, and Dirk
Zeidler¹

¹Carl Zeiss Microscopy GmbH, Carl-Zeiss-Str. 22, D-73447 Oberkochen, Germany

²SEMATECH, 257 Fuller Rd, Suite 2200, Albany, NY 12203, USA

³SUNY Polytechnic Institute, 257 Fuller Road, Albany, NY 12203, USA

INTRODUCTION

The continuing decrease of structure size in semiconductor devices has produced a demand for measuring patterns and detecting defects of few nanometer in size. Scanning electron microscopes (SEM) can resolve these structures, but not with throughput sufficient for screening large areas such as whole wafers with high resolution [1]. We have recently reported on a multi-beam SEM that uses 61 parallel electron beams in a single column [2] and its corresponding first enhancement using 91 beams [3] to overcome these limitations. Here, we report on applications of multiple-beam SEMs on semiconductor wafers.

PRINCIPLE OF OPERATION

We use a multi-beam, single column for the multiple beam SEM that has been described elsewhere [2, 3]. We therefore only give a short summary here. In figure 1 (left), an array of electron beams generated by a multi-beam source is focused by a lens arrangement onto the specimen. A regular pattern of 61 (or 91) primary electron spots is formed on the sample, and the secondary electrons (SE) that emanate from each primary electron spot are imaged onto a multi-detector that records all beams simultaneously. A magnetic beam splitter separates primary and secondary electron beams. The bundle of electron beams is scanned over the sample (Figure 1, middle and right). One single scanning pass thus produces many images in parallel, yielding a complete image of the sample area under the primary beams that currently contains between several hundred million and one billion pixels.

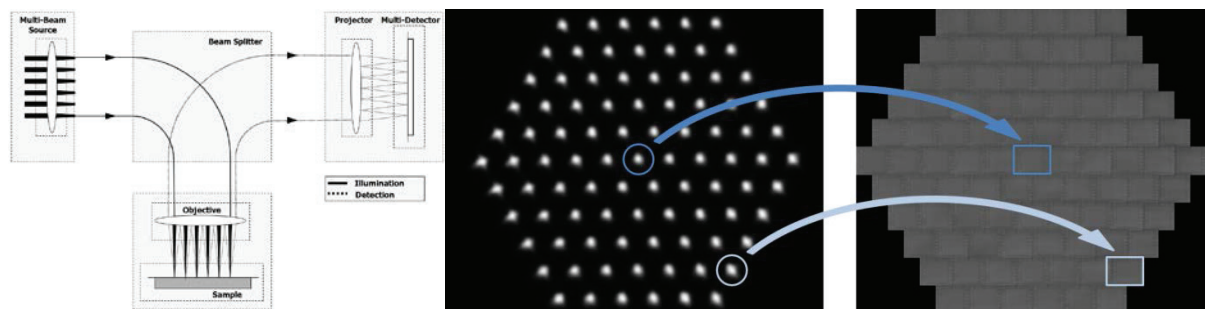


FIGURE 1. Left: Schematic drawing of the multi-beam SEM. Primary electrons (solid lines) are focused onto the sample and separated by a beam splitter from the secondary electrons (dotted lines) that are detected simultaneously in the multi-detector unit. Middle: Secondary electron spots at the plane of the multi-detector. Each spot corresponds to one emitted secondary beam acquired by one detector. All beams are scanned simultaneously. For example, the beams marked in dark and light blue simultaneously acquire the images marked in dark and light blue, respectively. Right: Stitched image of 91 single-beam images recorded in one shot with a total field of view of $\sim 200 \mu\text{m}$ in this case (sample: etched silicon test chip)

The maximum achievable scan speed of a SEM is limited by the electron dose per pixel required to generate a desired minimal signal-to-noise ratio (SNR) at a given spot size [4]. Two fundamental effects limit the maximum

scan speed of single beam SEMs. First, reducing the dwell time per pixel while maintaining SNR means that the beam current must be increased. The increasing Coulomb interactions between the electrons will then blur the electron beam spot at the sample. Second, efficient detectors for secondary electrons produce a useful signal only at detection rates lower than determined by the detector decay time. With multiple electron beams in a single column, Coulomb interactions will be lower than within a single-beam configuration. We therefore are able to maintain high resolution and high total current at the same time. The total possible detector bandwidth of the multiple beam SEM is the single detector bandwidth times the number of beams. We thus circumvent single beam throughput limitations. Furthermore, as almost all secondary electrons reach the multi-detector unit, we very efficiently use primary electrons to generate a secondary electron signal, ensuring a minimum electron beam damage of the sample. When imaging electron dose sensitive samples, such as critical dimension (CD) metrology or inspection on photoresist structures during semiconductor processing, where the electron beam illumination often causes changes in resist structures (“resist shrinkage”), minimizing the electron dose is of high importance.

IMAGING SEMICONDUCTOR SAMPLES

To demonstrate the capabilities of the multi-beam SEM for semiconductor samples, we show two application examples: Figure 2 exhibits a test wafer patterned with the SEMATECH AMAG6L reticle that contains test features for metrology experiments, such as line patterns with different nominal line widths and pattern recognition features. The line-to-line spacing in Figure 5 is 60 nm [5].

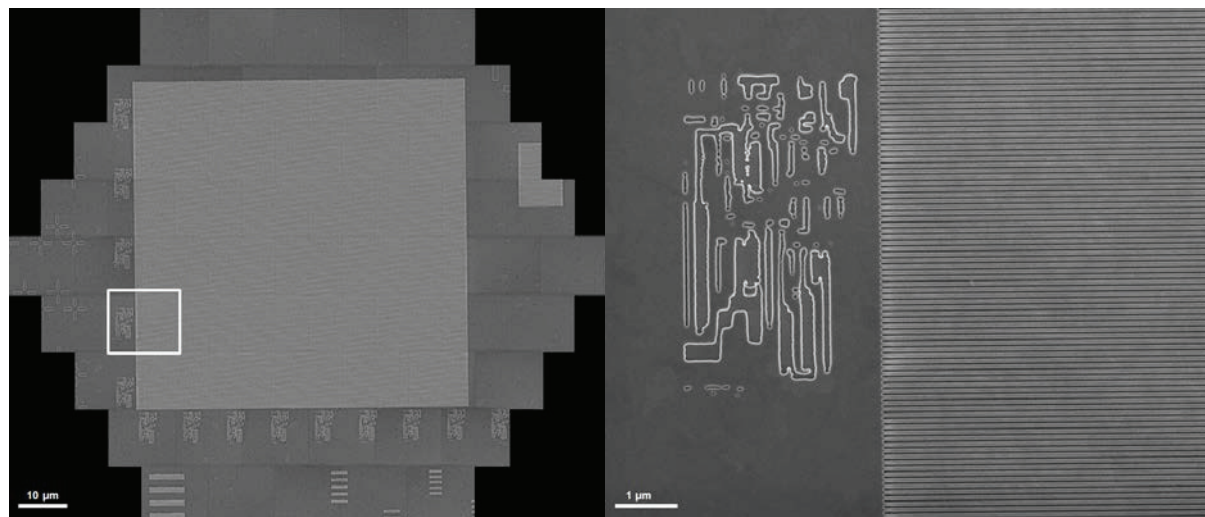


FIGURE 2. Semiconductor test sample with line patterns for metrology experiments. The imaged sample contains 60 nm amorphous silicon patterns on a 2 nm SiO₂ gate oxide. The features were patterned with 193 nm immersion lithography and dry-etched. Left: Full hexagon overview. Right: 12 µm × 10 µm single-beam sub-image detail of the full multi-beam image (Sample by SEMATECH).

Figure 3 shows a multi-beam SEM image from a SEMATECH intentional defect array (IDA) sample. IDA samples are commonly used to assess the performance and ultimate sensitivity of defect inspection equipment such as bright field and e-beam wafer and mask inspection tools at 15nm half-pitch [6]. The samples were created by exposing hydrogen silsesquioxane (HSQ) resist with e-beam direct write lithography. In both examples, uniform imaging properties and good SNR have been achieved for all beams for fast scan rates.

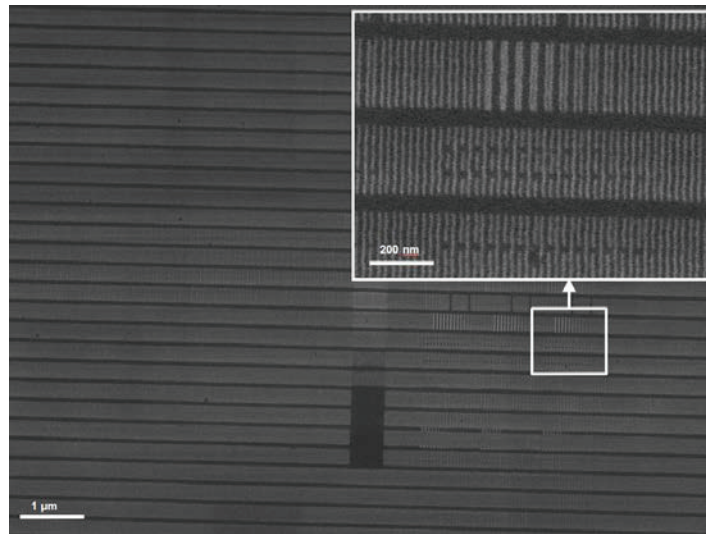


FIGURE 3. Single beam image of a multi-beam SEM full hexagonal image. The example shown is of a 15nm half-pitch IDA pattern that was produced by exposing hydrogen silsesquioxane (HSQ) resist with e-beam direct write lithography. The inset shows a magnified sub-area with line-break and misplaced line type programmed defects at various sizes (Sample by SEMATECH).

DESIGN SCALABILITY AND OUTLOOK

The obvious way to enhance the throughput of the multi-beam SEM is to increase the number of beams and detectors, for which we already have demonstrated the transition from 61 to 91 beams [3]. In this demonstration, we also ensured that good SNR can be achieved at high scan speeds by increasing the total current of all beams by a factor of about seven and still kept both good absolute resolution and good resolution similarity between all beams at the same time. Other than increasing the number of detectors and inserting a 91-beam source into the electron optics that features higher current per beam, no changes to the multi-beam SEM design have been required. This demonstrates that the single-column, multiple beam concept ensures simple scalability in beam number and total current. This multi-beam concept is thus adaptable for much higher beam numbers still [7], and will meet the throughput needs for semiconductor applications such as defect inspection in the future.

REFERENCES

1. Thiel, B. et al., "Assessing the viability of multi-electron beam wafer inspection for sub-20nm defects," Proc. SPIE 9236, (2014) [doi:10.1117/12.2069302].
2. Keller, A. L., Zeidler, D. and Kemen, T., "High throughput data acquisition with a multi-beam SEM," Proc. SPIE 9236, (2014) [doi:10.1117/12.2069119]
3. Kemen, T., et al. "Further advancing the throughput of a multi-beam SEM", Proc. SPIE 9424, (2015), submitted
4. Bright, D. S., Newbury, D. E. and Steel, E. B., "Visibility of objects in computer simulations of noisy micrographs," J Microsc 189(1), 25–42 (1998).
5. Ito, W. et al., Proc SPIE 9050 (2014) 90500D
6. Raghunathan, A. et al., "13nm gate Intentional Defect Array (IDA) wafer patterning by e-beam lithography for defect metrology evaluation", Microelectronic Engineering, vol. 88, no. 8, pp. 2729-2731, 2011. [doi:10.1016/j.mee.2011.02.109]
7. Malloy, M., et al., "Massively Parallel E-Beam Inspection: Enabling next-generation patterned defect inspection for wafer and mask manufacturing", Proc. SPIE 9424, (2015), submitted

KEYWORDS

Multi-beam, SEM, high speed imaging, beam splitter

Silicidation and Strain Analysis of Silicon Nanowires

M. Löffler^{1,3}, W. M. Weber^{2,3,4}, S. Banerjee^{1,3}, A. Heinzig^{2,3}, M. Grube^{2,3}
D. Deb^{3,4}, T. Baldauf³, U. Mühle⁵, A. Erbe^{3,4}, T. Mikolajick^{2,3,4}, E. Zschech^{1,3,5}

1) Dresden Center for Nanoanalysis, TU-Dresden, Dresden, Germany 2) NaMLab gGmbH, Dresden, Germany
3) Center for Advancing Electronics Dresden CfaED, TU-Dresden, Dresden, Germany
4) NanoNet Research School, Helmholtz-Center-Dresden-Rossendorf, Dresden, Germany
5) Fraunhofer Institut IKTS-MD, Dresden, Germany

INTRODUCTION

Silicon nanowire (SiNW) transistors are considered successors of finFETs due to their ideal electrostatic channel control. Nevertheless, accurate doping control and reliable metal-silicide contact formation to source and drain are some of the key challenges to be solved. In this respect we study reconfigurable field effect transistors (RFET) [1] as an alternative technology to CMOS that makes use of intruded nickel silicide junctions in intrinsic Si nanowires and strain management to adjust the charge carrier polarity and concentration. These four-terminal devices deliver unipolar n- and p- FET switching characteristics from the same device as selected simply by an electric signal and without the need for doping enabling complementary CMOS operation with a single kind of transistor. RFETs make use of two sharp NiSi₂ / silicon interfaces [2] with individual gates for the selective injection of electrons and holes into the channel region [3]. Here we investigate the effect of 1 silicidation reactions and strain incorporation as key enablers of RFETs.

SAMPLE PREPARATION

Nominally intrinsic SiNWs were grown at 450°C via the vapor liquid solid (VLS) growth mechanism in a low pressure chemical vapor deposition (LPCVD) furnace in 1:10 SiH₄ and H₂ flow at 50 Torr total pressure. Si (001) and amorphous SiO₂ were used as growth substrates. Au nano-clusters decorating the substrates were employed as catalytic mediator particles for the SiNW growth. SiH₄ is decomposed catalytically on the Au surface subsequently leading to diffusion of Si atoms into the particles until a Au-Si melt is formed. Excess amount of Si leads to Si super-saturation within the melt, which in turn condenses as a Si monolith extending between the Au-Si melt and the substrate. Two sets of SiNWs are studied here, epitaxially nucleated <110> SiNWs with mean diameter of ~20 nm and <112> SiNWs with mean diameter of ~30 nm. Both SiNW types are characterized physically and electrically in terms of their behavior while forming intruded Ni silicides and in terms of strain formation during oxidation as needed for the realization of RFETs. For further processing, the Au/Si particles were removed selectively to Si by a sequence of wet etch steps including HF and aqua-regia. As a radial mechanical stressor, dry oxidation of the as-grown SiNWs followed in a rapid thermal anneal furnace at 850°C for 10 minutes. For sufficiently small nanowire diameters, this leads to a self-limited SiNW oxidation as described in [4]. The silicide formation is formed by local etching of the oxide shell in HF and subsequent Ni deposition. Contact annealing at 450-480°C in forming gas for 1 to 5 minutes lead to the solid-state formation of intruded nickel silicides.

The imaged samples consist in their simplest realization in a SiNW which is surrounded by the oxide and connected to two Ni electrodes on either side. From these electrodes, NiSi_x phases stretch along the nanowire such that only the central part of the nanowire remains Si. The phase boundary is responsible for the formation of the Schottky junction and is investigated by TEM. In order to achieve the necessary sample thickness for TEM, the sample is prepared via a lift-out process with a focused ion beam (FIB) within a dual-beam instrument. Since the area of interest is only about (20 nm)³, the demands on lamella thickness and precise positioning are very high. It is commonly known that ion beams create amorphous and damaged surface layers in nearly all materials. In Si, at

30 keV Ga⁺ ion energy, such an amorphous layer is typically around 20 nm thick. The ion beam voltage has to be reduced accordingly for the final polishing steps in order to preserve the crystalline structure of the nanowire. Here, voltages as low as 1kV have been used for the final step, yielding amorphous surface layers of about 1-2 nm.

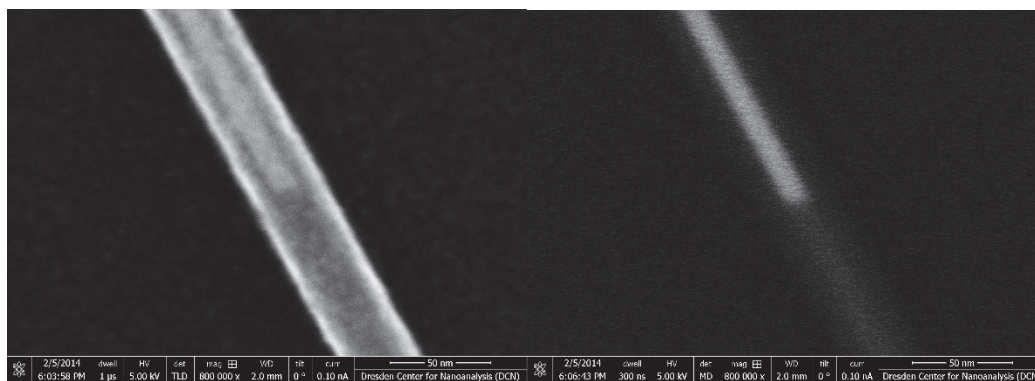


FIGURE 1. SEM images showing topography and work function contrast using secondary electrons (left) and elemental contrast using backscatter electrons (right). The backscatter image additionally allows for a distinction between Si and SiO₂.

MORPHOLOGICAL & COMPOSITIONAL CHARACTERIZATION

Samples are characterized with SEM both in secondary electron (figure 1, left) and backscatter (figure 1, right) mode for topography and elemental contrast, respectively. Especially the latter allows for a clear identification of the Ni distribution and also allows for a clear distinction between Si and SiO₂ (Figure 1b). The abrupt interface between the metallic Ni silicide and the pristine Si can be clearly observed. From these samples, adequate positions are prepared via lift-out and observed in the TEM. Using EDX mapping, the elemental composition across the junction can be traced and the phases identified as NiSi₂ and Si. Concomitant analysis of the diffraction patterns confirms the structure as of the silicide as NiSi₂, which only has a small mismatch to the Si structure.



FIGURE 2. TEM image of a cross section of an oxidized Si-NW, showing lattice fringes.

In our experiments we have observed that <110> oriented SiNWs have a direct formation of cubic NiSi₂ limited by a lattice matched interface reaction. In contrast, <112> nanowires exhibit the sequential formation of Ni-rich, monosilicide and Si rich phases with distinctly different lattice types and constants. This reproducible behavior is observed for the Ni silicidation of both oxidized and un-oxidized SiNWs. The silicidation of <112> nanowires behaves similar to that of the well-known bulk system. For comparison, Fig. 3 shows a cross section of a bulk-like, top-down prepared Si (100) structures annealed with Ni with the same conditions. At the Si interface sharp NiSi₂-Si junctions form. In addition, the Ni-rich Ni₃₇Si₂₃ phase is found. EFTEM (energy filtered TEM) images of the different phases can be seen in Fig. 3 The differences are attributed to the different nanowire faceting and thus formation energies of the silicide layers.

Strain incorporation in the SiNWs due to oxidation is expected to be compressive, but asymmetric along the direction perpendicular to the substrate due to oxidation process kinetics. HRTEM images such as in Figure 2 are used together with STEM and diffraction techniques to accurately measure the lattice strain. An average

value was determined from an ensemble of multiple SiNWs by micro-Raman spectroscopy. For $\langle 110 \rangle$ SiNWs a Raman shift corresponding to a radially compressive strain of 1.3 GPa was determined [5].

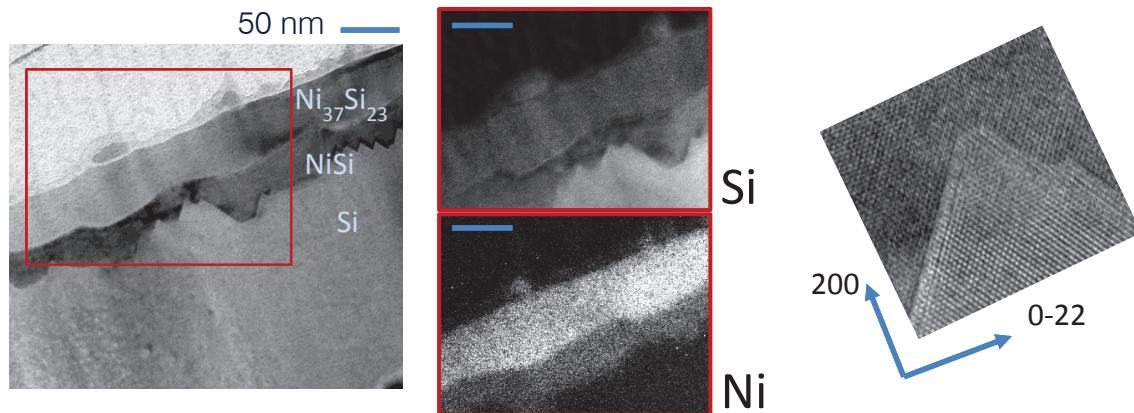


FIGURE 3. Left: TEM image showing the intermediate and disilicide phase in Top-down prepared NiSi₂-Si junctions. Middle: EFTEM Si and Ni maps. Right: HRTEM image showing preferential 111 interfaces

ELECTRICAL CHARACTERIZATION

Figure 4a shows an SEM of a typical RFET device built of a $\langle 110 \rangle$ Si nanowire. Individual gating of the Schottky electrodes leads to the selective injection of electrons and holes giving the unipolar p- and n-type characteristics as programmed by the program gate PG. The mean radial compressive strain of 1.3 GPa by oxidation was successfully employed to equalize the electron and hole injection and thus the on-currents of p- and n- program.

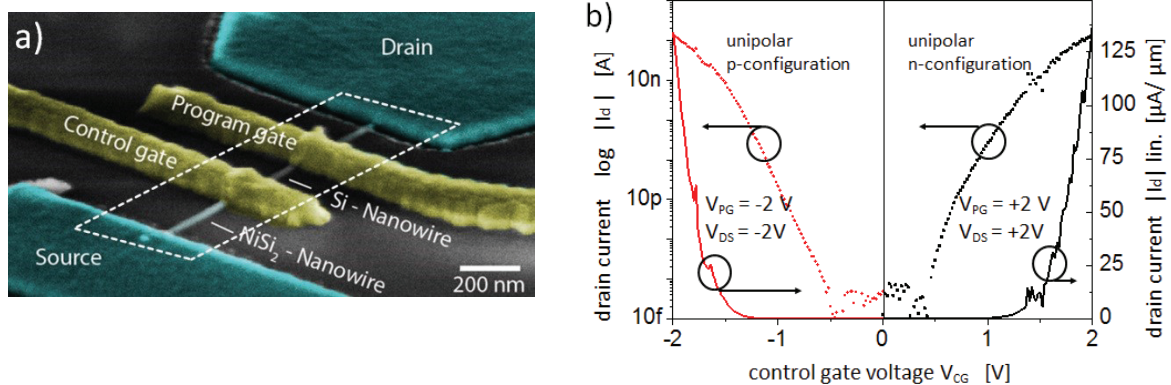


FIGURE 4. a): Schematic diagram of the nanowire RFET, composed of a NiSi₂ / Si / NiSi₂ longitudinal heterostructure. b) Measured transfer characteristics of the device in a). Depending on the bias at the program gate p- or n- type behavior can be set. The on-currents are aligned through the application of strain.

REFERENCES

1. W. M. Weber, A. Heinzig, J. Trommer et al. *IEEE Transactions on Nanotechnology* **13**, 1020-1028 (2014)
2. W. M. Weber, L. Geelhaar, A. P. Graham et al. *Nano Letters* **6**, 2660-2666 (2006)
3. D. Martin, A. Heinzig, M. Grube et al. *Physical Review Letters* **107**, 216807, (2011)
4. J. Kedzierski et al. *J. Vac. Sci. Technol. B* **15** (6), 2825 (1997)
5. A. Heinzig, S. Slesazek et al. *Nano Letters* **13**, 4176 (2013)

KEYWORDS

Silicon nanowire, transistor, reconfigurable transistor, HRTEM, strain engineering, silicidation

2D Materials Beyond Graphene For Future Electronics

Frank Schwierz

Technische Universität Ilmenau, Fachgebiet Festkörperelektronik, PF 100565, 98684 Ilmenau, Germany

INTRODUCTION

During the past 10 years, 2D (two-dimensional) materials have attracted substantial attention in the electronic device community. The first 2D material studied in detail was graphene and many groups explored it as a material for transistors. Particularly the high carrier mobilities observed in gapless large-area graphene raised early expectations that graphene could be the perfect material for high-performance FETs and become the successor of the conventional semiconductors. It soon turned out, however, that the missing bandgap causes serious problems for proper operation of graphene transistors. Therefore, meanwhile the prospects of graphene transistors are considered less optimistic. This, however, does not mean the end of the 2D materials in electronics. In contrary, recently researchers have extended their work to 2D materials beyond graphene. Meanwhile, several hundred of these materials are known and part of them is considered to be useful for electronic applications. The present paper provides an overview of the classes of 2D materials that currently are of interest for transistor electronics, describes the state of the art of 2D transistors, and discusses metrology issues specifically related to 2D materials.

OVERVIEW OF 2D MATERIALS

Motivated by the successful preparation of graphene, researchers have examined options to realize stable 2D materials beyond graphene. These efforts include real-world experiments where 2D materials have been prepared and analyzed [1] as well as computational experiments where the thermodynamic stability and the band structure of hypothetical 2D materials have been studied [2]. Particularly worth mentioning is the *Atlas of 2D Materials* established by the Heine group from Jacobs University Bremen, Germany, reporting the calculated the properties of more than 140 different 2D materials [3]. Recent efforts have shown that a variety of 2D materials beyond graphene do or should exist and that their electronic properties span the full range from metallic to insulating. Potentially of interest for transistors are the semiconducting and, to a lesser extent, the gapless semi-metallic 2D materials. Figure 1 shows a condensed overview of the different classes of the 2D materials relevant for electronics.

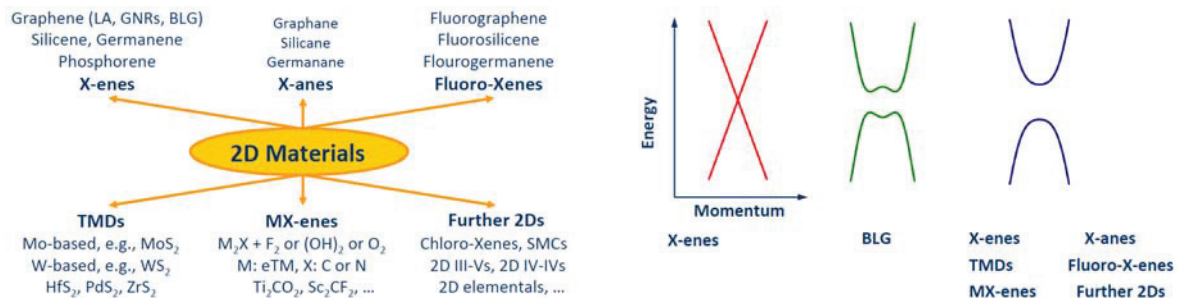


FIGURE 1. 2D materials with potential for electronics. Left: Classes of 2D materials. LA: large-area, GNR: graphene nanoribbon, BLG: biased bilayer graphene, TMD: transition metal dichalcogenide. Right: Band structure of 2D materials.

MOSFETs for complex digital logic should show good switching characteristics and on-off ratios in the range of $10^4 \dots 5 \times 10^7$ [4]. To achieve this target, the bandgap of the FET channel material should be around 0.4 eV or wider [5,6]. For other applications, such as analog/RF (radio frequency) amplifiers, a gap is desirable, although the requirements are less stringent compared to logic. On the other hand, a high carrier mobility in the channel is

crucial for high-performance RF FETs. It is well known that the carrier mobility of semiconductors tends to decrease and the carrier effective masses increase with increasing bandgap. Thus, device engineers always face a gap-mobility tradeoff. So far, most transistor-related work has been focused on the X-enes and TMDs. Therefore, we now introduce these two material classes.

X-enes. Single-layer materials consisting of atoms of one single element arranged in a hexagonal lattice are called X-enes. So far, graphene as well as its Si-, Ge-, and P-based counterparts silicene, germanene, and phosphorene have experimentally been realized [7-9]. Large-area silicene and germanene are gapless as graphene while phosphorene is a semiconductor with a 1-eV gap for single-layer material [10]. A gap can be opened in graphene by either forming narrow GNRs or by applying a perpendicular electric field to bilayer graphene. The gap of GNRs is inversely proportional to the ribbon width and very narrow ribbons (less than 10 nm wide) are needed to open a gap of 0.4 eV as required for logic [6]. For FET-relevant BLG structures, gaps of 130 meV at maximum can be expected [11] what might be helpful for RF FETs but is not sufficient for digital logic.

TMDs. The TMDs comprise a group of materials consisting of a transition metal M and a chalcogene Q, i.e., sulfur (S), selenium (Se), or tellurium (Te). These M and Q elements form covalently bonded 2D layers of the MQ₂ type (e.g., MoS₂) with a hexagonal lattice. Single-layer TMDs consist of three atomic layers where one layer of metal atoms M is sandwiched between two layers of chalcogene atoms Q. While part of the TMDs is metallic, the TMDs containing Mo and W (i.e., MoS₂, WSe₂, etc.) as well as several of the Hf-, Pd-, Pt-, and Zr-based TMDs are semiconductors with bandgaps of the order of 1 ... 2 eV [3].

2D TRANSISTORS

Up to now, most experimental work on 2D transistors has been focused on graphene and MoS₂ MOSFETs. Quite recently, however, the first phosphorene MOSFETs and MOSFETs with TMD channels other than MoS₂ have been demonstrated.

X-ene MOSFETs. The vast majority of experimental graphene MOSFETs has large-area gapless channels. Due to the missing gap, these transistors do not switch off and show on-off ratios of only 2 ... 10. Thus, large-area graphene is not a suitable material for logic MOSFETs. A lot of work has been done on RF graphene MOSFETs with gapless channels. The best of these transistors show cutoff frequencies f_T in excess of 400 GHz [12] and maximum frequencies of oscillation f_{max} around 100 GHz [13]. While these numbers are impressive, one should compare them with those of conventional III-V RF FETs, for which record numbers of $f_T = 688$ GHz [14] and $f_{max} = 1200$ GHz [15] have been reported. A major problem of graphene transistors is the unsatisfying saturation of the drain current due to the missing gap which deteriorates power gain and f_{max} . Thus, graphene MOSFETs with gapless channels certainly show GHz capabilities but cannot compete with conventional high-performance RF FETs, particularly in terms of f_{max} [6].

GNR MOSFETs with narrow semiconducting GNR channels showing on-off ratios of $10^4 \dots > 10^6$ have been demonstrated, e.g., [16]. The gap opening in GNRs, however, is accompanied by a dramatic mobility reduction. We note that in the recent past the industry has replaced bulk Si channels with its rather moderate mobilities by strained Si offering enhanced mobilities and is currently intensively working on the introduction of III-V and Ge channels with even higher mobilities into Si CMOS technology. Therefore, in the short to medium term the application of GNR MOSFETs in digital logic is rather unlikely. Things may change at 5-nm and below gate length levels (i.e., beyond the current ITRS horizon) when direct source-drain tunneling becomes an issue [17]. Since this tunneling mechanism can be suppressed by using channels with heavy carrier effective mass (and thus low mobility), GNRs may become a viable option at these gate length levels. On the other hand, due to the relatively low mobilities, GNR MOSFETs are not expected to be a promising candidate for high-performance RF electronics.

Recently the first phosphorene MOSFETs have been reported [9]. Due to their semiconducting channels, these transistors show good switch-off and the measured mobilities of up to 1000 cm²/Vs look promising.

TMD MOSFETs. Several groups are currently working intensively on TMD MOSFETs and many experimental transistors, mainly with MoS₂ channels, with excellent switching behavior and on-off ratios fulfilling the requirements of digital logic have been reported [18]. The good switching properties are related to the sizeable gap of the TMDs which, however, is accompanied by only moderate mobilities. Thus, we rate the prospects of TMD MOSFETs in complex logic and high-performance RF circuits similar as those for GNR MOSFETs.

Flexible MOSFETs. So far, our discussion on the prospects of the 2D materials in transistor electronics had a rather reserved tenor that could lead to the impression that in the short to medium term 2D transistors are only of academic interest. This, however, is not correct. First, the progress in the area of 2D materials is extremely rapid and breakthroughs are always possible. Second, there are many applications beyond complex digital logic and high-

performance RF electronics. One example is the emerging field of flexible electronics [19]. Here, (i) organic and amorphous semiconductors as well as metal oxides, (ii) thin Si and III-V membranes, and (iii) the 2D materials are potential candidates. While the materials of group (i) are meanwhile well established, they suffer from very low mobilities of typically $0.1\text{-}10\text{ cm}^2/\text{Vs}$. Si and III-V membranes show much higher mobilities but their bendability is limited [19]. The 2D materials (including large-area graphene), on the other hand, offer competitive mobilities, combined with a high bendability, and therefore are perfect candidates for flexible electronics. Recently reported highlights of flexible 2D transistors are a 260-nm gate graphene MOSFET showing an f_T of almost 200 GHz and an f_{max} of 28 GHz [20], a MoS₂ MOSFET with 68 nm gate length showing 13.5 GHz f_T and 10.5 GHz f_{max} [21], and a 300-nm gate phosphorene MOSFET with $f_T = 12\text{ GHz}$ and $f_{\text{max}} = 20\text{ GHz}$ [22]. Moreover, excellent switching behavior of flexible MoS₂ MOSFETs has been demonstrated [23]. These impressive results show that the 2D materials are promising for flexible electronics and show the potential to realize low-power medium-to-high-speed digital logic and RF GHz electronics "on plastic".

METROLOGY NEEDS FOR 2D ELECTRONICS

From the device engineer's point of view, the following (certainly not complete) list summarizes metrology issues related to 2D materials and transistors:

- (1) Analysis of the crystallographic and structural quality of 2D layers.
- (2) Identification of the layer number.
- (3) Accurate measurement of the width, edge configuration, and bandgap of narrow GNRs.
- (4) Correct extraction of the mobility of 2D top-gated MOS channels.
- (5) Measurement of the heat transport properties of 2D materials, in particular the thermal conductivity and the thermal boundary resistance between 2D materials and the substrate or insulator underneath.
- (6) Analysis of the properties of contacts between metals and 2D materials (contact type, i.e., Schottky or Ohmic, contact resistance).

In the following, we exemplarily discuss entries (2) and (3) of our list in more detail. Since frequently not only single-layer but also few-layer 2D materials are used in transistors and key properties of the 2D materials, such as the bandgap, depend on the layer number, it is crucial to get reliable information on the layer number.

TABLE 1. Bandgap (in eV) of single- and few-layer MoS₂, WS₂, and phosphorene.

Material	Single-layer	Bilayer	4 layers	6 layers	Ref.
MoS ₂	1.96	1.49	1.28	1.22	24
WS ₂	2.07	1.48	1.33	1.33	24
Phosphorene	1.0	0.67	0.48	0.41	10

As can be seen from Tab. 1, the gap of WS₂ decreases by 0.6 eV from single- to bilayer material, and the gap of phosphorene reduces by more than 0.3 eV from single- to bilayer, i.e., by more than 30 %. Since important characteristics of transistors depend exponentially on the gap, e.g., the on-off ratio, knowing the number of layers and the corresponding bandgap of 2D materials is extremely important.

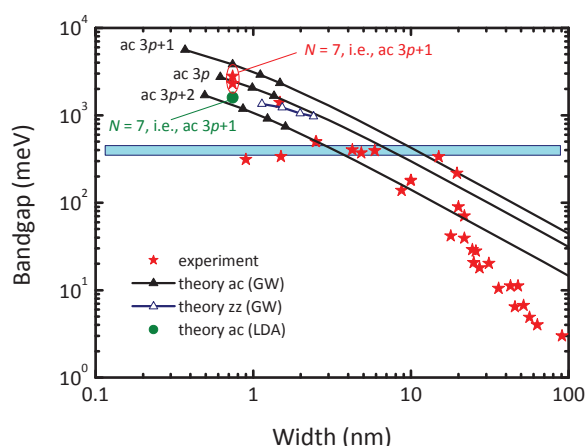


FIGURE 2. Bandgap of GNRs vs ribbon width. ac: armchair. zz: zigzag. Experimental data taken from the compilation in [25] and from [26,27], calculated gaps from [28].

Figure 2 shows the bandgap of GNRs as a function of ribbon width. As mentioned above, knowing the bandgap of a transistor channel material is extremely important. Thus, for GNR MOSFETs the width of the GNRs channel and its bandgap must be known and therefore be measured with high accuracy. The fact that the gap changes significantly if the number of atoms N along the GNR width varies by only one single atom, e.g., from $3p+1$ to $3p+2$ (p is an integer), underlines the enormous demands on measurement accuracy. Moreover, the gap depends on the edge configuration (armchair or zigzag) and therefore the edge configuration should also be known. We note that, although the general trend of a shrinking gap for increasing ribbon width can clearly be seen in Fig. 2, the data scatters considerably. Let us take a $3p+1$ ac GNR with $N = 7$ acGNR. Using the GW method, a gap of 3.8 eV has been calculated for this ribbon compared to 1.6 eV obtained from LDA calculations [28] and 2.3-2.8 eV obtained from measurements [26,27].

CONCLUSION

We have shown that intensive research on 2D materials and their implementation in transistors, particularly MOSFETs, is underway. Regarding the prospects of 2D transistors, we conclude that they are promising for flexible electronics while we believe that 2D MOSFETs will not play a major role in complex logic in the near to medium term and in high-performance RF electronics in general. On the other hand, the semiconducting 2D materials, in particular very narrow GNRs and the Mo- and W-based TMDs might become important beyond the current ITRS horizon, when 5-nm and below gate length MOSFETs are required. In MOSFETs with such short channels, the heavy carrier effective mass of GNRs and TMDs will be help to suppress direct source-drain tunneling. Finally, we have composed a list of metrology issues related to the 2D materials.

REFERENCES

1. S. Z. Butler et al., *ACS Nano* **7**, 2898-2926 (2013).
2. H. L. Zhuang, A. K. Singh, and R. G. Hennig, *Phys. Rev. B* **87**, 165415 (2013).
3. P. Miro, M. Audiffred, and T. Heine, *Chem. Soc. Rev.* **43**, 6537-6554 (2014).
4. The International Technology Roadmap for Semiconductors, <http://www.itrs.net>.
5. K. Kim, J.-Y. Choi, S.-H. Cho, and H.-J. Chung, *Nature* **479**, 338-344 (2011).
6. F. Schwierz, *Proc. IEEE* **101**, 1567-1584 (2013).
7. P. Vogt et al., *Phys. Rev. Lett.* **108**, 155501 (2012).
8. M. E. Davila, L. Xian, S. Cahangirov, A. Rubio, and G. Le Lay, *New J. Phys.* **16**, 095002 (2014).
9. L. Li et al., *Nature Nanotech.* **9**, 372-377 (2014).
10. H. Liu et al., *ACS Nano* **8**, 4033-4041 (2014).
11. G. Iannaccone et al., *Tech. Dig. IEDM*, 245-248 (2009).
12. R. Cheng et al., *PNAS* **109**, 11588-11592 (2012).
13. Z. H. Feng et al., *Carbon* **75**, 249-254 (2014).
14. D.-H. Kim, B. Brar, and J. A. del Alamo, *Tech. Dig. IEDM*, 319-322 (2011).
15. W. Deal et al., *IEEE Trans. THz Sci. Technol.* **1**, 25-32 (2011).
16. X. Li, X. Wang, L. Zhang, S. Lee, and H. Dai, *Science* **319**, 1229-1232 (2008).
17. S. S. Sylvia et al., *IEEE Trans. Electron Devices* **59**, 2064-2069 (2012).
18. B. Radisavljevic, A. Radenovic, J. Brivio, V. Giacometti, and A. Kis, *Nature Nanotech.* **6**, 147-150 (2011).
19. D. Akinwande, N. Petrone, and J. Hone, *Nat. Commun.* **5**, 5678 (2014).
20. N. Petrone, I. Meric, T. Chari, K. L. Shepard, and J. Hone, *J. Electron Device Soc.* **3**, 44-48 (2015).
21. R. Cheng et al., *Nat. Commun.* **5**, 5143 (2014).
22. H. Wang et al., *Nano Lett.* **14**, 6424-6429 (2014).
23. J. Lee et al., *Tech. Dig. IEDM*, 491-494 (2013).
24. A. Kuc, N. Zibouche, and T. Heine, *Phys. Rev. B* **83**, 245213 (2011).
25. F. Schwierz, *Nature Nanotech.* **5**, 487-496 (2010).
26. P. Ruffieux et al., *ACS Nano* **6**, 6930-6935 (2012).
27. S. Linden et al., *Phys. Rev. Lett.* **108**, 216801 (2012).
28. L. Yang, C.-H. Park, Y.-W. Son, M. L. Cohen, and S. G. Louie, *Phys. Rev. Lett.* **99**, 186801 (2007).

KEYWORDS

Two-dimensional material, MOSFET, graphene, phosphorene, nanoribbon, transition metal dichalcogenide, MoS₂, flexible electronics.

Raman Spectroscopy in Graphene

Andrea C. Ferrari

Cambridge Graphene Centre, University of Cambridge, Cambridge, CB3 0FA, UK

Raman spectroscopy is a well-established characterization technique for carbon nanomaterials and is being developed for layered materials[1].

Raman spectroscopy is an integral part of graphene research[2]. It is used to determine the number and orientation of layers, the quality and types of edge, and the effects of perturbations, such as electric and magnetic fields, strain, doping, disorder and functional groups[3]. This, in turn, provides insight into all sp²-bonded carbon allotropes, because graphene is their fundamental building block. I will review the state of the art, future directions and open questions in Raman spectroscopy of graphene[3].

REFERENCES

- 1 A.C. Ferrari, J. Robertson, J. (eds), Raman spectroscopy in carbons: from nanotubes to diamond, Theme Issue, Phil. Trans. Roy. Soc. A 362, 2267 (2004).
2. A. C. Ferrari et al. Phys. Rev. Lett. 97, 187401 (2006) 3. A.C. Ferrari, D.M. Basko, Nature Nano. 8, 235 (2013)

Metrology Challenges Towards N7

Philippe Leray, Dieter Van den Heuvel, Sandip Hadler, Anne Laure Charley,
Stephane Godny, Vincent Truffert, Christiane Jehoul, Bart Baudempez

imec

Kapeldreef 75, 3000 Leuven, Belgium

INTRODUCTION

In preparation of N7 process development in imec, we investigated the metrology challenges in a short BEOL loop using N10 design rules. In a dual damascene scheme, 3 types of metal patterning have been investigated. Using a 193 immersion scanner with a SADP and a LE3 process and a third one using an EUV scanner in a single exposure scheme. The final pitch of the metal is 48 nm in representative logic and SRAM structures. In the immersion scheme NTD and PTD resist are used, meanwhile the EUV resist thickness after development is between 30 and 20 nm.

METROLOGY IN TRIPLE PATTERNING BEOL SHORTLOOP

In this paper we are looking into the impact of target segmentation in the determination of accurate overlay correctables and correlation with device. In figure 1, we compare the overlay fingerprint of traditional image based overlay with measurements in device (SRAM for overlay X and Logic in overlay Y). The agreement between the 2 techniques is good.

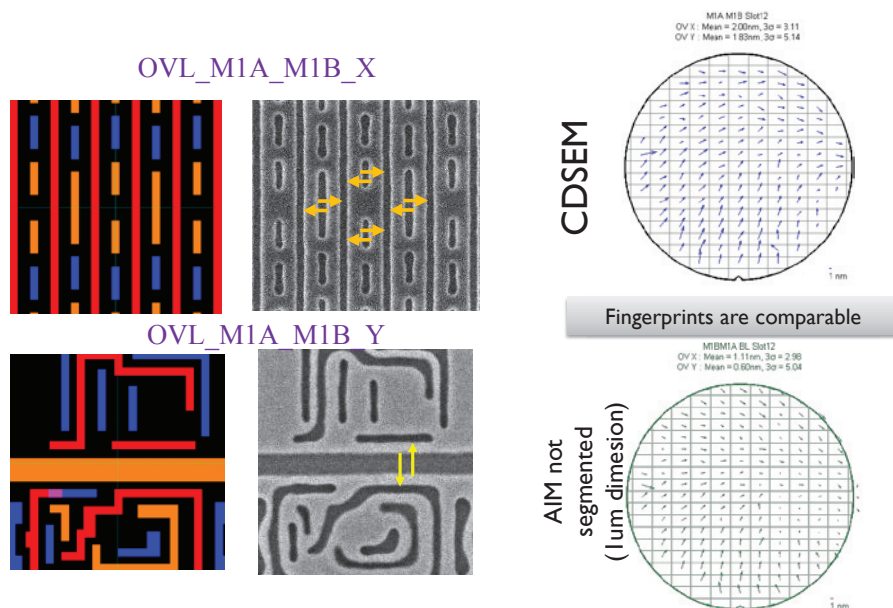


Figure 1. Overlay measurements of M1B to M1A with CDSEM on TiN etched wafer

The scatterometry challenges due to complex material and the impact in the stability of the solution is shown. Figure 2 shows that the uniformity of optical properties over the wafer can not be assumed anymore. Optical properties of thin metallic film is not uniform over the wafer and this fingerprint is wavelength dependent. These 2 additional parameters need to float in the scatterometry solution, it creates new correlation between parameters.

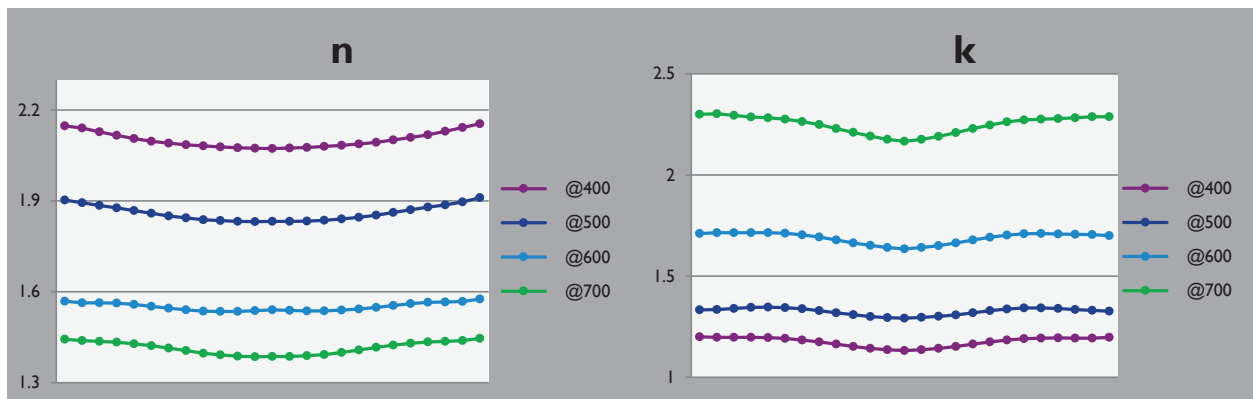


Figure 2. Optical properties of thin metallic film through wafer diameter at different wavelength.

The difficulty to identify hot spots using different defectivity inspection methods is presented. In figure 3, the challenge is illustrated with the dark spots indicated by the 2 black arrows. These dense features are a challenge for bright field inspection as the sensitivity in the dense area is much lower than in the isolated areas.

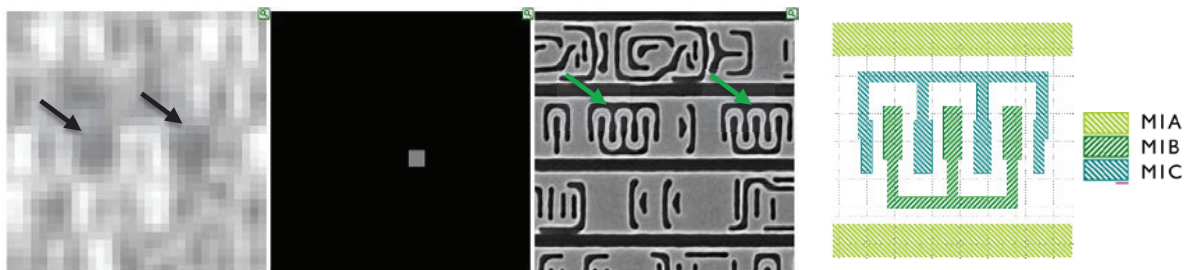


Figure 3. Density variation in design is a challenge for bright field inspection in N10 node.

For CD, overlay and defectivity, we compare the results between different techniques to validate or challenge the solutions.

Materials in the stacks used are becoming thinner and thinner (EUV resist thickness, hard mask for etch). We present the difficulties that these thin layers are creating for metrology (alignment, sensitivity, performance).

CONCLUSIONS

In conclusion, we summarize the metrology limits identified and we discuss the needs for hardware improvements to allow robust metrology for N7 node. The strengths and the weaknesses of the different techniques are driving our industry towards more interaction between different metrology. The techniques should be combined compensate the weaknesses of each technique with the strengths of an other.

KEYWORDS

Metrology, Defectivity, Overlay, Scatterometry, Focus, Control, Hybrid

Current Status of CDSAXS: Is it Fab-Ready?

Daniel F. Sunday, Donald Windover, R. Joseph Kline

*Materials Measurement Laboratory, National Institute of Standards and Technology, Gaithersburg, MD USA
20899*

INTRODUCTION

The semiconductor industry continues to follow Moore's Law with continuously shrinking device dimension sizes. The 14 nm node is now in production and the 10 nm node is rapidly under development. In addition to the substantial challenges of simply fabricating these tiny structures, the current suite of metrology tools are also running against fundamental limits. Current production fabs use optical scatterometry (OCD) for dimensional metrology to track the size and shape of their tiny nanostructures. The three dimensional nature of the latest finFET devices and shrinking sizes result in parameter correlations and size dependent refractive index. Critical dimension small angle X-ray scattering (CDSAXS) is a potential replacement metrology tool that uses X-rays instead of the visible and ultraviolet light used in OCD.¹ The much smaller wavelength of X-rays results in a much smaller diffractive resolution limit. CDSAXS is a variable angle, transmission SAXS measurement where the X-rays go through the entire wafer. It is essentially single crystal diffraction where the lattice is the periodic grating and the individual lines/vias/posts are the atoms. The scattering pattern is solved to determine the size and shape of the periodic features that created it. CDSAXS results in an ensemble average structure and is not sensitive to low concentration defects. Most reported measurements of CDSAXS were done at a synchrotron to take advantage of the much higher X-ray flux. Moving CDSAXS to the laboratory or fab will require the development of new high brightness, compact X-ray sources. Current compact X-ray sources do not have sufficient brightness for a high throughput measurement. The following section will discuss the current status of CDSAXS and discuss the prospects for higher brightness X-ray sources. We will also discuss the required performance metrics for an X-ray source to provide sufficient resolution in a short enough time. Synchrotron measurements have demonstrated that CDSAXS fundamentally works, the primary limitation is getting enough photons from a compact source to make it a high throughput measurement.

GETTING CDSAXS TO THE FAB

Current high throughput OCD measurement times are on order of a few seconds. With current compact X-ray sources, comparable CDSAXS measurements would take a few hours. The CDSAXS measurement time is strongly dependent on the composition of the material being characterized. The X-ray scattering strength depends on changes in the electron density. Samples with high Z elements such as Hf will scatter much more strongly than low Z elements such as C and N. Similarly since it is the change in electron density, silicon-air interfaces will scatter more strongly than silicon-silicon oxide interfaces. The difference in measurement times between a sample with a HfO dielectric and a sample with photoresist could be as large as 2 orders of magnitude. It is also important to note that the measurement is the result of constructive and destructive interference of an ensemble of periodic nanostructures. The scattering patterns cannot be directly converted to the original periodic image that created them. The measured intensity is the square of the amplitude of the scattered wave and the phase information is lost. Obtaining the original image requires an iterative inverse algorithm to compare the calculated scattering of trial solutions to the original data. The size and shape of the trial solutions are modulated until a satisfactory solution is obtained. This solution might not be unique, so a large portion of the viable parameter space must be tested to estimate the uniqueness. This becomes particularly important for rapid measurements with lower signal to noise and less data. As with most measurements, there will be a trade off between measurement speed and parameter uncertainty.

The CDSAXS measurement is made at a number of different incident angles. Tilting the sample increases the contribution of the vertical structure to the scattering signal. A single normal incidence image will provide the pitch of the periodic pattern and a measure of the presence of pitch walking. Obtaining shape profile information requires the measurement of additional incident angles. The number of angles and specific angles measured will depend on the sample being measured and the required uncertainty. Algorithms can be used to determine which angles have the greatest information content for a specific sample. The spacing of fringes in the vertical direction of a reciprocal space map is inversely proportional to the distance, so thick sample will require a smaller range of incident angles than thin samples. Another ramification of reciprocal space is that the parts of the scattering pattern with the most information about high resolution features are the highest order diffraction peaks. These peaks also tend to be relatively weak and are most affected by signal to noise.

High throughput CDSAXS is a demanding measurement for compact X-ray sources. The small scattering angle necessitates that the beam divergence be very small to allow the resolution of the diffraction spots. The small target size requires a small beam spot. The combination of small beam spots and low divergence can only be accomplished by using apertures to reduce the beam size, resulting in substantial loss of flux. To compensate, the source must have a very large initial brightness so that sufficient photons are left over in the beam spot. CDSAXS is not particularly sensitive to energy resolution, so the energy bandwidth can be relaxed. The beam energy must be high enough that absorption from the silicon wafer is minimized. Current sources are based on microfocus rotating anodes. Their intensity is limited by the rate at which heat can be removed from the target anode. The electron beam power is limited by target melting and evaporation. Rotating anodes allow greater power density than a static anode due to the constantly changing impact zone. Several new potential sources include liquid metal jet anodes² and inverse Compton scattering (ICS) sources.^{3,4} A liquid metal jet anode replaces the solid anode with a high speed metal jet of a low temperature liquid metal. The liquid metal jet allow a higher heat flow than rotating anodes and the source is constantly replenished by the metal jet. The higher heat flow allows a greater power density and a smaller source size, resulting in enhanced brightness. ICS sources interact a high intensity laser beam with a high energy electron beam to produce X-rays. ICS is similar to a short period undulator with many poles. The short period and many poles allow an ICS source to produce a high energy X-ray or gamma ray with a much lower energy electron beam than a conventional synchrotron undulator requires, allowing it to be a relatively compact accelerator. ICS sources have the potential to create synchrotron-like X-ray beams with a small footprint.

TABLE 1. X-ray Source Requirements for <10 s Measurements

Source Parameter	Value
X-ray Flux (ph/s)	>10 ⁹
Divergence (mrad)	<0.5
Energy (keV)	>20
Energy bandwidth (%)	<2
Spot size (μm)	<100

In conclusion, CDSAXS has great potential for providing high resolution dimensional metrology of periodic nanostructures for the semiconductor industry. The primary remaining hurdle for implementation is the limits on throughput and spot size imposed by current compact X-ray sources. A variety of new compact, high brightness sources are on the horizon and potentially can be commercialized in time to have CDSAXS fab-ready when it is needed.

REFERENCES

1. Jones, R. L.; Hu, T.; Lin, E. K.; Wu, W.-L.; Kolb, R.; Casa, D. M.; Bolton, P. J.; Barclay, G. G. Small Angle X-Ray Scattering for Sub-100 Nm Pattern Characterization. *Appl. Phys. Lett.* 2003, 83, 4059.
2. Hemberg, O.; Otendal, M.; Hertz, H. M. Liquid-Metal-Jet Anode Electron-Impact X-Ray Source. *Appl. Phys. Lett.* 2003, 83, 1483.
3. Huang, Z.; Ruth, R. D. Laser-Electron Storage Ring. *Phys. Rev. Lett.* 1998, 80, 976.
4. Graves, W. S.; Bessuille, J.; Brown, P.; Carbajo, S.; Dolgashev, V.; Hong, K.-H.; Ihloff, E.; Khaykovich, B.; Lin, H.; Murari, K.; et al. Compact X-Ray Source Based on Burst-Mode Inverse Compton Scattering at 100 kHz. *Phys. Rev. Spec. Top. - Accel. Beams* 2014, 17.

KEYWORDS

Dimensional metrology, X-ray scattering, CDSAXS

CMOS Characterization/Metrology Challenges for the Lab to the Fab

Paul van der Heide, Michael Gribelyuk, Jeremy Russell

GLOBALFOUNDRIES, 400 Stone Break Road, Malta, NY, 12020, U.S.A

INTRODUCTION

Due to a multitude of technological advances identified and implemented since 1963 (the year the CMOS patent was filed), CMOS device fabrication has moved to within the realm of atomic scale engineering. Indeed, moving beyond the classical Dennard scaling regime ($<130\text{nm}$)^[1] to finFETs required the introduction of additional technologies such as strain, HKMGs, and a move from planar toward 3D structure. As a result, characterization/metrology of a multitude of solid state properties is now required. Examples of some of the properties of interest include: Structural dimensions, surface roughness, surface/interface chemistry, film composition, distributions of dopants and other minor/trace elements, bonding, phase, grain size, crystal orientation, strain, etc.

This information is extracted using one or a combination of a growing number of analytical capabilities whether in the lab or the fab. This arises since there is no one technique (typically referred to as an *instrument* when used in the research sense, or a *tool* when used in the metrology sense) that provides all the information of interest in one shot. Note: Those used in the lab provide R&D needs, initial and ongoing process/tool qualification needs, and an understanding of manufacturing issues. Those used in the fab provide the metrology needs essential to enable in-line process control and near immediate input on manufacturing issues.

The primary analytical techniques used within the lab tend to include (in alphabetical order): AES, AFM (inclusive of electrical variants such as C-AFM, SCM, SSRM, etc.), APT, C-V measurements, EELS, EDX (also referred to as EDS), ellipsometry, OM, porosimetry, SAXS, SEM, SIMS, TEM/STEM, XPS, XRD, XRF, XRR, etc. Some require highly specific sample preparation methodologies that may include the use of FIB. Those used in the fab include a highly specialized subset of those listed above (CD-AFM, CLM being an in-fab FIB, EDX, CD-SEM, OCD which includes ellipsometry and scatterometry, XPS, XRD, XRR, XRF, etc.) along with more specific variants (LEXES being a low energy form of EDX, four point probe, therma-wave, C-V measurements, etc.).

There, however, exist questions as to whether these and/or the associated methodologies can support the next generation CMOS characterization/metrology needs. Indeed, many are rapidly approaching their fundamental limits, with one referred to as the *Abbe diffraction limit*^[2]. This defines the best possible dimensional resolution that can be attained once all aberrations and distortions are minimized. Note: In some cases, the diffraction limit drops below atomic dimensions, hence, is of little concern. TEM is one example. In other cases, the diffraction limit can be circumvented. This is noted in APT as well as various SPM based techniques.

One avenue that has had some success in improving the capabilities of techniques affected by the diffraction limit lies in comparing the analytical output with modeled results (*a-priori* structural information is needed). An example that is used in the fab is Scatterometry. This can provide spatial resolution values below the wavelength of the incoming/scattered photons by comparing the output with a modeled response from specific test structure libraries. CD-SAXS/GI-SAXS may push the envelope in this area. Another example related to SAXS lies in the use of XRD to relay fin pitch, fin walk, and sidewall angle from a fin array^[3]. This possibility arises since an array of fins takes on a grating like structure which introduces its own set of Bragg reflections. This, along with the more traditional forms of information can then be extracted through comparison with simulations. Due to lack of source brightness, however, such studies are presently too time intensive for either the lab or the fab. This brings up another limit of concern, namely the detection limit/sensitivity per unit of time deemed acceptable.

To fully satisfy future CMOS device characterization/metrology needs, further work on modeling / simulations of the structure of interest, as well as in the following areas is needed:

- 1) Technological developments/breakthroughs in instrumentation/tools with capabilities beyond those presently available. Speed, reliability, repeatability and cost are also of major concern
- 2) Analysis methodology development. An example of this, albeit not applicable to CMOS devices, allows for conventional optical microscopy to image to 50 nm spatial resolution^[4].
- 3) Hybrid approaches, i.e., the use of multiple techniques to provide information beyond the capabilities of the individual techniques. A recent example lies in the simultaneous XPS/XRF measurement of Cu lines which provides both the line width and depth (XPS defines line width due to its much shallower probe depth which when fed into the XRF Cu volume data allows the Cu line depth to be extracted)^[5]
- 4) New test structures (arrays) that more effectively mimic the region/s of interest.

For fab based instruments/tools, speed is attained through the limitation of the parameter/s measured and the use of intense sources. Speed is paramount since this governs wafer throughput. Reliability (uptime) and repeatability (precision) are also standard expectations for similar reasons. The cost of implementation stems primarily from the technological developments required (particle contamination must be minimized along with any of the potential deleterious effects resulting from the act of analysis, i.e. structural and/or electrical damage, deposition of foreign material, etc. along with the infrastructure needed to support the respective tools).

For lab based instruments/tools, these constraints are far less rigid. Speed, however, remains important since this results in faster product ramp-up times, manufacturing tool requalification or return to production following issues.

Following is a discussion of various recognized technological issues along with some possible future analysis scenarios. The technological issues are discussed in order of those pertaining to photon probes, electron probes, ion probes and near atomically sharp physical probes. This is not to be considered a comprehensive overview.

In the case of the photon probe based techniques, the requirement of more intense photon beams has already been identified. Indeed, much work has gone into this with, for example, liquid metal based x-ray sources initially developed for XRD of biological systems^[6]. These were conceived since the heat resulting from electron impact on the anode (the x-ray source), is more effectively dissipated in a flowing versus static medium. More effective heat dissipation allows for higher electron currents and thus higher brightness x-ray sources. Note: XRD is presently utilized in both the lab and fab to answer more rudimentary questions (phase, composition, thickness, etc.). Some other techniques that will benefit from more intense sources include SAXS, XPS, XRR, and XRR.

For similar reasons, research labs may more heavily utilize synchrotron sources. This is anticipated since such sources provide significantly higher brightness along with the ability to tune the photon energy (continuously variable) to the signal of interest. This also allows the application of other techniques. One example lies in the use of NEXAFS to define the speciation of elements at buried interfaces (due to lack of spatial resolution blanket film deposition would be assumed). Note: More traditional methods typically require removal of any pre-existing over-layers via sputtering or wet etching, both of which invariably modifies the interface of interest. Another example includes photoemission spectromicroscopy (LEEM or PEEM) whether using un-polarized or polarized beams to map sub-micron scale regions. Polarized beams allow for magnetic properties to be mapped.

Increased use of other techniques such as PL and APT on specific structures may also occur. In the case of PL, specific film/test structures are required such that the output can be related to some property of interest (sub-surface defects, dopants, impurities). For APT, improvements in evaporation rate uniformity, data reconstruction, and insulator analysis capabilities are needed. Note: APT provides 3D volume renditions to atomic scale resolution with all elements identified (H-U). APT is, however, expected to remain within the lab environment since like TEM, this is a highly localized but destructive technique with FIB milling required to access the volume of interest.

As for electron probe based techniques, the introduction of spherical aberration corrected SEM optics, as already used in TEM, has allowed SEM to achieve <1 nm spatial with a 100 eV beam (0.4 nm is theoretically possible)^[7]. Due to the minimal damage expected (a result of the short electron path length among other things) this could see transition from the lab to the fab.

In the case of TEM, sample preparation is the prime area needing improvement. Since this is carried out via FIB, this discussion is deferred to the ion beam probe section below. It is predicted that elemental and STEM Tomography in the aberration corrected TEM will become a “must-have” capability in the industrial failure analysis laboratories to help understand defects in 3D structures. For this, further development is necessary to reduce the acquisition time through automation and implementation of high sensitivity detectors. Development of the 3D reconstruction algorithms should aim to achieve the <1 nm spatial resolution and high sensitivity to species with both low and high atomic numbers. The aim is to achieve the robustness of tomographic analysis comparable to that of the currently

deployed TEM based EDX / EELS analysis. Dopant mapping by electron holography has been utilized for more than 15 years as applied to CMOS planar devices. Its extension to finFETs, however, requires the development of new sample preparation methods and improvement in sensitivity and spatial resolution.

In the case of ion probe based techniques, SIMS, which is heavily used in the lab for dopant distribution analysis, may see introduction into the fab, albeit using a heavily simplified geometry for analysis of highly specific sacrificial test structures. Likewise, for LEIS. This is envisioned, again with a highly simplified geometry using Ne⁺ since this can follow/model ALD processes on test structures in a manner complementary to RHEED, albeit *ex-situ*. Note: He⁺ ions are expected to induce greater electrical damage as a result of their longer path length relative to Ne⁺ or electrons (this damage has been noted in HIM [7]). Sacrificial test structures would again have to be used.

Improvements in FIB/CLM are also likely to encompass the addition of a Ne⁺ beam, since these provide for smaller probe sizes relative to Ga⁺, Ne is inert (a consideration since metals are electrically active) and for reasons outlined above, such beams result in less damage. Indeed, Ne⁺ has already shown to be useful in the final milling step as well as in circuit editing [8]. This should serve to alleviate TEM sample preparation issues, namely, the damage of the sample surface needs to be decreased as the size of the active regions to be analyzed approaches the thickness of the damaged layers. Lastly, the accuracy and reproducibility of the navigation algorithms employed in the FIB systems to locate the area of interest needs to be improved.

Near atomically sharp physical probe based techniques are attracting greater attention since not only are these SPM based techniques not affected by the diffraction limit, but due to the extremely close proximity of the tip to the surface on interest, most analysis can be carried out under ambient conditions. Indeed, hybrid CD-AFM/CD-SEM/Scatterometry algorithms appear to be highly effective. One area needing improvement is tip robustness. As for lab based systems, SSRM appears useful in that it provides complementary information to electron holography, APT and SIMS. This is complimentary in the sense that SSRM yields the carrier distribution, electron holography provides electrostatic potential of electrically active dopants, while APT and SIMS provide the summed concentration of active and inactive dopants. There, however, remain questions as to how far these techniques can be pushed. This effort will also be critical in aiding the development of future TCAD models.

REFERENCES

1. R.H. Dennard, F.H. Gaensslen, H-N. Yu, V.L. Rideout, E. Bassous, A.R. LeBlanc, *Design of ion-implanted MOSFET's with Very Small Physical Dimensions,* IEEE Journal of Solid-State Circuits, Vol. 9, 256, (1974)
2. S.G. Lipson, H. Lipson, D.S. Tannhauser, *Optical Physics,* Cambridge, (1998)
3. M. Manasa, G.R. Muthinti, J. Fronheiser, V. Kamineni, M. Wormington, K. Matney, T.N. Adam, E. Karapetova, A.C. Diebold. *Measurement of periodicity and strain in arrays of single crystal and pseudomorphic Si_{1-x}Ge_x fin structures using x-ray reciprocal space mapping.* J. Vac. Sci. Technol. B, 32, 021804, (2014)
4. R. Attola, R.G. Davidson, *Resolving three dimensional shape of sub 50 nm wide lines with nanometer scale sensitivity using conventional optical microscopes,* Appl. Phys. Lett. 105, 043101, (2014)
5. B. Lherreron, W.T. Lee, K. Motoyama, R. Chao, B. Deprosio, K. Kim, *In-line dimensional measurement via simultaneous small spot XPS and XRD for Cu CMP process control,* AVS-61 Presentation, Baltimore, USA, (2014)
6. Product sheet SC-XRD 49
7. B. Bundy, A. Cepler, A. Cordes, A. Arceo, *CD-SEM metrology for sub 10 nm width features,* Proc. SPIE, 9050, 90500T, Metrology, Inspection and process control for microlithography XXVIII, (2014)
8. R.H. Livengood, S. Tan, *Circuit edit nano-machining study using Ne⁺ and He⁺ focused ion beam,* AVS-61 Presentation, Baltimore, USA, (2014)

KEYWORDS

Moore analytical needs, Future analysis methodologies, Hybrid metrology, Novel test structures...

Recent Progress in Advanced In-line Metrology For High-Mobility Semiconductors

Andreas Schulze^{1,*}, Wilfried Vandervorst^{1,2} and Matty Caymax¹

(1) imec, Kapeldreef 75, 3001 Leuven, Belgium

(2) KU Leuven, Dept. of Physics and Astronomy, Celestijnenlaan 200D, 3001 Leuven, Belgium

(*) Andreas.Schulze@imec.be

INTRODUCTION

Future CMOS technology generations will require the integration of advanced semiconductor materials such as Germanium (Ge) and III-V compound semiconductors (InP, InGaAs, InAlAs) in order to fulfill the stringent performance demands.[1] Although Ge and III-V compound materials can be grown epitaxially on Si substrates to date, the large differences in lattice constant and material characteristics typically lead to very high defect densities in these layers, causing a degradation of the material properties and hence device performance. Therefore, a qualitative and quantitative assessment of the crystal quality of such materials is of utmost importance. Moreover, determining geometrical parameters (film thickness, fin height/width, fin pitch, pitch walking, sidewall angle...), material composition and strain becomes at the same time more challenging. Considering the transition toward three-dimensional (3D) device architectures (fins, potentially nanowires), it becomes apparent that adequate metrology techniques need to cope with the confined nature (i.e. small active volume requiring high sensitivity) of the latter device structures. While the aforementioned material properties can be assessed using highly sophisticated lab metrology concepts (TEM in combination with EDX and NBD, SIMS, APT etc.; cf. *Paradigm Shift in Metrology for Probing 3D-Structures and Confined Volumes*” by W. Vandervorst), the complexity (i.e. measurement time) as well as the destructive nature of these techniques limit their application during process development and for process control in an actual fab environment. Moreover, it is important to note that high resolution microscopes such as a TEM can visualize individual crystalline defects in great detail, however, the reduced specimen size and the limited field of view hamper the assessment of defect densities below $\sim 1e8 \text{ cm}^{-2}$.

The focus of this presentation is therefore on the exploration of those analysis techniques that can cope particularly with the demands of in-line metrology (non-destructive, better turn-around-times, massive data processing) and assess their applicability towards characterizing 3D heteroepitaxial device structures with respect to the properties stated above.

HR-XRD FOR THE ANALYSIS OF HETEROEPITAXIAL STRUCTURES

The composition (e.g. Ge content of a SiGe buffer) as well as the degree of strain relaxation (e.g. in a strained Ge channel layer of a p-FET device) can severely impact the device performance and hence represent crucial material properties which need to be monitored during process development and device fabrication. HR-XRD is a well-established non-destructive metrology technique which is being used for characterizing the strain of thin films as well as e.g. the Ge content of un-patterned, pseudomorphic SiGe composites on a Si substrate. In order to make the technique applicable for the characterization of sub-10nm node FinFETs, one should be aware that the spot size of the most advanced in-line XRD tools still is a few tens of μm in diameter, i.e. significantly larger. As a consequence, one needs to design dedicated metrology windows containing arrays of identical fins. Considering the 3D nature of fins it furthermore that one actually needs to determine the lattice parameter in all three directions in order to fully

characterize the strain state of the channel in a 3D FinFET device. On the example of state-of-the-art Ge and III/V based heterostructures (Figure 1a) we will demonstrate that recording reciprocal space maps (RSM) with the scattering plane parallel as well as perpendicular to the fin (Figure 1b/c) can provide the necessary information and therefore aid in understanding the relaxation mechanisms in confined volumes. As an alternative metrology tool for strain and compositional analysis we will consider Raman spectroscopy. Electrical field enhancement driven by the confined geometry of narrow FinFETs thereby significantly improves the S/N ratio of the technique.[2]

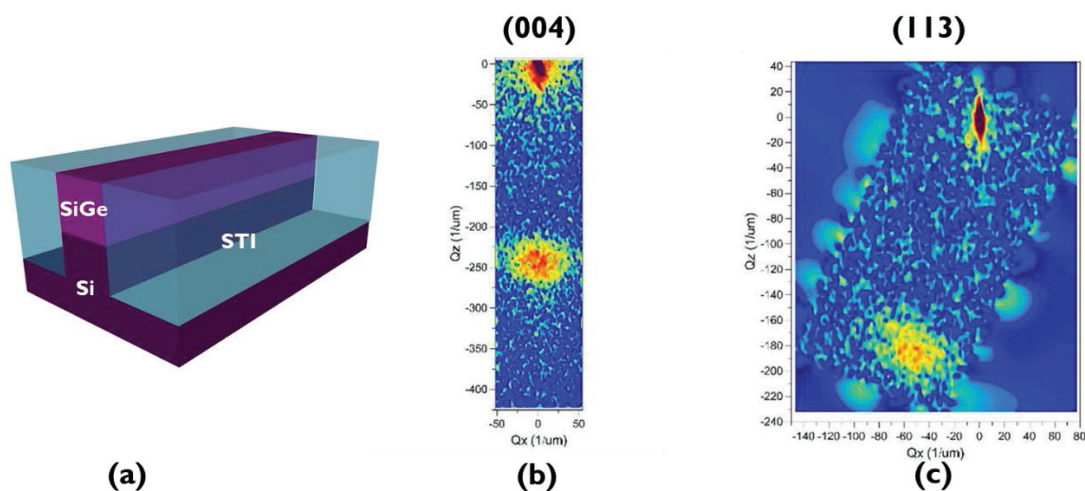


FIGURE 1. (a) Device structure consisting of SiGe selectively grown into STI matrix. (b) Symmetric (004) RSM showing Si and SiGe peak. (c) Asymmetric (113) reflection acquired along the fin and therefore reflecting the strain relaxation of SiGe in the longitudinal direction.

We will also discuss the requirements for the x-ray source and detector which are mainly arising from the reduced active volume available in μm -sized metrology windows containing 3D fin arrays on production wafers. Besides compositional and strain analysis, regular omega rocking curves can be applied to determine the lattice tilt of crystalline materials. We will demonstrate how defect densities can be extracted from the measured lattice tilt and discuss the opportunities and limitations of this approach. Moreover, we will show that the periodicity of fin arrays is reflected by satellite peaks in a regular RSM. From the satellite peak pattern we can derive information on fin geometry and dimensions as well.

ASSESSING MATERIAL QUALITY USING CATHODOLUMINESCENCE

Cathodoluminescence (CL) is a non-destructive metrology technique whereby excess carriers are generated by a focused electron beam in a SEM setup while the luminescence as a function of photon energy or wavelength is recorded. The spatial resolution of CL is determined by the diffusion length and thus by the life time of the generated excitons. Figure 2 exemplifies CL spectra taken at different depth values of a step graded SiGe strain relaxed buffer (SRB). In an SRB the defects are confined to the graded region whereas the constant composition layer on top exhibits a low defect density (see TEM image in Figure 2a). From Figure 2b it becomes apparent that the CL spectra recorded at the different positions clearly reflect variations in defectivity. It is important to note that in case of indirect bandgap semiconductors the diffusion length of the excitons cannot be neglected due to their inherently long life times. This hampers a direct visualization of an individual threading dislocation as a non-radiative recombination center (i.e. dark spot) in a CL intensity map as demonstrated earlier for GaN. Moreover, the recombination of excitons on the layer surface causes the overall CL intensity to drop and therefore hampers the analysis. This becomes particularly crucial in case of 3D fin structures due to their increased surface-to-volume ratio. For this reason we investigate the efficiency of various surface passivation approaches for SiGe and III/V materials before applying the technique on fin structures.

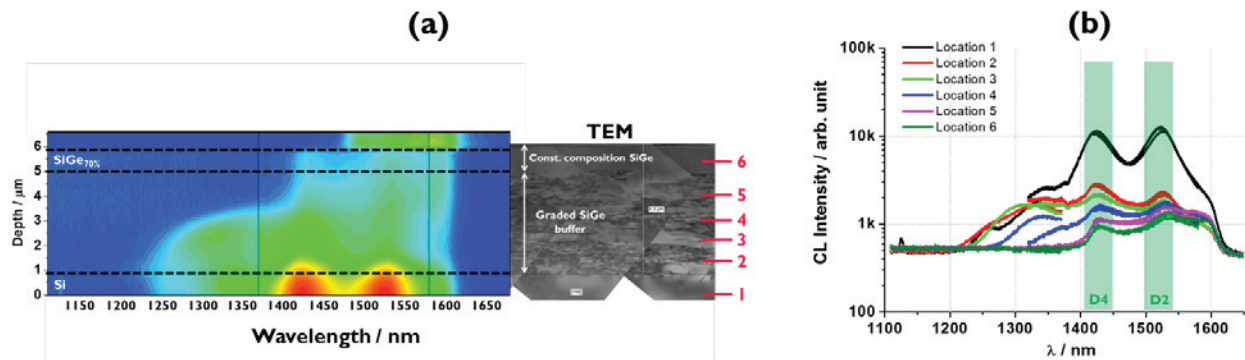


FIGURE 2. (a) CL map obtained across the cross-section of SiGe strain relaxed buffer. Starting from the surface of the Si substrate the Ge content is stepwise increased. Topmost layer consists of constant composition SiGe_{0.7}. (b) CL spectra taken at different depth values.

ACKNOWLEDGMENT

The authors acknowledge Attolight and Jordan Valley for support.

REFERENCES

- [1] M. M. Heyns, M. M. Meuris, and M. R. Caymax, "Ge and III/V as Enabling Materials for Future CMOS Technologies," *ECS Trans.*, vol. 3, no. 7, pp. 511–518, 2006.
- [2] T. Nuytten, T. Hantschel, D. Kosemura, A. Schulze, I. D. Wolf, and W. Vandervorst, "Edge-enhanced Raman scattering in narrow sGe fin field-effect transistor channels," *Appl. Phys. Lett.*, vol. 106, no. 3, p. 033107, Jan. 2015.

KEYWORDS

Heterostructures, Metrology, Defectivity, Strain, Composition, Cathodoluminescence, XRD

Thermal Wave Analysis of Implanted Layers in Semiconductors: Measurement Performance vs. Process Requirements

Nicolas Siedl, Moriz Jelinek, Mario Lugger and Gerrit Schutte

Infineon Technologies Austria AG, Siemensstraße 2, 9500 Villach, Austria

INTRODUCTION

Monitoring process stability and controlling process parameters are key issues for metrology applications in modern fab environment. Consequently, three major demands arise for metrology tool performance, i) appropriate sensitivity to monitor process changes within given specifications, ii) adequate repeatability and therefore, long-term stability of the equipment and iii) the development of standardized qualification and approval procedures to guarantee the equipment capability to fulfill process requirements.

On the basis of non-destructive measurements of implanted layers in semiconductors by thermal wave analysis with tunable modulation frequencies, it is shown how optimization of measurement parameters and statistical data evaluation lead to process relevant key numbers in order to evaluate the tool performance in fab environment and therefore the equipment capability for specified process windows.

THERMAL WAVE ANALYSIS

Photo-thermal response techniques are widely used as on-line metrology to control dose homogeneity and process stability of ion implantation in silicon.^[1] The present measurements were done using a TWIN SC4 system (PVA Metrology and Plasma Solutions GmbH) comprising variable laser modulation frequencies. The basic principle of photo-thermal response analysis in ion implanted silicon layers consists in the periodical generation of excess carriers by the absorption of laser radiation and decay-measurements of the resulting plasma wave due to non-radiative recombination at centers of ion beam induced lattice damage. The energy of the plasma wave is converted to thermal energy giving rise to a thermal wave. These response waves follow the excitation with different phase shifts and amplitudes, which depend on the excitation modulation frequency Ω and the material parameters for electronic and thermal relaxation. Because the refractive index of semiconductors depends on the free carrier density and on the temperature, the reflected part of the exciting wave will be modulated by the local amplitudes and phases of the response waves. The thermal wave inspection system (TWIN) detects carefully this part of modulated reflectivity by detection of the partial beam signals amplitude $|K|(\Omega)$ and Phase $\Psi(\Omega)$ separately. As a result every response measurement supplies several data sets, the complex conversion coefficient K (amplitude $|K|$, and phase Ψ or real and imaginary part $\text{Re}\{K\}$ and $\text{Im}\{K\}$, respectively) and the DC reflectivity R_0 .

Optimization of Dose Measurement Parameters

The amplitude of the conversion coefficient K and the phase Ψ , and therefore $\text{Re}\{K\}$ and $\text{Im}\{K\}$, are functions of the modulation frequency Ω . Thus, it is necessary to evaluate the influence of the modulation frequency on the sensitivity and repeatability carefully for different implantation process conditions. The present results were measured on Boron implanted wafers with a dose of $d \approx 10^{11}$ ions \cdot cm⁻² and an implantation energy of $E \approx 160$ -180 keV.

The sensitivity of the measurement can be defined by the observed signal change divided by the implemented dose variation. Therefore, three wafers with different implantation doses were prepared (target dose,

+10% dose, -10% dose) and measured with 19 different modulation frequencies ranging from $\Omega = 0.15$ MHz to $\Omega = 13.5$ MHz.

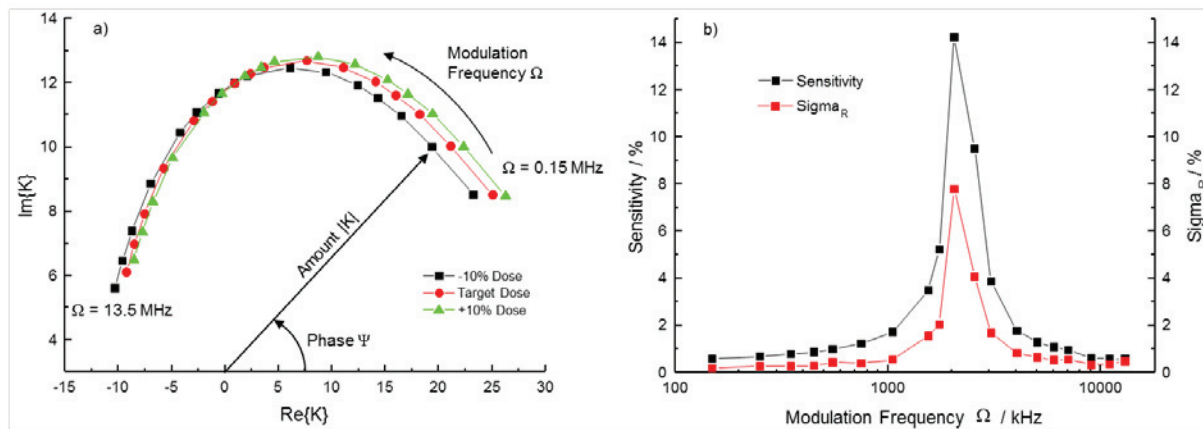


FIGURE 1. a) $Re\{K\}$ and $Im\{K\}$ as a function of the modulation frequency. b) Sensitivity (black squares) and repeatability (red squares) of $Re\{K\}$ as a function of the modulation frequency. The measurement was repeated for three times at 25 measurement points.

To avoid the influence of self-annealing on the measured signal the wafers were stored for one week after implantation to guarantee stable conditions. As well as the self-annealing the beam induced annealing of the sample has to be taken into account. Therefore, it has to be assured, that the measurement points are in adequate distance from each other in order to avoid interaction between adjacent measurement points. On the other hand, distributing them too far over the wafer possible wafer inhomogeneities may falsify the repeatability. The circle plot of the conversion coefficient K versus the modulation frequency (Figure 1a) displays the characteristic dependence of the damage in case of silicon. Implanted ions cause lattice damage due to nucleus energy transfer. As a consequence, displaced atoms and displacement spikes up to amorphous zones influence the electrical and thermal properties of the implanted layers, resulting in reduced lifetime and mobility of the excess charge carriers and reduced thermal diffusivity. All described effects lead to a reduction of the carrier wave and in turn increase the amplitude of the thermal wave.^[2]

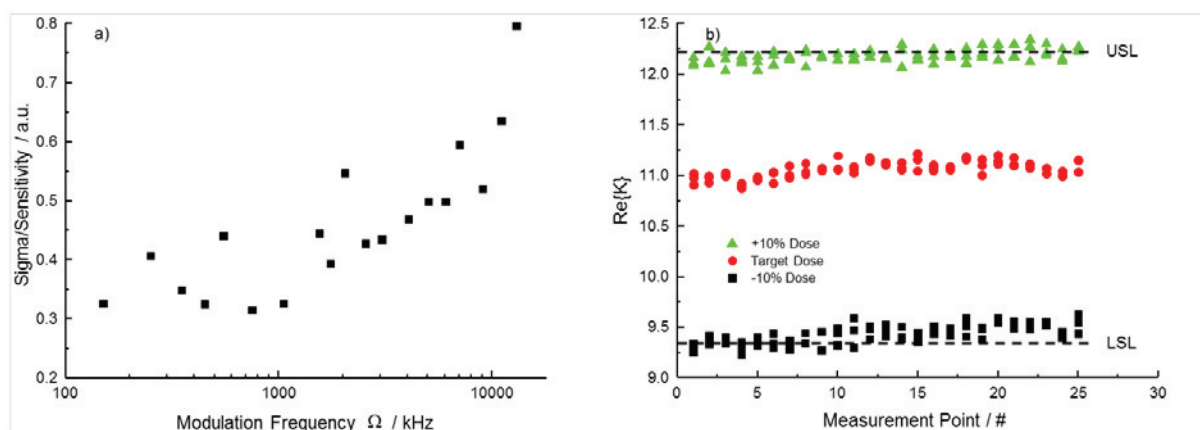


FIGURE 2. a) Ratio of repeatability and sensitivity as a function of modulation frequency. b) $Re\{K\}$ measured at the optimized modulation frequency ($\Omega = 0.75$ MHz) for three different implantation doses (target dose, +10% dose, -10% dose) to determine upper (USL) and lower specification limit (LSL), sensitivity and repeatability for the implantation process of interest.

Following the tool supplier's recommendations and measurement method (single point frequency sweep) the modulation frequency showing the maximum sensitivity should be chosen for the final measurement. We added additional measurement points to the existing modulation frequency sweep to gain information about the point to point repeatability. Finally each of the 19 modulation frequencies was represented by 25 points, repeated for 3 times and measured for three different ion doses. Figure 1b shows the sensitivity (black squares) and point to point

repeatability (red squares) of $\text{Re}\{K\}$ versus the modulation frequency Ω . It is obvious, that the modulation frequency with the optimum sensitivity shows the worst sigma-repeatability. To evaluate the optimum modulation frequency, taking into account sensitivity as well as repeatability, we analyzed the ration of sigma-repeatability and sensitivity. The optimum measurement frequency can be determined by locating the minimum of the resulting characteristic. By analysis of the data in Figure 2a a modulation frequency of $\Omega = 0.75$ MHz was chosen for the final measurements to collect the relevant data for the measurement system analysis (MSA).

MEASUREMENT SYSTEM ANALYSIS (MSA)

The main purpose of the measurement system analysis (MSA)^[3], as an instrument to assign systematic and random measurement errors, is to determine the impact of measurement errors on product verification, process capability (C_p), statistical process control (SPC) and functional relationships. The gained information enables the safe release of new tools for process control as well as reliability monitoring during long term equipment usage. The MSA is based on three major pillars, i) calibration, ii) capability analysis and iii) statistical process control (Figure 3). In the following we will focus on the capability analysis, in this case a Gage repeatability study, to evaluate the tool performance, in terms of sensitivity and repeatability, in fab environment and therefore the equipment capability for specified process windows.

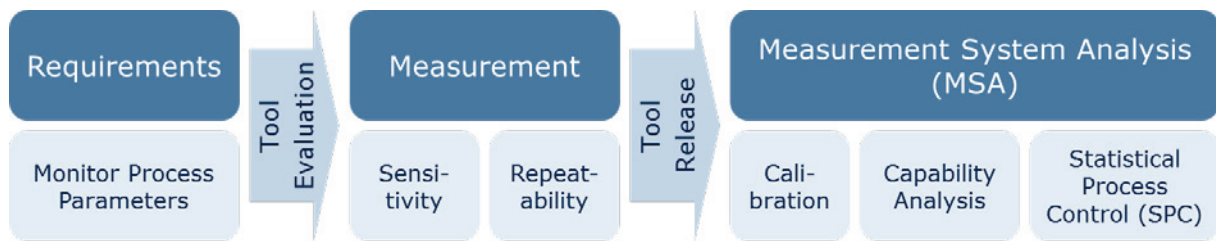


FIGURE 3. Flowchart showing principle steps from production driven requirements to final tool release.

The capability index for the repeatability study is shown in Equation 1. An important fact to mention is that the sigma repeatability in Equation 1^[3] is based on a point-to-point repeatability and its measured range.

$$G_r = \frac{5.15\sigma}{USL-LSL} \cdot 100\% \quad \text{EQUATION 1.}$$

The measurement is capable if $G_r \leq 10\%$ which means that 99% of all measured values are within 10% of the process specifications (USL-LSL, Figure 4), conditionally capable if $10\% \leq G_r \leq 30\%$ and incapable if $G_r > 30\%$. In case of the present measurements the definition of USL and LSL cannot be done directly. It is not possible to calibrate the values for the conversion coefficient K and the phase Ψ because there are no traceable standards available till now. Therefore, USL and LSL have to be determined indirectly by measuring ion implantation doses at the upper and lower limit of the required process window with optimized measurement parameters as shown in Figure 2b.

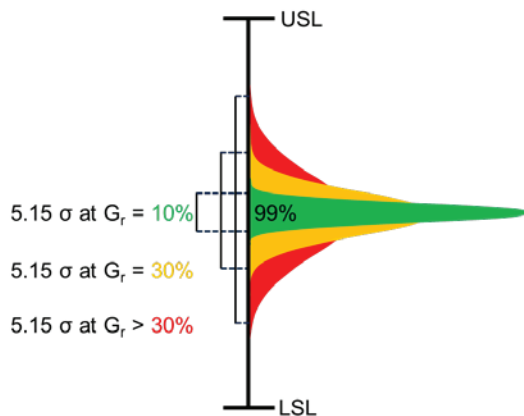


FIGURE 4. Illustration of Equation 1. $G_r \leq 10\%$ capable (99% of all measured values are within 10% of the process specifications USL-LSL), $10\% \leq G_r \leq 30\%$ conditionally capable, $G_r > 30\%$ incapable.

Comparing the capability of measurements applying two different modulation frequencies $\Omega = 2.05$ MHz, as a result of the optimization procedure recommended by the tool supplier and $\Omega = 0.75$ MHz, as a result of the here presented study, reveals that the measurement at $\Omega = 2.05$ MHz is conditionally capable $G_r = 14\%$ whereas the measurement at $\Omega = 0.75$ MHz is capable $G_r = 8\%$. This improvement of the measurement capability is directly correlated to the process capability and therefore, substantial for the reliability of on-line process control.

REFERENCES

1. H.D. Geiler, H. Karge, M. Wagner, A. Ehlert, M. Kerstan and D. Helmreic, *J.Appl.Phys.* **1**, 1997, pp. 7548.
2. H.Schlemm, H.D. Geiler and A. Kluge, *J.dePhysique IV Coll.C7 suppl.* **4**, 1994, pp. 167.
3. AIAG Reference Manual, Measurement System Analysis (MSA), 2003, 3rd ed., Chrysler Ford General Motors

KEYWORDS

Thermal Wave Analysis, Implantation Dose, Process Monitoring, Measurement System Analysis,

Combined Nanoindentation And AFAM For Mechanical Characterization Of Ultra Low-k Thin Films

André Clausner¹ and Ehrenfried Zschech¹ and Martin Gall¹ and Elham Moayed¹ and Yvonne Standke¹ and Uwe Mühle¹ and Malgorzata Kopycinska-Mueller¹ and Kong Boon Yeap² and Khashayar Pakbaz³ and Sukesh Mahajan³

¹*Fraunhofer Institute for Ceramic Technologies and Systems – Materials Diagnostics, Maria-Reiche-Str. 2, 01109 Dresden, Germany*

²*GLOBALFOUNDRIES, 400 Stone Break Road Extension Malta, NY 12020, USA*

³*SBA Materials, Inc., Albuquerque, 9430-H San Mateo Blvd. NE, New Mexico 87113, USA*

INTRODUCTION

Nano-porous dielectrics used as insulating materials between on-chip interconnects are an important component in metallization stacks of leading-edge microelectronic products to reduce electrical signal delay and power loss. The main drawbacks of these porous dielectrics are their weak mechanical properties. Therefore, nano-porous organosilicate glasses (OSGs) exhibiting a pore topology with a high degree of intermittency were developed to improve those properties. To study the effect of the pore topology on the mechanical properties of these porous OSG thin films, their hardness and elastic modulus need to be measured.

In this study, we will therefore show the possibilities and limits for the mechanical characterization of nano-porous OSG thin films using nanoindentation as well as Atomic Force Acoustic Microscopy (AFAM). Both contact mechanics based methods complement each other very well because of their contact force ranges covering different orders of magnitude. By using both methods it is not only possible to determine the mechanical properties of the OSG thin films but even to measure gradients in those properties. Based on these results as well as on simulations and TEM studies, we will discuss the relationship between porosity, pore topology, and elastic modulus of nano-porous OSG films. Additionally, using AFAM in contact stiffness mapping mode we will show the possibilities of the determination of the homogeneity of the OSG film adhesion.

MATERIAL AND METHODS

The OSG films are prepared using a sol-gel process [1] by spin coating silane precursor sols on a silicon substrate. An introduced porogen consisting of triblock copolymers causes a self-assembly process and creates an ordered pore topology and a narrow pore size distribution in the nano-meter range. The porogen is later evaporated using thermal curing. The final films exhibiting thicknesses of about 200nm to 500 nm were produced with varying porogen loading, leading to varying porosities of 0% to 50% and k-values from 3.0 to 1.8, respectively.

Miniaturized depth and force sensing hardness measurements, so called nanoindentation experiments are widely used standard measurements to determine the local hardness and elastic modulus. At that, the maximum contact force, the contact area, and the contact stiffness are determined by solely using the indentation force-displacement curve together with a power law fit of it, a calibration function of the tip shape, and the device compliance. The full procedure is described by Oliver and Pharr [2] as well as ISO 14577-1 [3]. Due to the very high resolution of modern nanoindentation devices in the ranges of only a few Angstrom and micro-Newton, extremely small volumes can be probed and it therefore e.g. becomes possible to mechanically characterize thin film structures by determining their hardness and elastic modulus.

The second method used to determine the elastic modulus of OSG thin films is Atomic Force Acoustic Microscopy (AFAM) in single-point spectroscopy mode. There the contact resonance frequencies (bending vibrations) of an AFM cantilever in contact with the sample are excited by an ultrasonic transducer placed below the sample. The resonance frequencies are measured for at least two modes in air as well as in contact with the sample surface with varying static contact forces. Using those contact resonance frequencies and reference measurements, the values of the contact stiffness and the elastic modulus [4] can be derived.

RESULTS

The nanoindentation experiments were performed with varying contact forces so that a depth dependent measurement of the hardness and elastic modulus became possible. This is important because for thin film systems the substrate influence on the measurements has to be identified. Based on this a contact depth range for the experiments has to be identified where the substrate influence has faded away. This was possible for the hardness measurements which is due to the limited extent of the yield zone around the contact tip on which the hardness values are mainly based on. Consequently, for the substrate influence free, depth resolved hardness values, surface gradients in the OSG film structures became visible. Unfortunately, for the more important elastic modulus measurements this is not true anymore. Due to the larger spatial range of the elastic field within the sample, the substrate influence on the measurements does not diminish completely for the OSG thin films within the accessible force range of the used nanoindentation device. This becomes visible by potentially further decreasing values in the elastic modulus of the nanoindentation measurements below the smallest possible contact forces (Fig. 1a).

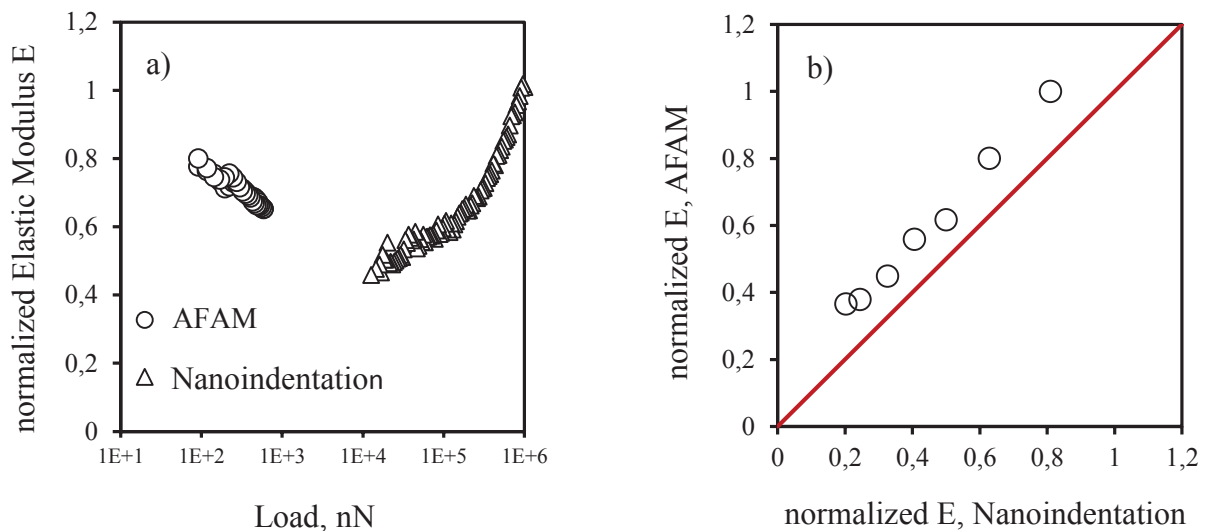


FIGURE 1. Comparison between the elastic modulus values from nanoindentation and AFAM measurements. In Fig. 1a the contact force dependent normalized elastic moduli of a porous OSG thin film (thickness 400nm and porosity 42%) are shown. The data shows the increasing substrate influence in the nanoindentation force range and a surface gradient in the AFAM measurements. Fig. 1b shows a comparison between the elastic moduli from nanoindentation and AFAM experiments for samples with different porosities. There, constantly slightly higher values for the AFAM technique are found. (Here, the lowest measured values for the elastic modulus are taken for both techniques).

In comparison to nanoindentation the AFM-based AFAM technique allows much lower contact forces and thus, lower contact depths. This makes it possible to exceed the range of the substrate influence on the elastic modulus measurements of the OSG thin films. For the AFAM measurements then indeed surface gradients for the elastic moduli became visible, which was not possible in the force range of the nanoindentation experiments (Fig. 1a).

As a first conclusion it can be said that for the hardness of an OSG thin film system nanoindentation is a very powerful technique to access a depth resolved film hardness profile. To do the same for the elastic modulus, this techniques comes quickly to its limits but can be nicely supplemented by AFAM. There, due to the much lower contact forces, also for the elastic properties a depth profile of the thin film can be accessed.

A comparison of the results of the two techniques reveals slightly higher values for the elastic moduli from the AFAM technique against nanoindentation (Fig. 1b), but the difference in the results of the two techniques stays relatively constant for samples with varying porosity. This relatively good comparability of the determined elastic properties is a very promising result, given the very different measurement techniques.

In microelectronic applications of those materials preferably high elastic moduli at given porosities are needed. Therefore, the next step was to study the influence of the pore topology of the porous OSG films on their elastic properties. To do so finite element simulations have been performed to show the effect of different pore topologies on the global elastic properties of porous materials [5]. Using this simulation results it can be shown that at given porosities the elastic modulus is lowest for a pore topology that is characterized by an overlapping spherical solids structure (Fig. 2). The elastic modulus then increases dramatically if the pore topology is changed to a random overlapping spherical pore structure and increases further if the pore topology exhibits an ordered non-overlapping pore structure. The latter is of course preferable for microelectronic applications where a high elastic modulus at a given porosity is needed. The measured values for the elastic moduli of three sets of thin OSG film samples are correlated to the simulation results as well as to TEM studies of the pore structure. Based on this a conclusion of the pore topology of the studied OSG films is given.

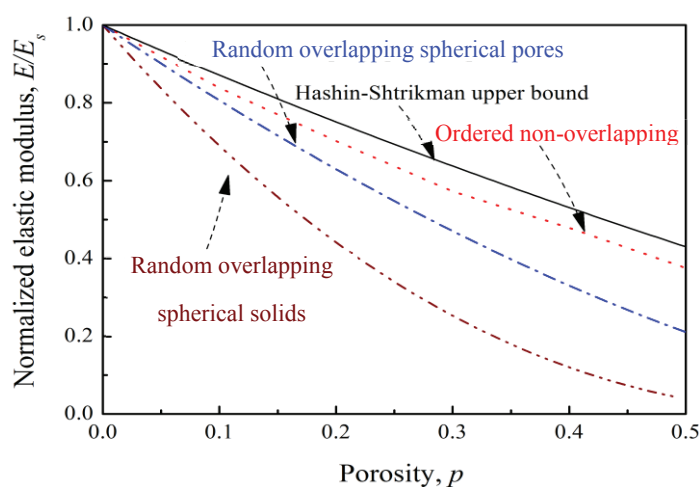


FIGURE 2. Simulation results for the elastic modulus of porous materials as a function of porosity and pore topology [5].

REFERENCES

1. D. Y. Zhao, J. L. Feng, Q. S. Huo, N. Melosh, G. H. Fredrickson, B. F. Chmelka, G. D. Stucky, *Science* 279, 548 (1998).
1. W. C. Oliver, G. M. Pharr, *J. Mater. Res.* Vol. 7, No. 6, 1564-1583 (1992).
3. ISO 14577-1, CEN, (2002).
4. U. Rabe, S. Amelio, M. Kopycinska, S. Hirsekorn, M. Kempf, M. Goecken, and W. Arnold, *Surf. Interface Anal.* 33, p. 65 (2002)
5. K. B. Yeap, M. Kopycinska-Mueller, L. Chen, Y. Chen, M. Jungmann, R. Krause-Rehberg, S. Mahajan, J. Vlassak, M. Gall, E. Zschech, *J. Mater. Res.*, Vol 28, No. 0 (2013).

KEYWORDS

ULK, OSG, Elastic Modulus, Nanoindentation, AFAM

Phase Change Properties and Strain Engineering in 2D Materials

*Karel-Alexander Duerloo, Yao Li, Evan J. Reed
Department of Materials Science and Engineering
Stanford University, Stanford, CA 94304
Contact: evanreed@stanford.edu*

INTRODUCTION

Two-dimensional (2D) crystals like MoS₂ are of widespread interest due in part to their flexible and transparent nature. Mo- and W-dichalcogenide compounds such as MoS₂ have a 2D monolayer form that can potentially have more than one crystal structure. One of the crystal structures has a bandgap > 1eV and the others are metallic, suggesting significant differences in electronic and optical properties across the transition. The first part of this talk focuses on structural phase transformations that we predict can occur under tensile strain and potentially other conditions.¹ This discovery suggests that some 2D materials may also find applications as phase change materials. This work is based on density functional theory calculations.

The second part of this talk focuses on strain engineering in monolayer materials. The relatively weak interactions between a monolayer and its substrate place limitations on the magnitudes and types of strain that can be imparted to the monolayer. Using atomistic calculations, we study a new method for engineering strain states into monolayer materials using patterned adatom adsorption. We find that tensile strains of several percent can be engineered into single layer materials using this approach.²

STRAIN-INDUCED STRUCTURAL PHASE TRANSITIONS

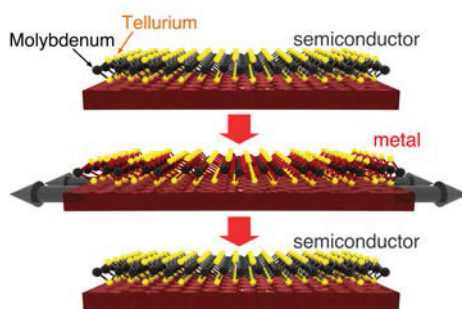


Figure 1: Schematic impression of a strain-driven structural phase transition between semiconducting 2H-MoTe₂ and metallic 1T'-MoTe₂.

Mo- and W-dichalcogenide compounds have a two-dimensional monolayer form that differs from graphene in an important respect: they can potentially have more than one crystal structure. Some of these monolayers exhibit tantalizing hints of a poorly understood structural metal-to-insulator transition with the possibility of long metastable lifetimes. If controllable, such a transition could bring an exciting new application space to monolayer materials beyond graphene. Here we discover that mechanical deformations provide a route to switching thermodynamic stability between a semiconducting and a metallic crystal structure in these monolayer materials. Based on state-of-the-art density functional and hybrid Hartree-Fock/density functional calculations including vibrational energy corrections, we discover that MoTe₂ is an excellent candidate phase change material.¹ We

identify a range from 0.3 to 3% for the tensile strains required to transform MoTe₂ under uniaxial conditions at room temperature. The potential for mechanical phase transitions is predicted for all six studied compounds.

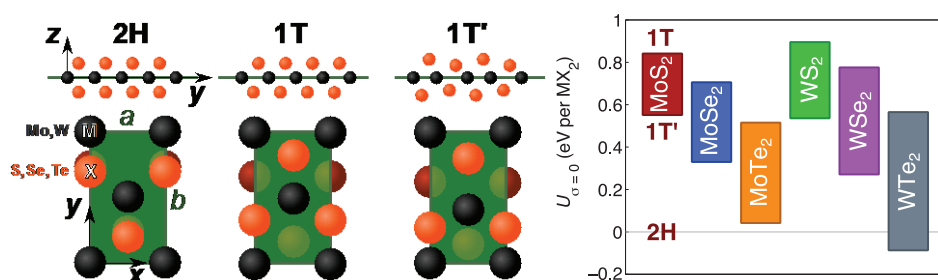


Figure 2: Left: The three crystalline phases of two-dimensional Mo- and W-dichalcogenide compounds. All three phases consist of a metal (Mo/W) atom layer sandwiched between two chalcogenide (S/Se/Te) layers. The semiconducting 2H phase is often referred to as the trigonal prismatic structure, and the metallic 1T and 1T' are called octahedral and distorted octahedral, respectively. The 1T' phase can be thought of as 1T after a symmetry-reducing distortion. Right: Ground state energy differences between monolayer phases of the six studied materials. The energy U is given per formula unit MX₂ for the 2H, 1T' and 1T phases. Its value is computed at the equilibrium (zero stress, σ) lattice parameters for each phase.

The energy differences between these three crystal phases is shown on the right side of **Figure 2**. We find that the Te-based monolayers exhibit the smallest energy differences between the 2H and 1T' crystal phases and are therefore most promising for phase change applications.

In MoTe₂ in particular, we find that small and readily accessible strains between 0.3% and 3% are predicted to drive a phase transition between the semiconducting and the metallic 2D crystal structures at room temperature (**Figure 3**). The structural nature of this metal-insulator phase transition has the potential to provide metastable lifetimes needed for phase change-based digital memory if the kinetics are appropriate. The kinetics of the transition are unknown.

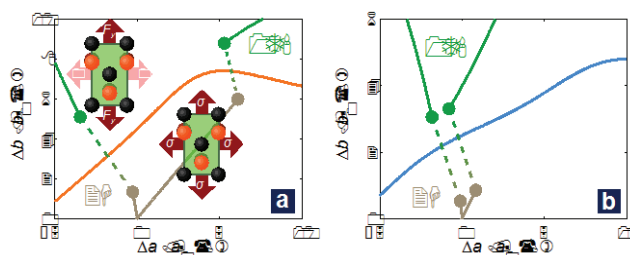


Figure 3: Load-specific trajectories and transitions of MoTe₂ at room temperature. Subfigure (a) uses the PBE functional to calculate the crystal energy, whereas the HSE06 functional is used in (b). Starting at their stress-free 2H equilibrium values a_0 and b_0 , the lattice constants a and b evolve in response to progressive application of a uniaxial load (F_y) or a “hydrostatic” isotropic tension (σ). At a certain load, the 2H and 1T' thermodynamic potentials cross. When this transition occurs, the lattice constants jump from their 2H to their 1T' values. A coexistence regime is expected to exist in the dashed regions, where increasing the b lattice constant while keeping $F_x = 0$ (uniaxial load) or increasing the area ab under hydrostatic conditions can yield regions of 2H and 1T' in the monolayer.

The goal of this study is to investigate the possibility of a mechanical route to thermodynamically driven phase transformations between metal and semiconducting crystal structures in all group VI TMDs. Our results show that these mechanical transformations are in fact possible and most easily accessible in the case of MoTe₂. Furthermore, the existence of multiple accessible phases in monolayers is an exciting feature beyond graphene that undoubtedly has broad implications for electronic, NEMS, thermal, energy and myriad other devices which can all benefit from the flexible, transparent nature of monolayers.

Strain Engineering in Monolayer Materials Using Patterned Adatom Adsorption

Advances in the isolation and fabrication of monolayer materials combined with their excellent mechanical strength have generated a lot of interest in their potential for use in novel electronic and optical devices, ranging from field effect transistors to solar cells and effective catalysts. Strain engineering has been proposed as the basis of a variety of such devices. One would like to produce strains over large areas in these monolayer materials using

methods comparable to standard lithographic techniques. In this work, we utilize reactive empirical bond order (REBO)-based interatomic potentials to explore the potential for the control of strain at the nanoscale in monolayer materials through patterned adatom adsorption.² Patterned adatom adsorption is a technique that has been employed in the laboratory for other purposes.

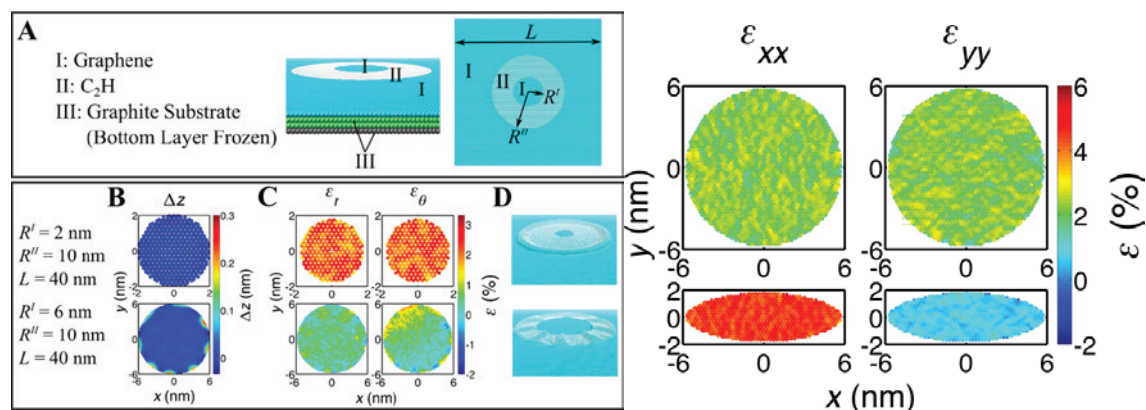


Figure 4: Left: (A) Side view and top view of the initial configuration of the system with annular adsorption pattern. (B) (C) Out-of-plane displacement and the strain inside the adsorption region. (D) Snapshots of the adsorption region at the end of simulations. Right: Strain in circular and elliptical adsorption regions. The strain in an elliptical region can deviate from equibiaxial.

In the context of graphene, we discover that the monolayer strain results from a competition between the in-plane elasticity and out-of-plane relaxation deformations. For hydrogen adatoms on graphene, the strain outside the adsorption region vanishes due to out-of-plane relaxation deformations. Under some circumstances, an annular adsorption pattern generates homogeneous tensile strains of approximately 2% in graphene inside the adsorption region. We find that an elliptical adsorption pattern produces strains of as large as 5%, close to the strain in the adsorbed region. Also, nonzero maximum shear strain ($\sim 4\%$) can be introduced by the elliptical adsorption pattern.

We find that an elastic plane stress model provides qualitative guidance for strain magnitudes and conditions under which strain-diminishing buckling can be avoided. We identify geometric conditions under which this effect has potential to be scaled to larger areas. These conclusions are expected to be qualitatively applicable to other monolayer materials, including monolayer transition metal dichalcogenides (TMDs), which are of interest in part due to their nonzero bandgap. We expect our investigation to provide guidance for the engineering of strain in electronic and optical devices made from monolayer materials.

REFERENCES

- 1 K.-A. Duerloo, Y. Li, and E. J. Reed, "Structural Phase Transitions in Two-Dimensional Mo- and W-Dichalcogenide Monolayers", *Nature Communications* 5, 4214 (2014). doi:10.1038/ncomms5214.
- 2 Y. Li, K.-A. N. Duerloo, and E. J. Reed, "Strain Engineering in Monolayer Materials using Patterned Adatom Adsorption", *Nano Lett.* DOI: 10.1021/nl500974t (2014). doi:DOI: 10.1021/nl500974t.

KEYWORDS

phase change material, graphene, MoTe₂, strain engineering, MoS₂, monolayer

Thermo-Mechanical Reliability of TSVs

Tengfei Jiang, Jay Im, Rui Huang and Paul S. Ho

*Microelectronics Research Center and Texas Materials Institute
University of Texas at Austin, Austin, TX 78712*

INTRODUCTION

Three-dimensional (3D) integration has emerged as a potential solution to overcome the wiring limit imposed on chip performance, power dissipation and packaging form factor beyond the 14nm technology node. In the 3D integrated circuits (ICs), through-silicon via (TSV) is a critical element connecting die-to-die in the integrated stack structure. The thermal expansion mismatch between copper (Cu) vias and silicon (Si) can induce complex stresses in the TSV structures to drive interfacial failure and Cu extrusion, degrading the performance and reliability of 3D interconnects. In this work, the thermal stresses and microstructure of a blind via structure were investigated by combining various experimental techniques and numerical analysis. First, the nature of thermal stresses for a TSV embedded in Si was analyzed and the distinct stress characteristics near the wafer surface was discussed. Next, the thermal stress in the TSV structure was studied by a precision wafer curvature technique which measures the curvature change of the TSV specimen during thermal cycling. Electron backscatter diffraction (EBSD) technique was used to study the microstructures evolution of the Cu vias. For samples underwent various thermal histories, synchrotron x-ray microdiffraction measurements were performed to investigate the stress characteristics and plasticity in the via. The effects of Cu microstructure on stress and reliability, particularly on via extrusion and device keep-out zone (KOZ) in TSV structures are discussed.

STRESS AND MICROSTRUCTURE CHARACTERIZATION

The stress field for TSV structures is generally 3D in nature, and the effect of stress near the wafer surface is of particular interest since most of the transistors are fabricated within a few microns of the wafer surface. A semi-analytic solution was deduced for the near-surface stress field of an isolated TSV embedded in the silicon wafer [1]. Good agreement was found between the deduced semi-analytic solution and numerical analysis. The distribution of different stress components in the via will be described. In particular, the implication on the driving force of interfacial delamination will be discussed.

Wafer curvature technique was used to measure the stress behavior of TSV samples subjected to thermal cycling from room temperature (RT) to 200, 300 and 400°C, respectively [2,3]. The sample for this study contains periodic arrays of blind Cu vias with the via diameter $D=10\ \mu\text{m}$ and via height $H=55\ \mu\text{m}$. To correlate the curvature behavior during heating to the microstructure in the Cu via, the as-received sample and the samples after thermal cycling were cross-sectioned by focused ion beam (FIB) and analyzed by electron backscatter diffraction (EBSD). As shown in Fig. 1a, the curvature behavior of TSVs shows distinct features with nonlinear curvature during heating and nearly linear curvature during cooling. The EBSD mapping of Cu grains is shown in Fig. 1b, where the vias were found to have random grain orientations. Continued grain growth can be seen from the average grain sizes in Fig. 1c. The Cu grain growth during heating causes the stress relaxation in Cu and lead to the nonlinear curvature. Subsequently, with the grain structure stabilized, the curvature behavior was nearly linear elastic during cooling. The increase of the grain size in the Cu vias with increasing thermal cycling temperature indicates that grain growth continued in the TSV, inducing more stress relaxation at higher temperatures and thus higher residual stress in both Si and Cu after cooling down to RT. The residual stress in the Cu via causes a bending deformation of the Si lattice near the top surface of the via, which increases with the temperature of thermal cycling up to 400°C.

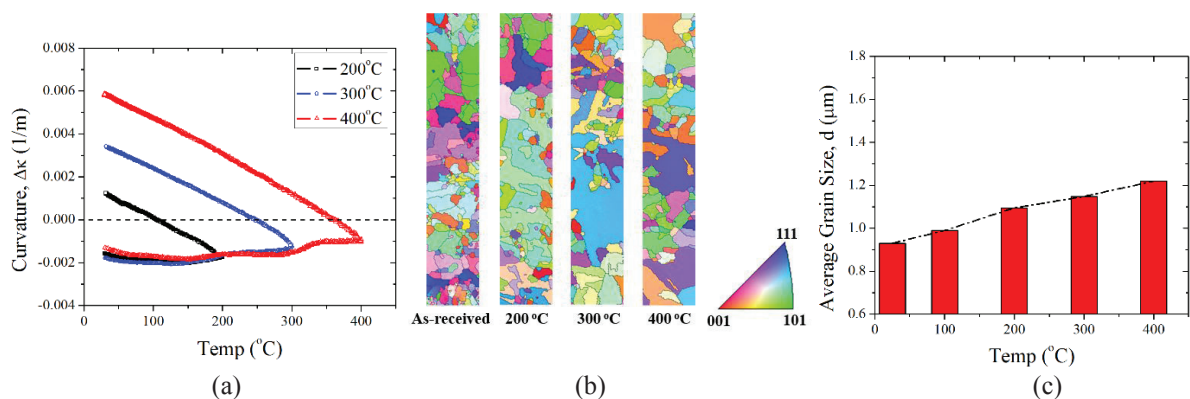


FIGURE 1 (a) Curvature-temperature measurements for TSV samples under thermal cycling to 200, 300 and 400°C. (b) Orientation map of Cu grains in the TSV. (c) Average Cu grain size for the as-received TSV and TSVs after single temperature thermal cycling.

VIA EXTRUSION AND KEEP-OUT ZONE

Synchrotron X-ray microdiffraction has the unique capability of measuring both Cu and Si with submicron resolution and was used to measure the local strain and plastic deformation in TSV structures [4-7]. Polychromatic (white beam) scans were conducted on the cross-section of the TSVs with x-ray energies from 5keV to 22keV and a beam size of $1 \times 1 \mu\text{m}$. The results revealed an asymmetric lattice bending of Si on either side of the Cu via, as measured by the relative change of the lattice orientation of Si, $\Delta\theta$ (Fig. 2a). The bending is induced by the near-surface stress and can be directly correlated to the residual stress in Si. For Cu, the shape of the Laue reflections showed an increase in the average peak width (APW) observed in Cu grains near the via surface after thermal cycling to 300°C and 400°C. As shown in Fig. 2b, the asymmetric broadening of APW was concentrated near the top of the via, which can be attributed to an increase in the geometrically necessary dislocation density in Cu, indicating local plastic deformation [8]. The result provided a direct evidence of local plasticity and was clearly observed after thermal cycling to 400°C, but only faintly observable after thermal cycling to 200°C. This suggests that local plasticity has occurred after thermal cycling to 400°C, but not after thermal cycling to 200°C.

Results from the wafer curvature measurements show overall stress build-up in the TSV structure during thermal cycling, while x-ray microdiffraction provided evidences of local plastic deformation near the top of the Cu via. Together, the stress and plasticity lead to via extrusion after thermal cycling, which was confirmed by atomic force microscopy (AFM) measurement as shown in Fig. 2d. Comparing to the as-received sample, the Cu via thermal cycled to 200°C was found to remain at 26 nm with no additional extrusion, which is consistent with the negligible peak broadening measured by x-ray microdiffraction. For vias thermal cycled to 300°C and 400°C, the average via extrusion was found to be 40nm and 110nm respectively, which can be correlated to the measured increased APW. Interestingly, the extrusion profile exhibits a “donut” shape, which was found to follow the grain structure near the surface of the via. This suggests a microscopically stochastic behavior and that the local plasticity of individual grains near the top could be important in controlling the amount and the statistics of via extrusion. An elastic-plastic finite element analysis (FEA) was performed to investigate the plastic deformation in the Cu via and the results will be discussed [4,5]. The effects of interfacial properties and via dimensions on via extrusion have also been studied by numerical simulations using FEA models and the results will be discussed [9].

The near-surface stresses in Si around the vias have been observed by micro-Raman spectroscopy [10-12], and the degradation of carrier mobility induced by the piezoresistivity effect was analyzed for the keep-out zone (KOZ) around the TSV [13]. The piezoresistivity effect was analyzed for a simple structural model consisting of a single TSV of 10 μm diameter and 200 μm height surrounded by an infinite Si matrix subject to a thermal load of $\Delta T = -250^{\circ}\text{C}$. The anisotropic elastic properties of Si were taken into account in calculating the mobility changes. Distinct KOZ was observed for n-type and p-type silicon with different channel directions. The effects of TSV diameters and Cu yield strength on KOZ were also studied and will be discussed.

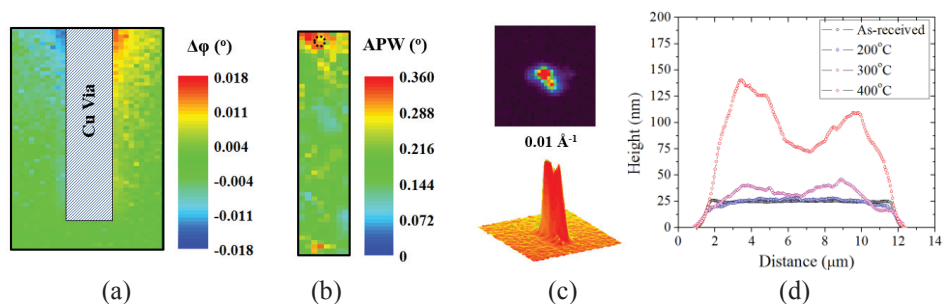


FIGURE 2. (a) Si lattice bending, (b) average peak width (APW) for Cu via, and (c) the shape of (024) reflection near the top of the via after thermal cycling to 400°C. (d) Average via extrusion induced by thermal cycling obtained from AFM measurements.

REFERENCES

1. S.K. Ryu, K.-H. Lu, X. Zhang, J. Im, P.S. Ho, and R. Huang, *IEEE Trans. Device and Materials Reliability* 11, pp. 35-43 (2011).
2. S.K. Ryu, T. Jiang, K.H. Lu, J. Im, H.-Y. Son, K.-Y. Byun, R. Huang, and P.S. Ho, *Appl. Phys. Lett.* 100, 041901 (2012).
3. T. Jiang, S.K. Ryu, Q. Zhao, J. Im, R. Huang, and P.S. Ho, *Microelectron Reliab.* 53, pp. 53-62 (2013).
4. T. Jiang, C. Wu, L. Spinella, J. Im, N. Tamura, M. Kunz, H-Y. Son, B. G. Kim, R. Huang, and P.S. Ho, *Appl. Phys. Lett.*, 103, 211906 (2013).
5. T. Jiang, C. Wu, N. Tamura, M. Kunz, B. G. Kim, H-Y. Son, M.-S. Suh, J. Im, R. Huang, and P.S. Ho, *IEEE Trans. on Device and Materials Reliability*, 14, 2, pp. 698-703 (2014).
6. A.S. Budiman, H.-A.-S. Shin, B.-J. Kim, S.-H. Hwang, H.-Y. Son, M.-S. Suh, Q.-H. Chung, K.-Y. Byun, N. Tamura, M. Kunz, and Y.-C. Joo, *Microelectron. Reliab.*, 52, pp. 530-533 (2012).
7. C. E. Murray, T. Graves-Abe, R. Robison, and Z. Cai, *Appl. Phys. Lett.* 102, 251910 (2013).
8. B. C. Valek, N. Tamura, R. Spolenak, W.A. Caldwell, A.A. MacDowell, R.S. Celestre, H.A. Padmore, J.C. Braman, B.W. Batterman, W.D. Nix, and J.R. Patel, *J. Appl. Phys.*, 94, 3757 (2003).
9. S.K. Ryu, T. Jiang, J. Im, P.S. Ho, and R. Huang, "Thermo-mechanical Failure Analysis of Through-Silicon Via Interface using A Shear-Lag Model with Cohesive Zone", *IEEE Trans. on Device and Materials Reliability*, 14, 318-326 (2014).
10. S.K. Ryu, Q. Zhao, J. Im, M. Hecker, P.S. Ho, and R. Huang, *J. Appl. Phys.* 111, 063513 (2012).
11. I. De Wolf, V. Simons, V. Cherman, R. Labie, B. Vandeveldel and E. Beyne, *Proc. Electronic Components and Technology Conference (ECTC)*, pp. 331-337 (2012).
12. W.S. Kwon, D.T. Alastair, K.H. Teo, S. Gao, and T. Ueda, *Appl. Phys. Lett.*, 98, 232106 (2011).
13. S.K. Ryu, K.H. Lu, T. Jiang, J. Im, R. Huang, P.S. Ho, *IEEE Trans. on Device and Materials Reliability*, 12, 2, p241-254 (2012).

KEYWORDS

3D integration, through-silicon via (TSV), stress, via extrusion, microstructure, FEA

Challenges and solutions for Chip Package Interaction

K. Vanstreels, V. Cherman, H. Zahedmanesh, I. De Wolf, M. Gonzalez

*Imec, Kapeldreef 75, B-3001 Leuven, Belgium
corresponding author: kris.vanstreels@imec.be*

Chip package interaction (CPI) has gained a lot of importance in the microelectronics industry due to the increased number of reported reliability problems at integrated circuit (IC) level^{1,2}. During package assembly of Cu/low-*k* chips and subsequent reliability tests or even under operation conditions, the thermo-mechanical deformation of the package can be directly transferred to the Cu/low-*k* interconnect, inducing large local stresses to initiate and drive cohesive and/or adhesive crack formation and propagation (Figure 1). The impact of CPI on the reliability of BEOL has recently generated extensive interest, especially for the advanced technology nodes³⁻¹⁰. To assure reliability during chip packaging and under field conditions, the semiconductor industry needs reliable, reproducible testing methods and strategies to monitor the mechanical stability of low-*k*, not only for thin films, but also for complete interconnect stacks. This work discusses the extensive development work that was performed at imec to mitigate CPI risks for the BEOL during IC package assembly.

A common way to study the different driving forces for CPI related failure modes is by using 3D finite element models (FEM). However, for advanced flip-chip packages, the scale differences between package and chip level features could be up to 5 orders of magnitude, which makes CPI analysis computationally challenging. Therefore, there is a great need for global-local modeling, multiple substructures as well as fracture and damage mechanics using cohesive zone elements, visco-elasticity, plasticity and creep of materials. Figure 2a illustrates a 3D FEM of a representative volume element (RVE) of a BEOL containing 7 metal layers and passivation. Different factors such as the low-*k* stiffness (Figure 2b) and the position and density of inter-layer metal via interconnections (Figure 2c) on the energy release rates (ERR) of interfacial cracks in the BEOL are investigated to identify the key design parameters needed to reduce the risk of failures in the BEOL. It can be concluded from these plots that if the technology requirements demand the use of ultralow-*k* materials with elastic modulus equal or below 4 GPa, the corresponding interconnect structures would need increased adhesion energy to maintain the mechanical stability equivalent to that of low-*k* with higher elastic modulus, while the BEOL mechanical stability can be reinforced by increasing the via density.

In order to have more accurate FEM simulations, experimental verification of the calculated local mechanical stress and realistic experimental values of material properties (elastic modulus, initial yield stress, hardening, fracture properties and interfacial adhesion) are required. A first approach to measure local stress in the chip is through the use of n-FET transistors^{11,12}. By grouping the n-FETs in 7 x 8 arrays (Figure 3a), these can be used to measure local stress or its variations near μ -bumps or Cu pillars or a combination of both^{11,12}. The results show that the sensors located below the μ -bump show 10% increased I_{on} in comparison with the sensors located outside the μ -bump, indicating a very high local stress in the area below the μ -bump (Figure 3b). On the other hand, the response of the sensors below the Cu pillar varies within 3-4% and indicates that the stress below the center of the Cu pillar is different from the stress at the periphery of the pillar (Figure 3c). A second approach to measure local stress in the silicon is by Micro-Raman spectroscopy (μ RS)¹³. However, the correlation between the measured Raman peak data and the stress is not straightforward and often uniaxial or biaxial stress is erroneously assumed, neglecting the vertical stress component¹⁴. Figure 4a compares the stress as calculated from μ RS measurements along a line crossing the active regions with the FETs assuming uniaxial stress, with the stress calculated from ΔI_{on} . The Raman shift predicts exactly the same shape, but a much smaller stress value than the n-FET stress sensors. This difference might be caused by several effects. One large effect is the assumption of uniaxial stress. Another important factor might be the cross sectioning of the devices, resulting in a lower value and a relaxation of the stress. Figure 4b demonstrates that by assuming tri-axial stress and taking into account the stress-relaxation caused by cross sectioning the sample, the

correlation between the μ RS experiments, FEM results and electrical results from stress sensors is considerably improved.

To date, nano-indentation (NI) is the most commonly used technique in the semiconductor industry to assess the mechanical properties of thin films, including elastic modulus, hardness, adhesion and fracture toughness. Recent developments of the technique have even made it possible to quantify the mechanical properties of small volumes such as intermetallic phases that are formed in μ -bumps by using nanoscale dynamic mechanical analysis (nanoDMA) (figure 5). Although measurement of elastic and plastic properties with nanoindentation seems almost a routine job, measuring the elastic modulus of porous low- k films requires some special attention due to the lack of fundamental understanding on how the measured elastic modulus value is influenced by the structure of the pores, the stiffness of the matrix and the material/probe interactions. This is illustrated on figure 6a, where the elastic modulus was evaluated using two different probe shapes and compared with a nondestructive technique like surface acoustic wave spectroscopy (SAWS). Careful examination of the internal pore structure and interconnectivity by positron annihilation lifetime spectroscopy (PALS) and ellipsometric porosimetry (EP) reveals a clear correlation between the internal pore structure of these films and their mechanical properties (figure 6b-c)¹⁵. Fracture toughness and adhesion of ultralow- k films can be measured by using cube corner indentation (Figure 7a), wedge indentation (Figure 7b) or 4-point bending (Figure 7c). In all cases, FEM simulations are always required for a complete understanding of the techniques.

To experimentally qualify the mechanical stability of multilevel interconnects, two different approaches are followed. In a first approach, direct observation of crack initiation, crack propagation, and interfacial delamination events in BEOL structures containing seven metal layers was captured using a high-resolution real time SEM technique (Figure 8)¹⁶. It was found that longer beams result in smaller critical loads, while wider beams result in larger critical loads. Such responses and also the extracted elastic modulus by FEM simulations appear to be dictated by the density of copper material that is available in the beams. A second approach to get an improved understanding of the BEOL failure process is the Bump-Assisted BEOL Stability Indentation-Scratch Technique (BABSIS)^{17, 18}. The BABSIS test has the capability to determine the conditions at the onset of fractures in a sensitive, fast and straightforward way. However, due to the complexity of the deformation induced by the shear displacement of the indenter tip, the local stresses underneath the copper bump cannot be easily quantified. In this work, we demonstrate that by coupling a BABSIS test with in-situ electrical monitoring the response of n-FET stress sensors below the Cu bump, good agreement was found between the applied loads to the BEOL stack, the response of stress sensors below the Cu bump during the test and FEM simulations¹⁹. As shown on figure 9, changes in the electrical response of the stress sensor were found before actual mechanical failures were detected. This emphasizes the importance of such in-situ stress monitoring during BABSIS tests and allows to retrieve the correct stress values in the BEOL stack at the moment of failure.

REFERENCES

1. Wang, G.T.; Ho, P.S.; Groothuis, S. (2005), *Microelectronics Reliability*, **45**(7-8), p 1079
2. Iacopi, F. et al, *Microelectronic Engineering* **75**, 54 (2004)
3. Wang, G.T. et al, *IEEE Trans Device and Materials Reliability*, **3**, 119 (2003)
4. Zhao, J. H.; Wilkerson, B.; Uehling, T., *AIP Conf. Proc.* **714**, 52-61 (2004)
5. Landers, W.; Edelstein, D.; Clevenger, L., *Proc. International Interconnect Technology Conference 2004*, 108 (2004)
6. Garner, L. et al., *Intel Technology Journal*, **9** (4), 297 (2005)
7. Chin, M.; Marathe, A., *Proc. IRPS 2010*, 4C.6 (2010)
8. Auersperg, J. et al., *Proc. EuroSimE conference 2010*, 125 (2010)
9. Kuechenmeister, F. et al, *Proc. of Electronics Packaging Technology Conference (EPTC) 2012*, 430 (2012)
10. Ryan, V. et al, *Proc. of Reliability Physics Symposium (IRPS) 2012*, 2E.1.1 (2012)
11. Ivankovic A. et al, *Proc. IEEE-International Reliability Physics Conference (IRPS)*, 2012, pp. 2E.3.1-2E.3.9
12. Cherman V. et al, *Proc. Electronic Components and Technology Conference (ECTC)*, Lake Buena Vista, FL, USA, May 2014, 309-315
13. De Wolf I. et al, *Proc. Electronic Components and Technology Conference (ECTC)*, San Diego, CA, USA, May 2012, 331-337
14. De Wolf, I. et al, *Proc. Electronics System-Integration Technology Conference (ESTC)*, Helsinki, Finland 2014, pp.978-983
15. Vanstreels K. et al, *Langmuir* **29**, 12025-12035 (2013)
16. Vanstreels K. et al, *Appl. Phys. Lett.* **105**, 213102 (2014)
17. Geisler H. et al, German patent DE 10 2010 002 453 A1 (September 01, 2011), for Globalfoundries
18. Geisler H. et al, *Proc. of International Reliability Physics Symposium (IRPS) 2013*, 5C.1.1 (2013)
19. Vanstreels K. et al, *Microelectronic engineering*, in press (2014)

KEYWORDS

Chip package interaction, Finite Element Modeling, nano-indentation, stress, adhesion

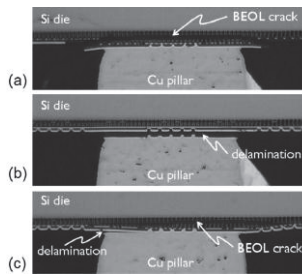


Figure 1: cross section of the outer line of solder interconnects after flip chip assembly. Different failures are observed. (a) Cracks in the BEOL; (b) Delamination of the Cu pillar; (c) a combination of failure in BEOL and delamination.

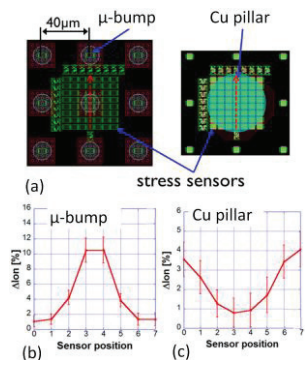


Figure 3: (a) Arrangement of the FEOL stress sensors around micro-bumps and Cu pillar. The green squares indicate the positions of the n -FET stress sensors; (b) variation of the I_{on} currents along the red lines indicated in Figure 3a.

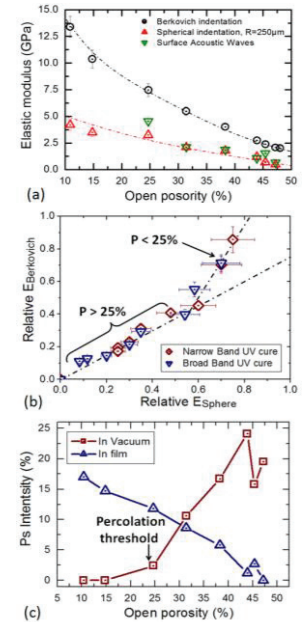


Figure 6: (a) Elastic modulus as a function of open porosity as determined by NI and SAWS; (b) Indentation modulus obtained by spherical and Berkovich indentation, normalized to the absolute values at zero porosity. (c) Positronium (Ps) intensity as a function of the open porosity.

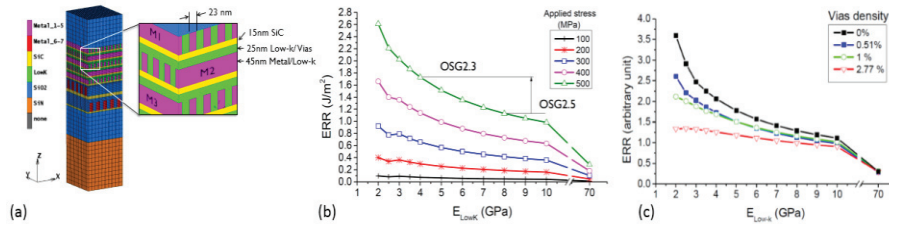


Figure 2: (a) A 3D FEM of a Representative volume element (RVE). The model represents a BEOL containing 7 metal layers and passivation; (b) influence of elastic modulus of low-k on the induced ERR at the crack tip; (c) influence of via density on the induced ERR at the crack tip. The ERR of interfacial cracks in the BEOL were calculated by introducing initial cracks at several relevant interfaces.

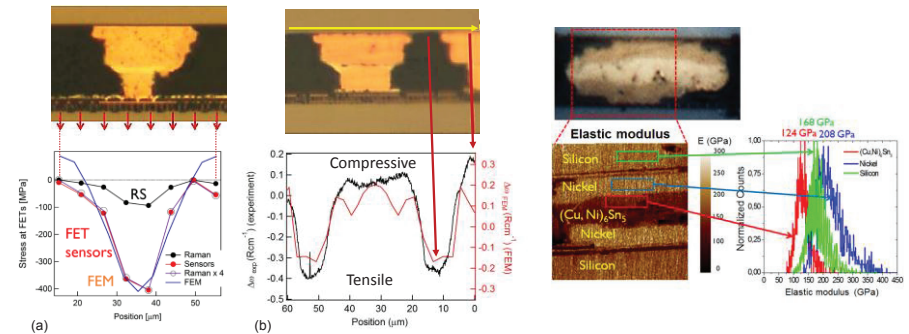


Figure 4: (a) Comparison of stress at the 8 FETs along the scanned line under the μ -bump deduced from μ RS assuming uniaxial stress and from ΔI_{on} of the FET; (b) Comparison of measured stress-induced Raman frequency shift (ΔI_{on}) and FEM-calculated stress induced Raman frequency (ΔI_{on_FEM}), neglecting shear stresses and taking into account the orientation of the cross section and all three stress components.

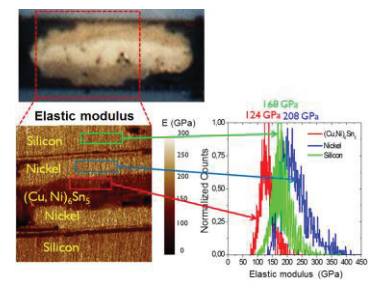


Figure 5: Optical image (top) and elastic modulus map (bottom) of a μ -bump with a $(Cu,Sn)_3Sn_5$ intermetallic phase, determined using nanoDMA. From each region, a statistical distribution of the elastic modulus can be derived.

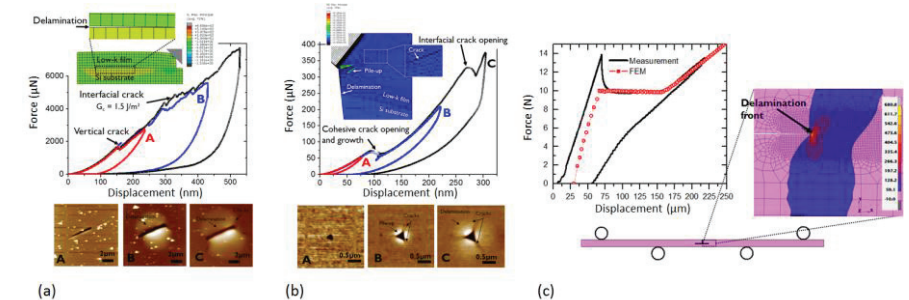


Figure 7: Force-displacement curves and corresponding topography images of (a) wedge indentation; (b) cube corner indentation. 2D and 3D FEM simulations of respectively the wedge indentation and cube corner indentation tests illustrate that cohesive and adhesive failure of the films can be captured; (c) comparison between experimental and FEM simulated force-displacement curve of a 4-point bending test using the virtual crack closure technique (VCCT). Good agreement in load plateau prediction was found.

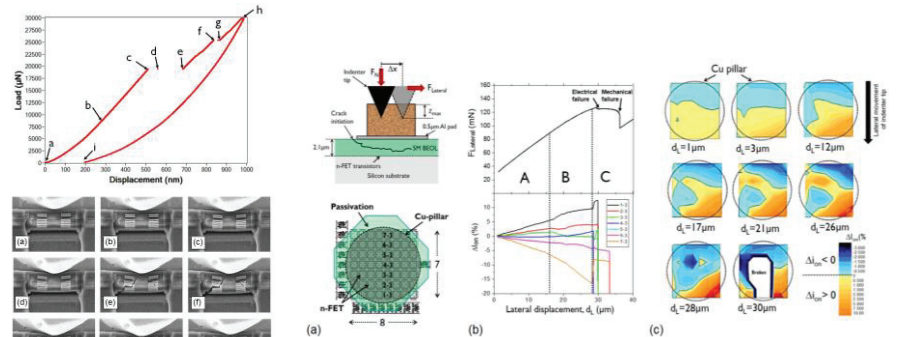


Figure 8: Typical force-displacement curve recorded from the in-situ beam bending tests and corresponding electron micrographs taken at different positions on the force-displacement curve.

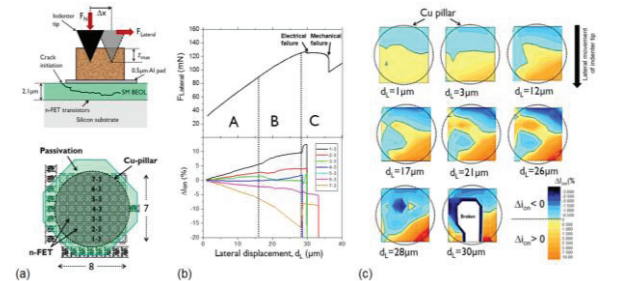


Figure 9: (a) schematic setup of the BABSI test and arrangement of the n -FET stress sensors below the copper pillar. The squares indicate the positions of the n -FET stress; (b) lateral force versus the lateral movement of the indenter tip during the BABSI test and the relative I_{on} current shifts for stress sensors positioned along and normal to the lateral movement direction. (c) 2D distribution of the relative I_{on} currents of the stress sensors below the Cu pillar during the scratch cycle of the BABSI test.

3D Stacked System DFM and DFR Requirements for Materials Data and Characterization Techniques

Valeriy Sukharev

Mentor Graphics Corporation, 46871 Bayside Parkway, Fremont, CA 94538, USA

INTRODUCTION

The paper addresses the growing need in a simulation-based design verification flows capable to analyze any design of 3D IC stacks and to determine across-layers implications in 3D IC reliability caused by through-silicon-via (TSV) and chip-package interaction (CPI) induced mechanical stresses. The limited characterization/measurement capabilities of 3D IC stacks and a strict “good die” requirement make this type of analysis really critical for the achievement of an acceptable level of functional and parametric yield and reliability. The paper focuses on the development of a design-for-manufacturability (DFM) and design-for-reliability (DFR) type of methodology for managing reliability threats during a sequence of designs of 3D TSV-based dies, stacks and packages. A set of physics-based compact models for a multi-scale simulation, to assess the mechanical stress across the dies stacked and packaged with the 3D TSV technology, is proposed. As an example the effect of CPI/TSV induced stresses on electromigration (EM) in the back-end-of-line (BEoL) interconnect lines is considered. A strategy for a simulation feeding data generation and respective materials characterization approach are proposed, with the goal to generate a database for multi-scale material parameters of wafer-level and package-level structures. A calibration technique based on fitting the simulation results to measured stress components is discussed.

FULL-CHIP EM ASSESMENT IN 3D IC STACK

Not so many results from EM studies in 3D TSV stacked systems have been reported so far. The reason seems to be the general believe that since the current density in TSVs is smaller than in the BEoL interconnect segments, the failure should be happened firstly in these segments. However, while this can be true in general, the die stacking can affect the degradation of the interconnect segments. As mentioned previously, a complex picture of the stress distribution is generated inside the thinned dies mounted in a 3D IC stack, [1]. These non-uniform stress distributions generated by thermal ramps cause the migration of atoms/vacancies that can generate void nucleation and growth even before an electrical current is applied. These distributions of residual stresses also affect the void nucleation kinetics caused by EM. Indeed, the critical hydrostatic stress, which is required for generating a critical void capable for growth, is a combination of the residual stress and stress caused by EM. Across die variation of residual stress makes the time for void nucleation to be layout dependent variable in addition to its dependency on the current density and wire length. Another critical characteristic, which is required for the proper EM assessment of the 3D IC design, is the temperature distribution across interconnect. Temperature effects both the void nucleation time and the void volume evolution kinetics, which is a primary cause of the interconnect segment resistance degradation. Therefore in order to accurately estimate the risk of EM induced failure, the full-chip EM assessment methodology should not account only the current densities but also the temperatures and residual stresses in different interconnect segments for different workloads, [2].

Thermal Analysis and Residual Stress Simulation Methodology

Thermal analysis flow that efficiently estimates the across-die temperature variation can be developed by employing a compact thermal model representing a die as arrays of cuboidal thermal cells with effective local thermal properties. The methodology includes three steps: (i) extraction of effective thermal properties of a thermal cell in a layer, (ii) generation of thermal netlist of the whole chip, and (iii) calculation of the temperature at each thermal node by electric solver. All considered composite layers (BEoL, RDL, Si-TSV, bumps-underfill, etc) are divided into a set of thermal cells. The effective thermal conductivities, which are functions of metal densities and routing directions of wires in each metal layer, are calculated based on the theory of effective thermal properties of anisotropic composite materials [3]. Based on the standard procedure the extracted thermal resistances/capacitances, estimated power sources, as well as the thermal boundary conditions, are used for the chip representation as a thermal net, where the nodal temperatures correspond to the nodal voltages and the powers corresponds to the currents. The electric circuit solver can be used to obtain temperatures for each thermal node. Fig. 1 demonstrates the characteristics extracted from the design of analyzed 32nm test-chip and the calculated temperature distribution across the M1 metal layer.

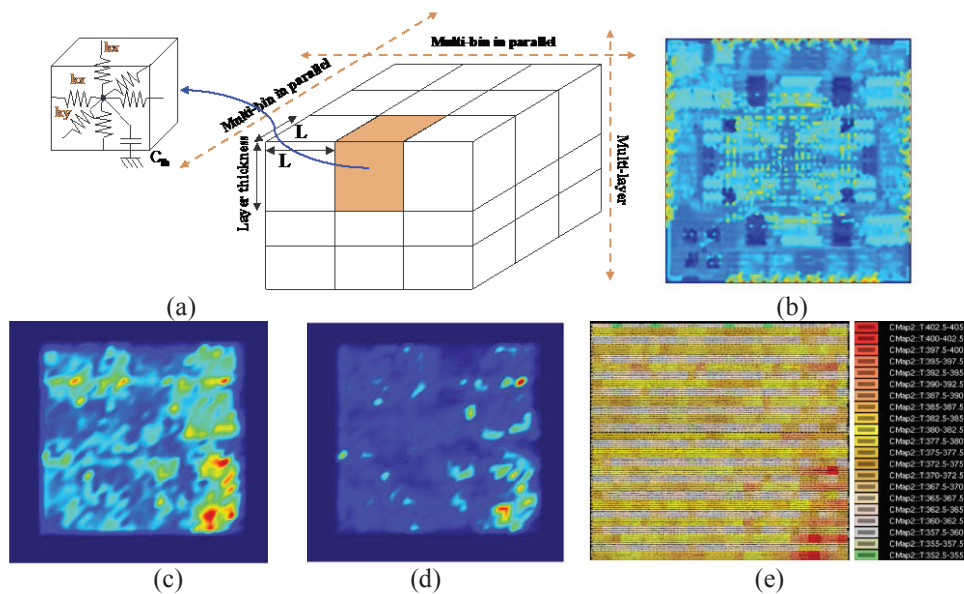


FIGURE 1. (a): schematics of the thermal cell approach, (b): one of the components of the effective thermal conductivity, (c): power dissipated in device layer, (d): Joule heating in M1, (e): temperature distribution across M1 layer.

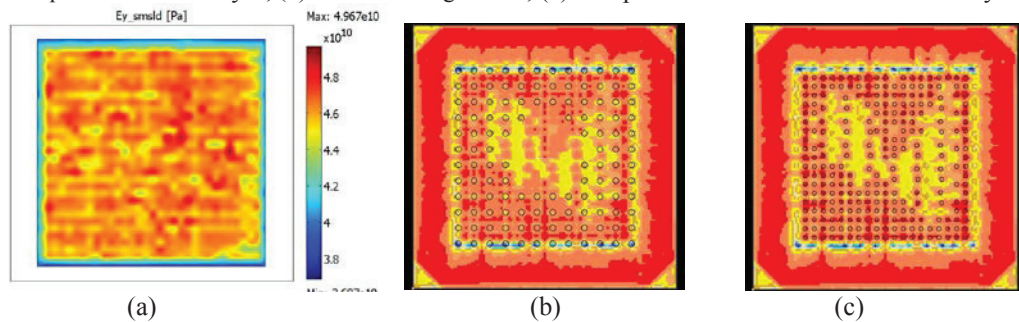


FIGURE 2. (a): distribution of the E_y component of Young's modulus across M1 layer, (b): residual stress distribution across M1 layer with the overlaid C4 bumps, (c): same stress with the overlaid u-bumps.

The previously developed multi-scale simulation methodology for assessing mechanical stresses during a sequence of designs of 3D IC dies, stacks and packages, [1], can be employed for residual stress extraction across any metal layer of the on-chip interconnect. A set of physics-based compact models for a multi-scale simulation to assess the mechanical stress is proposed. Each die is considered as a multi-layer stack consisting of the silicon, BEoL interconnect and BRDL. These layers are characterized by the spatial distributions of the elastic and thermal properties determined by their layouts. A calculation methodology of the effective Young's modulus, Poisson's

ratio, and coefficient of thermal expansion as functions of metal density in each metal layer have been developed based on the model of mechanical properties of anisotropic composite materials, [3]. Fig.2 demonstrates the Young's modulus distribution across the interconnect M1 layer and the stacking-induced residual stress distribution across this layer.

Full-Chip EM-Aware IR-Drop Analysis

It is a common point that the EM-induced degradation of the voltage drop can be considered as the most realistic criterion for the EM-induced chip failure, [4]. Indeed, EM-induced degradation of the resistances of individual wires results in the IR-drop increase, which can affect the timing and the signal integrity if it exceeds a specified threshold. So, the EM-induced chip failure has a parametric rather than a catastrophic character. Fig. 3 demonstrates the across-interconnect initial and final IR-drop distributions, the final configuration of the void containing segments, and the IR-drop and total number of voids kinetics. Obtained results clearly indicate on the important role played by residual stress and across die temperature in the degradation dynamics.

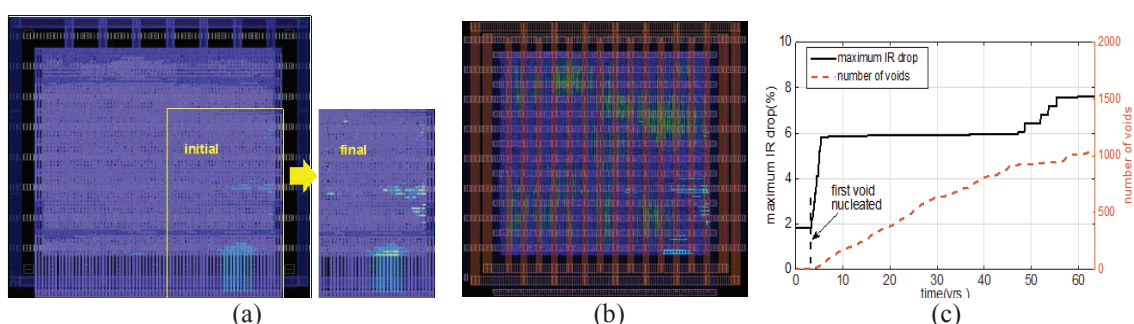


FIGURE 3. (a): EM-induced IR drops change in the power net, (b): branches with voids at the time when IR-drop has reached the threshold, and (c): the increase of the maximum IR drop and number of nucleated voids over time.

The multi-scale simulation methodology for the reliability assessment requires multi-scale materials data as input for the simulation. This multi-scale approach is of particular importance since for sub-micron and particularly for sub-100nm scales the materials properties are changing. In-situ experiments are necessary to study the time-dependent degradation of interconnects in integrated circuits and 3D stacks of integrated circuits and to understand the reliability-limiting processes in microelectronic products and to proof physics-based models. Tomography experiments (3D) while provide the whole spatial information, when are combined with the time-dependence 4D experiments and particularly 4D microscopy are the best possible approaches. Considering the multi-scale approach of modeling and simulation, and the respective approach for the analytical techniques to study the kinetic processes, X-ray tomography and electron tomography are the two experimental techniques that are supposed to be applied within the 4D microscopy approach. The generation of a database for multi-scale material parameters of wafer-level and package-level structures is a practical approach to provide a set of data in a particularly designed format to the chip design community.

REFERENCES

1. A. Kteyan, G. Gevorgyan, H. Hovsepian, J-H Choy, and V. Sukharev, *Journal of Micro/Nanolithography, MEMS, and MOEMS*, **13**, 011203 (2014).
2. V. Sukharev, *Microelectronic Engineering*, **120**, 99-105 (2014).
3. R. M. Christensen, "Mechanics of Composite Materials," Dover Publications, New York, 2005.
4. X. Huang, T. Yu, V. Sukharev, S. X-D Tan, "Physics-based Electromigration Assessment for Power Grid Networks", in ACM Design Automation Conference, San Francisco, CA, June 2014, pp. 1-6.

KEYWORDS

Reliability, electromigration, stress, design verification.

Process and Materials Characterization: Perspectives from Wafer Level Processing for Packaging

Sesh Ramaswami

Applied Materials

ABSTRACT NOT SUBMITTED AT TIME OF PRESS

X-ray Tomography for Process Development and Failure Analysis

Jürgen Gluch^{1,*}, Sven Niese^{1,2,**}, Adam Kubec³, Stefan Braun³, Ehrenfried Zschech^{1,2}

¹Fraunhofer Institute for Ceramic Technologies and Systems –Material Diagnostics, IKTS-MD, Maria-Reiche-Str. 2, 01109 Dresden, Germany

²Technische Universität Dresden, Dresden Center for Nanoanalysis, 01062 Dresden, Germany

³Fraunhofer IWS Dresden, Winterbergstrasse 28, 01277 Dresden, Germany

** now with AXO Dresden GmbH, Germany

*juergen.gluch@ikts-md.fraunhofer.de

INTRODUCTION

Due to the particular properties of X-rays, i. e. high penetration of matter and good material contrast in absorption, high resolution X-ray imaging is a versatile tool for the investigation of complex structures as found in today's micro- and nanoelectronics as well as in MEMS/NEMS. Especially nano X-ray tomography with a resolution better than 100 nm allows to investigate devices and structures non-destructively, to localize and to visualize defects like voids in on-chip interconnects and in TSVs, in (micro) solder bumps as well as delaminations and cracks in back-end-of-line structures. The kinetics of a defect evolution is accessible too using an experimental setup inside the X-ray microscope to provoke for example a crack propagation through an interconnect structure.

After having demonstrated the applicability of nano X-ray tomography to image voids in TSVs, the study of voids in on-chip interconnects, for leading-edge technologies with dimensions < 100 nm, requires an improvement of the resolution from today's 50 nm to values in the range of 10 nm. One approach is to substitute currently used Fresnel zone plates by new focusing X-ray optics. Two partial multilayer Laue lenses (MLLs) are prepared from a multilayer stack and assembled perpendicularly in series to form an X-ray lens (crossed MLL) for full-field imaging. Full-field imaging is demonstrated in a laboratory X-ray microscope using Cu-K α radiation. MLL have the potential to bring hard X-ray microscopy at high efficiencies to resolutions down to the 10 nm range and below.

APPLICATION OF LABORATORY BASED X-RAY TOMOGRAPHY

Two complementary computed tomography setups are available commercially for imaging at medium and high resolution in the lab. In this study, a micro-CT scanner (ZEISS Xradia Versa 520) was used in the medium resolution range down to 700nm resolution, and a laboratory based X-ray microscope (Xradia nano XCT 100) with Cu-K α radiation (E = 8.05 keV) for higher resolution studies up to 100 nm resolution.

The setup was utilized to image various electrical interconnect structures from several microelectronic products. One example are 3D stacked chips using a technology with through silicon vias (TSVs) and micro bumps. Partly filled Cu TSV structures are visible using sub-micron X-ray tomography, but filling voids in the range of 100 nm dimension require high-resolution X-ray tomography with sub-100 nm resolution. Cracks in microbumps and the variability in the formation of intermetallic phases in AgSn solder contacts are visualized too.

Another field of investigation is the extension of the static imaging of failures to the study of degradation kinetics, i. e. the evolution of defects. To investigate the crack propagation after a delamination has started, a miniaturized dual cantilever beam test was inserted into the beam path of the X-ray microscope in such a way that the region of

interest is exposed to the X-ray beam without limitations during tomography or laminography studies. With this setup it is possible to image the crack propagation while increasing the load stepwise between image recordings.

NEXT GENERATION OF X-RAY OPTICS

High-efficiency X-ray optics with sufficient spatial resolution and contrast are required to image structures in the sub-100nm range. While a variety of nano-focusing optics have been studied and developed for illumination of specimen with line and spot focus sizes in the range below 20 nm [1], the Fresnel zone plates (FZPs) still represent the state of the art for lenses intended for full-field imaging. An emerging approach for new X-ray optics to overcome current limits of FZPs are multilayer Laue lenses (MLLs). Like FZPs, the MLLs are diffractive optics consisting of alternating materials, distinguished by their different refractive indices. While FZPs consist of concentric zones, and thus, they have 2D focusing properties, the MLLs are based on layer stacks forming a 1D (line) focus, resembling a cylindrical lens. To achieve 2D focusing, two MLLs were assembled perpendicularly in series to form a crossed MLL [2]. The thicknesses of the layers follow the so-called zone plate law, which is applied for the design of FZPs. In both cases, FZP and MLL, the resolution for first order imaging is limited by thinnest layer. However, differently to FZPs which are manufactured by patterning processes using e-beam lithography and subsequent etching, the MLLs are manufactured by multilayer deposition using alternate magnetron sputtering, in the case reported here of amorphous Si and WSi_2 with thinnest zones of 11 nm thickness. As a consequence, and in contrast to FZPs, the aspect ratio of MLLs is practically unlimited. The lens element itself was prepared by focused ion beam (FIB) milling similar to the H-bar preparation of lamellae for transmission electron microscopy [3].

Experiments were carried out using a laboratory X-ray Microscope (Xradia nano XCT 100) with $\text{Cu-K}\alpha$ radiation ($E = 8.05$ keV). The imaging performance is demonstrated at an X-ray resolution target, possessing a Siemens star pattern with a minimum feature size of 50 nm, patterned by etching into a 500 nm thick Ta absorber (NTT-AT ATN/XRESO-50HC, NTT-AT, Tokyo, Japan) [2]. Initial tests show that sub-100 nm resolution at competitive contrast and improved efficiency values compared to FZP can be achieved with hard X-rays. That means, it was demonstrated that multilayer Laue lenses are a very promising approach to improve resolution and efficiency in laboratory-based hard X-ray full-field microscopy, which opens new analytical possibilities to process development and failure analysis in semiconductor industry.

REFERENCES

1. X. Huang, H. Yan, E. Nazaretski, R. Conley, N. Bouet, J. Zhou, K. Lauer, L. Li, D. Eom, D. Legnini, R. Harder, I. K. Robinson and Y. S. Chu, *Scientific Reports*, Vol. 3, p. 3562 (2014), doi: 10.1038/srep03562
2. S. Niese, P. Krüger, A. Kubec, S. Braun, J. Patommel, C. G. Schroer, A. Leson, and E. Zschech, *Optics Express*, Vol. 22, Issue 17, pp. 20008-20013 (2014), doi: 10.1364/OE.22.020008
3. S. Niese, P. Krüger, A. Kubec, R. Laas, P. Gawlitza, K. Melzer, S. Braun, and E. Zschech, *Thin Solid Films* Vol. 571 part 2, p. 321–324 (2014), doi: 10.1016/j.tsf.2014.02.095

KEYWORDS

Nano X-ray tomography, X-ray microscopy, multilayer Laue lens

Novel Scanning Acoustic Microscopy Technologies Applied To 3D Integration Applications

Peter Czurratis¹, Sebastian Brand², Tatjana Djuric¹, Peter Hoffrogge¹,
Matthias Petzold²

¹ PVA TePla Analytical Systems GmbH, Deutschordenstrasse 38, Westhausen, Germany

² Fraunhofer Institute for Mechanics of Materials IWM, Walter-Hülse-Str.1, Halle, Germany

SUMMARY

In semiconductor industry new approaches are employed for increasing functionality and complexity while reducing a systems footprint by integrating components in the third spatial dimension. However, this new design concept requires new and adapted methods for failure analysis and quality assessment. Acoustic microscopy is a powerful method providing detailed information of a samples interior while operating non-destructively. By employing the methods capability of acquiring the information in 3D by performing a rapid acquisition scan full access is given to the samples interior structure and parameters including the elastic properties. However, the new concept of 3D integration required the development of new solutions for providing the full performance of this technique to the developers, manufacturers and failure analysis engineers of 3D integrated technologies.

INTRODUCTION

Recent trends in semiconductor technologies utilize the third spatial dimension for increasing functionality and performance of microelectronic systems and components while continuously reducing a devices footprint. This new concept however, challenges existing and state of the art methods for diagnostics, failure analysis and quality assessment. Therefore the adjustment of existing methods for non-destructive inspection is strongly demanded since, especially in the development phase of a new technology, the non-destructive and total-view assessment of the condition and the localization of defects is of major importance.

Acoustic microscopy is capable of providing 3D information from a samples interior, allowing an exact depth localisation of defects and enabling the access to mechanical properties. New semiconductor chip technologies and technologies for 3D integration require exact these information of packaging and interface defects in 3 dimensions. In the current paper novel methodical approaches in acoustic microscopy for non-destructive failure analysis on 3D integrated TSV samples are introduced. The approach combines new concepts in transducer design, customized pulse excitation, high performance digitisation hardware systems and intelligent focus solutions for increased accuracy and sample through put. Also the potential of acoustic microscopy hardware operating in the frequency band of up to 2 GHz equipped with specific acoustic lenses allowing for lateral resolutions in the 1 μm range will be demonstrated.

SCANNING ACOUSTIC MICROSCOPY ON CHIP AND WAFER LEVEL

In case of full wafer inspection for high level 3D integration processes, non-destructive inspection commonly faces a high degree of wafer bow. This warpage however, will lead to significant artefacts interfering with features in the bond interface. Due to the high refractive indices encountered in acoustic imaging the spacing between the sample surface and the acoustic lens largely influences the focal position inside the sample. For avoiding these imaging

artefacts an intelligent z-axis has been developed that prevents an axial displacement of the focal area allowing for high imaging contrast and resolution with an increased performance in defect localization.

By aiming at ever higher imaging resolutions an increase in acoustic frequency is desired. However, acoustic attenuation exponentially increases with frequency resulting in spectral downshifts and decreased signal intensities. These issues are met by the design of application specific acoustic lenses allowing for a minimum propagation path in the coupling fluid. Acoustic signals received by these transducers contain a large variety of information about the interaction of the acoustic wave on the propagation path [1]. Newly developed signal analysis methods allow for the extraction of these information and also largely contributes to an increased imaging resolution and defect detection [2].

The increased performance of these novel approaches has been evaluated on a variety of flip-chip devices containing regular and micro-bump interconnects as well as TSV's. Acoustic imaging and defect localization will be shown on both the condition of the electrical connections as well as on the integrity of the underfiller required for ensuring mechanical and thermal stability in high performance 3D-integrated devices.

SCANNING ACOUSTIC GHZ-MICROSCOPY

The decreased lateral dimensions of structures contained in 3D- relevant technologies require imaging resolutions in the 1 μm range and detection limits even below that. For meeting those demands a novel high frequency acoustic microscope has been developed operating in the frequency band of up to 2 GHz providing an imaging resolution of approx. 1 μm (@ 1.2 GHz) combined with an excellent sensitivity to surface and near-surface features. Figure 1 contains an electron micrograph in direct comparison with an acoustic GHz-micrograph showing and verifying delaminations non-destructively found approx. 5 μm below the samples surface. The SEM image in the upper part of fig.1 verifies the acoustically found defects demonstrating the high potential of this new acoustic imaging technique.

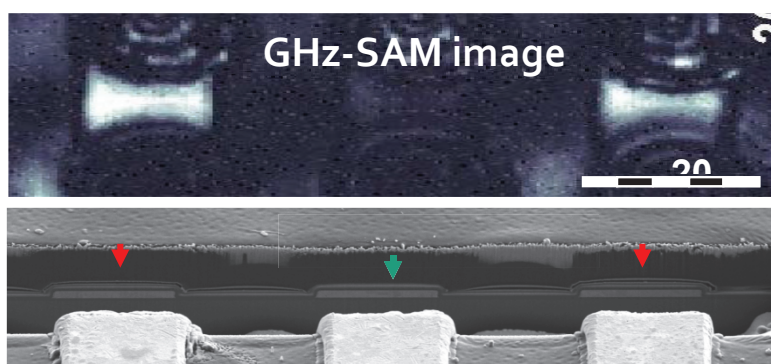


FIGURE 1. Acoustic GHz-Microscopy employed to an imaging sensor manufactured in 3D-technology. Top: GHz-SAM micrograph of an interconnect structure 5 μm below the surface. Increased intensity can be noted at the outermost routings. The central routing shows a significantly lower signal intensity. Bottom: SEM image of a FIB-prepared cross-section through the acoustically found defects. Delamination of the routings can be noted at the red arrows, while the central routing is well adhering.

ACKNOWLEDGEMENTS

The authors thank RTI International for providing the sample for conducting GHz-SAM inspection.

REFERENCES

- [1] A. Briggs, *Advances in Acoustic Microscopy*. New York and London, Plenum Press, 1995.
- [2] Brand, S., et al., Automated inspection and classification of flip-chip-contacts using scanning acoustic microscopy. *Microelectronics Reliability*, 2010. **50**(9-11): p. 1469-1473.

KEYWORDS

3D integration, Failure Analysis, Acoustic Microscopy, SAM, GHz-SAM, Acoustical Imaging, Non-Destructive Testing

Optical Constants of $\text{Ni}_{1-x}\text{Pt}_x$ and $\text{Ni}_{1-x}\text{Pt}_x\text{Si}$ for In-Line Contact Metrology

Lina S. Abdallah,^{1,*} Stefan Zollner,¹
Mark Raymond,² Ahmet S. Ozcan,³ and Christian Lavoie⁴

¹*Department of Physics, New Mexico State University, MSC 3D, P.O. Box 30001, Las Cruces, NM 88003, USA*

²*GLOBALFOUNDRIES, 255 Fuller Rd., Albany, NY 12203, USA*

³*IBM, 850 rue Jean Monnet, 38926 Crolles, France*

⁴*IBM Research Division, P.O. Box 218, Yorktown Heights, NY 10598, USA*

**Now at: Intel Corporation, 2501 Northwest 229th Avenue, Hillsboro, OR, 97124, USA*

INTRODUCTION

Spectroscopic ellipsometry (from the near-infrared to the near-ultraviolet) is the technique of choice for thickness measurements in the semiconductor industry.¹ Using automated in-line fab metrology tools, thicknesses of many layers can be determined in just a few seconds in small areas on product wafers. A late-generation CMOS process flow might contain 100 such thickness measurements, at least during the development of the technology. Thickness measurements of SiO_2 and metal gate oxides, silicon nitrides, $\text{Si}_{1-x-y}\text{Ge}_x\text{C}_y$ source-drain stressors, and back-end interlayer dielectrics are common, but optical thickness measurements of metals (contacts or interconnects) are rare. Usually, metal or silicide thicknesses are determined using sheet resistance, x-ray reflectance, or x-ray fluorescence measurements, which are much more cumbersome than ellipsometry and require specialized metrology tools. This paper describes measurements of optical constants for $\text{Ni}_{1-x}\text{Pt}_x$ unreacted metal and $\text{Ni}_{1-x}\text{Pt}_x\text{Si}$ monosilicide contact layers, suitable for optical inline metrology using spectroscopic ellipsometry. Especially, we focus on the dependence of these optical constants on Pt content.

WAFER PREPARATION

$\text{Ni}_{1-x}\text{Pt}_x$ metal alloy layers ($0 < x < 0.25$) with 100 Å thickness were deposited on 300 mm Si wafers using DC magnetron sputtering. To avoid reaction between the metal and the Si substrate, 200 nm thick thermal SiO_2 layers were grown before metal deposition. Similarly, to produce monosilicide contact layers, the same metal layers were deposited on clean Si substrates (without SiO_2) followed by thermal annealing at 500°C for 30 s. Wafers were roughened in the back after deposition and annealing to avoid reflections from the backside of the two-side polished Si wafers.

MEASUREMENTS AND DATA ANALYSIS

Spectroscopic ellipsometry data were taken from 0.5 to 6.6 eV on a J.A. Woollam variable-angle-of-incidence spectroscopic ellipsometer equipped with a computer-controlled Berek waveplate compensator. For the unreacted metal layers, the angle of incidence was varied over a broad range (20° to 80°) to take advantage of the interference enhancement from the thick thermal oxide. For the monosilicides, incidence angles between 65° and 75° were sufficient.

The data were analyzed using several different methods: For the unreacted metal, we first determined the metal and oxide thicknesses by expanding the optical constants of the metal with a sum of Drude-Lorentz oscillators and

varying the oscillator and thickness parameters until a good fit to the data was achieved. Once the thickness was determined, we used a B-spline expansion of the metal optical constants and a direct inversion of the ellipsometric angles (point-by-point fit) to determine the optical constants. All three methods yielded the same results, shown in Fig. 1. For the unreacted metal, it was necessary to assume that the metal was covered with about 50 Å of water. This water layer could be removed by annealing the metal in UHV followed by in situ measurements in a vacuum chamber. An ozone clean has the same effect of desorbing the water layer. Many modern fab metrology tools also have the ability to remove adsorbed layers of contaminants, such as water or other molecular atmospheric contamination. Details of the data analysis are described elsewhere.²⁻⁴

To analyze the data for the reacted monosilicide layers, we treated the thickness of the silicide as a variable parameter and determined the silicide optical constants for each thickness value. We then chose the silicide thickness for which the E_1 structure of Si is minimized in the silicide optical constants. Choosing the wrong silicide thickness leads to artifacts near the E_1 critical point of the Si substrate. (We also included a 1 nm thick native oxide consisting of SiO_2 in our model).

RESULTS AND DISCUSSION

The resulting optical constants for $\text{Ni}_{1-x}\text{Pt}_x$ alloys and $\text{Ni}_{1-x}\text{Pt}_x\text{Si}$ monosilicides are shown in Figs. 1-2. These figures display the optical constants as the real and imaginary part of the dielectric function. From these data, the refractive index n and extinction coefficient k can easily be determined. Both data sets are dominated by a strong Drude divergence in the infrared, as expected for metals. Therefore, it would be more convenient to display the optical constants as a complex optical conductivity, which removes the Drude divergence.³ The unreacted metal also has an interband absorption at 4.5 eV, which broadens with increasing Pt content, since the 5d states of Pt are less localized than the 3d states of Ni and have a wider bandwidth. The optical constants of the monosilicides show two interband absorption peaks at 1.9 and 4.4 eV, which are clearly visible in Fig. 2. A third interband transition in the infrared (near 0.8 eV) is also required to achieve a good fit, but this transition overlaps with the Drude divergence and is hard to see in the data.

As one might expect, the Drude term is more pronounced in the unreacted metal, while the interband transitions are stronger in the silicide. Our data are in qualitative agreement with previous literature data obtained from reflectance and ellipsometry measurements.⁶

Using the optical constants shown in Figs. 1-2, which are also available in tabulated form on our web site,⁵ it would be straightforward to implement metal and silicide thickness measurements on product wafers using inline ellipsometry fab metrology tools. One has to consider, however, that the optical constants of the unreacted metal depend on Pt content and also change after annealing due to grain growth (which increases the conductivity). Also, atmospheric molecular contamination must be removed for accurate thickness measurements. The optical constants also depend on thickness. In general, thicker metal films have larger grains and therefore are more conductive. Therefore, the optical constants must be determined separately for each metal process.

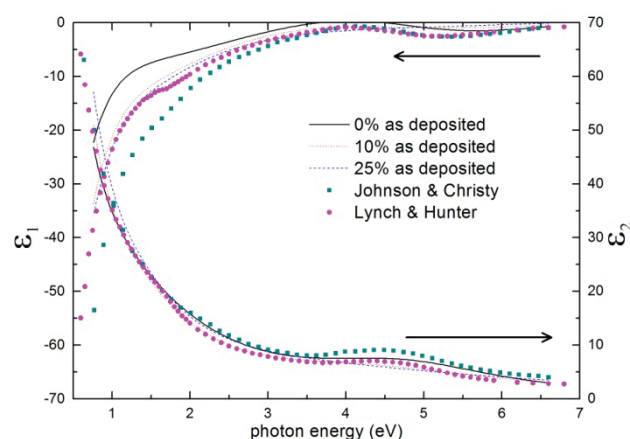


FIGURE 1. Optical constants (expressed as a complex dielectric function) for as-deposited $\text{Ni}_{1-x}\text{Pt}_x$ alloys as a function of Pt content in comparison to literature data. Tabulated data are available on our web site.⁵

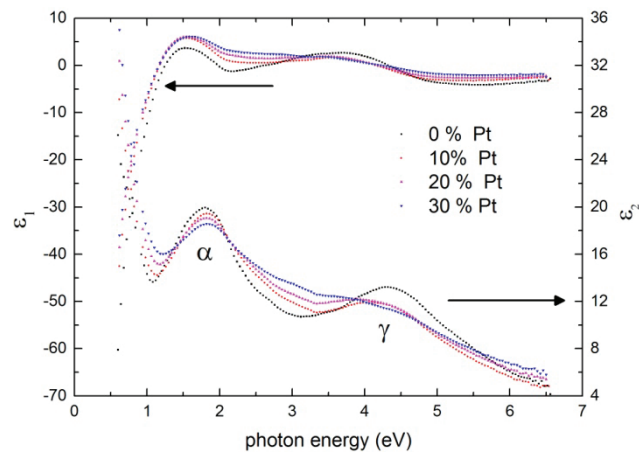


FIGURE 2. Optical constants (expressed as a complex dielectric function) for $\text{Ni}_{1-x}\text{Pt}_x\text{Si}$ monosilicides as a function of Pt content. Tabulated data are available at our web site.⁵

REFERENCES

1. S. Zollner, in *Ellipsometry at the Nanoscale*, edited by M. Losurdo and K. Hingerl, Heidelberg: Springer, 2013, pp. 607-627.
2. L.S. Abdallah, S. Zollner, C. Lavoie, A.S. Ozcan, and M. Raymond, *J. Vac. Sci. Technol. B* **32**, 051210 (2014).
3. L.S. Abdallah, T.M. Tawalbeh, I.V. Vasiliev, S. Zollner, C. Lavoie, A. Ozcan, and M. Raymond, *AIP Advances* **4**, 017102 (2014).
4. L.S. Abdallah, S. Zollner, C. Lavoie, A. Ozcan, and M. Raymond, *Thin Solid Films* **571**, 484-489 (2014).
5. <http://ellipsometry.nmsu.edu>.
6. V.W. Kamineni, M. Raymond, E.J. Bersch, B.B. Doris, and A.C. Diebold, *J. Appl. Phys.*, **107**, 092525 (2010).

KEYWORDS

Spectroscopic ellipsometry, contacts, nickel silicide, inline metrology

Metallic Contamination Analysis of 450 mm Wafers Using VPD-DC-ICPMS and LPD-ICPMS

C. Agraffeil¹, H. Fontaine¹, T. Lardin¹, V. Enyedi¹, D. Noventa¹, B. Charlet¹, G. Delpu², T. Brillouet².

(1) Univ. Grenoble Alpes, F-38000 Grenoble, France - CEA, LETI, MINATEC Campus, F-38054 Grenoble, France

(2) RECIF Technologies, 9 Rue des briquetiers, 31703 Blagnac, France

INTRODUCTION

The evolution of the microelectronic technologies is very challenging to follow due to complexity of devices using new materials and architectures (High-k, Pt silicide, 3D stacking,...). In the same time, semiconductor technology has to keep going the cost reduction and the alternative of 450 mm transition is an opportunity for challenging innovation on mass-production by developing advanced greener manufacturing [1,2]. Such transition is going along with the respect of industrial standards and among metrology needs, the metallic contamination control on the 450 mm wafers is mandatory. Indeed, it is well known that such contamination on Si wafer surfaces can drastically deteriorate the device performances [3]. Thus, implementation and development of metallic contamination analysis must evolve on time to characterize and qualify future 450 mm technologies.

The metallic contamination on Si-wafers is usually characterized by Total reflection X-Ray Fluorescence spectroscopy (TXRF) or by a chemical collection procedure, commonly a HF Vapor Phase Decomposition - Droplet Collection (VPD-DC) followed by Inductively Coupled Plasma Mass Spectrometry (ICPMS) [4,5]. TXRF enables the metals analysis with a relative accuracy ($\pm 20\%$ to $\pm 100\%$) and detection limits (DLs) of a few 10^9 at/cm² (Cr, Mn, Fe, Cu...) to 10^{12} at/cm² (Au, Pt...). VPD-DC automatic system coupled to ICPMS analysis is a more accurate ($\pm 15\%$) and sensitive analysis with DLs as low as 10^6 - 10^9 at/cm². Based on a diluted HF/H₂O₂ droplet solution, VPD-DC process allows an effective collection (>95%) for all "usual" metals (Na, Mg, Ca, Al, Ti, Cr, Fe, Co, Ni, Cu, Zn...) except for noble metals (Au, Pt, Ag, Pd...) due to their higher oxido-reduction potentials. For those noble elements, a Liquid Phase Decomposition collection procedure (LPD) was developed using a diluted HF/aqua regia mixture to address noble metals analysis reaching DL around 10^{10} at/cm² [5,6].

In this context, this work aims to develop reliable methods to be able to characterize metallic contamination of 450 mm wafers at detection level matching with required industrial expectations. To achieve this goal, we propose the implementation of manual VPD-DC and LPD collection methods coupled to ICPMS analysis dedicated respectively to usual metallic contaminants and noble metals on 450 mm Si substrates.

EXPERIMENTAL METHODOLOGY

Implementation of VPD-DC and LPD for 450mm Wafers

Device grade wafers 450mm (Monitor, cz-B doping <100> -thickness about $925\mu\text{m}\pm 25\mu\text{m}$) were used to implement both VPD-DC and LPD methods. All analyses were performed by an Agilent ICPMS7500cs.

The implementation of the VPD combined with a manual Droplet Collection for scanning 450 mm wafers surface required a specific reactor to expose Si wafer to HF vapors for its native oxide decomposition and leading to a hydrophobic surface. It was designed and manufactured (mainly with high purity PVDF and PTFE polymers) to be compatible with 450 mm wafer dimensions. Then, the collection step was performed manually, using the print of the droplet on the wafer surface to control the area scanning. Due to the moisture evaporation, two steps of VPD-DC are necessary to perform a manual collection, and each step scans an half of 450mm wafer area. The collection was performed using a well-defined droplet volume of HF 2% /H₂O₂ 2% solution. After adding both collection droplets,

the solution was completed to 1ml for analysis by ICPMS. To prevent cross-contamination from clean room air, handling, tools..., specific cleaning procedure and strict tool control (pipette, reactor and chuck) were defined precisely to reach and keep stable and low initial levels of contaminants.

In the same way, a home-made LPD set-up was designed in PTFE which enables wetting the whole surface excluding 10 mm edge ring with the selected chemistry based on a diluted HF/HCl/HNO₃. Operational conditions were adjusted at a few tens mL for a collection time of 5 minutes. This solution dissolves metal impurities on and/or in the near surface (a few tens nm [5]), and is then sampled in part for ICPMS analysis.

Evaluation of VPD-DC-ICPMS and LPD-ICPMS

A procedure of chemical collection is commonly assessed by the determination of collection efficiency (CE) from purposely contaminated wafers and by the establishment of Detection Limits (DLs).

Generally, CE higher than 80% allows demonstrating a robust analysis. Due to our manual collection, VPD-DC ICPMS method implied the CE verification. Indeed, the increase of droplet volume, collection on a larger area and manual process implied uncertainties on parameters such as scan speed and collection ability. LPD collection on 450 mm is performed with similar collection volume to wetted surface ratio than on 300mm. No CE control is required because of CE evaluated on 300mm as higher than 90% [4,5]. Controlled contaminated wafers were performed by spin-coating method at around $\sim 1.10^{11}$ at/cm² levels. Then, three consecutive VPD-DC-ICPMS were performed on one 450 mm contaminated wafer and CE was determined as :

$$CE = VPD1 / \sum_{i=1}^{n=3} VPDi$$

The DLs are determined from 4 VPD-DC or LPD ICPMS carried out consecutively on the same 450 mm wafer. The first one was excluded since it can be contaminated. Then, other results correspond to the global background of the whole analytical chain and were used to calculate the DL as $DL = 3 \sigma$, with standard deviation σ .

RESULTS

Verification of CEs and Estimation of DLs

Alkali (Na), alkali earth (Ca), transition (Cu, Fe, Mo, Ni, Ti, W, Zn) metals and Al were selected as representative elements for approving collection methodology. CE values of those metals are shown in figure1, CEs of Al, Ca, Fe, Mo, Na, Ni, Ti and Zn are higher than 95% and 91% for W. CE of Cu around 60% showed the difficulty to be collected with the selected chemistry.

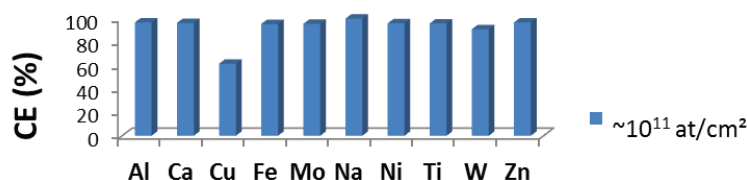


FIGURE 1. CEs of usual elements from VPD-DC ICPMS analysis of 450 mm wafer.

Those very good results of CEs confirm that the manual VPD-DC methodology implemented on 450 mm wafers is clearly as efficient as automatic system used for smaller wafers. About Cu case, CE result is not surprising considering its higher oxido-reduction potential than for other analyzed elements. An alternative for better collection and thus, an accurate analysis of Cu could be to analyze it with noble metals by LPD-ICPMS.

For both usual and noble metals, DLs on 450 mm compared to DLs on 300 mm wafers are reported in figure 2, respectively for, manual VPD-DC on 450 mm and automatic system on 300 mm (a) and for LPD both sizes (b). For 450mm DLs, Li, Ti, V, Cr, Co, Ni, Zn, Sr, Mo, In, Sn, Sb, Ta, W and Pb can be analyzed with DLs from a few 1.10^6 to lower than 1.10^9 at/cm². DLs of Na, Ca, K and Al are slightly upper, but they remain close to the most stringent ITRS recommendations (5.10^9 at/cm²)[8]. It can be attributed to manual process and environment contamination. For noble metals, determined by LPD-ICPMS, DLs values of all elements are in range of 4.10^9 - $2.5.10^{10}$ at/cm². The comparison with 300 mm DLs shows similar limits and even in many cases slight improvement. This demonstrates that both the VPD-DC and LPD- ICPMS methods implemented for 450mm is quite functional and fulfill sensitivity expectations.

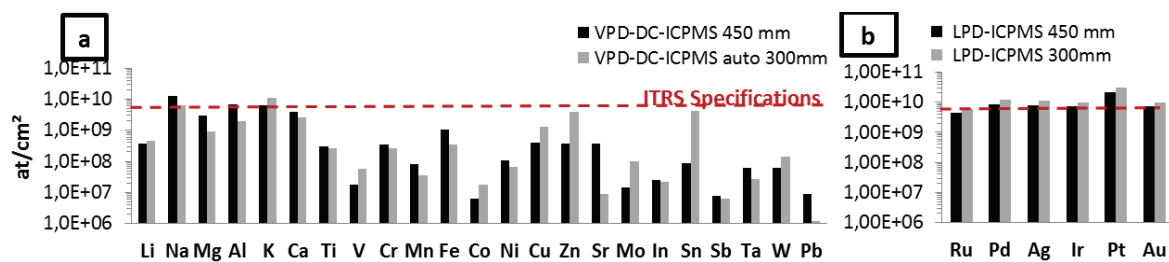


FIGURE 2. Results of DLs (Limits of Detection) from VPD-DC (a) and LPD (b) coupled to ICPMS of 450 mm wafer.

Application to the metallic contamination control

Developed methods were then applied to the metallic contamination determination of available 450 mm wafers and to the demonstration of the control of their environment. Measurements showed that significant improvement was obtained between the “mechanical” grade and the “device” grade wafers. Finally, tested device grade wafers present very low contamination (mainly Na, Ca, Al and Fe), in good agreement with ITRS recommendations [7].

Furthermore, VPD-DC and LPD coupled to ICPMS were used to qualify the cleanliness of a 450 mm sorter developed by RECIF in terms of metallic cross-contamination. This tool handles 450 mm wafers from their backside using a specific chuck and the tests were performed at RECIF in a modular clean room. A specific procedure was defined using 450 mm device grade wafers. The shipping box (MAC450) and transport contributions were evaluated from two control sample wafers for front side (FS) and back side (BS) contamination characterization. Whereas the contamination brought by the sorter was assessed from 500 entry/exit cycles inside the sorter of two clean wafers for FS and BS too. VPD-DC followed by LPD- ICPMS analyses were performed on each wafer. Results showed low concentrations close to DLs of Mg, Al, Ca, Ti, and Fe for all wafers (control sample and clean FS/BS wafers). No noble metals were detected. Only Sn was significantly added on both FS and BS by passing through the sorter in link with Sn soldering performed in the vicinity of the sorter assembly. However, even if tin is clearly added its level remains lower than 1.10^{10} at/cm². Those good results showed that the sorter environment and RECIF modular clean room were relatively well controlled and fulfil industrial expectations.

CONCLUSION

The implementation and development of manual VPD-DC and LPD coupled to ICPMS were successfully demonstrated on 450 mm silicon wafers to analyze respectively usual and noble metals. Both methods were qualified with similar good performances compared to smaller wafer size state of the art. Indeed, DLs in the range of 8.10^6 - 1.10^{10} at/cm² for usual elements and 4.10^9 - 2.10^{10} at/cm² for noble metals are similar or slightly better than current analysis capabilities for 300mm and then answer to the 450mm technology needs.

REFERENCES

1. J. Lin, P. Lin et al., IEDM, Albany NY USA : IEEE, **13** 365-68 (2013).
2. A. Maynes and F. Robertson, G450C, Albany NY USA : Solid State technology (2014).
3. L. Jastrzebski et al., Journal of the Electrochemical Society, **137**, 242-249 (1990).
4. A. Danel et al., Materials Sci. & Eng. B, **102**, 213-217 (2003).
5. H. Fontaine, D. Hureau et al., AIP Conf. Proc. **1395**, 222-226 (2011).
6. H. Fontaine et al., 15th ARCIS meeting, Gardanne, France, Nov. 28-29 (2012).
7. ITRS roadmap 2013 edition, Table FEP10: Front-End Surface Preparation technology requirements, www.itrs.net.

KEYWORDS

450mm, metallic contamination, VPD-DC-ICPMS, LPD-ICPMS

ACKNOWLEDGMENTS

These works are financially supported in the frame of the EU Catrene NGC450 project.

Positron Annihilation Spectroscopy: an Emerging Technique For Characterization of Oxygen Vacancies in Hf-based-high-k Materials?

M. Alemany^{1,4,3}, P. Desgardin⁴, A. Chabli², F. Bertin³, M. Gros-Jean¹,
M.-F. Barthe⁴

¹ *STMicroelectronics, 850 rue Jean Monnet, 38926 Crolles, France.*

² *Univ. Grenoble Alpes, INES, F-73375 Le Bourget du Lac, France, CEA, LITEN, Department of Solar Technologies, F-73375 Le Bourget du Lac, France*

³ *Univ. Grenoble Alpes, F-38000 Grenoble, France,*

CEA, LETI, MINATEC Campus, F-38054 Grenoble, France.

⁴ *CNRS, CEMHTI UPR3079, Univ. Orléans, F-45071 Orléans, France.*

INTRODUCTION

Nowadays, as the gate length of devices is scaled below 32 nm new materials are required. For example, high-k dielectrics (HfO₂) and metals (TiN) are used in transistor generations embedding High-k Metal gate (HKMG) stacks, raising new issues such as shifts in transistor threshold voltages [1, 2]. Oxygen vacancies in both HfO₂ and SiO₂ are usually invoked to explain this shift [3]. Charged oxygen vacancies are created during the activation spike annealing resulting in the formation of a dipole at the high-k/metal interface [1, 4, 5] which pins the TiN Fermi level [4] and thus causes the threshold voltage shift. In addition, the threshold voltage shift is enhanced by oxygen vacancies creation into the SiO₂ interfacial layer [6, 7]. To assess these mechanisms, techniques capable of characterizing oxygen vacancy density in the HKMG stacks for the 14 and 10 nm nodes are required. Today, two techniques are envisioned to meet these requirements: positron annihilation spectroscopy (PAS) the most sensitive characterization method of vacancy nature and concentration in solids [8] and electron energy loss spectroscopy (EELS) that is potentially sensitive to oxygen vacancies with a spatial resolution compatible with the dimensions of the HKMG structures [9]. Today as PAS is intensively used to characterize vacancy in diverse materials [10, 11, 12, 14] only few studies are dedicated to high-k dielectric [8, 13, 15].

In this paper, a slow positron beam coupled with a Doppler broadening spectrometer (DBS) [16] has been used to study vacancy defects in HfO₂ layers on silicon. First results on PAS capabilities in this configuration are presented and discussed in terms of layer thickness limitations.

EXPERIMENTAL

In this work, the DBS measurement system is a standard gamma-spectroscopy system equipped with a high purity germanium detector that offers a high energy resolution (<1.3 keV at 511 keV) and a high efficiency (>25% at 1.33 MeV). The positron emitted from a ²²Na radioactive source are first converted in a mono-energetic beam using a 5 μm thick tungsten foil and then accelerated at a kinetic energy ranging from 0.2 to 25 keV. The flux is ~10⁵ cm⁻² s⁻¹. The (e⁺, e⁻) pair momentum distribution is measured at 300 K by recording the Doppler broadening of the 511 keV annihilation line characterized by the low S and the high W momentum annihilation fraction in respectively the momentum windows (0-|2.80|x10⁻³m₀c) and (|10.61|-|26.35|x10⁻³m₀c), where m₀ is the rest mass of the electron and c the speed of light. The S fraction corresponds essentially to annihilations with low momentum electrons, thus more predominantly with valence electrons. The W fraction corresponds to annihilations with high momentum electrons, thus it is essentially related to positron annihilations with core electrons. The S and W parameters are extracted from the DBS measurements acquired at energies ranging from 0.2 to 25 keV with step increasing from 0.2 to 1 keV.

In order to assess the annihilation characteristics of the HfO₂ crystalline structure and to identify those due to oxygen vacancy, different deposition techniques have been used. Layers of HfO₂ with thickness ranging from 25 to

500 nm, as measured by spectroscopic ellipsometry, have been deposited on p-type 100-oriented Si substrates (B doped at $\approx 10^{15} \text{ cm}^{-3}$). For thick layers, Physical Vapor Deposition (PVD) technics have been used. The thicker 500 nm film was deposited using e-beam evaporation at 150°C from an HfO₂ target. Plasma sputtering of an Hf target with an Ar/O₂ plasma has been used to deposit layers on 300°C heated substrates with thicknesses ranging from 25 to 100 nm. In addition, Atomic Layer Deposition (ALD) films of 25 and 50 nm, the typical thicknesses used in microelectronics devices, were grown at 300°C, using HfCl₄ and H₂O precursors. After deposition, spike annealing under low N₂ pressure at 900°C has been used to induce either layer densification or oxygen vacancies creation [4, 7]. Figure 1.a and Fig. 1.b show the morphology change induced by the spike annealing in the 500 nm thick layer and reveals a rather inhomogeneous layer.

RESULTS AND DISCUSSION

According to positron implantation profile calculation (p.33 in [12]), the energy range of the DBS measurements allows to probe approximately the first 8 μm in bulk silicon. Below 1 keV, the S and W parameters mainly reflect positron annihilation at the sample surface. Also the FWHM of the implanted positrons distribution increases with the energy from 5 nm at 0.5 keV to reach $\sim 4 \mu\text{m}$ at 25 keV. Thus each point of the S(E) and W(E) curves results from the positron interaction on a quite large depth section of the sample compared to the HfO₂ layer thicknesses. Therefore the extracted curves are not only representative of the HfO₂ material and a complete interpretation of the results should be supported by DBS simulation that should allow evaluating the depth S and W profile. However some valuable information may be extracted from qualitative analysis of the measurements.

Figure 1.c shows the measured S and W curves for the 50 and 500 nm films after spike annealing. For both films S first decreases and W increases quickly up to approximately 1.5 or 3 keV. Then it increases and respectively decreases monotonically towards values very close to the ones reported for annihilation characteristics in the Si lattice [17] when the positron energy becomes higher than 1.5 keV or 6 keV according to the thickness of the HfO₂ layer. This variation is due to the increasing annihilation probability in the Si substrate as the positron beam energy increases. As the thickness of the layers decrease the substrate characteristic value is reached for lower positron energy. For the 500 nm thick film, S and W parameters remain steady in the 1-6 keV energy range, suggesting that these S and W values correspond to annihilation characteristics into the HfO₂. This is consistent with the positron implantation profile calculations which show that 6 keV positrons stopped in the first 500 nm of HfO₂. This observation and the quick S decrease at low energy (from 0.5 to 1.5 keV) indicate that the positron diffusion in the large HfO₂ layer is low and that they annihilate close to the place where they stop. It suggests that a large concentration of defects is detected by positrons in the layer as it can be observed in the SEM image (Fig. 1.b) performed on the cross section of this 500 nm thick film which is very heterogeneous. On the other hand, the sample with the 50 nm thick layer doesn't show any energy range of steady S and W parameters. This result is consistent with the corresponding implantation profiles that show a 1-3 keV range governed by the DBS characteristics of HfO₂. However, the S and W parameters begin to change towards the Si parameters earlier in the energy range suggesting that diffusion and/or an eventual electric field could increase the fraction of positron annihilated in the Si substrate. This observation and the low S and high W values compared to the one obtained in the 500 nm thick layer are consistent and could be related to a better quality of the thin HfO₂ film. These results highlight that even if the ultra-thin HfO₂ layers are difficult to analyze using PAS it is possible to distinguish them and to qualitatively assess their quality. Using thick layers would help to minimize substrate PAS signal and to establish intrinsic bulk PAS properties of HfO₂. Then these properties should be used to extract thin layer properties from DBS measurements using PAS simulation tools.

In Fig. 1.d, S and W curves are plotted for the 50 nm thick PVD as-deposited layer together with curves for the spike annealed one. After annealing, the Si substrate characteristics are more quickly reached in the high energy side of the plot, the low energy range governed by the PAS characteristics of the HfO₂ layer is significantly narrowed and the overall S values increase and the W ones decrease. This latter behavior reflects a rise of the defect concentration in the layer [8, 18, 19]. Moreover, the positron annihilation mechanism may also be affected by the layer internal electric field induced by charged defects created at the HfO₂/Si interface during the annealing. Indeed, according to the simulations of the DBS curves obtained by VEPFIT [20] and shown on Fig. 1.e, for a positive electric field both S(E) and W(E) curves are shifted towards lower energies resulting in the narrowing of the energy range governed by the HfO₂ layer. Positively charged defects present at the HfO₂/Si interface may induce an electrical field which has been measured by electrical characterization [21].

The S and W parameters are compared in Fig. 1.f for samples with 50 nm thick layer deposited by both ALD and PVD. Before annealing, the S(E) and W(E) curves of the ALD layer are very close to those of the annealed PVD layer (Fig.1.c) over the whole energy range. Unexpectedly, this result shows a higher initial defect concentration in ALD than in PVD layers. An explanation could be that the ALD process is usually optimized for nanometer range thicknesses. After annealing, the ALD layer shows an increase of the S values and a decrease of the W ones in the lower energy range as it is observed for the PVD layer. However, the trend is in the opposite direction for the higher energy range with a slower evolution towards the Si substrate DBS parameters. Moreover, the overall shape of the curves is significantly modified and very steady S and W values appear in the 1-5 keV energy range. Complementary structural characterization should be performed to identify the related evolution of the layer material during annealing. However, according to the simulation in Fig. 1.e, we can assess the existence of a negative electric field at the ALD HfO₂/Si interface that induces a shift of the DBS curves towards the high energy range. In contrast with the PVD layers, the annealed ALD layer presents a negative electric field effect, due to negatively charged defects present at the HfO₂/Si interface.

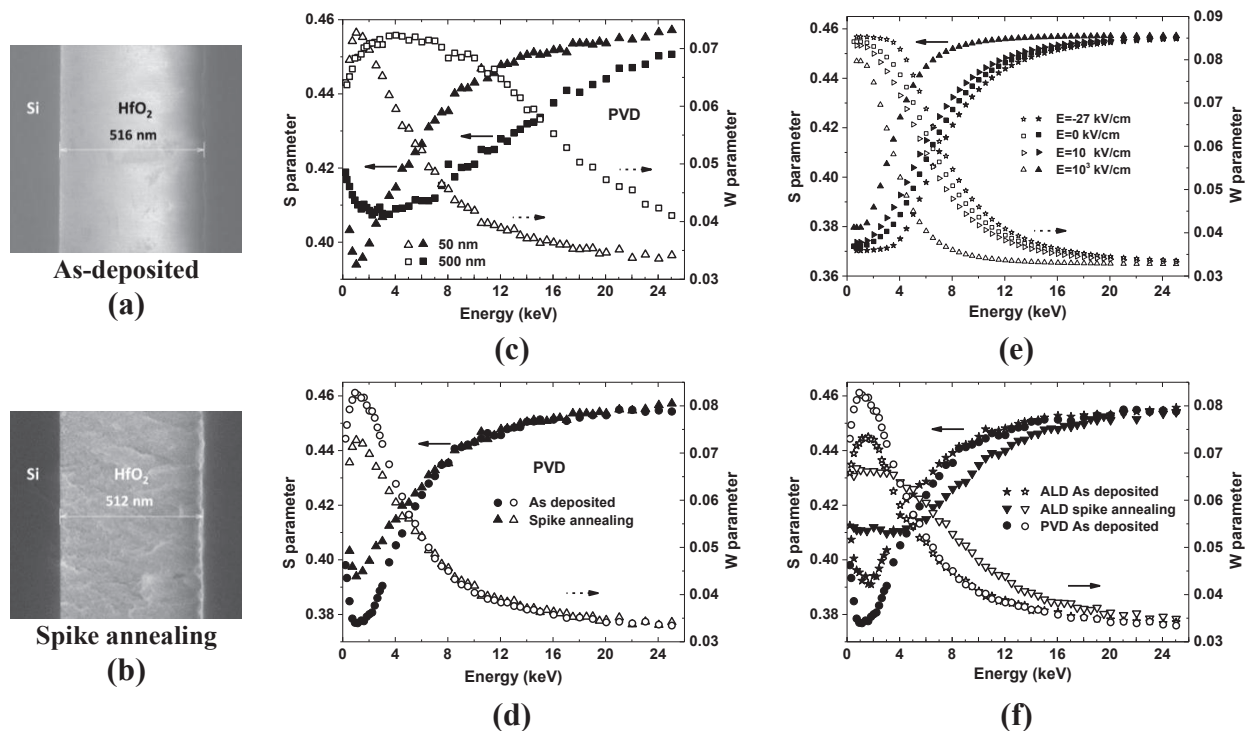


FIGURE 1. SEM observations on the cross-section of a 500 nm thick PVD layer of HfO₂ on Si: (a) as-deposited; (b) spike annealed. S and W parameters as function of incident positron energy measured in HfO₂-on-Si layers (S and W are plotted respectively in full and open symbols); (c) thickness effect for spike annealed PVD layers; (d) annealing effect for 50 nm thick PVD layers; (e) VEPFIT simulation with various electric field levels at the HfO₂/Si interface of 50 nm thick layers (electric field values are typical of the ones observed in HKMG stacks [21]); (f) deposition process effect for 50 nm thick layers.

CONCLUSIONS AND PERSPECTIVES

Doppler broadening measurements performed with a slow positron beam have shown an effective sensitivity to the properties of HfO₂ layers down to a thickness of 50 nm on a silicon substrate. The qualitative analysis of the DBS curves show that the void defect concentration in annealed layers is higher than in the as deposited ones either by ALD or PVD process. In addition, the as deposited ALD material is revealed to include more defects than the PVD one due to the out-of-range thickness for the ALD process. The role of a built-in electrical field related to charged defects at the HfO₂/Si interface is highlighted through simulation of the DBS parameters. It may explain the different behavior between ALD and PVD materials. However, a quantitative analysis based on data reduction using complete DBS simulations is still limited by the lack of the bulk parameters of the HfO₂ material. This requires thick layers of homogeneous properties that may be obtained through controlled long term annealing of

PVD material. Also, to fulfill the nano-electronic specifications, coupling PAS with EELS-TEM analyses is mandatory.

ACKNOWLEDGMENT

This work was supported by the National Research Agency (ANR) through the French "Recherche Technologique de Base" Program. The experiments were performed in the frame of the joint development program with STMicroelectronics and the Nanocharacterisation platform (PFNC) at MINATEC. We warmly thank, P. Hurley, K. Cherkaoui, their team, the Tyndall National Institute (Ireland) for providing the 500 nm HfO₂ layer and A. Roule, H. Grampeix from LETI for providing ALD and PVD deposition.

REFERENCES

1. K. Shiraishi, et al., in: "Proc. of SISPAD", 306–313 (2006).
2. K. Shiraishi, et al., *Thin Solid Films* **508**, 305-310 (2006).
3. S. Guha and V. Narayanan, *Physical Review Letters* **98**, 196101 (2007).
4. A. Kechichian, P. Barboux, and M. Gros-Jean, *ECS Transactions* **58**, 325-338 (2013).
5. J. Robertson, O. Sharia, and A.A. Demkov, *Applied Physics Letters* **91**, 132912 (2007).
6. G. Bersuker, et al., *Journal of Applied Physics* **100**, 094108 (2006).
7. G. Bersuker, et al., *IEEE Transaction on Electron Devices* **57**, 2047-2056 (2010).
8. A. Uedono, et al., *Japanese Journal of Applied Physics* **46**, 3214-3218 (2007).
9. P. Calka, et al., *Nanotechnology* **24**, 085706 (2013).
10. P.E. Lhuillier, et al., *Journal of Nuclear Materials* **416**, 13-17 (2011).
11. P. Desgardin et al., *Applied Surface Science* **252**, 3231–3236 (2006)
12. R. Krause-Rehberg, and H.S. Leipner, *Positron Annihilation in Semiconductors: Defect Studies*, Springer-Verlag, 1999.
13. A. Uedono, et al., *Journal of Applied Physics* **100**, 034509 (2006).
14. D.W. Gidley et al., *Annual Review of Materials Research* **36**, 49-79 (2006).
15. Z.W. Ma et al., *Thin Solid Films* **519**, 6349-6353 (2011).
16. P. Desgardin et al., *Materials Science Forum* **363-365**, 523-526 (2001).
17. H. Kauppinen et al., *Journal of Physics: Condensed Matter* **9**, 10595 (1997).
18. R.S. Brusa et al., *Radiation Physics and Chemistry* **76**, 189-194 (2007)
19. R.S. Yu et al., *Nuclear Instr. and Methods in Phys. Res. Section B: Beam Inter. with Mat. and Atoms* **267**, 3097-3099 (2009)
20. A. Van Veen et al., *AIP Conference Proceedings* **218**, 171-179 (1990)
21. S. Guha et al., *Applied Physics Letters* **90**, 092902 (2007).

KEYWORDS

High-k, HfO₂, Oxygen vacancy, Positron annihilation, Doppler broadening spectroscopy...

Further development of electron tomography

M. Birke; D. Utess; E. Langer; H.-J. Engelmann

GLOBALFOUNDRIES Module One LLC & Co. KG, Center for Complex Analysis, MS E23-MA, D-01109 Dresden, Germany

INTRODUCTION

Both process characterization and development in high performance semiconductor industry require transmission electron microscopy analysis. Due to the shrinkage in feature size, two-dimensional images are more insufficient. Semiconductor components become smaller than the thickness of a lamella. If different features overlap, it will be impossible to resolve them. Moreover, it is not achievable to study the complex three-dimensional geometry of an object in a two-dimensional projection.

ADVANTAGE OF DUAL-AXIS ELECTRON TOMOGRAPHY

To solve the above-mentioned problems, high-angle-annular-dark-field scanning transmission electron microscopy tomography is a well-established method in materials science. But Single-axis electron tomography does not show an adequate resolution and reconstruction artifacts because of the restricted tilting range and the resulting missing wedge. The effect can be limited by using the Dual-axis electron tomography. The advantages of this method will be shown with different examples.

The study examines structures which show mainly an axial spatial extent. To be more exact, typical tungsten contacts used in CMOS technology were analyzed by Single- and Dual-axis electron tomography. First, a lamella was prepared via lift-out. Subsequently, two tilt series were acquired in a tilt range of $\pm 70^\circ$ using the saxton scheme. Thus, the tilt increments between two projections are not the same throughout the tilting range but vary accordingly to the cosine of the current tilt angle. The second dataset was collected after rotating the sample by an angle of 90° . After the registration of both reconstructions, the missing wedge-induced elongation in the z-direction is reduced.

Furthermore, the presentation shows structures with a lateral spatial extent in general. Vertical interconnect accesses (vias) were prepared and examined as mentioned above. The Dual-axis reconstruction displays features of the object, which are missing in the single-axis reconstruction. This shows especially the trench on the right hand side in Figure 1. Moreover, the edges of the vias are sharper in the Dual-axis reconstruction. Consequently, due to the usage of Dual-axis electron tomography, fuzziness is reduced and the gain of information is increased.

Another huge advantage of Dual-axis tomography can be the dramatic reduction of artifacts. These artifacts are very pronounced in semiconductor single-axis tomography samples, because of the high contrast HAADF STEM images. Regions, which consist of elements with a high atomic number, are bright. As a result, the reconstruction of these parts show radial stripes (Figure 2 A). After the registration of the second dataset this artifact disappeared (Figure 2 B).

REALIZATION OF DUAL-AXIS ELECTRON TOMOGRAPHY

The study was performed using the “Advanced Tomography Holder” Model 2020 of Fischione. The acquisition was realized applying a Titan G2 with the corresponding software XPlor3D of FEI. The following processing of the data including the Dual-axis registration was achieved with the computer program Avizo Fire 8.1 of FEI. The

combination in Fourier space was done using the procedure, which was introduced by Mastronade [5]. The algorithm is performed in Fourier space.

After creating the 3D Fourier transform of each dataset, the combination is done. Principally, within the missing wedge there are only information from one tomogram applicable. In this case the available value is taken. In contrast, for every point beyond the missing wedge the mean of the values from the two tomograms is used. That way, a tomogram is generated, which contains the information of both initial datasets. Creating the inverse Fourier transforms results in the final tomogram.

Due to the combination of the two datasets, more points in Fourier transform about the specimen are available. The additional information result in a lower elongation in z-direction as shown by analyzing the contacts and the gain of information as presented on the basis of the vias. Averaging the other points weaken the artifacts because values are minimized, which are only in one dataset. This process is responsible for the better sharpness of contours, too.

SINGLE-AXIS ELECTRON TOMOGRAPHY VS. DUAL-AXIS ELECTRON TOMOGRAPHY

All in all, Dual-axis electron tomography should be used, especially when the three-dimensional metrology of semiconductor components is required, because false values in z-direction are minimized. Moreover, it is useful to inspect contours like the Cu seed barrier of vias more precisely and to receive more exact three-dimensional rendering, due to the fewer artifacts.

Indeed there are some disadvantages, too. The acquisition time for two tilt series lasts longer. On the one hand the effort both for acquisition and reconstruction for the analyst is higher whereby the efficiency is lower. On the other hand an electron beam-induced damage of the specimen is more probable. This injury can cause artifacts in the single tomograms. As a consequence, the Dual-axis registration could not be successful.

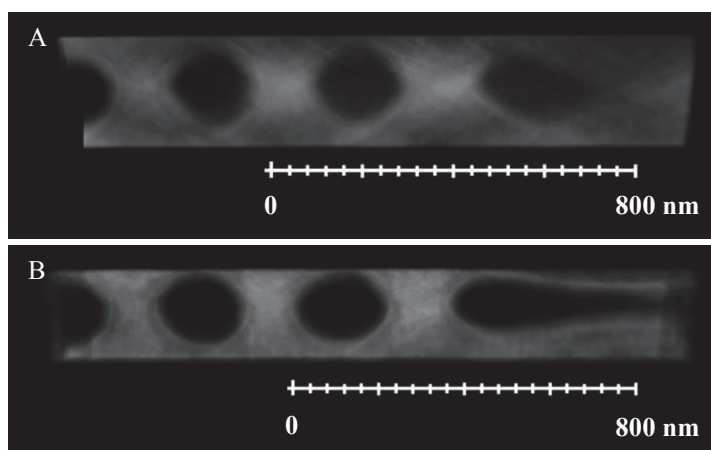


Figure 1: Reconstruction of vias. A) Single-axis electron tomography, B) Dual-axis electron tomography

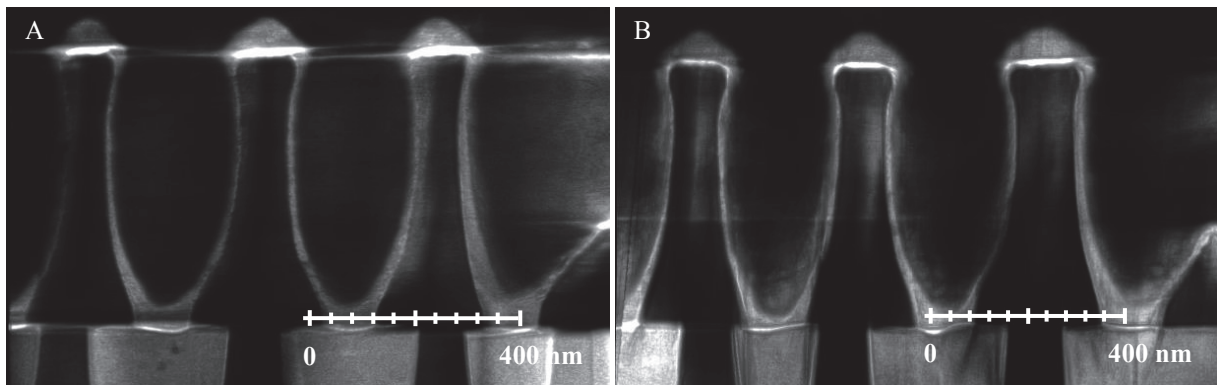


Figure 2: Reconstruction of Vias (after Cu Seed Deposition). A) Single-axis electron tomography, B) Dual-axis electron tomography

REFERENCES

1. S. J. Pennycook, P. D. Nellist and Editors, *Scanning Transmission Electron Microscopy Imaging and Analysis*, New York: Springer-Verlag, 2011.
2. M. Gruska, *Visualisierung zellulärer Strukturen mittels optimierter Methoden der Kryo-Elektronentomographie*, Dresden: Max-Planck-Institut für Biochemie, 2010.
3. J. Thomas and T. Gemming, *Analytische Transmissionselektronenmikroskopie*, Springer-Verlag, Wien 2013
4. R. A. Crowther, D. J. DeRosier, and A. Klug, *The Reconstruction of a Three-Dimensional Structure from Projections and its Application to Electron Microscopy*, *Proceedings of the Royal Society of London*, pp. 319-340, Jun. 1970.
5. D. N. Mastronade, *Dual-Axis Tomography: An Approach with Alignment Methods That Preserve Resolution*, *Journal of Structural Biology*, 1997.
6. M. Birke, *Weiterentwicklung der analytischen tomographischen Transmissionselektronenmikroskopie*, Masterarbeit, Dresden: Hochschule für Technik und Wirtschaft, 2014
7. C. Kübel et al., *Recent Advances in Electron Tomography: TEM and HAADF-STEM Tomography for Materials Science and Semiconductor Applications*, FEI Company, 2005.
8. M. Engstler, *Focused Ion Beam Technik*, Saarbrücken: Universität des Saarlandes, 2010.

KEYWORDS

scanning transmission electron microscopy; double-tilt; dual-axis; electron tomography

Development and Characterisation of Scatterometry Reference Standards

Bernd Bodermann¹⁾, Bernd Loechel²⁾, Frank Scholze¹⁾, Johannes Endres¹⁾, Juergen Probst²⁾, Matthias Wurm¹⁾, Max Schoengen²⁾, Michael Krumrey¹⁾, Sven Burger³⁾, Victor Soltwisch¹⁾

¹⁾ *Physikalisch-Technische Bundesanstalt, Bundesallee 100, 38116 Braunschweig and Abbestraße 2-12, 10587 Berlin, Germany,* ²⁾ *Helmholtz-Zentrum Berlin für Materialien und Energie GmbH, Albert-Einstein-Str. 15, D-12489 Berlin, Germany,* ³⁾ *JCMwave GmbH, Bolivarallee 22, D-14050 Berlin, Germany*

INTRODUCTION

Scatterometry is widely used for dimensional metrology in nanoelectronic manufacturing. However, currently applications are limited to relative measurements for process development and process control due to the lack of traceability [1, 2]. To establish scatterometry as a traceable and absolute metrological method for dimensional measurements and to improve the tool matching with alternative and complementing metrology tools such as CD-SEM or CD-AFM, we have developed suitable high quality calibrated scatterometry reference standard samples. The characterisation of structure details and the grating quality have been performed based on microscopic as well as scatterometric measurements [3]. The final characterisation and calibration of the standard samples will be based on hybrid metrology approaches including different scatterometric methods in the DUV to X-ray spectral range and microscopic measurements. In the following we present main specifications and design aspects of the developed standards and first measurement results obtained by DUV, EUV and X-ray scatterometry.

SCATTEROMETRY REFERENCE STANDARD

Design of the standard samples

The reference standard materials will base either on Si or on Si₃N₄ as a dielectric 'resist mimicking' material. A traceable calibration of these standards will be provided by applying and combining different scatterometric as well as imaging calibration methods. Therefore they are designed such that they are measurable also by microscopic methods (SEM, AFM). GISAXS measurements have proven to show an excellent performance and sensitivity for the characterisation of the grating quality and possible structure details such as line edge or surface roughness [4]. Since GISAXS requires, at least in one dimension, large interaction areas, the design of first test samples contained 1 mm • 15 mm large gratings both along as well as perpendicular to the grating lines and special (5 µm)² microscopy testing areas with reduced line-to-space-ratio of 1:4 for AFM characterisation. Structure details like roughness, edge profiles and side wall angles are characterised systematically mainly by AFM, SEM and by GISAXS measurement and these measurement data will be used as a-priori information in the final hybrid calibration of the reference standard.

Currently the grating dimensions cover a CD range between 25 nm and 100 nm and periods between 50 nm and 250 nm, but have the potential to be extendable to smaller periods well below 50 nm. The structures have design heights between 40 nm and 70 nm and design side wall angles of 90°.

Evaluation and calibration of the standard samples

The performance of the scatterometry standard samples have been tested with different types of scatterometry tools and approaches: polarised goniometric reflectometry at 266 nm with PTB's goniometric DUV scatterometer [5], soft X-ray (EUV-SAS) and Grating Incidence Small Angle X-ray Scatterometry (GISAXS) [6, 7]. Additionally further investigations using spectroscopic Ellipsometry and Mueller Polarimetry are currently performed.

In order to reconstruct the grating profile for all measurements we used a common trapezoidal model including corner rounding and comprising the Si substrate and an effective oxide layer. The reconstruction parameters are the middle CD, height, side wall angle (SWA), top and bottom corner rounding and the oxide layer thickness. The reconstruction was done by rigorous inverse simulation with the time harmonic FEM Maxwell solver *JCMsuite* in combination with both global and local nonlinear optimization routines. For the DUV measurements the refractive indices of the two layers are taken from reflectance measurements at unstructured areas of the sample. With the DUV scatterometer all measurements on the grating area have been carried out with both s- and p-polarized light at 266 nm and for a grating oriented perpendicular as well as along the plane of incidence [8]. Using these four different measurement configurations significantly increased the measurement information. Figure 1 illustrates the measurement configurations and shows the corresponding measurement results for one sample position.

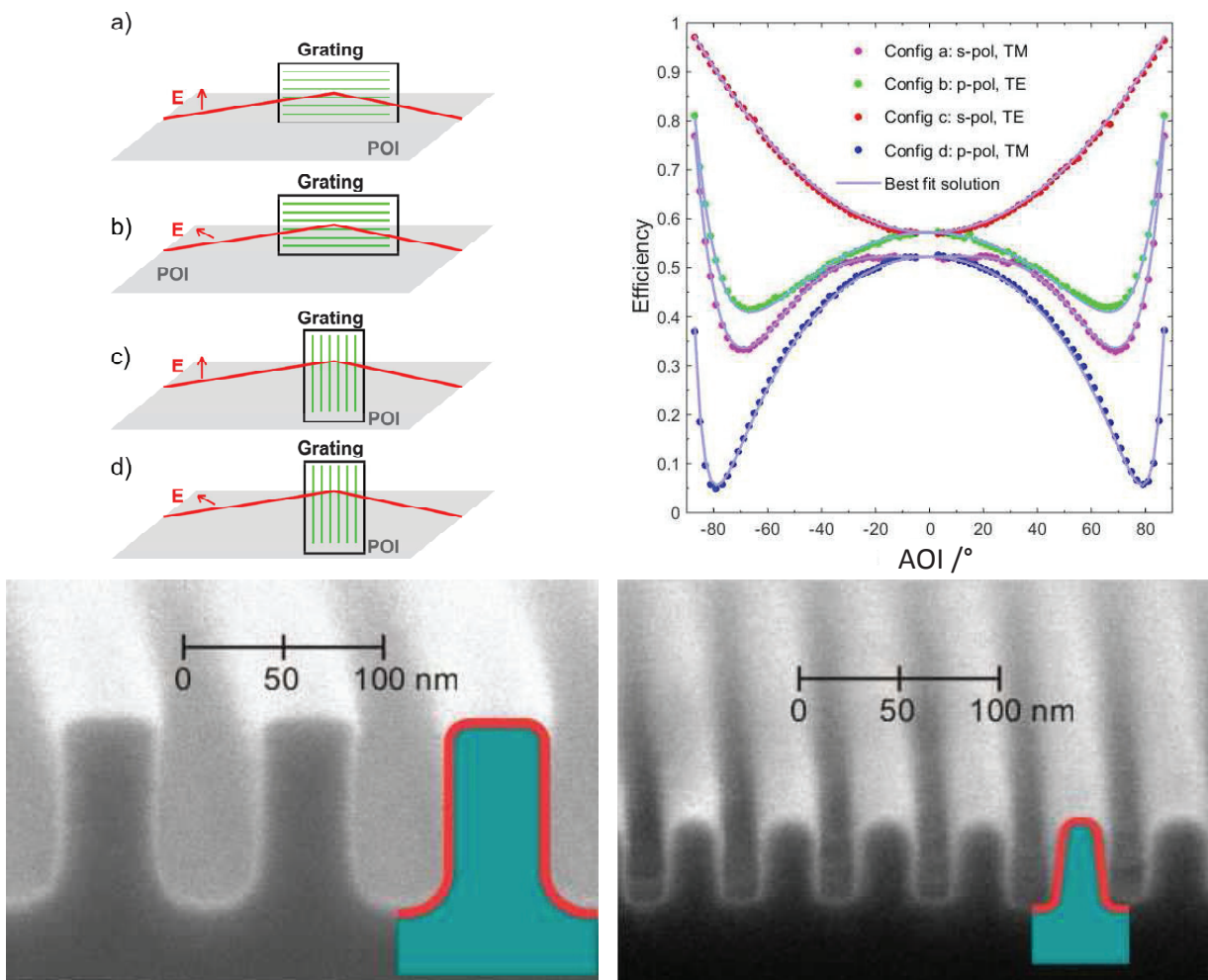


FIGURE 1. DUV (266 nm) reflectance measurements of Si-grating with nominal CD = 55 nm and pitch = 100 nm.

Top left: illustration of the four different measurement configurations. The grating lines and the polarization of the incident light are orientated with respect to the plane of incidence. Top right: measured efficiency versus the AOI for four different measurement configurations (marked by different colours). The solid line shows the reconstruction result for the simultaneous fit to all four data sets. Bottom: comparison of reconstruction results of DUV measurements with cross-section SEM images of nominal identical samples with nominal pitch/CD values of 100/55 nm (left) and 50/25 nm (right).

A quantitative comparison between the resulting reconstruction results and SEM cross section images of nominal identical grating samples (figure 1, bottom) for two different samples show a remarkable agreement even of structure details such as top and bottom corner rounding. Table 1 shows exemplarily a comparison of measurement results for one Si standard sample, as obtained by DUV, EUV and soft X-ray scatterometry. These individual measurements again show an at least reasonable, in many cases already excellent agreement of the significantly different measurement methods.

TABLE 1. Measurement results obtained by DUV, EUV and GISAX scatterometry for Si reference sample with design values CD = 55 nm, period = 100 nm, height = 100 nm and side wall angle (SWA) = 90 °; CR: corner rounding

Method	Si-height / nm	CD / nm	SWA / °	CR _{top} / nm	CR _{bottom} / nm	Oxide-height / nm
DUV	101.2	53.4	90.0	8.0	20.5	5.3
EUV	101.4	55.5	88.2	6.0	16.0	9.3
GISAXS	102.1	55.0	82.9	5.7	14.0	5.3

DISCUSSION AND OUTLOOK

The microscopic and scatterometric characterisations of the Si-samples show a very good performance of the test samples for the realisation of scatterometry reference standards. These will be complemented by currently performed ellipsometric and polarimetric measurements and a full validation of the corresponding Si₃N₄ samples. For the final calibration a hybrid approach combining at least one X-ray and one VIS/DUV measurement supplemented by microscopic measurements will be exploited to ensure the best calibration performance. The final standard design will compromise only one large GISAXS test field to monitor the process and structure quality. These will be supplemented by a grid of customer calibration samples with an array of varying duty cycle (0.25 to 1.1) and CD values and reasonable sized grating sizes of 1 mm² to improve the user applicability. The released duty cycle of 1:4 will enable also AFM measurements on the small CD line structures.

ACKNOWLEDGMENTS

The EMRP is jointly funded by the EMRP participating countries within EURAMET and the European Union. We thank the European commission and the EURAMET e. v. for financial support under the support code No 912/2009/EC within the Joint Research Project IND17 "Scatterometry".

REFERENCES

1. F. Scholze, B. Bodermann, H. Gross, A. Kato, M. Wurm: *First steps towards traceability in scatterometry*, Proc. SPIE **7985**, (2011), 79850G.
2. Heather J. Patrick, Thomas A. Germer, Progress toward traceable nanoscale optical critical dimension metrology for semiconductors, Proc. SPIE **6672**, (2007), 66720L
T. A. Germer, H. J. Patrick, R. M. Silver, B. Bunday: "Developing an Uncertainty Analysis for Optical Scatterometry", Proc. SPIE **7272** (2009), 72720T-1 - 72720T-11
3. B. Bodermann, P.-E. Hansen, S. Burger, M.-A. Henn, H. Gross, M. Bär, F. Scholze, J. Endres, M. Wurm: *First steps towards a scatterometry reference standard*, Proc. SPIE **8466** ((2012)) 84660E-1-8
4. J. Wernecke, F. Scholze, M. Krumrey: *Direct structural characterisation of line gratings with grazing incidence small-angle x-ray scattering*, Rev. Sci. Instrum. **83**, (2012) 103906-103916
5. M. Wurm, S. Bonifer, B. Bodermann, J. Richter: *Deep ultraviolet scatterometer for dimensional characterization of nanostructures: system improvements and test measurements*, Meas. Sci. Technol. **22** (2011), 094024-1 - 094024-9
6. V. Soltwisch, J. Wernecke, A. Haase, J. Probst, M. Schoengen, M. Krumrey, F. Scholze, *Nanometrology on Gratings with GISAXS: FEM Reconstruction and Fourier Analysis* Proc. SPIE **9050**-36 (2014) 9050-36
7. V. Soltwisch, J. Wernecke, A. Haase, J. Probst, M. Schoengen, M. Krumrey, F. Scholze, J. Pomplun, S. Burger: *Determination of line profiles on nano-structured surfaces using EUV and X-ray scattering*, Proc. SPIE **9235**, (2014) 92351D
8. J. Endres, M. Wurm, A. Diener, B. Bodermann, J. Probst: Scatterometric linewidth measurements on subwavelength gratings (to be published)

KEYWORDS

Scatterometry, OCD, reference standard, CD metrology, GISAXS, tool matching, rigorous modelling

Non-conventional structural and chemical characterisations for the industry of nano-electronics

E.Capria^{1,8}, J. Beaucourt², I.Bertrand⁶, N.Bicais³, E.Boller¹, C.Curfs^{4,5},
G.Chahine¹, A.Fitch¹, R.Kluender^{4,5}, T.A.Lafford¹, Y.M.Le-Vaillant⁶, F.Lorut³,
J.S.Micha^{4,7}, E.Mitchell¹, O.Robach^{4,7}, J.C.Royer^{4,5}, T.U.Schüllli¹, J.Segura-Ruiz^{2,8}

1: European Synchrotron Radiation Facility, Grenoble, France; 2: Institute Laue-Langevin, Grenoble, France; 3: ST Microelectronics, France; 4: Univ. Grenoble Alpes, F-38000 Grenoble, France; 5: CEA, LETI, MINATEC Campus, F-38054 Grenoble, France; 6: SOITEC, France; 7: CEA/INAC and CNRS, Grenoble, F-38054, France; 8: IRT NanoElec Advanced Characterisation Platform, Grenoble, France

INTRODUCTION

Large-scale synchrotron and neutron research infrastructures offer unrivalled performance for the advanced characterisation of micro- and nano-electronic devices and systems. Examples include X-ray spectroscopy to study RRAM switching mechanisms, grazing incidence X-ray scattering and neutron reflectivity for structural data on materials for interconnections, hard X-ray PES to understand electronic properties of layered materials, and nano- and micro-X-ray-tomography for unprecedented non-destructive 3D imaging of packaging, vias, etc.

There is an increasing realisation worldwide that large-scale research infrastructures are a key component, not only of academic and fundamental research, but also of the innovation cycle and industrial research and development. However, working with industry has its own special requirements, and can bring to the fore mismatches and clashes between a traditional academic culture and the needs of the market driven commercial world: research infrastructures are often based on an academic *modus operandi* which can limit their industrial impact.

A CHARACTERISATION PLATFORM FULLY DEDICATED TO THE MICRO- AND NANO-ELECTRONICS INDUSTRY

The IRT Nanoelec, a technological research institute for nanoelectronics, was founded in April 2012 through a joint venture between the French National Research Agency (ANR) and the French Atomic and Alternative Energy Commission (CEA). This public-private partnership comprises 17 public- and private-sector research partners - including the European research infrastructures European Synchrotron Radiation Facility (ESRF) and Institut Laue Langevin (ILL) which provide world-leading synchrotron light and neutron facilities for both academic and industrial communities. The IRT NanoElec research will be focused on a core technology programme encompassing 3D assembly integration, nanophotonics on silicon and via technologies, supported by technological infrastructure including a Micro- and Nano-Electronics Characterisation Platform.

This platform, being created as a pathfinder project, will largely enhance the effectiveness and attractiveness of the Grenoble-based neutron and synchrotron light source facilities for European micro and nano-technological research.

The NanoElec funding will provide staff to support electronics research at ESRF and ILL, as well as complementary facilities at the CEA Platform for Nano-Characterisation (PFNC) such as SEM, TEM and FIB. Off-line sample preparation facilities and complete characterisation processes from industry device to on-line experiment design and performance with data analysis will be made available as the large-scale facilities and industry learn how to work together. The experience gained and platform facilities will be available for European and international companies, as will opportunities for training in the synchrotron and neutron techniques

Preliminary experiments and industry tailored instruments

In order to demonstrate the relevance of the characterisation offered by the synchrotron x-ray radiation and the neutrons for the nano-electronics industry, an overview of a first set of industrial case studies will be presented. The following techniques will be presented: a) micro/nano-tomography analysis carried out on 3D structures, b) scanning nano-focused diffraction mapping on SOI substrates, c) powder and Laue diffraction on polysilicon thin films, d) identification of dislocations and crystalline defects via X-ray diffraction imaging (XRDI) on deep trench patterns on silicon wafers, d) study of delamination of silicon oxide on amorphous carbon by neutron and X-ray reflection analysis. Furthermore, a description of two new industry-tailored facilities at the ESRF will be provided: a) a high throughput nano-tomography imaging installation, b) a multi-use-multi-technique beamline dedicated to XRD-based techniques.

Particular emphasis will be given to the opportunities, limitations and viability of neutron and synchrotron X-ray characterisation, putting them in the economic context, driven by industrial needs and the value added to the products throughout their value chain. Finally, the opportunities for future developments, coherent with the electronics technology roadmaps and current main trends, will be given.

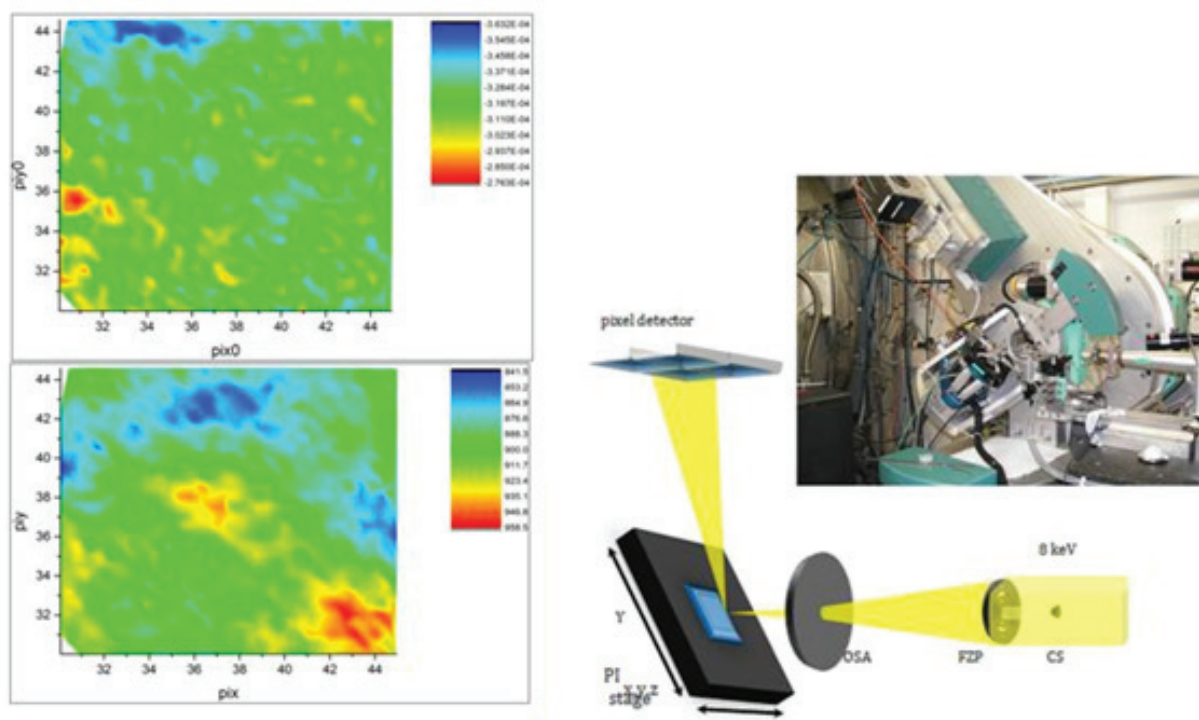


FIGURE 1. Main results and experimental setup for a scanning diffraction microscopy experiment

KEYWORDS

X-ray, synchrotron, neutron, characterization, industry, 3D integration, tomography, residual strain.

Nanostructure Imaging on Plasmonic Gratings by Epi-fluorescence Microscopy

B. Chen ^a, S. Bok ^a, S. Pathan ^a, D. Suresh ^b, A. Upendran ^c, R. Kannan ^d, C. Mathai ^a, K. Gangopadhyay ^{a,e}, and S. Gangopadhyay ^{a,*}

^a Department of Electrical and Computer Engineering, University of Missouri, Columbia, MO 65211, USA

^b Department of Bioengineering, University of Missouri, Columbia, MO 65211, USA

^c School of Medicine, University of Missouri, Columbia, MO 65211, USA

^d Department of Radiology and Biological Engineering, University of Missouri, Columbia, MO 65211, USA

^e Nanos Technologies LLC, 8650 Westlake Road, Columbia, MO 65202, USA

INTRODUCTION

Nanoscale optical imaging technologies are pivotal for the development of cell biology, chemical analysis, nanoelectronic, and nano-optic devices, particularly for monitoring dynamic changes. Overcoming the optical resolution limit, advanced super-resolution techniques rely on either tailored illumination, nonlinear fluorophore responses, or the precise localization of single molecules, such as confocal laser scanning microscopy (CLSM), near-field scanning optical microscopy (SNOM/NSOM), total internal reflection fluorescence (TIRF) and stimulated emission depletion (STED) microscopy.^{1,2} However, most of these approaches are costly, sophisticated, and demanding. Grating-based surface plasmon resonance (SPR) is a promising method to improve the nanoscale imaging capabilities through enhancing the interaction between the incident light and the metallic nanostructures.³ The light harvesting efficiency of the extant plasmonic gratings can be further enhanced by nano-singularities that concentrate EM fields atop the grating structures. Our previous work shows that the integration of plasmonic gratings and random nanogaps provides fluorescence enhancement exceeding 100-fold with respect to glass as well as visualization of nanogaps in bright field images.⁴ Such high enhancement may be sufficient to enable nanostructure imaging using less complex and less expensive epi-fluorescence microscopes. In this work, we utilized cost-effective silver plasmonic gratings as platforms for imaging various shapes of silver nanoparticles including nanoprisms, nanorods, and cubical nanocages using an epi-fluorescence microscope (as shown in Fig. 1a-b). Finite-difference time-domain (FDTD) simulation was used to study the fundamental science for nanoparticles imaging on this platform.

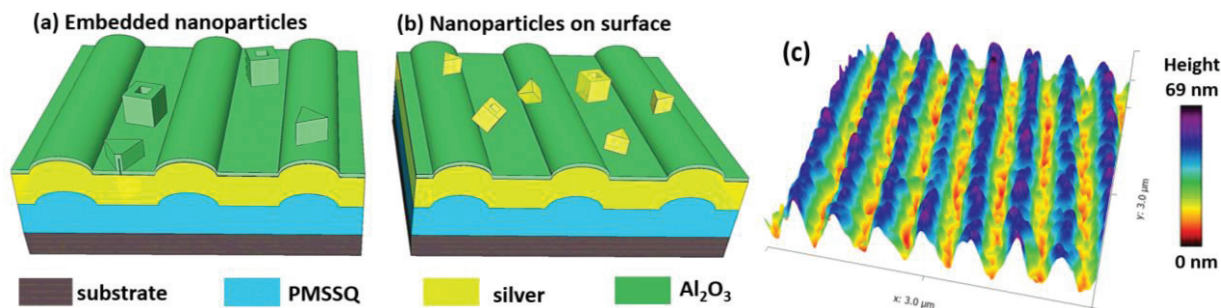


FIGURE 1. Schematic of Nanoparticles (Nanoprisms and Cubical Nanocages) on Silver Plasmonic Gratings Platform for Imaging: (a) embedded in gratings, (b) on the surface of gratings; (c) AFM 3D profile for thermal deposited silver gratings with 10 nm capping layer, the length and width is 3 μm .

METHODS

The silver plasmonic gratings were fabricated using nano-imprint lithography from commercially available HD DVDs as described previously.⁴⁻⁶ A 5 nm chromium adhesion layer and a 100 nm silver layer was deposited on poly-(methylsilsequioxane) (PMSSQ) gratings by thermal evaporator, followed by a 10 nm alumina capping layer by atomic layer deposition (ALD). Fig. 1c shows atomic force microscope (AFM) image for silver gratings with 400 nm grating period. Silver nanoparticles with different shapes were embedded in or deposited onto silver gratings to investigate the images by an epi-fluorescence microscope (Olympus BX51W1). The nanoparticles synthesized in size of 60~100 nm⁷, were prepared in DI water by propylene ethylene glycol (PEG) as a stabilizer to prevent aggregation. For bright field images, nanoparticles were spin-coated on silver gratings at 3000 rpm for 30 seconds to make nanoparticles on the surface of plasmonic gratings. The nanoparticle embedded gratings were prepared using a similar procedure by first spin-coating the nanoparticles on PMSSQ gratings followed by silver deposition.

RESULTS AND DISSUSION

The bright field images of both nanoparticles embedded (Fig. 2a, c) and on (Fig. 2e, g) plasmonic gratings show low-intensity regions with shapes of cubical nanocages (Fig. 2a, e) and nanoprisms (Fig. 2c, g), due to non-radiative dissipation of energy within the metal⁸. Notably, the actual size of these nanoparticles is less than 100 nm which is generally not possible to be visualized with an epi-fluorescence microscope. However, this realization of imaging the shapes of nanostructures is attributed to the fact nanoparticles can concentrate the incident light coupled by gratings, resulting in highly localized E-field. The difference between the actual size and imaged size (Fig. b, d, f, h) for nanoparticles is probably due to scattering and the photons near nanoparticles being absorbed as well. The real size can be achieved by deconvolution using computational post-processing. Additionally, owing to the incident photon coupled by silver plasmonic gratings, the gratings period can be visualized clearly to be 400 nm by an epi-fluorescence microscope (for example, in Fig. 2e, g), which is confirmed by AFM.

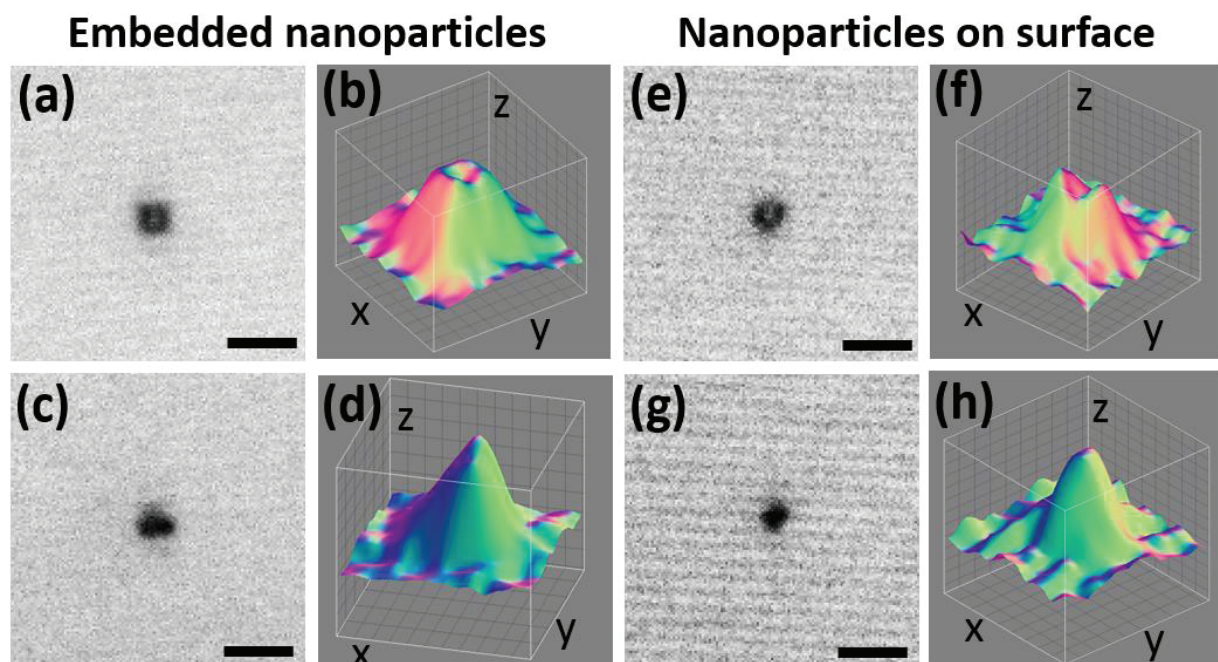


FIGURE 2. Bright Field Images for Nanoparticles Embedded (a-d) and on (e-j) Silver Gratings. (a) (c) (e) (g) Bright field image; (b) (d) (f) (h) Corresponding intensity 3D profile: the smallest gray lattice is 200 nm in length on x-y plane, and z axis is inverted intensity. All images were taken with 60 \times water-immersion objective. The scale bar is 2 μ m.

Quantitation of the morphology-mediated plasmonic-enhanced E-field strength is fundamental to understanding the associated nanoparticles imaging. Fig. 3a shows the FDTD simulation profile for silver plasmonic gratings with a nanoprism on the surface in an air environment. Considering that grating-based SPR is an angle-dependent

phenomenon, E-field (E_z) is investigated under 0° incident angle and the SPR angle for 532 nm excitation in this case. At 0° incident angle, light is weakly coupled by gratings (Fig. 3b), while E_z is mainly concentrated on the nanoprism, and the highest E_z is located on the top of nanoprism surface (Fig. 3c). At SPR angle, plasmonic gratings couple incident photons on the surface to create an evanescent field (Fig. 3d), and enhance E_z around the nanoprism compared to that at normal incidence. The highest E_z appears at the point where the nanoprism discontinues the propagation of surface plasmon, leading to highly localized E_z at 35 nm away from the top of the nanoprism surface (Fig. 3h). The difference of both E_z value and distribution at different vertical positions (Fig. 3e-i) is prospected to improve the resolution in the axial direction when utilizing this plasmonic grating platform for nanoscale imaging.

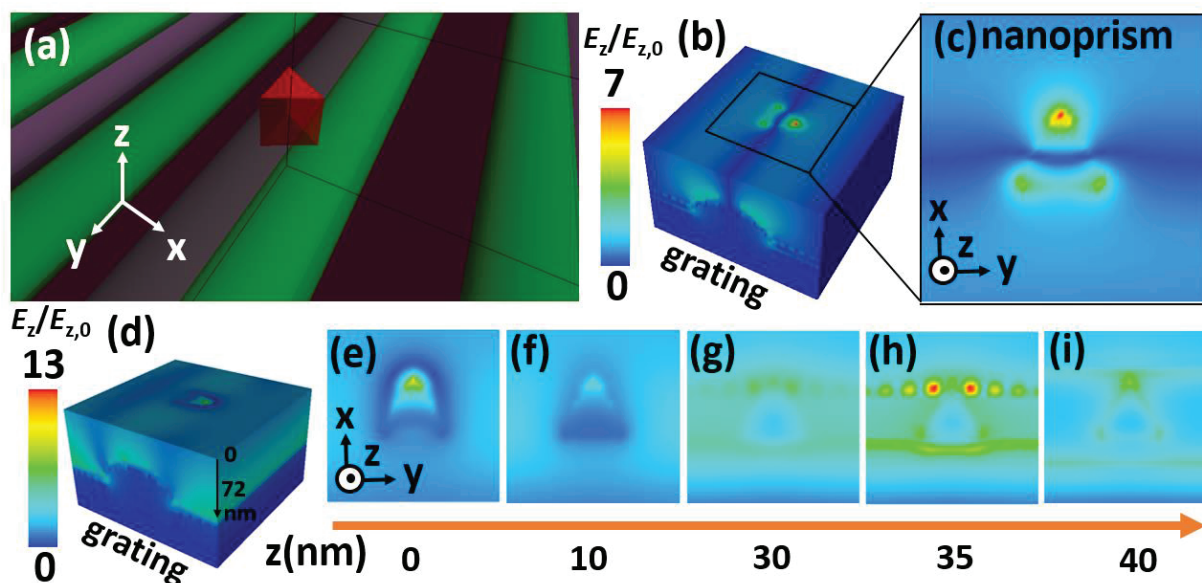


FIGURE 3. 3D FDTD Simulation for Nanoprisms on Plasmonic Gratings: (a) Simulation profile; 0° incident angle (b) 3D E_z distribution for one period of gratings with a nanoprism on the surface, and (c) E_z distribution on x-y plane to show the nanoprism; SPR incident angle (12.2°) (d) 3D E_z distribution, and (e-i) E_z distribution on x-y plane at different vertical positions from 0 to 40 nm away from the top of nanoprism surface.

REFERENCES

1. L. Schermelleh, R. Heintzmann, and H. Leonhardt, *J. Cell Biol.* **190**, 165–75 (2010).
2. T. Ha, *Nat. Methods* **11**, 1015–1018 (2014).
3. J. a Schuller, E.S. Barnard, W. Cai, Y.C. Jun, J.S. White, and M.L. Brongersma, *Nat. Mater.* **9**, 193–204 (2010).
4. K. Bhatnagar, A. Pathak, D. Menke, P. V Cornish, and K. Gangopadhyay, V. Korampally and S. Gangopadhyay, *Nanotechnology* **23**, 495201 (2012).
5. C.M. Darr, V. Korampally, B. Chen, K. Gangopadhyay, and S. Gangopadhyay, *Sensors Actuators B Chem.* **202**, 1088–1096 (2014).
6. B. Chen, C.J. Mathai, S. Mukherjee, and S. Gangopadhyay, *ECS Trans.* **61**, 69–82 (2014).
7. D. Suresh, A. Zambre, and N. Chanda, T. J. Hoffman, C. J. Smith, J. D. Robertson, and R. Kannan, *Bioconjug. Chem.* **25**, 1565-1579 (2014).
8. J.R. Lakowicz, *Anal. Biochem.* **337**, 171–94 (2005).

KEYWORDS

Nanostructures, plasmonic gratings, epi-fluorescence microscopy, nanoscale imaging

Quantifying Ellipsometric Precision for Multichannel Rotating-Element Spectroscopic Ellipsometers

Yong Jai Cho, Won Chegal, Jeong Pyo Lee, and Hyun Mo Cho

*Division of Industrial Metrology, Korea Research Institute of Standards and Science,
267 Gajeong-ro, Yuseong-gu, Daejeon 305-340, Republic of Korea*

INTRODUCTION

Various types of multichannel rotating-element spectroscopic ellipsometers (RE-SEs) have been widely used in semiconductor manufacturing processes since these devices provide high-precision, real-time, non-destructive, non-contact measurements. In this context, the current fabrication of complex 3D nano-patterned atomic-layer-thickness requires corresponding improvements in ellipsometry precision measurement [1].

From a study of earlier works, there appears to be no generally accepted method for characterizing RE-SE measuring uncertainty [2]. Aspnes's quantitative theoretical derivations [3] to determine the optimizing precision for RE-SEs is inapplicable to the measurement-uncertainty evaluation of state-of-the-art multichannel RE-SEs using an integrating photodetector. Johs and Herzinger suggest the impossibility of fabricating a reference sample with the ideal ellipsometric values being known to a level comparable with the ellipsometric precision. They propose a substrate-independent method for quantifying measurement uncertainty based on bulk-sample dielectric function [4]. However, their method requires variable-angle-of-incidence data while most industrial RE-SEs operate with a fixed incidence angle.

Here, we primarily focus on measuring precision among the evaluation processes of measurement uncertainty to determine the actual measurement limits. We first introduce a general theory for the data reduction process (involving extraction of ellipsometric sample parameters from the Fourier coefficients) to derive the theoretical expressions for the standard deviations of the ellipsometric sample parameters. Using a new Fourier analysis algorithm [5], we derive the analytic functions for quantifying the covariance between the Fourier coefficients extracted from a detected irradiance waveform. Finally, we compare the obtained functions with the experimental data.

ANALYTIC EXPRESSIONS OF ELLIPSOMETRIC PRECISION

In the general ellipsometric configurations, the collimated light beam irradiated from the light source passes through the polarization state generator (PSG), is reflected from (or transmitted through) the sample, passes through the polarization state analyzer (PSA) to impinge the photodetector element, which transforms the detected irradiance into electrical signals. The rotatable elements of the polarizers, analyzers, and compensators used in the RE-SEs are appropriately positioned at the PSG and the PSA depending on the optical configurations of the various types of RE-SE. At least one of the rotatable elements must rotate with a constant angular frequency and the others positioned at fixed azimuthal angles selected for a measurement. Therefore, the measured irradiance waveform can be represented by the Fourier series which are the functions of the azimuthal angle of the constantly rotating element.

By the Stokes representations, the Fourier coefficients of the detected irradiance waveform can be represented as the system of non-homogeneous linear equations for the entries of the Mueller matrix $\mathbf{M}^{(SP)}$ of the sample and expressed as $\mathbf{X} = \mathbf{\Omega}\mathbf{V}^{(SP)}$ where \mathbf{X} is a vector of which the entries are the nonzero Fourier coefficients, $\mathbf{V}^{(SP)}$ a vector with the entries of $\mathbf{M}^{(SP)}$, and $\mathbf{\Omega}$ the coefficient matrix. If $\mathbf{\Omega}$ is not singular the vector of the ellipsometric

sample parameters can be obtained as $\mathbf{V}^{(\text{SP})} = (\mathbf{\Omega}^T \mathbf{\Omega})^{-1} \mathbf{\Omega}^T \mathbf{X}$. If $Q(\mathbf{X})$ is one of the ellipsometric sample parameters, its standard deviation is given by

$$\sigma(\langle Q \rangle) = \left[\sum_{j=1}^{2N_{\text{ho}}+1} c_{Q,X_j}^2 \text{cov}(\langle X_j \rangle, \langle X_j \rangle) + 2 \sum_{j=1}^{2N_{\text{ho}}} \sum_{k=j+1}^{2N_{\text{ho}}+1} c_{Q,X_j} c_{Q,X_k} \text{cov}(\langle X_j \rangle, \langle X_k \rangle) \right]^{1/2}, \quad (1)$$

where $c_{Q,X_j} = \partial Q / \partial X_j$ represents the sensitivity coefficients, $\text{cov}(\langle X_j \rangle, \langle X_k \rangle)$ the covariance between the Fourier coefficients, and the angle bracket denotes the sample mean. We can calculate the values of the Fourier coefficients and the sensitivity coefficients for a sample with known optical properties. However, theoretical expressions of $\sigma(\langle Q \rangle)$ require the analytic functions for the covariance, which have not previously been calculated in general.

PRECISION LIMIT DUE TO PHOTON NOISES

In actual multichannel RE-SEs, there are temporal random noises due to stochastic fluctuations in the exposures measured during a given integration time by a pixel or binning pixel group in the CCD or photodiode arrays. It is well-known that the random noises of the exposures measured by a CCD or photodiode array originate from three primary sources: photon noise, dark noise, and read noise. Photon noise is associated with stochastically counting the number of photons that impinge the photodetector element during a given integration time. For RE-SEs, it is to be noted that the measurement conditions have to be set up to increase the signal-to-noise ratio (SNR) to as large an extent as possible for high-precision measurement. As the light irradiance is increased to obtain higher SNR, the photon noise correspondingly increases but the relative effects of the dark and read noises decreases. Therefore, we can ignore the dark and read noises in comparison with the dominant photon noise under the commonly used RE-SE measurement conditions. We term this measurement condition as the photon-noise-limited condition. Although additional temporal random noises in measuring the exposures can originate due to light-source instability, variation of the background photon flux, and speed ripple of the rotating element, these types of noise can be ignored as regards high-performance RE-SEs. It is well-known that photon noise follows the Poisson distribution, wherein the variance of the number of the photons detected by a photodetector element is equal to its mean. Therefore, under the photon-noise-limited condition, the population variance of the exposures S_j measured during a given integration time can be given as $\sigma^2(S_j) \cong \eta S_j$ where η is the scaling factor. Since the exposures measured in one integration time are not correlated with the other exposures in previous or subsequent integration times, i.e., $\text{cov}(S_j, S_k) = \sigma^2(S_j) \delta_{jk}$ where δ_{jk} denotes the Kronecker delta, we can obtain the unbiased sample covariances for the sample means of the Fourier coefficients extracted from a detected irradiance waveform using the new closed-form Fourier analysis. Finally, we can obtain stochastic model functions to describe the characteristics of the random error propagation processes from the measured exposures to the Fourier coefficients and subsequently from the Fourier coefficients to the ellipsometric sample parameters through the data reduction process [6].

To access the reliability of the derived stochastic model functions, we adopt a bare Si wafer as a sample, and a home-made multichannel rotating-polarizer spectroscopic ellipsometer based on a three-polarizer design [7]. The spectroscopic ellipsometer is composed of a light source, a fixed polarizer, a constantly rotating polarizer, a sample, a fixed analyzer, and a spectrometer. In our trials, each spectrum of the Fourier coefficients for the sample at angle of incidence $\phi = 70^\circ$ was measured at multiple azimuthal angles of the fixed analyzer from 0° to 358° in steps of 2° for the wavelength range of 245 nm~1000 nm. In the measurements, the fixed polarizer was positioned at 18.23° . The experimental data of the unbiased sample standard deviations and the correlation coefficients for the Fourier coefficients were measured. In the next phase, the unknown system parameters have to be firstly determined from the measured data. Consequently, the calculated data of the Fourier coefficients are closely agree with the corresponding experimental data. Using the calculated Fourier coefficients, we obtained the theoretical covariance values, which also closely agreed with the corresponding experimental data. We remark here that the ellipsometric sample parameters of N_{SP} and C_{SP} can be derived as the functions of the five Fourier coefficients, and subsequently, their sensitivity coefficient functions can be obtained from the derivatives of the sample parameter functions with respect

to the Fourier coefficients. Consequently, by substituting the sensitivity coefficient, standard deviation, and correlation coefficient functions into Eq. (1), we obtained the theoretical standard deviations of N_{SP} and C_{SP} as shown in Fig. 1. These analytic expressions exhibit excellent agreement with their corresponding experimental data.

In conclusions, the derived statistical functions for the ellipsometric sample parameters very reliably represent the corresponding experimental data measured by using a multichannel rotating-polarizer spectroscopic ellipsometer based on a three-polarizer design. For this instrument, the values of the system parameters can be determined from the sets of the experimental data measured at the multiple azimuth angles of the fixed polarizer and the fixed analyzer. Thus, we can theoretically calculate the variance values of the ellipsometric sample parameters induced by changing the azimuthal angles of the fixed elements and use them for determining the measurement limit.

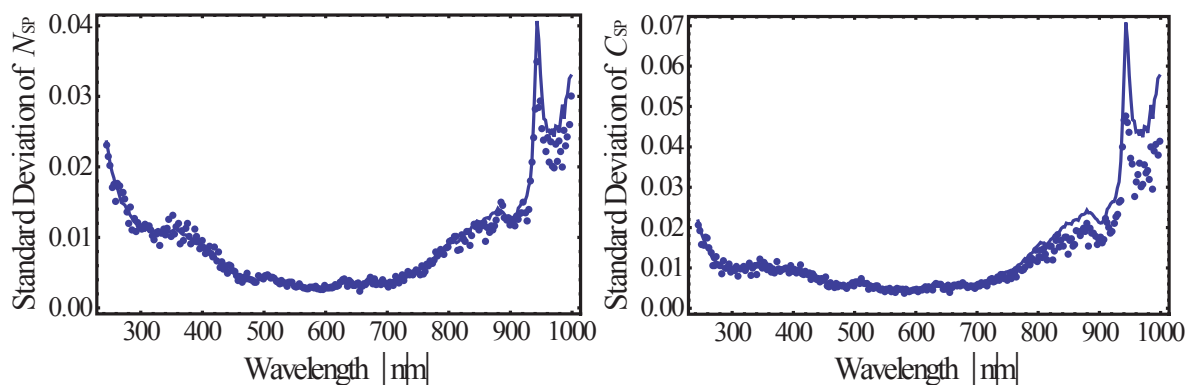


FIGURE 1. The simulated (lines) and measured (dots) spectra of the ellipsometric sample parameters, N_{SP} and C_{SP} , for the native oxide film grown on a c-Si wafer using the home-made RTSE.

REFERENCES

1. S. Zollner, in *Ellipsometry at the Nanoscale*, edited by M. Losurdo and K. Hingerl, Berlin: Springer, 2013.
2. M. Losurdo, *Thin Solid Films* **519**, 2575 (2011).
3. D. E. Aspnes, *J. Opt. Soc. Am. A* **21**, 403 (2004).
4. B. Johs and C. M. Herzinger, *Phys. Stat. Sol. C* **5**, 1031 (2008).
5. Y. J. Cho, W. Chegal, and H. M. Cho, *Opt. Lett.* **36**, 118 (2011).
6. Y. J. Cho, W. Chegal, J. P. Lee, and H. M. Cho, unpublished.
7. W. Chegal, J. P. Lee, H. M. Cho, S. W. Han, and Y. J. Cho, *J. Opt. Soc. Am. A* **30**, 1310 (2013).

KEYWORDS

Ellipsometers, Fourier analysis, inversion problem, measurement and error theory.

Sub-10 nm-thick-carbon nanotube tip for AFM

J. Choi^{1,2}, K. Y. Jung³, S. K. Kanth^{1,4}, B. C. Park^{1*}, H. S. Kim⁴, L. Joon²

¹*Korea Research Institute of Standards and Science, Daejeon 305-340, South Korea*

²*Chungnam National University, Daejeon 305-764, South Korea*

³*Nanofocus Inc., Seoul 152-050, South Korea*

⁴*Sunmoon University, Asan 336-708, South Korea*

**bcpark@kriss.re.kr*

INTRODUCTION

Atomic force microscopy (AFM) is a powerful tool for dimensional metrology at the nanometer scale, and linewidth metrology in the semiconductor industry is one of the most important applications. While ITRS dictates more and more aggressive application of AFM to 3D nano structures, in some cases, the high aspect ratio tips cannot even enter the narrow trenches, beyond the region where we can at least estimate the tip-induced artifact. The limitations come from not only geometrical considerations but also tip-sample interactions at the vertical sidewall. Researches are necessary obviously in both the tip control and tip itself. As to the tips, carbon nanotube (CNT) has been regarded as one of the ideal tips, and several companies already sell the multi-walled nanotube (MWNT) tips. MWNT are thicker than 10 nm, becoming too large for the future devices. In this work, the double walled carbon nanotube (DWNT) tip was fabricated and employed in AFM to study the behavior at the vertical sidewalls.

FABRICATION OF CARBON NANOTUBE TIP

CNT tip was made using the manipulation method, which, at present, is considered to produce the more accurately oriented/length-controlled CNT tips compared to CVD method. With the attocube-based manipulator installed in an SEM, a CNT is mounted on the FIB-milled rear surface of the pyramidal silicon mother tip, being cut using electron beam, and then is glued using electron beam deposited hydro-carbon-platinum. CNT used for AFM tip fabrication so far in the lab is MWNT having the diameter of 14 nm. For sub-10 nm CNT tip, we used double-walled nanotubes from NANOCYL (model NC2100). Fabrication procedure of DWNT tip is the same in principle, but technically has advantages and disadvantages over MWNT tip. DWNT looks thinner and darker on the SEM live images. The carbon deposition needs to be more tightly controlled. The DWNT tip should be shorter which necessitates more precise CNT cutting. Its flexibility makes the manipulation more challenging. To address this, the attocube controller was changed from digital to analog model for more smooth manipulation. In contrast, being thinner, DWNT is much easier to cut. Figure 1 shows the fabricated DWNT tip. The CNT direction is perfect from both the rear side view directions, while the tip length is 183 nm.

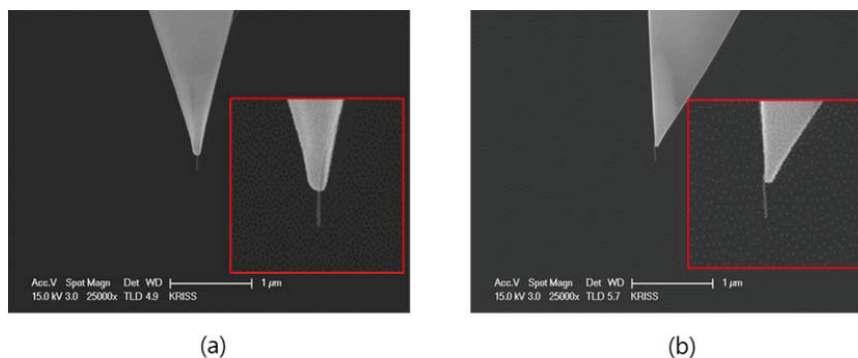


FIGURE 1. SEM pictures of the made double-walled carbon nanotube tip taken in rear view (a) and side view (b), respectively. The area around the nanotube tip is digitally magnified for display in red-line enveloped insets.

MEASUREMENT AND RESULTS

Silicon dioxide grating on flat silicon substrate has been measured with the fabricated DWNT tip in commercial atomic force microscope having an adaptive scan mode (Autoshot, Nanofocus). For comparison, a commercial high aspect ratio tip (MSS-FMR, Nanotools) was also employed to measure the same sample. The grating sample (see Figure 2) has nominally the period of 220 nm, the height of 200 nm, and the linewidth of 50 nm.

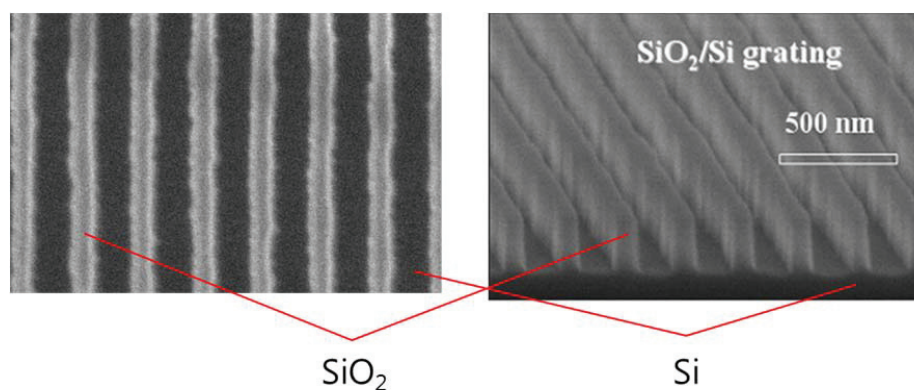


FIGURE 2. Top view (left) and perspective view (right) SEM pictures of the sample used for AFM imaging with CNT tip.

Figure 3 top shows the resultant AFM images obtained with DWNT and MSS-FMR tip, respectively. In the bottom each line profile represents a selected trace in the image. From the profile, we clearly see that DWNT tip successfully scans the sample, even inside the nominally 180 nm-wide and 200 nm-deep trench, except at the proximity of the sidewall where the tip chatters. We note that MSS-FMR also chatters at the sidewall but less than DWNT tip so that the resultant image of the sidewall is more stable with the smaller apparent linewidth. It may be attributed to the fact that MSS is tapered, being thicker at the level of the top surface of the sample, as well as the radius of the tip end (~ 2 nm) is smaller than DWNT. We found out that DWNT tip-producing image did not change over the repeated scan during a day, which means DWNT hardly wears out, while MSS-FMR was not so strong against tip wear.

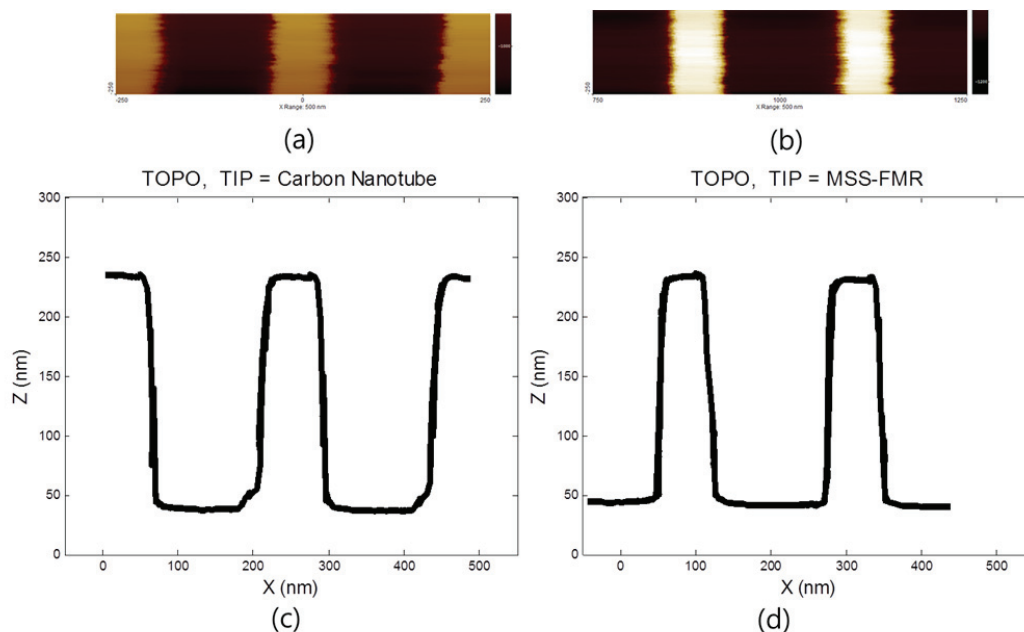


FIGURE 3. Top view AFM pictures of the grating sample obtained with CNT tip (a) and MSS-FMR. (c) and (d) are line profiles corresponding to (a) and (b), respectively. For the easier comparison, the profile lines are made thick to mask the sidewall chatter.

CONCLUSION

Double-walled nanotube tip for AFM was fabricated using nano-manipulation in SEM, and then the rectangular grating sample was measured with the made tip. The sample was also measured with a commercial high aspect ratio tip and compared. With adaptive scan mode, we obtained reasonable and promising results. More improvement is expected by the further optimization of the tip control as well as tip fabrication. We plan TEM analysis and the mechanical test for the fabricated tip.

REFERENCES

1. International Technology Roadmap for Semiconductors 2013 Edition
2. Johann Foucher, Pavel Filippov, Christian Penzkofer, Bernd Irmer, Sebastian W. Schmidt, Proc. of SPIE. **8681**, 651819 (2013).
3. R. Dixon, et al., *J. Micro/Nanolith. MEMS MOEMS* **11** (1), 011006, (2012).
4. N. G. Orji and R. Dixon, *Meas. Sci. Technol.* **18**, 448-455 (2007).
5. B. C. Park, J. Choi, S. J. Ahn, D-H Kim, J. Lyou, R. Dixon, N. G. Orji, J. Fu, and T. V. Vorburger, Proc. of SPIE. **6518**, 86811 (2007).
6. B. C. Park, J. Kang, K. Y. Chung, W. Y. Song, B.-h. O, T. B. Eom, Proc. of SPIE. **5038**, 935 (2003).

KEYWORDS

Critical dimensional metrology, critical dimensional atomic force microscope, carbon nanotube tip, sidewall chatter

300mm and 450mm Standard Calibration Wafers - A Standard Tool for Semiconductor Metrology Calibration and Matching

Rand Cottle¹, Menachem Shoval², Yuval Agami², Frank Tolic³, Stephen Bennett³,
Martin Rodgers³

¹ *Global 450mm Consortium
Colleges of Nanoscale Science and Engineering at SUNY Polytechnic Institute
257 Fuller Road
Albany, NY 12203*

² *Metro450 Consortium
Office of Chief Science, MAGNET program
29 Ha'mered St.
Tel Aviv, Israel*

³ *CNSE
Colleges of Nanoscale Science and Engineering at SUNY Polytechnic Institute
257 Fuller Rd
Albany NY 12203*

INTRODUCTION

Metrology tool companies, as well as Semiconductors manufacturers are sharing the same problem: Is 'my' Metrology tool calibrated? The tool manufacturer would like to know if the tool met the expected performances and is ready to be delivered; the IC manufacturers would like to ensure that a tool is 'back in spec', after PM. Both would like to compare tool-to-tool and even Fab-to-Fab performances.

Evaluating and comparing manufacturing tool performances (Etchers, Scanners etc.) may even be more complicated as some parameters affect the final result. Only by developing a 'module monitors' will metrology tool companies and Semiconductor manufacturers be able to ensure stability.

Unfortunately, each tool maker and each user generally develop their own test wafers. Sometimes a tool maker must develop several test wafers to meet the needs of various end users. The end result leads to extended lead times, costs, and additional development efforts. A unilaterally accepted metrology wafer standard helps minimize the latter challenges.

The transition to 450mm wafer processing offers additional challenges and opportunities. Early metrology tools are, mostly, best in class 300mm tools scaled up to handle 450mm wafers. In most cases, 450mm calibration/qualification wafers are not yet available. 300mm wafers are being used for initial testing. Potential differences between 300mm and 450mm wafers and film stacks add to the measurement uncertainty. An early priority for the G450C metrology team will be collecting true 450mm reference standards: wafers made with the actual 450mm process tools, not pocket or coupon wafers on 450mm substrates.

A COMMON/AGREED RULER IS NEEDED

The initial G450C pilot line will consist of a distributed tool set with some process and metrology tools at supplier and other locations. Reference artifacts are required to correlate tools from around the globe.

Traceability from organizations like NIST would also be highly desirable to make sure all users are not just on the same page, but on the right page.

This will be achieved by deep collaboration between industry, consortia, academia, and a state-of-the-art research and development facility. The SUNY Polytechnic Institute's College of Nanoscale Science and Engineering (CNSE), the Global 450mm Consortium, and the State of Israel's Metro450 consortium have joined together to develop a next generation metrology standard. The metrology companies are sharing their most relevant 'tool calibration and design targets'; CNSE their process and integration knowledge, and G450C adding 'module stability targets'. A 'short loop' process will be developed and masks will be designed. The printability and proof of fabrication of those targets on advanced-node substrates with advanced-node materials will be performed on 300mm and 450mm wafers at CNSE's Albany nanotech fabrication facilities to become a worldwide standard.

The developer will face real challenges, from IP issues (competing companies to share targets), to technological issues (how many layers, different materials, one/some calibration wafers etc.). Developing a 'Defects Calibration Wafer' is even more challenging as some of the printed 'defects' should be smaller than the most aggressive CD.

Developing such a standard will enable a common platform between the different Metrology tool makers and the Semiconductor manufacturers within the IC manufacturing world, which will ensure reduced cost of ownership, time to market, and process variation to wafer performance.

KEYWORDS

450mm, metrology, SPC, calibration, reference standards, semiconductor, IC, CD, ellipsometry, inspection

Non-Destructive Compositional Metrology of NAND Memory and Emerging Non-Volatile Memories

Olivier Dulac, Anna Meura, Anne-Sophie Robbes, Mona Moret and David J. Larson

CAMECA, 29 quai des Grésillons, 92 622 Gennevilliers, France

INTRODUCTION

For at least a decade, the semiconductor industry has been shifting volume production from devices based on silicon to devices based on compound material, mostly SiGe. This shift involves very demanding manufacturing process specifications in order to achieve logic devices exhibiting both high performance and low power.

Shallow Probe metrology instrumentation based on low energy electron X-ray emission spectrometry (LEXES) was successfully introduced in the late 90's to accompany this active channel material evolution, which induced additional changes in the gate materials composition. With the introduction of more complex stacks, the Shallow Probe's unique capability to measure the composition and thickness of buried films (without contact) became the reference tool for fab ramp-up of the advanced nodes in logic device.

Following the same trend of power consumption reduction and faster operation, we note that the memory market, mainly dominated by NAND (NOR) type of Non-Volatile Memory (NVM), has been evolving for decades. New types of NVM are emerging, like Phase change RAM (PRAM), Resistive RAM (ReRAM) or Spin Torque Transfer RAM (STT-RAM), all of which use compounds materials that call for the unique compositional capabilities of the Shallow Probe.

After reviewing briefly the technique and showing some applications developed for NAND, the current work presents detailed measurements using Shallow Probe to characterize some specific materials used in the emerging NVMs.

LOW ENERGY ELECTRON X-RAY EMISSION SPECTROMETRY

Low energy Electron X-ray emission spectrometry – also sometimes called EXES [1] - is a non-destructive characterization technique which probes full wafers with a low energy electron beam and analyses the emitted soft X-rays through wavelength dispersive spectroscopy (WDS). This technique is similar to electron probe micro analysis, except that the low energy, high current, electron column has been specifically designed to optimize near-surface instead of bulk analysis. The probing energy can vary from a few hundreds eV to 10keV and the electron beam current can be adjusted from 0.1 to 30 μ A. The resulting sampling depth ranges typically from top the surface down to ~800nm. The beam diameter can be adjusted from 15 to 100 μ m according to the application. The dose of a specific element is measured directly by selecting the corresponding X-ray emission line. For a given energy, the peak minus background (P-B) signal (c/s/ μ A) is proportional to the dose of the element in atoms/cm² in the probed volume. The P-B quantification is performed from sensitivity factors determined from reference samples. All elements heavier than beryllium can be measured by LEXES. Typical performance will be shown on lanthanum in high-k metal gate materials and for implants in Si.

NAND CHARACTERIZATION

To improve NAND-based memory charge trapping when scaling down devices, cell structures are engineered by introducing Hf and Al based oxides instead classical oxides (Titanium, Alumina, Nitride, Oxide, Silicon (TANOS), Titanium, Hafnium, Nitride, Oxide, Silicon THNOS)). These Hf and AlO₃ layers are rather difficult to measure using conventional optical techniques due to a very low film thickness, varying composition and, additionally, being buried under a Titanium nitride. Figure 1 shows typical measurement results on HfO₂ over SiO₂ using Shallow Probe demonstrating capabilities of simultaneous thickness measurement of both layers over the whole wafer.

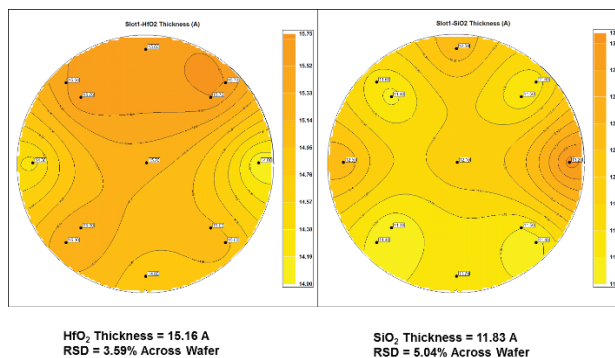


FIGURE 1. Typical HfO₂ thickness mapping within an HfO₂/SiO₂ stack

EMERGING NON VOLATILE MEMORIES CHARACTERISATION

PRAM

PRAM, based on the amorphous/crystalline change that occurs upon heating of alloys such as Ge₂Sb₂Te₅ (GST), is one of the candidates for low power NVM. The challenge when manufacturing the stack is to control the composition and monitor the amount of incorporated nitrogen used to adjust the crystallization temperature. The composition and thickness determination by the Shallow Probe for an example GST alloy is in Table 1 with excellent thickness precision.

Table 1 Composition and thickness determination in GST layers

Wafer	Ge at%	Sb at%	Te at%	N at%	Thickness (Å)	RSD thickness
1	19.95	19.826	44.9114	15.3128	736.92	0.88
2	27.08	24.875	48.048	N/A	686.76	0.32
3	25.94	24.089	49.971	N/A	649.22	0.47

STT-MRAM

One of the challenges in the area of STT MRAM (in addition to quantification of the magnetic effect involved in the spin torque structure) is to control the early stages of fabrication of the MgO barrier layer. This layer, which is often made of ultrathin MgO (typically 1nm), is positioned between two ferromagnetic layers and a nm-scale Ru top electrode. The Shallow Probe technique, with its depth and resolution capabilities, is able to investigate the buried MgO to produce layer composition and uniformity with high precision. The latest results on this topic will be presented.

REFERENCES

1. P. F. Staub, *Microscopy and Microanalysis* **12** (6), 340 (2006).

KEYWORDS

Compositional Metrology, Non-destructive, LEXES, STT-RAM, thin films, non-volatile memory

Liquid-metal-jet X-ray tube technology for nanoelectronics characterization and metrology

E. Espes¹, B. A. M. Hansson¹, O. Hemberg¹, G. Johansson¹, M. Otendal¹,
T. Tuohimaa¹, P. Takman¹

¹ Excillum AB, Torshamnsgatan 35, 164 40 Kista, Sweden

INTRODUCTION

Several X-ray based techniques are applicable for characterization and metrology for nanoelectronics. Most X-ray based techniques are limited by the available X-ray flux from conventional X-ray tubes.

As illustrated in Fig 1a, a conventional X-ray tube generates X-rays when highly energetic electrons are stopped in a solid metal anode. The fundamental limit for the X-ray power generated from a given spot size is when the electron beam power is so high that it locally melts the anode. The liquid-metal-jet anode (MetalJet) technology solves this thermal limit by replacing the traditional anode by a thin high-speed jet of liquid metal (see Figure 1b). Melting of the anode is thereby no longer a problem as it is already molten, and significantly (currently about 10x) higher e-beam power densities can therefore be used.

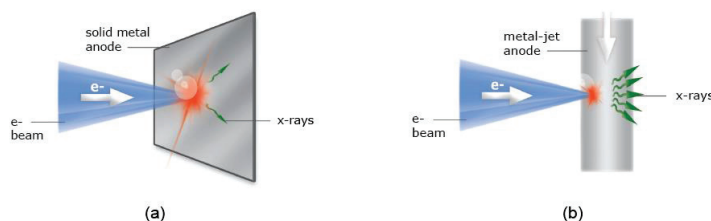


FIGURE 1. The principle of a solid anode X-ray tube (a) and a liquid-metal-jet X-ray tube (b).

SYSTEM DESCRIPTION

Figure 2 illustrates a complete MetalJet X-ray source. The upper part is the source head with the electron gun and the vacuum pump. This part is similar to any open-type X-ray tube apart from the metal-jet anode that is formed by ejecting a $\sim 200\ \mu\text{m}$ diameter metal jet through what is essentially a standard water cutting nozzle. One key requirement to achieve 24/7 operation is that the liquid-metal-alloy can be 100% recirculated. The path of the circulating liquid alloy is illustrated by the arrows in Fig. 2.



FIGURE 2. A complete MetalJet X-ray source with source head, pump box, support electronics and water-chiller.).

The engineering aspects of closed-loop recirculation are significantly relaxed if anode alloys molten at room temperature can be used. This limits the corrosiveness of the alloys, that tend to increase rapidly with temperature, and also simplifies the draining of the system at times of service. The first available sources use either a mainly gallium based alloy or an alloy which also contain significant amounts of indium. The gallium $K\alpha$ line is at 9.2 keV, which makes it an attractive high-brightness replacement of copper $K\alpha$ at 8.0 keV. The indium $K\alpha$ is at 24.2 keV making it an attractive high-brightness replacement of silver $K\alpha$ at 22.2 keV. Figure 3 shows the emitted Ga and In spectra as well as the Cu and Ag spectra, for comparisons.

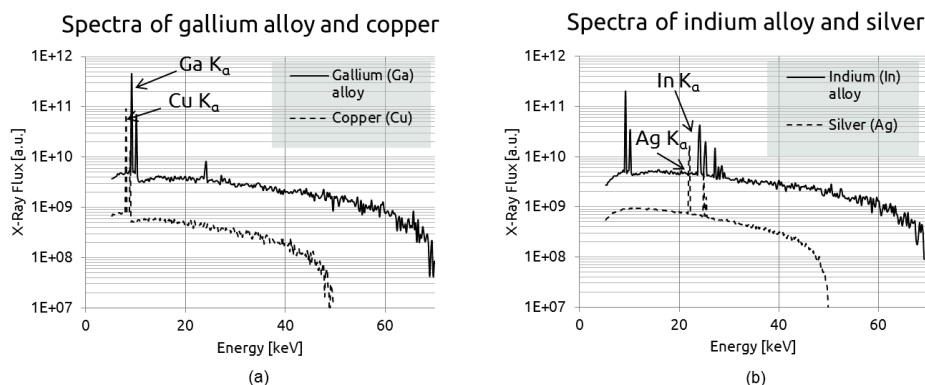


FIGURE 3. Typical spectra at 70 kV acceleration voltage for gallium alloy (a) and indium alloy (b).

TYPICAL SOURCE PERFORMANCE

The main specifications of current MetalJet sources are listed in Table 1. Table 2 summarizes typical source parameters for operation in four different configurations. Normally we employ 1:4 e-beam line focus which results in a round spot with angled viewing. For example, for X-ray diffraction the source is typically operated at 200 W with an approx. $20 \times 80 \mu\text{m}^2$ spot viewed at an angle to generate an effective $\sim 20\text{-}\mu\text{m}$ -diameter spot. However, the spot shape may be freely tuned from larger sizes, limited only by the size of the liquid jet, down to 5-6 μm diameters, limited by the e-beam focus and electron scattering. The aspect ratio is also freely tuneable. The brightness is given as the $K\alpha$ (double) line brightness.

TABLE 1. Typical source specification.

Voltage	Power	Max. current	Min. focal spot size	Min. spot-object distance	Available beam angle
10-160 kV	0-300 W	4.3 mA	$\sim 5 \mu\text{m}$	18 mm	18°

TABLE 2. Typical source performance.

Alloy	Acceleration voltage [kV]	Apparent Spot Size ^a	E-beam power	Line	$K\alpha$ peak brightness [photons/(s·mm ² ·mrad ² ·line)]
Gallium alloy	70	20	200	Ga K-alpha	2.6×10^{10}
Gallium alloy	70	10	100	Ga K-alpha	5.2×10^{10}
Indium alloy	70	20	200	In K-alpha	1.3×10^9
Indium alloy	70	10	100	In K-alpha	2.6×10^9

^a Actual e-beam spot has a 1:4 aspect-ratio line focus, but the projected diameter is essentially circular.

APPLICATIONS

CD-SAXS

Research on critical dimension small angle X-ray scattering (CD-SAXS) [1] have identified that lab-based X-ray sources with higher brightness than previously available, at energies higher than 20 keV are needed for non-

synchrotron CD-SAXS. The MetalJet source technology with indium K- α emission at 24 keV show great promise towards meeting the requirements.

XRD

Various X-ray Diffraction (XRD) [2] techniques can benefit significantly from the high brightness achievable with the MetalJet X-ray source technology.

X-ray Microscopy

The highest available resolution in lab-based X-ray microscopes is achieved with zone-plate based projection microscopes [3] Such microscopes, however, typically use Cu K α radiation which is not so well suited to see copper structures in silicon due to poor contrast between copper and silicon. As illustrated by figure 4, the K α of gallium used in MetalJet sources, is just above the K-absorption edge of copper [4] and thus much better suited to create a sufficient contrast between copper and silicon.

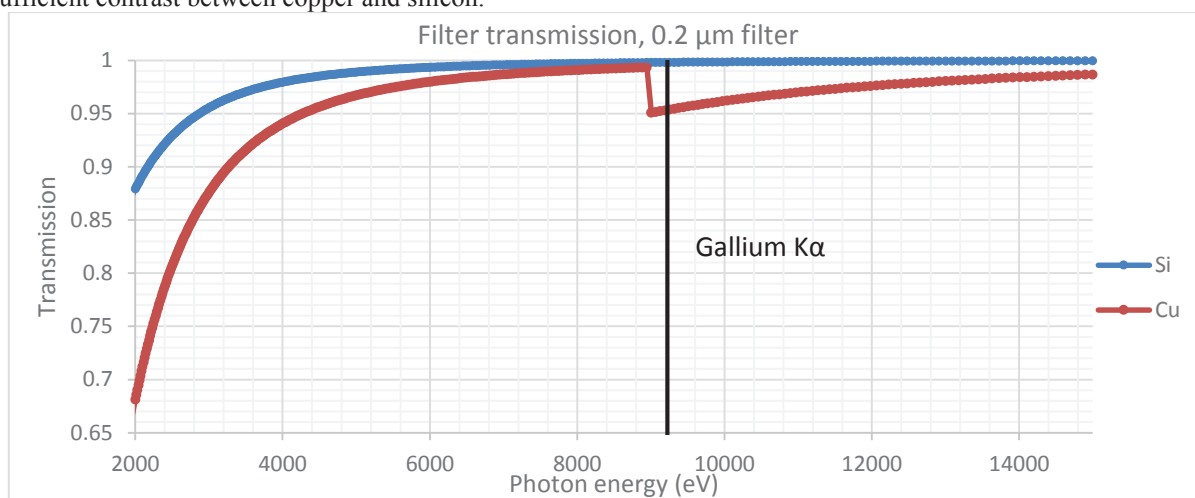


FIGURE 4. X-ray transmission through a 0.2 μm filter of silicon and copper. The black line indicates the K α of gallium [4].

TXRF

Recently a group at the Atominstitut, in Vienna, used the liquid-metal-jet technology to do TXRF-investigations [5]. The high brightness and small spot-size, which results in a low divergence of the primary beam, leads to a very low spectral background. In a non-optimal set-up, they still achieved detection limits in the high femtogram range.

REFERENCES

1. R. J. Kline, D. F. Sunday, D. Windover and W. Wu, 'Bringing CD-SAXS to the Fab', SEMICON West 2014, 2014.
2. D. Bowen and B. Tanner, *X-ray metrology in semiconductor manufacturing*. Boca Raton: CRC/Taylor & Francis, 2006.
3. T. Beetz, 'High-resolution X-ray Tomography Imaging Systems', CHESS Users' Meeting Ithaca, NY, 2008.
4. E. Gullikson, *Filter transmission*, http://henke.lbl.gov/optical_constants/filter2.html, visited on 2015-03-24.
5. A. Maderitsch, S. Smolek, P. Wobrauschek, C. Strelj and P. Takman, *Spectrochimica Acta Part B* **99**, 67–69 (2014).

KEYWORDS

x-ray, tube, source, microfocuss, metaljet, liquid-metal-jet, gallium, indium, TXRF, microscopy, imaging

Breakthrough of STEM and FIB Automation in Critical Dimension Metrology of Wafer Manufacturing

Jianxin Fang, Wei Hong, Jose Garjado, Juanita Castillo, Zhipeng Li, and Haifeng Wang*

Western Digital Corporation, 44100 Osgood Road, Fremont, CA 94539, U.S.A.

*Haifeng.wang@wdc.com, +1-510-683-7448

INTRODUCTION

As modern electronics becomes increasingly portable and power efficient, it has put tremendous pressure on designers and manufacturers to miniaturize components while maintaining or increasing the system performance, particularly in data storage and semiconductor industries. With ever-increasing demand for data storage capacity driven by a vast amount of online social activities and rapid transition to digital content generation by worldwide population, areal density boost is becoming a technical challenge as well as an economic viability for the storage industry. This has resulted in the thin film magnetic recording head dimension inside the drive continuously shrinking mercilessly. Many critical layers in both writing and reading sections of the recording head have been reduced to nanometers and some of them are in angstrom range. Manufacturing control capability at the sub-nanometer scale is essential to consistent high yield wafer production. Conventional scanning electron microscopy (SEM) based in-line metrology, e.g., critical dimension scanning electron microscopy (CD-SEM), despite of its high volume and instant access to data, is becoming less sensitive to nanometer to sub-nanometer structural variation due to imaging resolution limitation. Other optical based metrologies rely on specially designed test areas to correlate to device level structures. Transmission electron microscopy (TEM) imaging has been used successfully and limited to building the correlation between test site metrology and actual device dimensions.

PROCEDURES

The technique, critical dimension scanning transmission electron microscopy (CD-STEM) as opposed to CD-SEM, consists of the three key steps: (1) focused ion beam (FIB) sample preparation, (2) ex-situ sample transfer, and (3) automated imaging and measurement. Each step is described below:

FIB sample preparation: TEM samples are automatically sectioned from the wafer using recipe-driven FIB processes. Automated FIB milling includes creating reference marks for milling accuracy and drift compensation, fine tuning stage movement, rough trim on both sides of the lamellae, bottom release milling, and final polishing to achieve the required thickness. The FIB automation provides high positioning accuracy and precision to achieve about 60nm-thick TEM lamella with ~1 sigma of 3nm consistency, as shown in Figure 1.

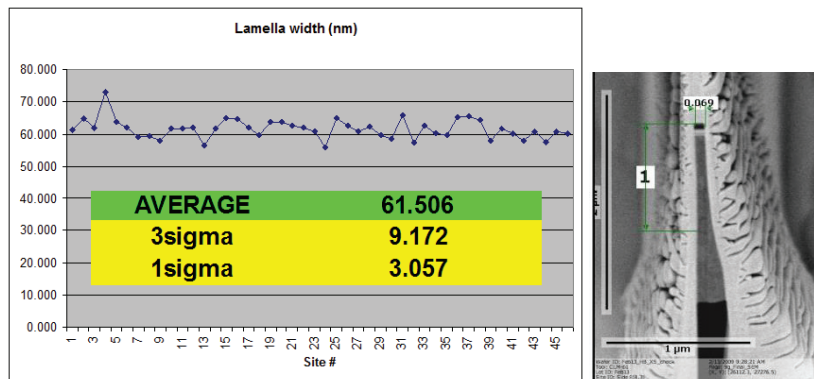


Figure 1. Thickness consistency of TEM samples prepared via automated FIB

Ex-situ sample extraction and transfer: Lamella sectioned on the wafer are extracted and transferred to a 3mm TEM grid via a semi-automated proprietary procedure. The process includes innovative probe design and a computer controlled motorized stage. The new probe, a hollow glass tube, uses vacuum force to ensure a reliable pick and place operation. A host computer controls the motorized stage of the transfer station, navigating automatically to sample locations reported from the FIB system to pick samples from the wafer and to grid locations to place samples onto the grid. Automation has greatly improved the speed, precision, and reliability of the transfer process, which provides a uniquely high success rate and high throughput. A large number of samples are placed on a single grid with each sample similarly oriented, as shown in Figure 2. Placing multiple samples in similar orientation simplifies the tilt adjustment during imaging and allows acquisition of edge-on STEM images of multiple samples by one single adjustment of the common orientation.

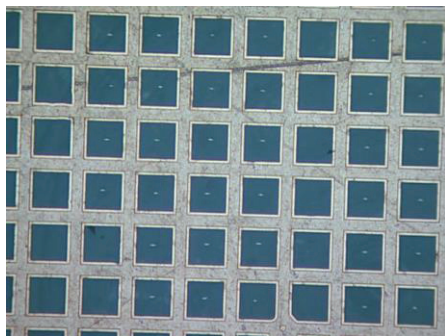


Figure 2. TEM grid with multiple samples

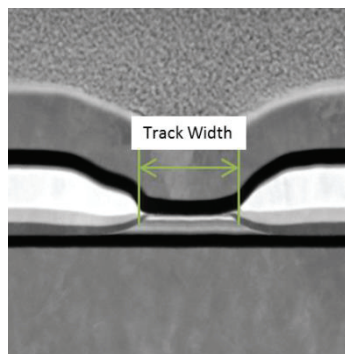


Figure 3. STEM image showing strong material contrast of a GMR reader

Automated imaging and measurement: STEM images shown in Figure 3 are acquired using sophisticated imaging automation on TEM, including auto-eucentric height and auto-tilt adjustment. Dimensions are measured on the acquired STEM images using image analysis, including feature recognition and edging finding algorithms. Gauge study has shown that one sigma of 1.0 Å has been achieved, as shown in Table 1.

Table 1 Gauge study of track width (nm) of a GMR reader

Site	ai value	Operator 1					Operator 2					Operator 3					Mean	Var<m>	<Var>
		M1	M2	M3	Mean	Var	M1	M2	M3	Mean	Var	M1	M2	M3	Mean	Var			
1	0_6_14_	38.63	38.73	38.44	38.6	0.022	38.44	38.68	38.44	38.5	0.019	38.37	38.37	38.49	38.4	0.005	38.509	0.0089	0.0151
2	2_30_16_	38.94	39.04	39.01	39.0	0.002	39.04	39.31	39.01	39.1	0.028	39.18	39.01	39.27	39.2	0.017	39.090	0.0067	0.0160
3	3_18_5_	38.66	38.55	38.56	38.6	0.004	38.44	38.61	38.56	38.5	0.008	38.90	38.44	38.45	38.6	0.071	38.574	0.0011	0.0275
4	a_66_22_	39.03	38.87	38.96	39.0	0.006	38.76	38.71	38.96	38.8	0.018	38.77	38.97	38.90	38.9	0.010	38.881	0.0051	0.0112
5	c_67_17_	36.47	36.46	36.48	36.5	0.000	36.35	36.59	36.48	36.5	0.014	36.47	36.49	36.41	36.5	0.002	36.467	0.0001	0.0055
6	f_66_10_	38.47	38.53	38.41	38.5	0.003	39.38	38.57	38.41	38.8	0.270	39.29	38.29	39.17	38.9	0.299	38.725	0.0534	0.1910
7	h_44_18_	34.87	34.56	34.89	34.8	0.035	34.73	34.95	34.89	34.9	0.013	34.72	34.84	34.71	34.8	0.005	34.796	0.0028	0.0178
8	k_31_17_	36.00	35.91	35.78	35.9	0.012	35.63	36.06	35.78	35.8	0.046	35.63	35.87	35.76	35.8	0.015	35.826	0.0050	0.0244
9	w_4_22_	38.38	38.36	38.07	38.3	0.031	38.45	38.21	38.07	38.2	0.037	38.51	38.27	38.31	38.4	0.016	38.292	0.0040	0.0280
10	m_28_14	37.72	37.67	37.62	37.7	0.002	37.69	37.74	37.62	37.7	0.004	37.82	37.62	37.72	37.7	0.010	37.691	0.0006	0.0052
															Global Mean:	37.685			
															Reproducibility sigma:	0.094			

CONCLUSION

Automated CD-STEM metrology includes automated FIB sample preparation, ex-situ sample extraction, and automated imaging and measurement. With these advances, CD-STEM can provide both the resolution required to accurately characterize nanoscale structures, speed and repeatability, and the reproducibility required for high volume manufacturing processes in the magnetic head industry. These remarkable benefits can also be appreciated in many other microelectronics industries that focus on controlling nanostructures in the manufacturing process.

KEYWORDS

Transmission electron microscopy, scanning transmission electron microscopy, metrology, ex-situ sample transfer, focused ion beam, automation, wafer manufacturing, CD-STEM, CD-SEM

Electron Energy-Loss Spectroscopy (EELS) Analysis on MoS₂ Layers Transferred on Silicon

Karine Florent^a, David MacMahon^b, Andrea Brothers^b and Santosh Kurinec^a

^aMicroelectronic Engineering, Rochester Institute of Technology, Rochester NY, USA

^bMicron Technology Inc, Manassas, VA, USA

INTRODUCTION

Layered two-dimensional (2D) materials that can be mechanically exfoliated into single monolayers have great potential for novel information processing such as spin-based and valley-based electronics. With the advancement of microscopic and analytical techniques, significant insight knowledge has been obtained on the structure and properties of 2D materials. In this paper, the authors have carried out high resolution TEM and electron energy loss spectroscopy (EELS) to investigate MoS₂ layers interface with silicon dioxide. The results show a conformable coverage of MoS₂ on SiO₂ with interfacial reaction between MoS₂ and SiO₂. Further high resolution analyses are in progress and will be presented at the conference.

EXPERIMENTAL AND RESULTS

Layers of MoS₂ are obtained through mechanical exfoliation of bulk MoS₂ crystals (SPI Supplies) on top of thermally grown SiO₂ layer on highly doped p-type silicon substrate. The crystalline phase of the crystal was confirmed by XRD showing a Molybdenite-2H phase (PDF card no: 00-037-1492). The parallel electron energy loss spectroscopy (PEELS) studies were carried out by employing a Hitachi HD-2300A STEM fitted with a Gatan Enfina PEELS Spectrometer at Micron Inc's Manassas facility. Figure 1 shows an HR STEM image of a MoS₂ flake which is composed of ~ 16 layers. Each dark line represents MoS₂ single-layer and each lighter line corresponds to the inter layer spacing ~ 6 Å as reported in the literature [Radisavljevic, 2011].

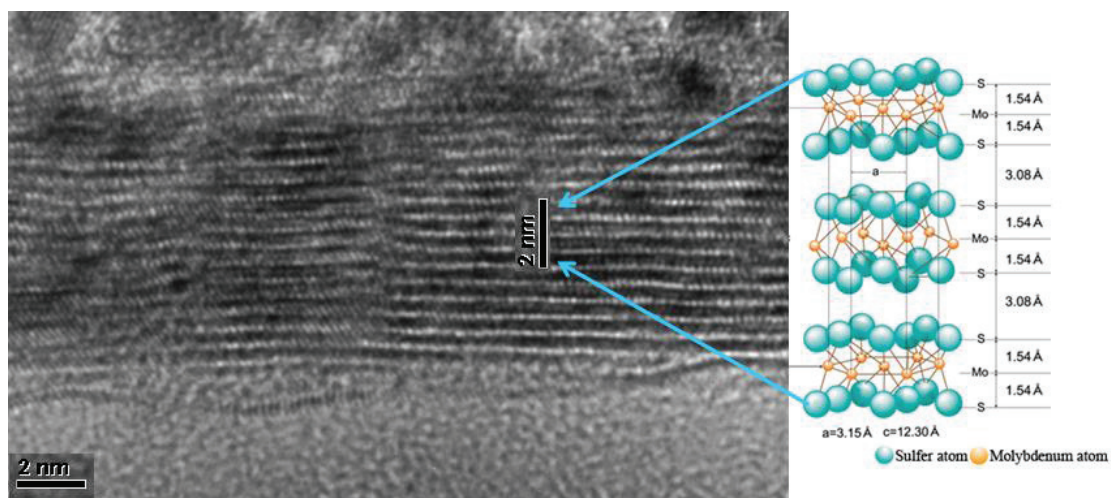


FIGURE 1. Cross sectional TEM image of a MoS₂ exfoliated flake, composed of ~ 16 layers with structure schematic on the right [1, 2].

Figure 2 shows area EELS scans for Mo, S, Si and O. Line scans shown in Figure 3 may be showing possible molybdenum oxidation at the interface. To confirm this observation, high resolution line scan with a smaller probe are needed in addition to experimenting with conditions to get data with minimal artifacts.

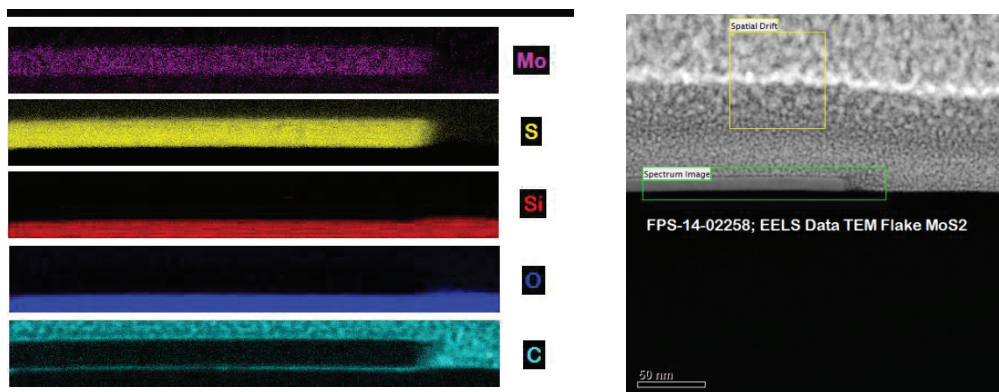


FIGURE 2. EELS area scans for Mo, S, Si and O on a MoS₂ flake shown on the right

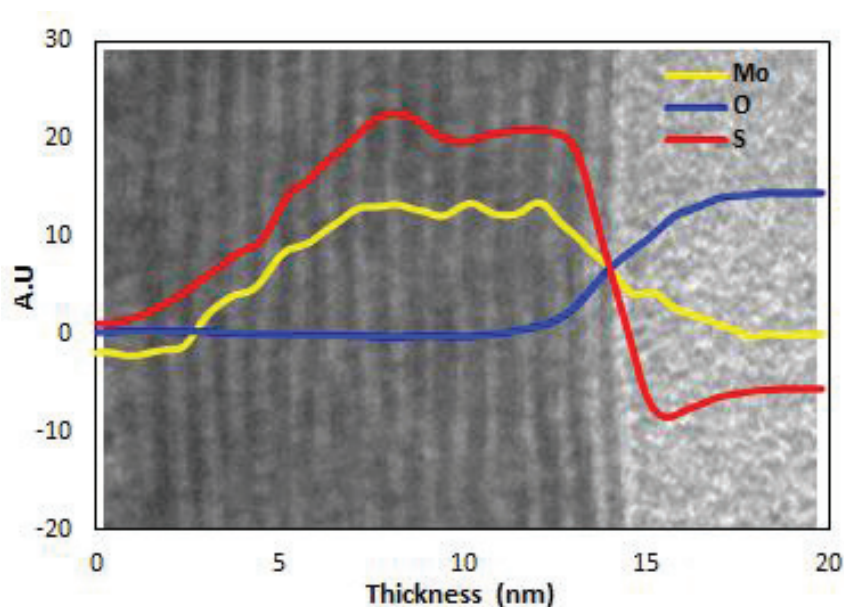


FIGURE 1. EELS line scan analysis on 16 layers of MoS₂ on SiO₂ showing an interfacial mixing at the MoS₂-SiO₂ interface which may be attributed to beam induced effects of operation under 200kV STEM.

REFERENCES

1. B. Radisavljevic, A. Radenovic, J. Brivio *et al.*, *Nature Nanotechnology* **6**, 147-150 (2011).
2. <http://www.drilube.co.jp/english/product/molybdenum.html>

KEYWORDS

MoS₂, TEM, Electron energy loss spectroscopy (EELS), Exfoliated layer transfer

Characterization of Near- to Far-Field Transformers by Interferometric Fourier-Scatterometry

K. Frenner, V. Ferreras-Paz, W. Osten

*Institut für Technische Optik (ITO), Universität Stuttgart,
Pfaffenwaldring 9, D-70569 Stuttgart*

INTRODUCTION

Plasmonic superlenses, which allow optical imaging below the diffraction limit, are subject of intense research. Features necessary for such plasmonic devices are a high transmittance through the metallic layers on the one hand and a structure which is able to convert evanescent near-fields into propagating modes on the other hand. This part of a superlens is called near- to far-field (NTFF) transformer. Plasmonic superlenses in the traditional sense, which are indeed not available yet, would allow to image sub-lambda samples directly with a conventional optical microscope. However, we use another feature of these structures to characterize NTFF-performance. In this paper we show that such a NTFF-element can be used to increase the sensitivity of a standard scatterometry setup which measures CD and pitch of an underlying line grating. With the increased sensitivity one can read off how well the desired NTFF-functionality is present in these structures.

NEAR- TO FAR-FIELD TRANSFORMERS

The NTFF transforming structures used in our work consist of nano-rods with dimensions below 100 nm up to 300 nm. High aspect ratio NTFF structures could be obtained using two-photon polymerization (2PP)-techniques [1] and focused ion-beam lithography.

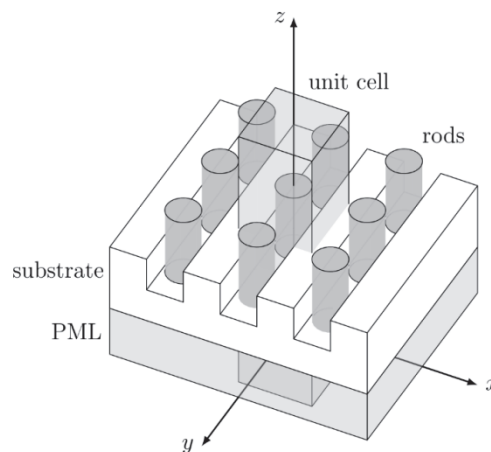


FIGURE 1. Line grating with metallic nanorods.

INTERFEROMETRIC FOURIER-SCATTEROMETRY

Scatterometry [2] is a standard-method to measure structure parameters of a periodic arrangement of nanostructures. This is done by using model-based metrology methods. There have been various approaches to improve sensitivity in scatterometry like changing illumination wavelength, increasing illumination incidence angles, using a very high numerical aperture, using combinations with other measurement methods as for example white light interferometry. Background of all these methods is the collection of a complete set of information which is transmitted by propagating modes. Another approach is to use information which is not propagated by the scattered light. This information is contained in evanescent modes that move closely along the surface. In order to get access to this information, these waves are detected directly on the surface by antenna-like metallic nanostructures. However, these waves produce plasmons at the surface of the nanostructures, which in turn emit light, this time with a spatial frequency, which allows propagation in the surrounding space.

While we have already shown some promising results based on simulations [3] we now want to verify these results with experimental data. We use a Fourier-scatterometer [4] to detect the backscattered light of test line gratings. We then analyze the influence of nearfield structures on the sensitivity. In contrast to the mentioned simulation study [3] we now use brightfield illumination, which contains a broad range of incident directions and therefore much more information.

The experimental setup consists of a fiber-coupled, high power LED with a wavelength of 617nm as a light source, which is imaged on the back focal plane of a high NA (0.95) microscope objective. A linear polarizer allows to select s- and p-polarized illumination. The image of the fiber covers the complete aperture producing a homogeneous illumination of the sample. The reflected light is collected by the same objective in conjunction with a Bertrand-lens which images the back focal plane to a CCD with low aberrations. In addition to the illumination and imaging path of the Fourier-Scatterometer, a reference arm for a Linnik-type setup is included as well. This reference path gives access to the phase of the reflected diffraction orders but is not used for the following study. A typical measurement procedure consists of recording the pupil plane images for both polarisation directions. Using structures that only vary in the width of the structure and comparing the taken images allows extracting the sensitivity in signal towards changes in line width.

MODEL BASED RECONSTRUCTION

Simulation of the Fourier scatterometry technique was done with our simulation tool "MicroSim" [5] which is based on the rigorous coupled wave analysis (RCWA) method [6]. MicroSim calculates diffraction from arbitrary three-dimensional structures and includes some improved convergence methods [7]. An extended illumination pupil is discretized by planar waves on a grid, which is sampled with 99×99 equidistant points corresponding to different incident angles. Due to the symmetry of the studied structure, only one-quarter of the pupil was modelled. Such a fine sampling is needed due to the tiny features in the pupil images generated by higher diffraction orders. For each of the 99×99 pupil points separate diffraction calculations have to be performed. To obtain the resulting pupil images, calculated fields for every incidence angle are coherently superposed. The width of the lines (CD) is varied and the sensitivity towards those changes is obtained from the difference in the corresponding pupil images. These sensitivities are compared to the ones calculated after the introduction of nano-rods between the lines of the gratings acting as NTFF-transformers.

EXPERIMENTAL RESULTS

Pupil images for the structures shown in Fig.1 were measured for both s- and p-polarization with and without nano-rods between the lines. The resulting images and the intensity difference in the pupil plane are shown in Figure 2. The most important reason for differences between measurement and simulation is the simplified simulation model that had to be used due to the very large calculation times. The grating is modelled with perfectly steep walls without roundings or line edge roughness. The LED is modelled perfectly homogenous and with a very narrow band of only 1nm wavelength range, while realistically 20nm should be assumed.

The measured and simulated results show comparable absolute differences in pupil intensity. From this it follows that the grating with rods is much more sensitive because the CD-difference is 40nm for lines and rods compared to 100nm for the line grating without rods. Thus it appears that metallic nano-rods show the desired NTFF-functionality.

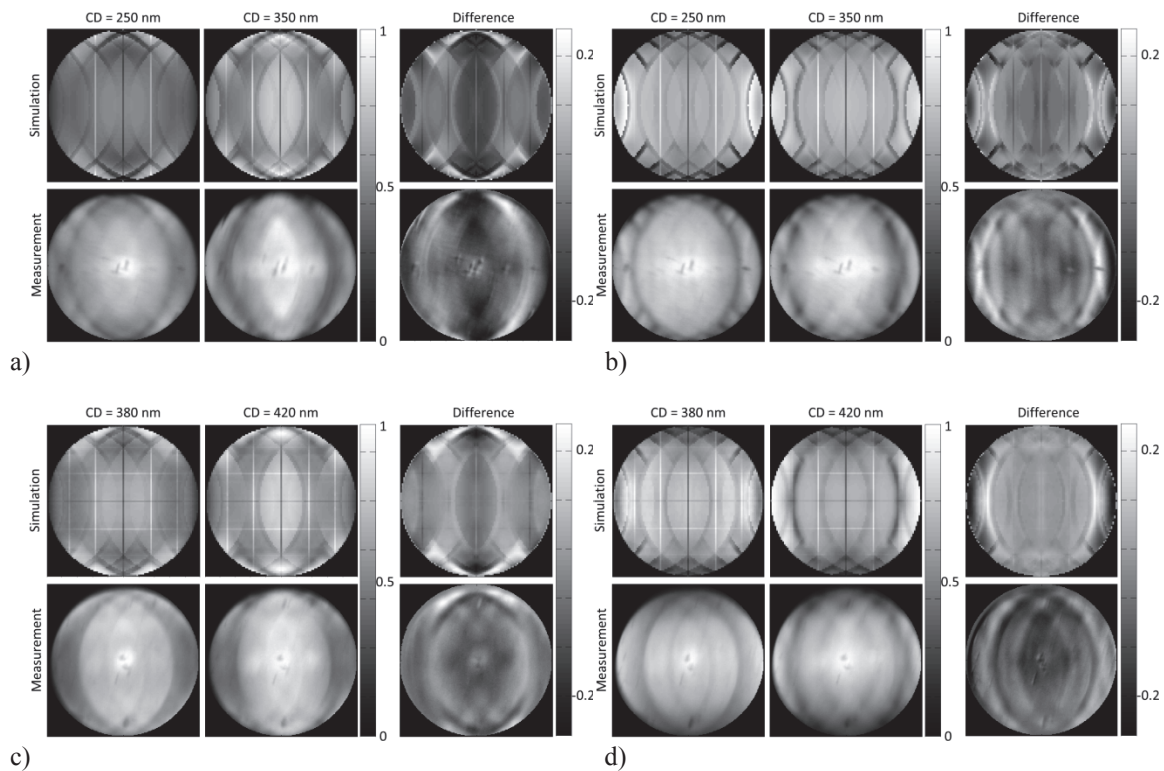


FIGURE 2. Fourier-scatterometry: a) line grating p-pol, b) line grating s-pol, c) lines+rods p-pol d) lines+rods s-pol

This research is funded by the German National Science Foundation (Deutsche Forschungsgemeinschaft, DFG) under the umbrella of the priority program (Schwerpunktprogramm) SPP1327 “Optisch erzeugte Sub-100nm Strukturen für biomedizinische und technische Applikationen”

REFERENCES

1. C. Reinhardt, R. Kiyon, S. Passinger, A. L. Stepanov, A. Ostendorf, and B. N. Chichkov, Rapid laser prototyping of plasmonic components, *Applied Physics A* 89, pp. 321 – 325 (2007)
2. C. J. Raymond, Scatterometry for Semiconductor Metrology. In A. C. Diebold (Ed.), *Handbook of silicon semiconductor metrology* (pp. 477–513). CRC Press. (2001)
3. V. Ferreras Paz, K. Frenner, W. Osten, Increasing Scatterometric Sensitivity by Simulation Based Optimization of Structure Design. In W. Osten (Ed.), *Fringe 2013 - 7th International Workshop on Advanced Optical Imaging and Metrology* (pp. 345–348). Springer Berlin Heidelberg. (2014)
4. V. Ferreras Paz, S. Peterhänsel, K. Frenner, W. Osten, Solving the inverse grating problem by white light interference Fourier scatterometry, *Nature Light: Science & Applications*, 1(11), e36. (2012)
5. M. Totzeck, Numerical simulation of high-NA quantitative polarization microscopy and corresponding near-fields. *Optik - International Journal for Light and Electron Optics*, 112(9), 399–406. (2001)
6. M. G Moharam, T. K. Gaylord, Rigorous coupled-wave analysis of planar-grating diffraction. *Journal of the Optical Society of America*, 71(7), 811. (1981)
7. T. Schuster, J. Ruoff, N. Kerwien, S. Rafler, W. Osten, Normal vector method for convergence improvement using the RCWA for crossed gratings. *Journal of the Optical Society of America A*, 24(9), 2880. (2007)

KEYWORDS

interferometric fourier-scatterometry, plasmonic superlenses, near- to far-field transformer, model based reconstruction

Transmitted Small Angle X-Ray Scattering Intensity Enhancement with a Designed Grating

Wei-En Fu*, Yen-Song Chen, Yun-San Chien and Wen-Li Wu*

*Center for Measurement Standards, Industrial Technology Research Institute
321 KuangFu Rd Sect 2, Hsinchu, Taiwan, ROC*

*corresponding authors: wenli.nist@gmail.com; weienfu@itri.org.tw

INTRODUCTION

Transmission SAXS (tSAXS) has been identified as a potential solution [1] for measuring nanoscale features by interrogating structures with sub-nanometer wavelength X-ray radiation. Most relevant parameters describing critical dimensions (CDs) of nanoscale features are pitch, pitch variations, side wall angle, line edge roughness, line width roughness and so forth. Based on the spacing of diffraction peaks along the pitch can be readily extracted from the tSAXS scattering pattern [2,3]. The line width of individual structure can be extracted from the envelope function of the scattering intensity. Another advantage of tSAXS is that the issues related to optical properties, e.g. n and k , their wavelength and size dependences can be avoided since tSAXS is based on classical X-ray elastic scattering, the observed scattering intensity depends only on variation in local electron density [4].

tSAXS has mostly been performed using a synchrotron X-ray source for its high beam flux or high brilliance which enables tSAXS measurements of samples with a minuscule scattering volume. However, they are simply too large and too expensive for daily industrial deployment. A lab system with a Mo rotating anode X-ray source has been successfully demonstrated for tSAXS applications in National Institute of Standards and Technology (NIST), but the measurement speed is too slow for high volume manufacturing (HVM). In this article, a technique, as show in Figure 1, is proposed to provide some enhancement in the X-ray scattering intensity from a target object (the structures of interests). The enhancement of X-ray scattering intensity can lead to an increase in measurement speed as well as an improvement in signal quality.

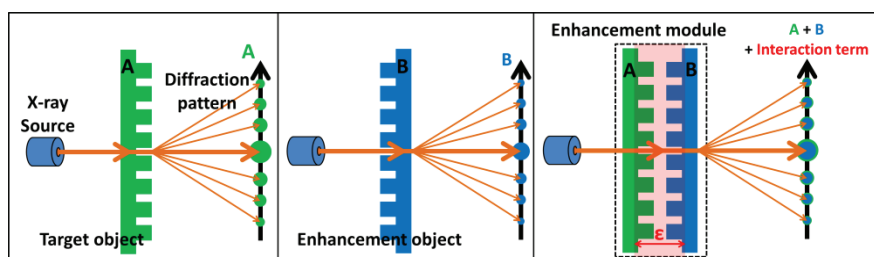


FIGURE 1. Illustration of transmission Small Angle X-Ray Scattering.

SCATTERING ENHANCEMENT

In order to increase the throughput for the HVM the X-ray scattered intensity merits some enhancement in order to shorten the collection time. In this work a technique is introduced to enhance the X-ray scattering intensity and simple line gratings are used to demonstrate its principle.

Figure 1 shows that the transmitted Small X-ray Scattering (tSAXS) is applied for measuring a patterned CD-the target grating (shown in one-dimension). The X-ray scattered pattern can be measured by the spatially resolved detector. The scattering intensities from the target grating can be described as:

$$I \propto \Delta b_1^2 \times F_1^2(q) \quad (1)$$

where Δb_1^2 is the contrast factor of the target grating and its value is rather small as for most nano-patterns. An additional pattern- an enhancement grating with strong scattering cross section, as shown in Figure 1, is added into the path of the transmitted SAXS adjacent to the target grating. Upon this weak scattering grating (the target grating) a strong scattering grating is placed within the longitudinal coherence length ε of the incident X-rays, as shown in Figure 1. The observed scattering intensities now become

$$I(q) \propto |\Delta b_1 \times F_1(q) + \Delta b_2 \times F_2(q)|^2 \quad (2)$$

where the subscription 2 denotes the enhancement grating with a strong scattering contrast factor.

For simplicity both the target and the enhancement gratings are chosen to have a rectangular cross section. Since all the diffraction spots appeared along q_x with $q_y = 0$, the function $F_i(q)$ can be replaced by $F_i(q_x)$ and explicitly the Eq. (2) can be expressed as:

$$I(q_x) = \Delta b_1^2 \times F_1^2(q_x) + \Delta b_2^2 \times F_2^2(q_x) + 2\Delta b_1\Delta b_2 \cos(q_x\eta) |F_1(q_x)F_2(q_x)| \quad (3)$$

where $2\Delta b_1\Delta b_2 \cos(q_x\eta) |F_1(q_x)F_2(q_x)|$ is the interaction term between target grating and enhancement grating and is the origin of signal enhancement over $(F_1(q_x))^2$

The value η indicates the mis-alignment between two gratings in x-direction. By definition, it has to be less than half of the pitch of the target grating. In deriving the above equation, both gratings are taken to be symmetric about their origin, hence both $F_1(q_x)$ and $F_2(q_x)$ are real. The interaction term carries information of target grating, and its magnitude can be significantly greater than $\Delta b_1^2 \times F_1^2(q_x)$ alone when the value of Δb_2^2 is designed to be much greater than that of the target grating.

EXPERIMENTS AND RESULTS

To demonstrate the scattering enhancement according to Eq. (3), experiments were performed in the National Synchrotron Radiation Research Center (NSRRC) in Taiwan with the conditions specified in Table 1. The X-ray beam conditions in the NSRRC are listed in Table 2. A target grating was made of Si with 200 nm pitch as the baseline sample. The other set of samples with a layer structure was included to demonstrate the scattering enhancement effect. The layer structure consists of a bottom layer of a Si 200 nm pitch grating, a SiO₂ interlayer with 5 nm thickness and a top layer of an Al grating also with a 200 nm pitch. The interlayer thickness was used to ensure that these two gratings were within the X-ray longitudinal coherence length which was estimated to be about 350 nm. The size of all the grating was 500×500 μm². In order to demonstrate the validity of the interaction term shown in the Eq. (3), the Al grating was purposely laterally shifted with respect to the Si grating by nominal 0 nm, 44 nm, 47 nm, 85 nm, 100 nm and 103 nm.

TABLE 1. Dimensions of target (Si) and enhancement (Al) gratings

Gratings	Pitch (nm)	Width (nm)	Height (nm)
Al	200	100	200
Si	200	100	20

Area of grating pattern: 500×500 μm²
X-ray beam-line condition: Photon Energy: 18 keV; Energy resolution: $\Delta E/E \sim 2 \times 10^{-4}$ (Si (111) Double Crystal Monochromator), Flux (0.5×0.6 mm²): $\sim 10^{10}$ photons/sec

Figures 2 and 3 show the amplifications of the scattering intensity by the enhancement grating. Comparing the peak intensities of the third peak of the Si grating (the baseline) versus that from the layer structure the intensity of the latter is ~170 times of that from the Si grating (the baseline). To be noticed, the intensity of the enhancement gratings includes the scattering intensities from both Si grating and Al grating, as well as the intensity from interaction term described in the Eq. (3).

Figure 3 shows the peak intensities varied significantly depending on the value of offset, η , of the Al grating with respect to the Si grating. The intensity variation can be as large as $\sim 34\%$ for the peak intensity as shown in Figure 3. This fluctuation amplitude of the third peak intensity of the layered structure is ~ 44 times that from the Si baseline grating. In other words, we have demonstrated that the scattering intensity of the third peak from the Si grating can be amplified by a factor ~ 44 by placing an aluminum grating over it. The above results also demonstrate that tSAXS can be used as an overlay metrology as long as the distance between them are within the longitudinal coherence length of the incident X-ray.

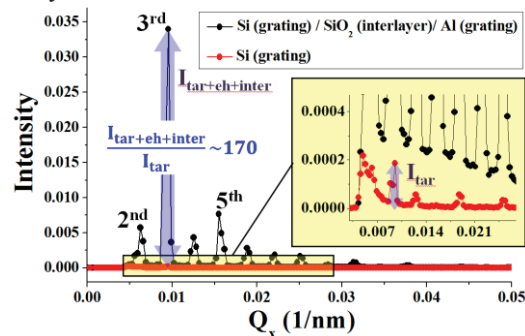


FIGURE 2. The scattering intensity of the target grating Si (red line) and that from the enhancement grating (black line) which includes the scattering intensity from both Si grating and Al grating, as well as the contribution from the interaction term described in the Eq. (3)

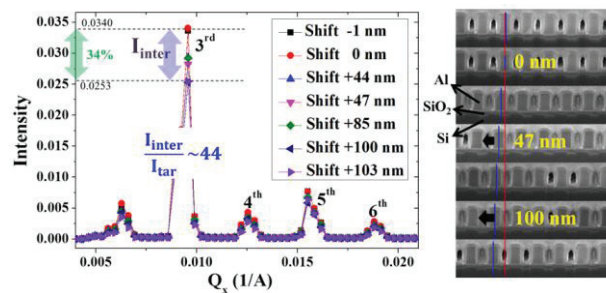


FIGURE 3. The peak intensities of the enhancement structure varied significantly depending on the shifts (η) of the Al grating with respect to the Si grating.

SUMMARY

A simple technique was proposed to amplify the scattering intensities from a target grating in transmission small angle X-ray scattering measurements. The details of the amplification depend strongly on the alignment of the enhancement grating (Al grating) with respect to the target Si grating as being described theoretically and demonstrated experimentally. This scheme of intensity amplification holds the promise to facilitate the use of tSAXS for HVM in semiconductor industries. In addition the results presented in this work demonstrate that tSAXS can also be used as an high precision overlay metrology.

REFERENCES

1. *The International Technology Roadmap for Semiconductors (ITRS)*, 2013.
2. Hu, T.; Jones, R.; Wu, W.; Lin, E. and Lin, Q., *Journal of Applied Physics* **96**, 1983 (2004).
3. Wang, C.; Jones, R.; Lin, E.; Wu, W. and Leu, J., *Applied Physics Letters* **90**, 193122 (2007).
4. B. Bunday, T. A. Germer, V. Vartanian, A. Cordes, A. Cepler, and C. Settens, *Proc. of SPIE* **8681**, 86813 (2013).

KEYWORDS

Transmission small angle X-ray scattering, gratings, longitudinal coherence length, Critical Dimensions, overlay metrology

Potential Of The EsB Detector In The Low Voltage Scanning Electron Microscopy (LVSEM): Application In Microelectronics

Aránzazu Garitagoitia Cid^{1,2}, Rüdiger Rosenkranz¹, Martin Gall¹, Ehrenfried Zschech^{1,2}

¹ *Fraunhofer Institute for Ceramic Technologies and Systems - Materials Diagnostics (IKTS-MD), Maria-Reiche-Str. 2, 01109 Dresden, Germany*

² *Dresden Center for Nanoanalysis (DCN), TU Dresden, 01062 Dresden, Germany*

Aranzazu.Garitagoitia@ikts-md.fraunhofer.de

In addition to high-resolution imaging, two challenges to application of Scanning Electron Microscopy (SEM) in semiconductor industry are: the detection of small differences in the composition of layers and structures in microelectronic products, and a low damage of structures. In this paper, we will focus on the application of Low Voltage Scanning Electron Microscopy (LVSEM), i. e. using lower values of primary beam voltage (E_p), for the studying of Cu/low-k on-chip interconnect stacks, and particularly on the study of dense and porous organosilicate glass (OSG) thin films which are used as insulating material with low permittivity between the metal interconnects. Since the beam/specimen interaction volume is significantly reduced for LVSEM compared to high voltage operation, essential information originated at the sample surface is obtained.

The differentiation between OSG and etch stop layers, with different chemical compositions, and the exact determination of geometrical data of the Cu/low-k structures at a cross-sectioned samples are important tasks for analytical labs in semiconductor industry, for both process control and physical failure analysis. In this paper we will show that SEM at low acceleration voltages in combination with an Energy-selective Backscattered (EsB) electron detector improves the compositional contrast and mitigates the shrinkage of the OSG caused by electron beam-induced material damage.

LVSEM has already been widely used thanks to the advances in electron gun design, aberration-corrected optics and the improvements in the sensitivity of recording images and obtaining analytical information. However, little attention has been paid to detector testing or optimization. By improving the Detector Quantum Efficiency (DQE), a higher signal-to-noise ratio (SNR) is obtained [1, 2]. In the case of the Energy selective Backscattered (EsB) electron detector, it is possible to detect only electrons with a certain energy by controlling the grid bias. This energy window technique is based on a cut off of secondary electrons (SE) and backscattered electrons (BSE) with high or moderate energy loss. As a consequence, the influence of the low-loss BSEs to the signal is increased and even small differences in the composition of the sample provide a contrast difference which can't be seen with conventional BSE imaging.

Another advantage of LVSEM is the mitigation of sample damage which is of particular interest for biological and organic samples, as well as for some types of hybrid materials. In the case of OSG, the glass network is densified during the electron beam/sample interaction which phenomenologically causes a significant shrinkage of the material [3]. The spatial resolution and OSG thin film degradation during SEM imaging are studied systematically as a function of the primary beam energy with a Carl Zeiss SEM/FIB system NVision40 with Gemini column and three types of detectors, the conventional Everhart-Thornley detector, the Inlense detector and the Energy selective Backscattered electron detector (EsB). By combining the advantages of using a low accelerating voltage with the EsB detector, the compositional contrast is increased and the shrinkage phenomena is significantly mitigated, as shown in Figure 1.

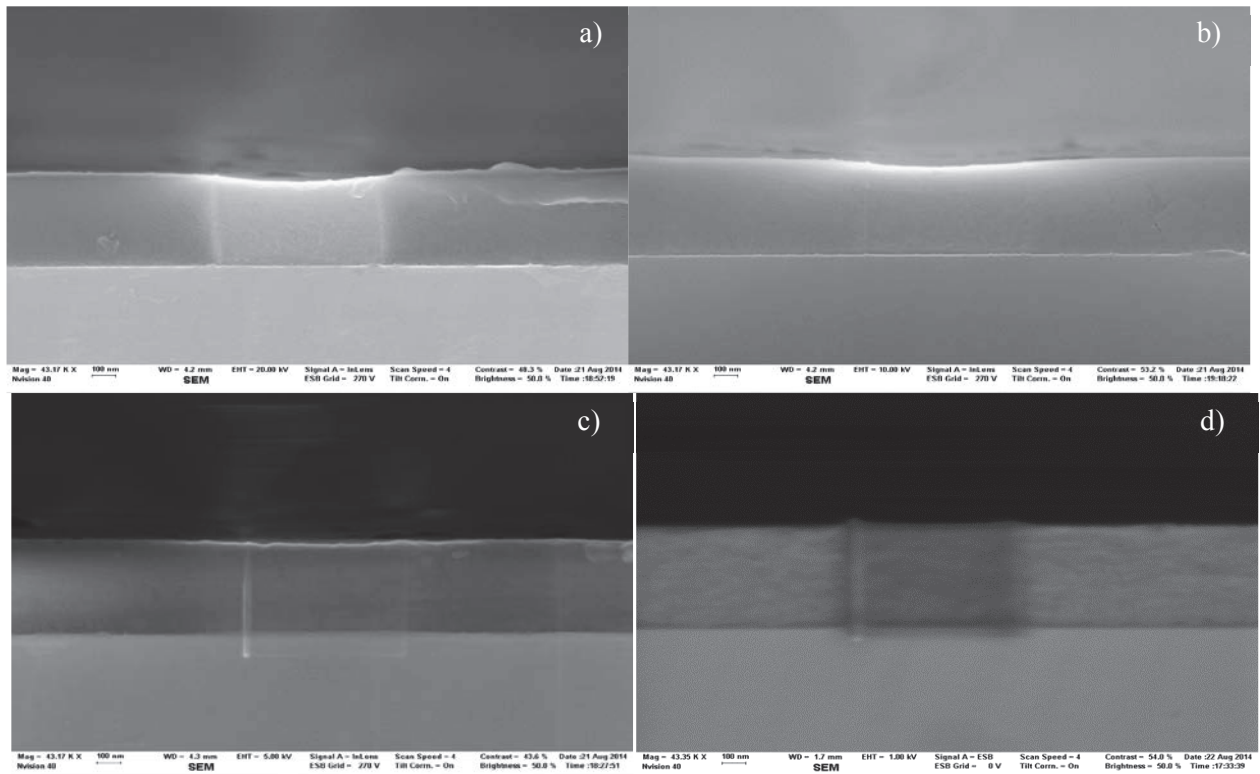


FIGURE 1. InLens images of shrinkage (a), (b), (c) in a OSG thin film on Si substrate after 3 min. scan with high magnification at $E_p = 20$ kV. The EsB image (d) shows no shrinkage with $E_p = 1$ kV.

ACKNOWLEDGMENTS

We kindly thank Carl Zeiss Microscopy GmbH, Oberkochen, Germany, for funding the investigations in the framework of the project “Untersuchungen zur Charakteristik und Applikation des EsB Detektors”. Constructive discussions with the Carl Zeiss Microscopy team, particularly with Markus Boese, are acknowledged.

REFERENCES

- [1] D. C. Bell, N. Erdman, *Low Voltage Electron Microscopy: Principles and Applications*, John Wiley & Sons, United Kingdom **2013**.
- [2] H. Schatten, J. B. Pawley, *Biological Low-Voltage Scanning Electron Microscopy*, Springer, USA **2008**.
- [3] H. Geisler, D. Chumakov, E. Zschech, *Nanomechanical Probing Techniques*, NanoS 01.08, 27–33, **2008**.

KEYWORDS

Low Voltage Scanning Electron Microscopy (LVSEM), Energy selective Backscattered (EsB) electron detector, Organosilicate Glass (OSG) thin film, shrinkage, Backscattered electron (BSE)

Correlative atom probe and STEM-HAADF tomography of nanodevices

A.Grenier¹, S.Duguay², R.Serra¹, J.P. Barnes¹, G Audoit¹, D Cooper¹, D. Blavette²,
N. Rolland², F. Vurpillot²

1. Univ. Grenoble Alpes, F-38000 Grenoble, France

CEA, LETI, MINATEC Campus, F-38054 Grenoble, France.

*2. Groupe de Physique des Matériaux, UMR 6634 CNRS —Université de Rouen, BP 12,
76801 Saint Etienne du Rouvray Cedex, France.*

INTRODUCTION

The next generation of CMOS transistors for the sub-22 nm nodes requires the use of new three dimensional architectures such as FinFET, GAA, FDSOI. The development of such complex structures involves a precise control of their morphology, dimensions and composition. This control remains a major challenge for the microelectronic industry. Hence, this technological development requires the development of 3D characterization techniques at the sub-nm or atomic scale, as mentioned in the ITRS¹ roadmap. Transmission electron microscopy remains the reference technique for characterization of nanodevices and, using electron tomography² (ET), can also perform 3D mapping of a sample at the nm-scale. However, the limited sensitivity and spatial resolution of chemical analysis in the TEM can be overcome by performing atom probe tomography (APT)^{3,4} on the same specimen.

RESULTS

Experimental Conditions

A PMOS test structure with a gate surrounded by a SiO₂ layer to improve the electrostatic control of the gate was investigated. Electron and atom probe tomography require the use of a needle-shaped specimen prepared by FIB (FEI Strata 400) using in situ lift-out followed by successive Ga ion annular milling at 30 keV and a very low energy cleaning at 2 keV. Electron tomography experiments were performed in the HAADF-STEM mode using a FEI 80-300 kV Titan microscope. A dedicated tomography holder (Fischione Model 2050) compatible with APT needles was used to tilt the specimen. Atom probe tomography characterizations were performed using a FlexTAP instrument (CAMECA). An amplified ytterbium doped laser operating at a wavelength of 343 nm, with a 450 fs duration, an energy of 35 nJ/pulse and a 100 kHz repetition rate was used. The tip temperature was maintained close to 70 K during analysis.

3D Analysis of a PMOS Structure

The PMOS structure that has been prepared with a tip shape is presented on the HAADF STEM image [figure 1(a)]. The dark and bright contrasts are assigned to the Si and SiO₂ contributions respectively. The morphology of gate and surrounding oxide has been determined using a reconstructed ET volume from 160 projection series using a simultaneous iterative reconstruction technique algorithm. The spatial resolution is close to 2 nm. As the average atomic number is too small, the boron spatial distribution is not visible.

Figure 1(b) shows the APT reconstructed volume that has been obtained using a tip profile method. Boron atoms have been detected in the poly Si-gate, as expected, but also in the surrounded oxide. Unfortunately, a tip failure has been occurred in the gate oxide, preventing analysis of the source and drain. Compared to the HAADF image, the APT reconstructions show strong deformations from the nominal structure. These deformations are generated by local magnification effects due to the difference of evaporation fields between the silicon oxide and silicon components of the sample. They are responsible for ion trajectory aberrations. Simulation of the evaporation of surface atoms from a tip containing the device structure has been performed to understand the origin of the distortions. These simulations take into account the values of evaporation fields and reproduce artefacts that are in the experimental reconstructed volume.

A reconstruction method based on an atomic density correction⁵ has been used to minimize the distortions. These improvements of APT reconstructions have been validated iteratively by matching the electron tomography volume with the corrected APT volume. This allows the best parameters for APT reconstructions to be found. Finally, as shown in figure 1 (c) this combination gives rise to a more realistic boron distribution in the 3D APT data within the complete device characterized by electron tomography. Hence, a 3D characterization of the PMOS structure is obtained and can be used to better understand the electrical properties.

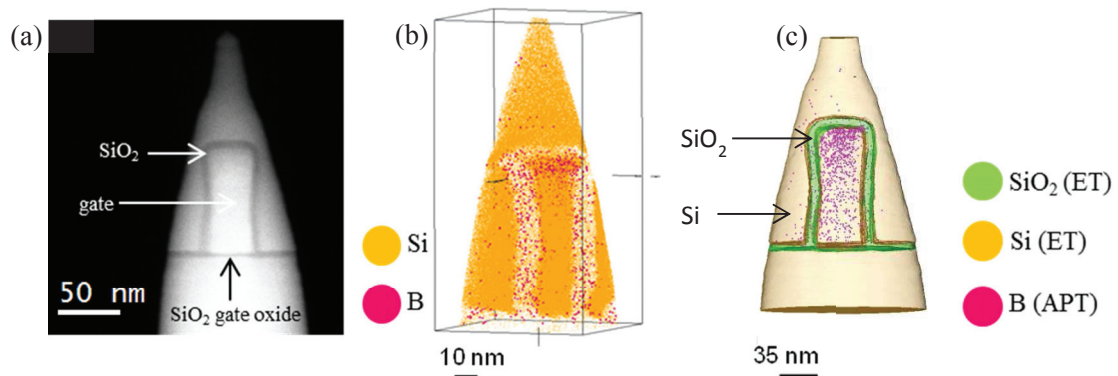


Figure 1: HAADF-STEM image of the PMOS device (a), boron and silicon APT volumes reconstructed according to the tip profile method (b), combination of the ET reconstructed volume with 3D boron corrected APT volume (c).

CONCLUSIONS

Complementary analyses using electron and atom probe tomography have been performed on simplified microelectronic structures. A morphological and chemical composition at the nm-scale is obtained by the use of the two techniques, which are essential for the development of new transistor architecture. However, atom probe tomography analyses on such device are distorted and required the use of advanced reconstructed algorithms, which are still in the development stage. The combination of atom probe tomography with electron tomography volumes is essential to identify the deformations of the raw reconstructions and validate advanced reconstructed methods.

ACKNOWLEDGEMENT

This work has been funded by the Recherche Technologique de Base (RTB) and APTITUDE project (ANR-12-NANO-0001) of the French National Research Agency. The experiments were performed on the Nanocharacterisation platform (PFNC) at MINATEC. Authors would like to thank Pierre Morin for providing samples.

REFERENCES

1. h. w. i. n. International Technology Roadmap for Semiconductors 2013 Edition Design.
2. P. A. Midgley and M. Weyland, *Ultramicroscopy* **96** (3-4), 413-431 (2003).
3. D. Blavette, A. Bostel, J. M. Sarrau, B. Deconihout and A. Menand, *Nature* **363** (6428), 432-435 (1993).
4. D. J. Larson, D. Lawrence, W. Lefebvre, D. Olson, T. J. Prosa, D. A. Reinhard, R. M. Ulfing, P. H. Clifton, J. H. Bunton, D. Lenz, J. D. Olson, L. Renaud, I. Martin and T. F. Kelly, *Journal of Physics: Conference Series* **326** (1), 012030 (2011).
5. F. De Geuser, W. Lefebvre, F. Danoix, F. Vurpillot, B. Forbord and D. Blavette, *Surface and Interface Analysis* **39** (2-3), 268-272 (2007).

KEYWORDS

Electron tomography, atom probe tomography, CMOS devices

Impact Of Line Edge Roughness Patterns On The Reconstructed Critical Dimensions In Scatterometry

H. Gross, S. Heidenreich, M.-A. Henn¹, F. Scholze, G. Dai, A. Rathsfeld² and M. Bär

Physikalisch-Technische Bundesanstalt, Braunschweig and Berlin, Abbestr. 2-12, 10587 Berlin, Germany

¹*NIST, 100 Bureau Drive, M/S 8212 Gaithersburg, Maryland 20899-8212, USA*

²*Weierstrass Institute for Applied Analysis and Stochastic, Mohrenstr. 39, 10117 Berlin, Germany*

INTRODUCTION

In angular resolved scatterometry, the measured diffraction intensities are effected by structure roughness. We investigate this impact by rigorous finite element method (FEM) calculations for an EUV photomask with periodic line-space structures. Repeated calculations for large FEM domains with stochastically chosen line and space widths are applied. Complementary simulations based on 2D-Fourier transforms for samples of binary 2D gratings confirm the FEM results. The edge roughness of the binary 2D gratings are modelled by a power spectrum density (PSD) function providing a more realistic approach for line roughness.

SCATTEROMETRY

Scatterometry as a non-imaging optical method in wafer metrology is also relevant to masks designed for Extreme Ultraviolet Lithography ($\lambda \sim 13.5 \text{ nm}$). The goal is to determine the critical dimensions (CD), i.e., the geometric profile parameters of the mask from measured diffracted light pattern and to estimate their uncertainties. The numerical simulation of the diffraction process for 2D periodic structures is done by FEM solution of the two-dimensional Helmholtz equation. If the light diffraction patterns are given by the measured diffraction intensities $\mathbf{y}^{meas} = (y_1, \dots, y_m)$, the geometry by the parameter vector $\mathbf{p} = (p_1, \dots, p_n)$, and the FEM solution by the nonlinear operator mapping $\mathbf{f}(\mathbf{p}) = (f_1(\mathbf{p}), \dots, f_m(\mathbf{p}))$, then the inverse problem of scatterometry is solved minimizing the norm $\|\mathbf{y}^{meas} - \mathbf{f}(\mathbf{p})\|$.

We consider the j th measured value as the sum of the model function and a noise contribution $y_j = f_j(\mathbf{p}) + \varepsilon_j$. This means that the measurements are noisy realizations of the model. Supposing independent measurements and no systematic errors, the variances of the noise contributions can be modelled as being normally distributed with zero mean, and composed of two independent random variables: $\sigma_j^2 = (af_j(\mathbf{p}))^2 + b^2$. The first term $af_j(\mathbf{p})$ indicates a linearly dependent noise, the second term b an independent background noise.

We apply a maximum likelihood estimation for reconstruction of the CDs. A likelihood function composed as the product of Gaussian functions of the residuals has to be maximized.

LINE EDGE ROUGHNESS (LER) MODELING

In order to examine the impact of line roughness, first we perform a large number of simulations for FEM domains with large periods, each containing many pairs of line and space with stochastically chosen widths (cf. Fig. 1, left part). Secondly, we apply a 2D Fourier transform method (FTM) during Fraunhofer approximation to calculate the diffraction pattern for samples of rough apertures composed of several slits. The rough apertures are representing binary 2D gratings (cf. Fig. 1, right part).

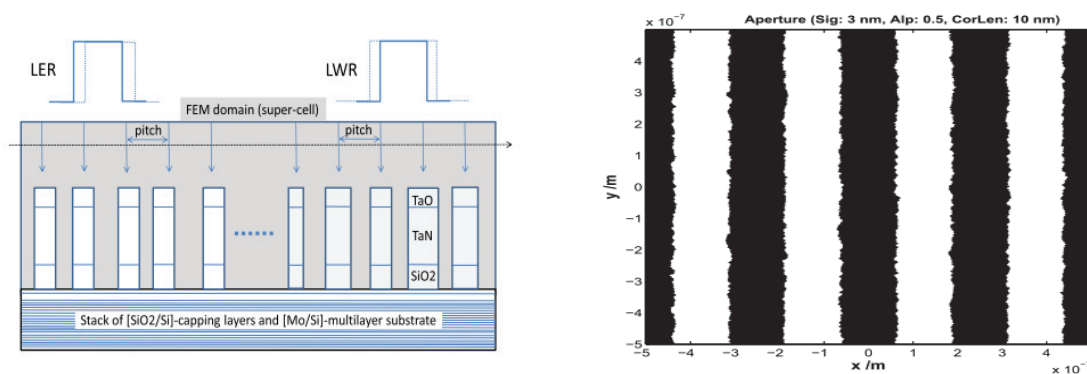


FIGURE 1. Profile models used for LER; **left:** cross section of large FEM domain containing many lines with randomly changed center positions and widths; **right:** aperture model for a 2D binary grating with line edges created by a power spectrum density function depending on a standard deviation of the roughness amplitude, a correlation length and a roughness exponent.

IMPACT ON EFFICIENCIES

For both methods we compare the calculated light efficiencies of the rough samples with those of the unperturbed line-space structures, i.e., the relative deviations from the 'non-rough' reference structures are investigated. Fig. 2 (a) reveals the details of an FEM example. A systematic decrease of the mean efficiencies for higher diffraction orders along with increasing variances is observed and established for different degrees of roughness. For the 2D FTM approach, very similar results are obtained confirming the FEM results (cf. Fig. 2 (b)). Note, that the line edge roughness of the 2D binary gratings is already fairly realistic. As a consequence the revealed LER-bias has to be included in the evaluation model by a diffraction order dependent damping factor.

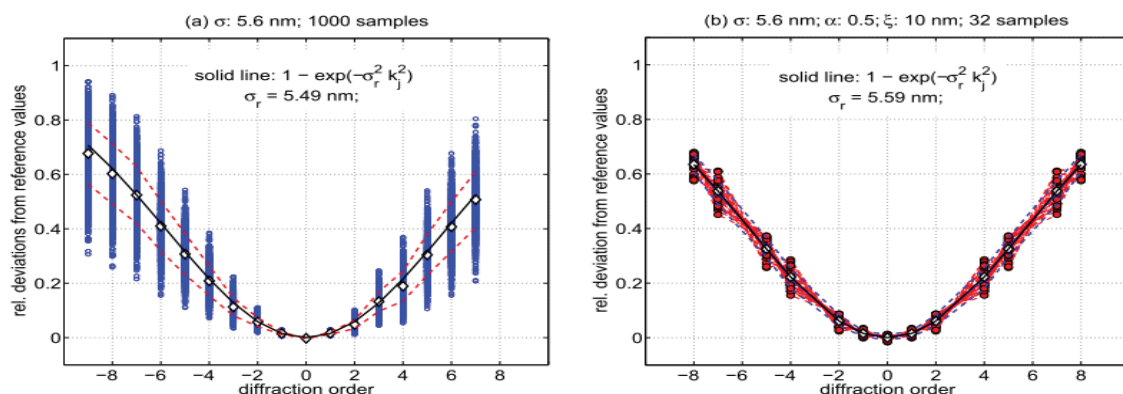


FIGURE 2. Normalized deviations from the efficiencies of the unperturbed line structure (a) for FEM simulations and (b) for 2D-Fourier transform simulations of 2D binary gratings; solid lines show the exponential approximation.

REFERENCES

1. H. Gross, S. Heidenreich, M.-A. Henn, G. Dai, F. Scholze and M. Bär, *J. Europ. Opt. Soc. Rap. Public.*, 9, 14003 (2014).
2. H. Gross, S. Heidenreich, M.-A. Henn, M. Bär, and A. Rathsfeld, *Discrete and Continuous Dynamical Systems Series S*, 8 No 3, pp 497-519, June 2015.

KEYWORDS

Scatterometry, line edge roughness (LER), finite element method (FEM), Fourier optics, Fraunhofer approximation

Acknowledgement: Results are part of project IND17 Scatterometry within the European Metrology Research Programme (EMRP).

Electron Tomography of Advanced Transistor Architectures

Andrew A. Herzing¹ and Jiong Zhang²

*Material Measurement Laboratory, National Institute of Standards and Technology, Gaithersburg, MD 20899 USA
Intel Corp., 2501 NW 229th Ave, Hillsboro, OR, 97124 USA*

INTRODUCTION

Continued improvement in the computing power of modern semiconductor devices relies critically on ever smaller components. For example, nanoscale transistor architectures exhibit a combination of fast switching capabilities, low power consumption, and high areal density on the silicon wafer. From a metrology standpoint, these structures pose an extreme challenge as they are comprised of nanoscale features which are structurally and chemically complex. The aberration-corrected scanning transmission electron microscope (STEM) combines atomic-scale spatial resolution with compositional spectroscopy, and is therefore an indispensable tool for characterization of modern architectures. However, in these instruments, data is collected in projection such that critical structural and chemical details in the through-thickness direction are often difficult to discern.

This problem has often been solved using tomographic techniques, in which a three-dimensional structure is calculated from a series of two-dimensional projections acquired over a range of specimen orientations. However, the quantitative and even qualitative interpretation of features in the reconstructed volume is hampered by instrumental constraints and issues related to data quality and processing. These factors can be reduced by improved specimen preparation and data collection methods [1] as well as by employing advanced reconstruction algorithms [2].

RESULTS

We have studied the nanoscale structure and composition of 22 nm tri-gate transistors. Specimens were prepared by focused ion beam (FIB) milling and lift-out techniques resulting in either cross-sectional lamellae containing several transistors or in cylindrical sub-regions of the array. Tomographic analysis was carried out in an FEI Titan 80-300 TEM/STEM [3] using the XPlor3D automated acquisition software.

Image alignment based on an iterated cross-correlation analysis was utilized, with results that appeared to be adequate when viewing the aligned tilt series by eye. However, significant artifacts due to residual mis-alignment between the images became apparent when the reconstructed tomogram was inspected. These artifacts make quantitative analysis of the resulting dataset problematic, due to difficulties with image segmentation. To improve the alignment, a multi-resolution technique based on minimization of the least-squares difference of image intensities was employed [4], resulting in a significant reduction in the reconstruction artifacts in the tomogram.

Cross-correlation alignment was particularly ill-suited to data collected from cylindrical specimens. Again, the multi-resolution alignment technique was found to work quite well. However, with this type of specimen, a particular difficulty often arises due to the orientation of the long axis of the specimen with respect to the tilt axis of the microscope stage. Because of the method of specimen preparation and mounting to the holder, these axes are often not coincident or even parallel which causes the cylinder to precess about the stage axis as the tilt data is acquired. This in turn results in significant reconstruction artifacts, which are often corrected by manually inspecting the reconstructed slices and minimizing the artifacts by eye. We have employed a more objective method to perform this alignment based on an iterative approach first suggested by Wolf *et al.* [5] and implemented using custom code written in Python 2.7. In this method, the center of mass of the cylinder is tracked as a function of tilt at three different

locations along the specimen axis. By fitting the observed path to that expected for a cylinder located at some arbitrary location from the true tilt axis of the stage, the specimen could be properly aligned in the field of view of the image stack.

The reconstruction from the more fully aligned dataset show that all remaining artifacts have been removed, with a significant increase in reconstruction quality and interpretability (Fig. 1). Because of this, subtle structural features which had previously been obscured are now clearly visible and can be quantitatively assessed.

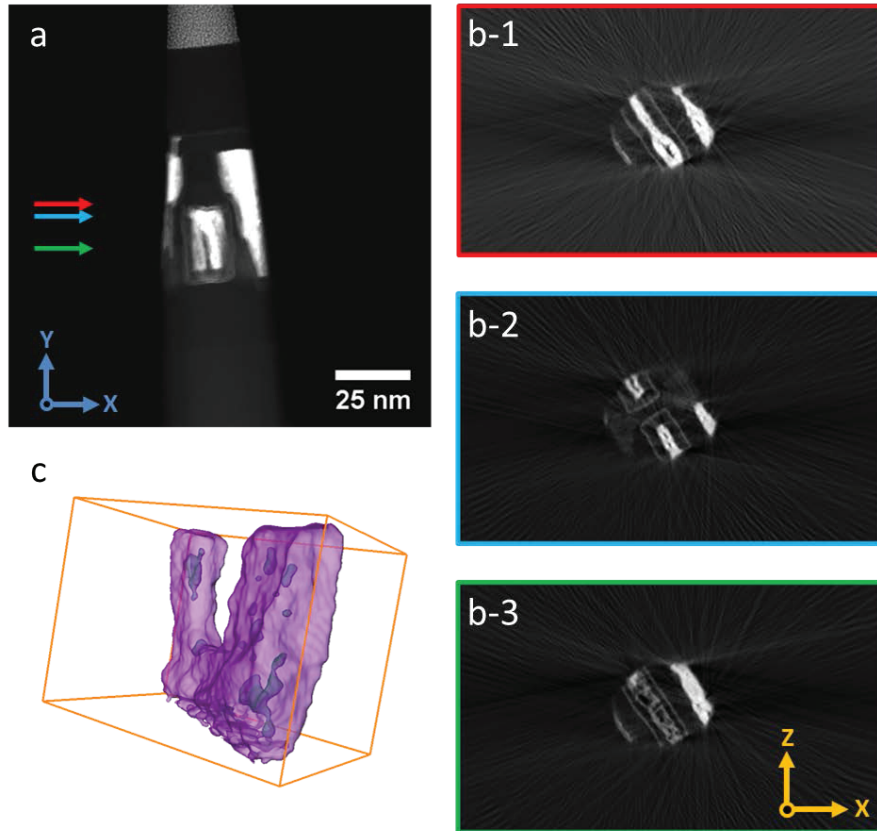


FIGURE 1. (a) Single annular dark-field projection image of pillar-shaped transistor specimen and (b) the corresponding results of tomographic reconstruction after automatic alignment. Slices were extracted along the row of pixels indicated by the colored arrows in (a). (c) Three-dimensional rendering of the gate (purple).

SUMMARY

Electron tomography is a powerful method for the characterization of the three-dimensional features in advanced transistor architectures. Proper interpretation of the subtle features present in the reconstructed data requires that artifacts resulting from microscope limitations and the quality of both the translational and rotational alignment of the image stack. The approach we have outlined has the advantage of being completely automated, with little to no user input required, and results in quantifiable data that can be used to develop correlations between device manufacturing parameters and the structural features which they produce.

REFERENCES

1. N. Kawase, M. Kato, H. Nishioka, and H. Jinnai, *Ultramicroscopy*, **107**, 8-15 (2007).
2. S.V. Venkatakrisnan, L.F. Drummy, M. Jackson, M. De Graef, J.P. Simmons, and C.A. Bouman, *IEEE Trans. Image Process.*, **22**, 1-13 (2013).
3. Any mention of commercial products is for information only; it does not imply recommendation or endorsement by NIST.
4. P. Thévenaz, U.E. Ruttimann, and M. Unser, *IEEE Trans. Image Process.*, **7**, 27-41 (1998).
5. D. Wolf, *Proc. of 15th Euro. Microsc. Cong.*, Manchester, UK, Sept. 16 – 21, 2012.

KEYWORDS

Electron tomography, STEM, microscopy

Reference-free, Depth-dependent Characterization Of Nanoscaled Materials Using A Combined Grazing Incidence X-ray Fluorescence And X-ray Reflectometry Approach

Philipp Hönicke¹, Blanka Detlefs², Claudia Fleischmann³, Matthias Müller¹, Emmanuel Nolot², Helen Grampeix² and Burkhard Beckhoff¹

1: Physikalisch-Technische Bundesanstalt (PTB), Abbestr. 2-12, 10587 Berlin, Germany

2: CEA-LETI, 17 rue des Martyrs, 38054 Grenoble, France

3: imec, Kapeldreef 75, BE-3001 Leuven, Belgium

INTRODUCTION

The accurate in-depth characterization of nanoscaled layer systems is of importance for current developments in many fields of materials research. Thin high- κ layers, gate stacks and ultra-shallow dopant profiles involving many different chemical elements are technologically relevant for current and future electronic devices. The reliable characterization of such systems presents several metrological challenges and requires further development of the available analytical techniques. Furthermore, quantitative analysis usually relies on nanoscaled reference materials or calibration samples of sufficient quality and equality with respect to the actual analytical problem.

The rather limited availability of such nanoscaled reference materials can be addressed with the reference-free X-ray fluorescence spectrometry methodologies [1,2] of the Physikalisch-Technische Bundesanstalt (PTB), Germany's national metrology institute. Using in-house build radiometrically calibrated instrumentation [1] and tabulated or experimentally determined [3] atomic fundamental parameter-based quantification, these techniques do not require any reference - or calibration standard.

Reference-free grazing incidence X-ray fluorescence (GIXRF) analysis in combination with X-ray reflectometry (XRR) is one of these methodologies allowing for a quantitative, in-depth characterization of nanoscaled materials such as nanolaminate composites [4] and ultra-shallow dopant profiles [5].

COMBINED GIXRF/XRR ANALYSIS

The GIXRF elemental depth profiling is based on the incident angle induced changes of the XSW field intensity distribution. The XSW field arises between the incident and the reflected X-ray beam and is convolved with the depth profile of the element of interest, creating a specific angular fluorescence curve during a GIXRF measurement. This GIXRF curve can be modeled by modifying the shape of an assumed depth profile [5] and a calculation for the XSW field.

These calculations rely on the knowledge of the optical constants of the materials involved. In some cases, e.g. for selected ion implants, tabulated optical constants without taking the implant into account can be used. However, for nanoscale layers, the physical properties are often very different from the bulk properties, hence the tabulated optical constants and other relevant parameters are not available.

XRR provides access to the optical properties of the sample and can be conducted in parallel to the GIXRF measurements. The combined data analysis of both the XRR and the GIXRF data provides an almost complete description of the sample [6] with respect to the composition in depth, layer thicknesses as well as interfacial roughnesses.

EXPERIMENTAL

Thin $\text{Al}_2\text{O}_3/\text{HfO}_2$ nanolaminate layer stacks in different sequences with up to three layers and thicknesses in the nanometer range have been deposited on silicon wafers with a native oxide layer using atomic layer deposition (ALD). A description of the samples with respect to their layer sequence can be found in Table 1. In addition, several ultra shallow arsenic ion implants into silicon were fabricated and analyzed using the XRR combined GIXRF approach.

The experiments were carried out using PTB's in house built setup [7] for total-reflection X-ray fluorescence (TXRF) at very shallow angles of incidence, grazing-incidence X-ray fluorescence (GIXRF) at variable angles of incidence and conventional XRF. The emitted fluorescence radiation is detected by a calibrated silicon drift detector (SDD) mounted at 90° with respect to the incident beam. Photodiodes on the 2θ axis allow for XRR measurements simultaneously with the GIXRF measurements.

The samples were measured at two PTB beamlines [8,9] at the electron storage ring BESSY II. Two photon energies were used for optimal excitation conditions for Al-K fluorescence radiation ($E_0 = 1622$ eV) and the Hf-L lines ($E_1 = 10$ keV). At both photon energies, a GIXRF and a XRR measurement were conducted in parallel. The As ion implant samples were measured at 1540 eV. The recorded fluorescence spectra were deconvoluted using known detector response functions for the fluorescence lines of interest as well as relevant background contributions. The fluorescence intensities for oxygen, aluminium and hafnium can directly be transferred into mass depositions due to the reference-free XRF approach [1]. The used fundamental parameters are either derived from databases or from dedicated experiments at PTB [3].

TABLE 1 Description of the different layer sequences of the nanolaminate samples used in this work.

Sample	Layer sequence
S1	$\text{Al}_2\text{O}_3/ \text{HfO}_2/\text{SiO}_2$ on Si
S2	$\text{HfO}_2/ \text{Al}_2\text{O}_3/ \text{HfO}_2/ \text{SiO}_2$ on Si
S3	$[\text{Al}_2\text{O}_3/ \text{HfO}_2]_3/ \text{SiO}_2$ on Si
S4	$\text{Al}_2\text{O}_3/ \text{HfO}_2/ \text{Al}_2\text{O}_3/ \text{SiO}_2$ on Si
S5	$\text{Al}_2\text{O}_3/ \text{HfO}_2/ \text{Al}_2\text{O}_3/ \text{SiO}_2$ on Si

Furthermore, XRR measurements using a Bruker D8 Fabline instrument handling 300 mm wafers with a $\text{Cu K}\alpha$ X-ray source were conducted at CEA-LETI and fitted using the Bruker LEPTOS software to derive layer thicknesses independently and to estimate systematic errors due to the choice of the structural model.

RESULTS

The reference-free quantification results of the $\text{Al}_2\text{O}_3/\text{HfO}_2$ nanolaminate layer stacks [4] can be compared to calculated mass depositions from XRR fitting results. Therefore, XRR determined values [4] for the layer thickness and density are multiplied and added up if more than one layer of the same species is present on the sample. A comparison of the mass depositions for Al determined with the reference free GIXRF setup and the XRR determined values is shown in Fig. 1. The stated experimental uncertainties are estimated for the XRR results, whereas the total uncertainty budget is calculated for the values obtained by GIXRF [10]. Main contributions to the uncertainty budget come from the used FPs and the solid angle of detection.

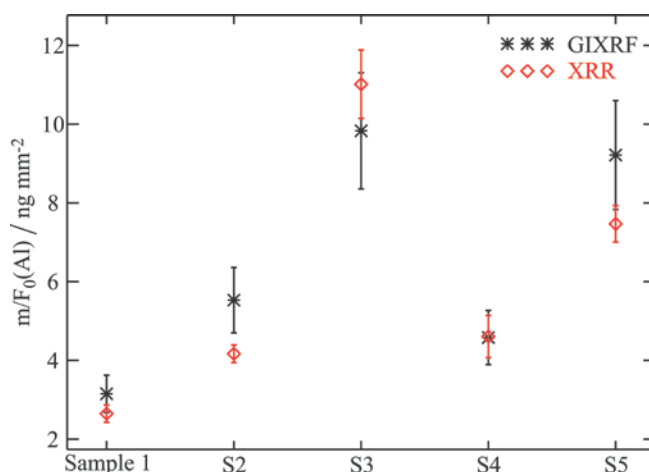


FIGURE 1. Quantification results of the Cu-K α XRR instrument [4] in comparison to reference-free GIXRF for the mass deposition of Al.

For a part of the samples investigated, the results of the XRR measurements do not agree with the GIXRF data. For sample S2, the difference is larger than the uncertainties indicating an underestimated uncertainty budget for the XRR. For the results on Hf, shown in table 2, the behavior is very similar.

This demonstrates the necessity to model the GIXRF and XRR results in a combined approach in order to take advantage of their complementarity. Further details and results of the combined data evaluation of XRR and GIXRF experimental data will be shown.

TABLE 2 Comparison of quantification results for the mass deposition of Hf.

Sample	GIXRF / ng/mm ²	XRR / ng/mm ²
S1	8.6 ± 0.9	9.8 ± 0.8
S2	5.6 ± 0.6	8.6 ± 1.2
S3	36.2 ± 3.7	41.9 ± 2.5
S4	12.3 ± 1.3	12.8 ± 0.8
S5	2.9 ± 0.3	4.4 ± 0.6

REFERENCES

1. B. Beckhoff, *J. Anal. At. Spectrom.* **23**, 845 (2008).
2. B. Beckhoff, R. Fliegauf, M. Kolbe, M. Müller, J. Weser, G. Ulm, *Anal. Chem.* **79**, 7873 (2007).
3. P. Hönicke, M. Kolbe, M. Müller, M. Mantler, M. Krämer, B. Beckhoff, *Phys. Rev. Lett.* **113(16)**, 163001 (2014).
4. P. Hönicke, B. Detlefs, M. Müller, E. Darlatt, E. Nolot, H. Grampeix, B. Beckhoff, *PSSC* (2014).
5. P. Hönicke, Y. Kayser, B. Beckhoff, M. Müller, J.C.I. Dousse, J. Hozzowska, S.H. Nowak, *J. Anal. At. Spectrom.* **27**, 1432 (2012).
6. A.J.G. Leenaers, D.K.G. De Boer, *X-ray Spectrom.* **26**, 115 (1997).
7. J. Lubeck, B. Beckhoff, R. Fliegauf, I. Holfelder, P. Hönicke, M. Müller, B. Pollakowski, F. Reinhardt, J. Weser, *Rev. Sci. Instrum.* **84**, 045106 (2013).
8. F. Senf, U. Flechsig, F. Eggenstein, W. Gudat, R. Klein, H. Rabus, G. Ulm, *J. Synchrotron Rad.* **5**, 780 (1998).
9. M. Krumrey, G. Ulm, *Nucl. Instrum. Meth. A* **467-468**, 1175 (2001).
10. M. Müller, P. Hönicke, B. Detlefs, C. Fleischmann, *Materials* **7(4)**, 3147 (2014).

KEYWORDS

GIXRF, XRR, depth profiling, ultra-shallow implants, nanolaminates

Extreme Ultraviolet Nanometrology for Imaging of New Dynamics in NanoSystems

Kathleen Hoogeboom-Pot^{1*}, Jorge Hernandez-Charpak¹, Dennis Gardner¹, Matthew Seaberg¹, Bosheng Zhang¹, Travis Frazer¹, Elisabeth Shanblatt¹, Christina Porter¹, Robert Karl¹, Erik Anderson², Weilun Chao², Justin Shaw³, Margaret Murnane¹, Henry Kapteyn¹, Daniel Adams¹ and Damiano Nardi¹

1. JILA, 440 UCB, University of Colorado, Boulder CO 80309

2. Center for X-Ray Optics, Lawrence Berkeley National Laboratory, Berkeley, CA 94720

3. Electromagnetics Division, NIST, Boulder, CO 80305

hoogeboo@jila.colorado.edu

INTRODUCTION

Advanced materials development and device design require reliable characterization tools to discover, optimize and monitor new nanoscience and nanomanufacturing techniques. Moore's Law scaling has pushed the frontiers of nanofabrication so far that the thinnest films and smallest nanostructures being made today cannot easily be measured using current metrology techniques. Yet precise characterization of materials and surfaces in nanostructured devices is necessary for understanding and harnessing the unique physics that applies to such small-scale systems: how elastic properties change with scaling from monolayers to bulk material, for example, or how phonon spectra in materials govern thermal dissipation in the deep nanoscale regime $\ll 100\text{nm}$.

To overcome the challenges, we implement a non-contact, non-destructive technique that uses coherent extreme ultraviolet (EUV) light from tabletop high harmonic generation (HHG)¹ in place of more conventional visible-wavelength laser probes. The shorter wavelength of EUV beams can achieve near-wavelength-resolution 3D imaging of surfaces and is sensitive to picometer-scale displacements. In addition, the femtosecond duration of HHG pulses is fast enough to capture the fastest thermal, magnetic and acoustic dynamics in few-nm scale structures. Moreover, with photon energies spanning many relevant element-specific absorption edges, element-mapping, contamination detection and identification, and studies of element-resolved dynamics are possible.

Here we demonstrate powerful new capabilities of EUV HHG sources for dynamic elastic and thermal characterization of materials and nanostructures with $\ll 100\text{ nm}$ characteristic dimensions. We show how this technique can be extended to fully spatially-resolved imaging of localized dynamics by combining the tabletop HHG source with coherent diffractive imaging (CDI) techniques. In exciting recent work, we achieved record spatial resolution tabletop 45 nm full field 3D imaging using an illumination wavelength of 30 nm. Moreover, we uncovered a new regime of collective heat dissipation that can improve thermal transport from closely-packed nanoscale hot spots. This new HHG light source, which now extends into the soft X-ray region, will enable new revolutionary capabilities for observing nanoscale systems on their intrinsic length and time scales.

DYNAMIC ACOUSTIC AND THERMAL NANOMETROLOGY

In order to study the elastic and thermal transport properties unique to nanostructured systems, we use a pump-probe setup to directly observe their dynamics. Our samples consist of periodic arrays of metallic nanostructures deposited on dielectric or semiconductor substrates, in some cases with an additional low-k dielectric ultrathin film on top of the substrate. As shown in Fig. 1, a femtosecond 800nm laser pump pulse is focused onto the samples to

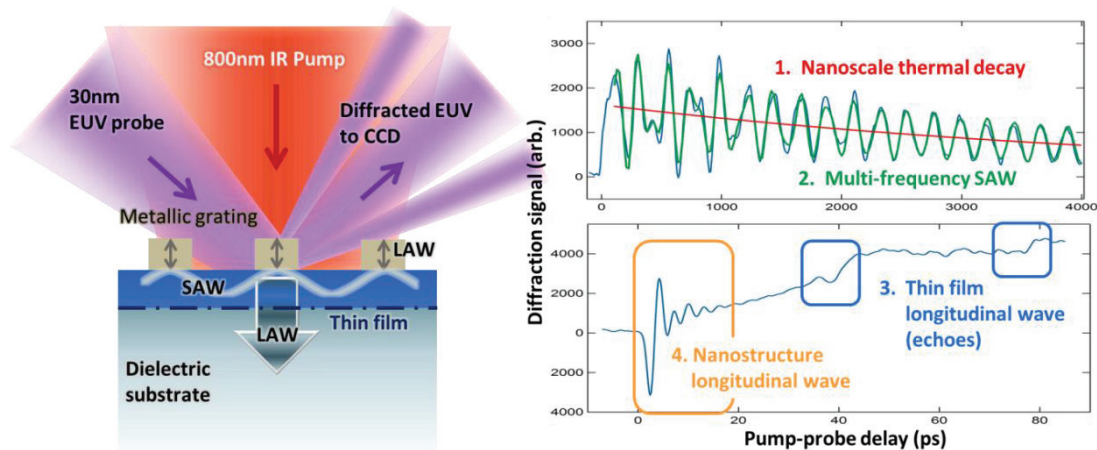


Figure 1. A periodic array of metallic nanostructures is impulsively excited with a femtosecond infrared pump pulse, depositing heat and launching acoustic waves into the system. Changes in the diffracted intensity of an EUV probe pulse are collected as a function of pump-probe delay to follow the acoustic and thermal transport dynamics in the system.

impulsively heat the nanostructures and launch acoustic waves: longitudinal waves (LAWs) within the nanostructures, LAWs traveling across the depth of the film and transverse surface acoustic waves (SAWs) in the film and substrate with a wavelength set by the grating period.

All these dynamics can be monitored simultaneously by diffracting a 30nm-wavelength EUV HHG probe beam from the surface². Compared with other EUV/X-ray sources, such as large-scale synchrotron facilities or X-ray free-electron lasers, HHG has the advantage of being a compact tabletop source. This fact, coupled with high spatial and temporal coherence (short wavelength and short pulse duration) makes HHG an ideal probe for capturing structure and ultrafast processes at the nanoscale. Expansion and cooling of the nano-gratings, as well as acoustic wave propagation change the EUV diffraction efficiency, and this signal is recorded by a CCD camera as a function of delay time between pump and probe pulses (see Fig. 1).

The SAW and LAW resonances of the nano-gratings yield information about the mechanical properties of the materials. In particular, by studying how these resonances shift for bilayer nickel-tantalum (Ni-Ta) structures as the Ta capping-layer thickness is varied between 1 and 6nm (with Ni at a constant thickness of 10nm), we determine the densities and longitudinal acoustic velocities of both materials in the ultrathin layers. In doing so, we confirm for the first time that the densities of Ni and Ta are not changed substantially by their confinement to such thin layers, but the elastic properties differ significantly from their bulk values. The LAW echoes and the short-wavelength SAWs which are confined within ultrathin film layers (as thin as 10nm) between the nanostructures and substrate can also be used to characterize both the Young's modulus and Poisson's ratio for an isotropic film in a single measurement².

In very exciting recent work, we analyzed the thermal decay signal which uncovered transitions to a new heat dissipation regime as the Ni heat source (nanowire or nanodot) linewidth varies between 1 μm and 20 nm. While previous work showed a decrease in thermal transport efficiency from nanoscale heat sources as the heat transfer process becomes increasingly non-diffusive³, we observe for the first time that collective diffusion from closely-spaced nanoscale heat sources can restore heat dissipation efficiency toward the diffusive limit⁴. This surprisingly allows closely-spaced nanoscale heat sources to cool more efficiently than widely-spaced heat sources of the same size. Furthermore, the direct relationship between this new 'collectively-diffusive' regime and the particular phonon spectrum of the substrate material enables the characterization of these spectra in novel materials with the detail necessary for accurate predictions of heat dissipation in nanostructured systems.

HIGH RESOLUTION IMAGING WITH EUV CDI

While the dynamic metrology applications discussed involve the average elastic properties over many square microns of the surface or the average thermal dissipation from hundreds or thousands of individual nanostructures, many other applications require more localized sensitivity. These could include surface or buried defect detection, mapping local differences in elastic properties such as those near fabricated structures, or tracking heat flow through complicated device structures. Such applications require spatially-resolved dynamic imaging of systems, which can be obtained by combination of the techniques discussed above with full-field high-resolution

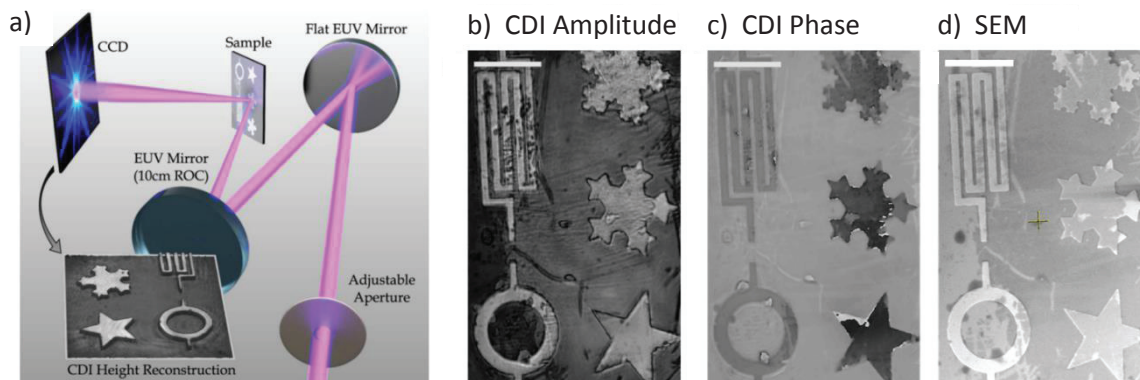


Figure 2. a) Schematic of a typical EUV CDI reflection-mode microscope. The HHG beam passes through an adjustable aperture to put a hard edge on the beam allowing reconstruction of extended samples. The beam is spectrally filtered by two multilayer mirrors and focused onto the sample. The inset shows the computationally reconstructed image of the sample. **b-d)** Comparison of CDI images with SEM. The scale bar in the upper left of each image represents 10 μm . Note the higher contrast attainable by using EUV wavelengths in CDI.

microscopy enabled by lensless CDI using the HHG EUV light source. Since most samples of interest to the semiconductor community are many times thicker than the absorption length of EUV wavelengths, we developed the first fully general reflection-mode EUV microscope, shown schematically in Fig. 2a⁵. Our technique works with any wavelength, at any angle of incidence, with no numerical-aperture (and thus resolution) limiting apertures between the sample and the detector.

To overcome the lack of focusing elements available for EUV microscopy, we use a CDI technique known as ptychography. This requires scanning a probe beam across the sample and recording the scattered light. Unlike point scanning microscopy, where the resolution is limited by the spot size, the resolution in ptychography is limited only by the wavelength of illumination and the numerical aperture (NA).

While a CCD can only capture the amplitude of the scattered light from the sample, an iterative computer algorithm such as ePIE⁶ can be used to reconstruct the missing phase information and thus retrieve a full 3D map of the sample surface. For the example images shown in Fig. 2b-d, a total of 198 diffraction patterns were recorded from the titanium-on-silicon sample. Each diffraction pattern has an exposure time of 0.3 second. After 350 iterations the algorithm sufficiently converged, resulting in an image with 45 nm lateral resolution and <1 nm height resolution which captures as much detail as a comparable SEM image, though with significantly higher contrast. Moreover, this technique is directly scalable to higher spatial resolution by decreasing the wavelength of illumination or increasing the NA and can be applied to surfaces of any material – conducting and insulating alike.

By combining reflection-mode CDI with dynamic nanometrology techniques using HHG sources in the kiloelectronvolt photon energy region, it will be possible to capture nanoscale surface dynamics and characterize materials properties with femtosecond temporal and nanometer spatial resolution.

REFERENCES

1. T. Popmintchev et al., *Science* **336**, 1287 (2012).
2. D. Nardi et al., *Proc. SPIE* **8681**, 868110N (2013).
3. M. Siemens et al., *Nature Mater.* **9**, 26 (2010).
4. K. Hoogeboom-Pot et al., *submitted*, arXiv 1407.0658 (2014).
5. M. Seaberg et al., *Optica* **1**, 39 (2014).
6. A. Maiden et al., *Ultramicroscopy* **109**, 1256 (2009)

KEYWORDS

Nanoscale Metrology, Extreme Ultraviolet, High-Harmonic Generation, Tabletop, Ultrafast, Coherent Diffractive Imaging

Simulation of Ga Ion Induced Amorphization in Si during FIB using TRIDYN simulation

Jin Huang¹, Markus Loeffler¹, Wolfhard Moeller² and Ehrenfried Zschech^{1,3}

¹ Technische Universität Dresden, Dresden Center for Nanoanalysis (DCN), Helmholtzstrasse 18, 01187 Dresden, Germany

² Institute of Ion Beam Physics and Materials Research, Helmholtz-Zentrum Dresden-Rossendorf, Bautzner Landstr. 400, 01328 Dresden, Germany

³ Fraunhofer Institute for Ceramic Technologies and Systems (IKTS), Maria-Reiche-Strasse 2, 01109 Dresden, Germany

INTRODUCTION

It is well known in the microscopy community that crystalline silicon (c-Si) is partially amorphized during Focused Ion Beam (FIB) preparation. Typically, a 30 kV Ga ion beam incidence with a small glancing creates a 15-30 nm thick amorphous layer at the c-Si surface [1]. However, the precise mechanism remains not well understood. In this work, as the initial phase of a more sophisticated study, we use a Binary Collision Approximation code, TRIDYN, to simulate the amorphization of c-Si during Ga ion irradiation.

BINARY COLLISION APPROXIMATION

The question whether to adopt Molecular Dynamics (MD) or Binary Collision Approximation (BCA) for simulations of ion-solid interactions has been widely discussed in literature. While MD is a much more precise simulation technique, BCA is more computationally efficient [2-4]. In principle, MD simulates the physical movement of atoms and molecules in the context of multi-body effects, whereas in BCA, the ion is approximated to travel through a material by experiencing a sequence of independent binary collisions with sample atoms. A large simulation volume has to be considered for FIB simulation [5]. Therefore a BCA code named TRIDYN is used in this study.

Principles of TRIDYN and Assumptions for Simulation

TRIDYN is a computer software that treats the deceleration of ions in solids, and the associated formation of recoil atom cascades in the BCA. It takes into account dynamic alterations of the local composition which arise from the implantation process for ions and the collisional transport movement of target atoms. In this way, phenomena such as implantation profiles, atomic mixing, sputtering and recoil implantation, which occur during high-fluence ion bombardment, can be simulated [6, 7].

Due to the limitation of BCA, TRIDYN is not able to simulate the translation symmetry of crystalline materials. Therefore, alternative criteria for the amorphization of c-Si needs to be established. It has been demonstrated by Monte Carlo simulation and experimental studies that silicon amorphization can be described by host-atom displacement. The threshold displacement for amorphization in silicon is 5 Å [8]. On the other hand, it has also been shown that, in terms of atom displacement, MD and BCA do not have a significant difference for < 5 Å atom

displacement [9]. Therefore, it is feasible to use TIRDYN for the simulation of silicon amorphization during FIB, under the mentioned assumptions.

TABLE 1. Si amorphous layer thickness as a function of ion energy, for 3°, 5° and 7° glancing angles (thickness values are rounded to one digit after the decimal point)

Ga Ion Energies /kV	with 3° Glancing Angle /nm	with 5° Glancing Angle /nm	with 7° Glancing Angle /nm
30	25.4	26.4	27.1
16	15.0	15.6	16.0
8	8.5	8.9	9.0
5	5.7	6.4	6.2
4	4.7	5.4	5.3
3	3.8	4.4	4.2
2	2.7	3.4	3.2
1	1.8	2.1	2.0
0.5	1.2	1.4	1.4
0.2	0.7	0.9	0.8

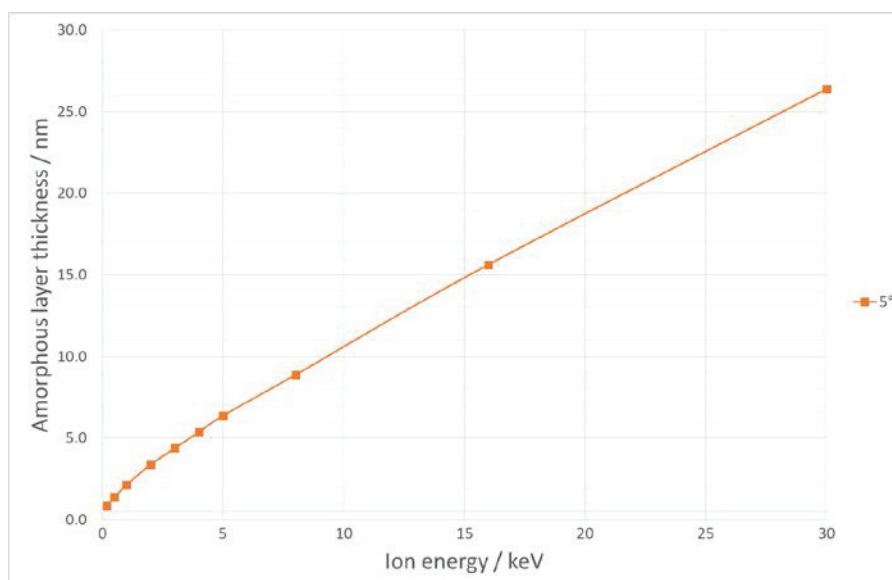


FIGURE 1. Si amorphous layer thickness as a function of ion energy, with 5° glancing angle.

Simulation Results

Table 1 shows the amorphous thicknesses for several simulation parameters. It can be seen that the glancing angle does not have a significant effect here, especially for low energies. Figure 1 shows the amorphous layer thickness for several gallium ion energies at 5° glancing angle. The curve is more or less linear except for in the lower energy range. This result indicates that the amorphization mechanism might be different for higher and lower energies of Ga ion, or even the lower bound of the amorphization.

SUMMARY

In this study, we have employed TRIDYN as a simulation tool to determine the amorphous layer thickness for several FIB conditions, assuming that silicon has an amorphization threshold of 5 Å atom displacement and that BCA is valid for > 5 Å atom displacement. Preliminary comparison to experimental literature data shows that the simulation data is trustworthy [10-12].

REFERENCES

- [1] H. J. Engelmann et al., *Microscopy Today* **11**, 22-24 (2003).
- [2] M. T. Robinson, *Radiation Effects and Defects in Solids: Incorporating Plasma Science and Plasma Technology* **130-131:1**, 3-20 (1994).
- [3] M. F. Russo Jr. et al., *Applied Surface Science* **255**, 828-830 (2008).
- [4] M. F. Russo Jr. et al., *Microsc. Microanal.* **14**, 315-320 (2008).
- [5] L. A. Giannuzzi et al., *J. Vac. Sci. Technol.* **A25**, 1417-1419 (2007).
- [6] W. Moeller and W. Eckstein, *Nuclear Instruments and Methods in Physics Research* **B2**, 814-818 (1984).
- [7] W. Moeller and W. Eckstein, *Computer Physics Communications* **51**, 355-368 (1988).
- [8] L. J. Gracia et al., *Journal of Applied Physics* **109**, 123507 (2011).
- [9] L. Bukonte et al., *Nuclear Instruments and Methods in Physics Research Section B: Beam Interactions with Materials and Atoms* **297**, 23-28 (2013).
- [10] E. Holmstroem et al., *AIP Advances* **2**, 012186 (2012).
- [11] L. A. Giannuzzi et al., *Microsc. Microanal.* **11**, 828-829 (2005).
- [12] L. Lechner et al., *Microsc. Microanal.* **18**, 379-384 (2012).

KEYWORDS

Focused Ion Beam, Silicon Amorphization, Binary Collision Approximation

Characterization of Cross-Sectional Profile of Resist Pattern Using Grazing-Incidence Small Angle X-Ray Scattering

Yoshiyasu Ito, Akifusa Higuchi, Kazuhiko Omote

Rigaku Corporation, 3-9-12 Matsubara-cho, Akishima, Tokyo, Japan 190-8666

INTRODUCTION

The scale of semiconductor devices is continuously shrinking, and the critical dimension is now expected to reach down close to ten-nanometers in the near future. The performance of such a fine device can be easily affected by a slight variation in the shape of the resist pattern. It is, therefore, important to carry out quality control over the cross-sectional profile of resists.

Critical dimension scanning electron microscope (CD-SEM) is used for CD metrology on mass production lines. However, the CD-SEM cannot measure cross-sectional profile, especially when there is an inverse tapered shape. In addition, it is well known that the electron beam can make a serious damage on the resist pattern. This arouses a doubt whether cross-sectional electron microscope methods, either scanning (SEM) or transmission (TEM), measure correct shapes.

Small angle x-ray scattering (SAXS) is one of the candidates for measuring cross-sectional profile non-destructively. Generally, x-ray metrology is suitable for detecting a slight shape variation as the wavelength (0.05-0.2 nm) is well shorter than the critical length of the pattern structure.

Two kinds of measurement systems have been proposed. One is transmission geometry and the other is grazing incidence geometry. While the transmission geometry is suitable for measuring a small area, it requires a longer collecting time due to its small scattering volume. Also, the scattering from the underlayers can easily affect the results because the x-rays pass thorough all the layers. On the other hand, the grazing incidence geometry, whose measurement area is typically 300 times larger than that of the transmission method, is suitable for measuring surface structure in a short collecting time without being affected by the underlayer scattering. For that matter, transmission geometry is suitable for measuring deep trench or hole (>250 nm) and grazing incidence geometry is suitable for measuring shallow trench or hole (<250 nm).

CD-SAXS INSTRUMENT

We have developed a new SAXS-based metrology tool (RIGAKU CD-SAXS)¹⁻⁴. The system utilizes the grazing incidence geometry in order to perform quick measurements on mass production lines. Figure 1 shows the appearance of the CD-SAXS instrument and its measurement geometry. The x-ray generator is operated at 30W (40 KV, 0.67 mA). Monochromatic x-ray with wavelength of 0.15418 nm (Cu K α line) irradiates the sample surface. The vertical and lateral dimensions of the cross section of the beam at the sample position are about 0.015 mm and 2 mm, respectively. The incident angle is set to be very close to the critical angle of total external reflection. The sample has to be rotated around the vertical axis at the irradiated point during the measurement because diffraction occurs only when the diffraction condition in the lateral plane is satisfied. Diffraction peaks corresponding to the pitch size of the sample pattern appear in the lateral direction, and are detected by a two dimensional pixel detector. The average pitch and the width of pattern lines can be determined by the diffraction angle and the intensity ratio of these peaks, respectively. Each diffraction peaks has a characteristic fringe pattern in the vertical direction. Depth, sidewall shape, and corner rounding shape can be determined by the periodicity and the phase of the fringe patterns, which strongly depend on the order of diffraction h .

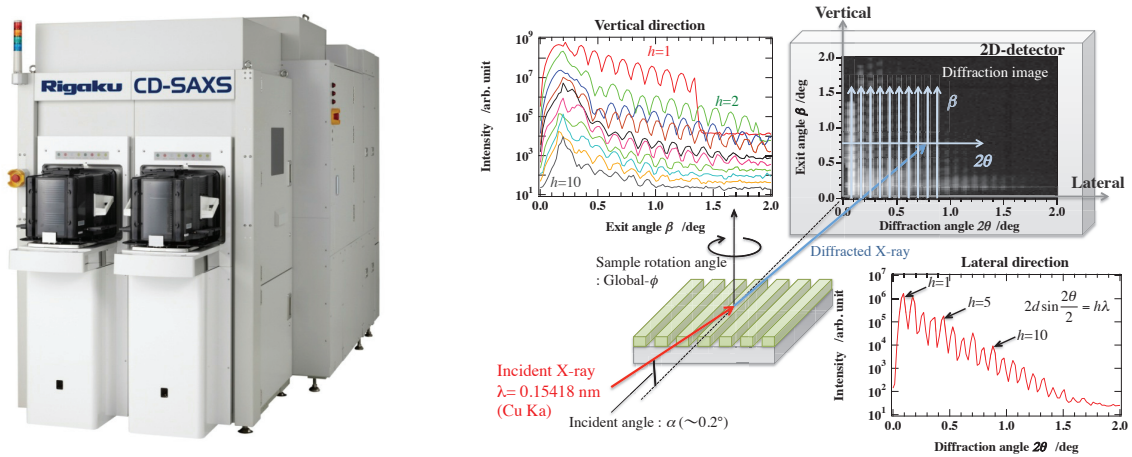


FIGURE 1. CD-SAXS instrument (left side) and its measurement geometry (right side).

CROSS-SECTIONAL PROFILE ANALYSIS OF RESIST L/S PATTERN

Two kinds of resist L/S pattern wafers were prepared as the samples. The both have a 130 nm pitch size, but they were fabricated with different material composition and exposure condition in order to obtain different cross-sectional profile between two resists. Figure 2 shows their cross-sectional SEM images, which, although not very clear, indicate that both samples have an inverse tapered structure and that the shape of the top corners are different between resists A and B.

Figure 3 shows diffraction patterns and cross-sectional profiles of these samples measured by the CD-SAXS instrument. The cross-sectional profiles were determined by a model fitting method using the line-width, depth, sidewall angle, top corner rounding (ellipsoidal shape), and bottom corner rounding (ellipsoidal shape) as fitting parameters. In addition, fluctuation parameters such as pitch variation, width variation, and depth variation were also optimized. Obtained cross-sectional profiles, which show an inverse tapered shape in the two resists and a difference in the top corner rounding shape between the two can be regarded as consistent with the observation on the cross-sectional SEM results.

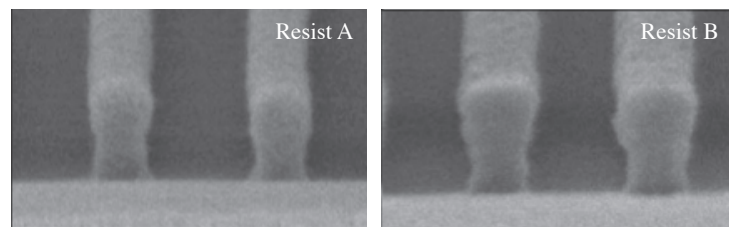


FIGURE 2. Cross-sectional SEM images of resist L/S patterns.

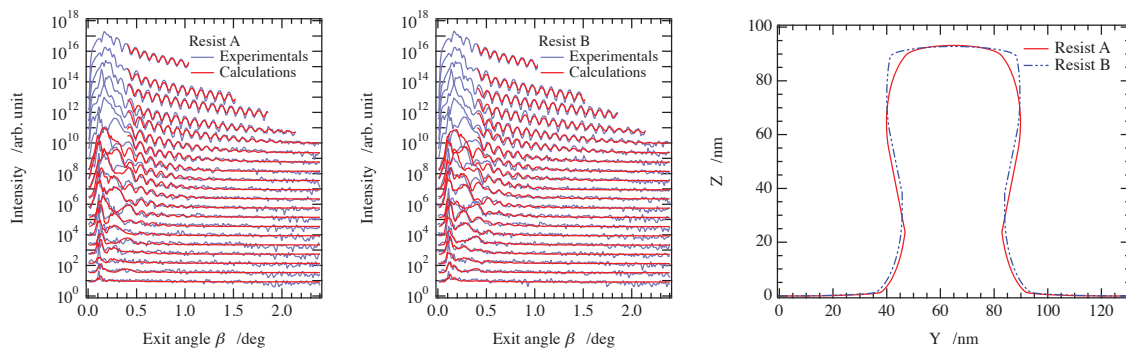


FIGURE 3. Diffraction patterns and obtained cross-sectional profiles of resist L/S patterns.

CROSS-SECTIONAL PROFILE ANALYSIS OF RESIST CONTACT HOLES

Two kinds of resist hole-patterned wafers were fabricated using different material composition and exposure condition. The holes are arranged in a 2D square lattice-like form in the lateral plane with a 90 nm pitch. Figure 4 shows cross-sectional SEM observation.

Figure 5 shows diffraction patterns and cross-sectional profiles of these samples obtained by the CD-SAXS instrument. Diffraction data were collected in two directions $[1\ 0]$ and $[1\ -1]$. Again, the CD-SAXS results reproduced the characteristics obtained by the cross-sectional SEM observation, i.e., the rather vertical cylindrical hole shape of the resist C and the heavily undercut hole shape of resist D. It can be considered that the results obtained by CD-SAXS are consistent with those obtained by cross-sectional SEM also for this example.

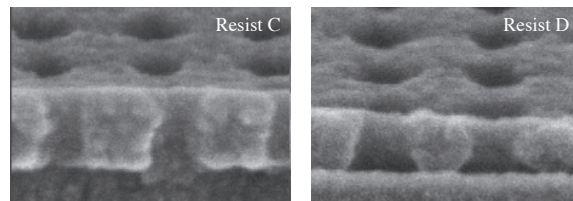


FIGURE 4. Cross-sectional SEM images of resist hole patterns.

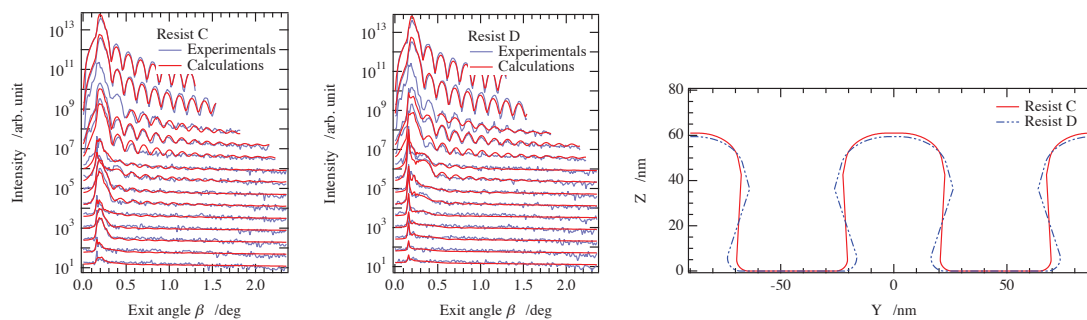


FIGURE 5. Diffraction patterns and obtained cross-sectional profiles of resist hole patterns.

CONCLUSION

Our newly-developed x-ray metrology tool, CD-SAXS, has been demonstrated. Cross-sectional profiles of resist patterns were measured by the instrument. The results obtained by the CD-SAXS were consistent with those obtained by cross-sectional SEM observation. CD-SAXS has a capability for measuring cross-sectional profile non-destructively. Our new x-ray method is very effective in CD metrology on mass production lines.

ACKNOWLEDGEMENTS

The authors would like to thank FUJIFILM Corporation for preparing resist samples.

REFERENCES

1. K. Omote, Y. Ito, Y. Okazaki, and Y. Kokaku, *Proc. of SPIE* **7488**, 74881T (2009).
2. K. Omote, Y. Ito, and Y. Okazaki, *Proc. of SPIE* **7638**, 763811 (2010).
3. Y. Ishibashi, T. Koike, Y. Yamazaki, Y. Ito, Y. Okazaki, and K. Omote, *Proc. of SPIE* **7638**, 763812 (2010).
4. H. Abe, Y. Ishibashi, C. Ida, A. Hamaguchi, T. Ikeda, and Y. Yamazaki, *Proc. of SPIE* **9050**, 90501L (2014).

KEYWORDS

X-ray metrology, CD-SAXS, GI-SAXS, Resist, Cross-sectional profile,

Metamorphic Growth-Related Defects and Electrical Properties in III-Sb Materials for High-Mobility p-MOSFETs

A. P. Jacob¹, S. Madiseti², S. Sasaki³, V. Tokranov², M. Yakimov², M. Hirayama², S. Bentley¹, and S. Oktyabrsky²

¹ GLOBALFOUNDRIES, Malta, NY 12020, USA

² SUNY College of Nanoscale Science and Engineering, Albany NY 12203, USA

³ SUMCO Corporation, Minato-ku, Tokyo 105-8634, JAPAN

INTRODUCTION

(In)GaSb compound semiconductors are considered as a complimentary PMOS material to N-type InGaAs due to the superior hole transport properties in III-Sb's. Both these materials also have similar chemistry that helps in CMOS process integration. However, the surface/interface electrical properties are in a sense opposite in InGaAs and (In)GaSb: a neutral surface occurs when the Fermi level is close to the conduction band in InGaAs with high In content, and when Fermi level is close to the valence band in (In)GaSb at any In content. Therefore, an (In)GaSb p-MOSFET operates with low interface charge and has lower resistivity p-type source/drain contacts, while InGaAs is better suited for n-MOSFET. In addition to p-type surfaces and interfaces, various intrinsic defects in (In)GaSb introduce dominant acceptor levels. When III-Sb materials are grown on metamorphic substrates, the introduced defects creates unintentional p-type doping, causes additional scattering, increase junction leakages and affects the interface properties. In this abstract, the results on correlations between the defects in various designs of metamorphic superlattice buffers on electrical properties of GaSb and InGaSb QW layers are presented.

RESULTS AND DISCUSSION

III-Sb structures were grown by MBE on GaAs(100), SOI and Si(100) and 6° off (100) Si substrates using different metamorphic buffer layers to accommodate large lattice mismatch and minimize defect density [1,2]. In order to identify the correlations between the defects and electrical properties of GaSb films and InGaSb QW layers, multiple techniques such as AFM, SEM and TEM for physical characterization and Hall resistivity and CV measurements for electrical characterization were employed.

GaSb-on-Si

Table I shows bulk electrical properties of thick undoped GaSb layers grown by MBE on SOI and semi-insulating GaAs substrate. The layer on SOI shows 4x higher hole concentration and lower mobility due to the higher defect density. The structure grown on SOI (Fig. 1) has a super lattice (SL) metamorphic buffer consisting of strained 8/8nm GaSb/Al_{0.5}Ga_{0.5}Sb layers with inserted three InSb quantum dot layers to reduce microtwin (MT) density. Fig. 2 compares AFM images of the surfaces of the two structures. The MT density reaching the GaSb surface on SOI is about 4x higher than on GaAs, 4.4x10⁷ cm⁻² and 0.9x10⁷ cm⁻², respectively. In addition, the sample on SOI has 7000 cm⁻¹ antiphase domain boundaries. The MT number density is typically close to the perfect threading dislocation density in the same sample.

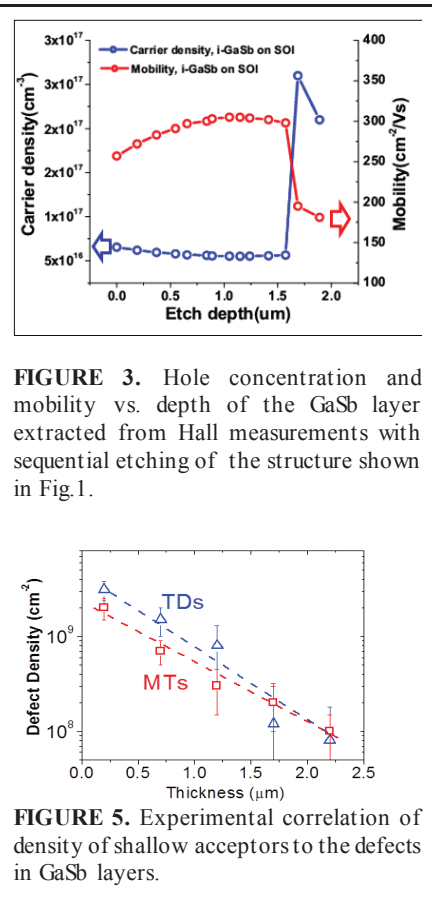
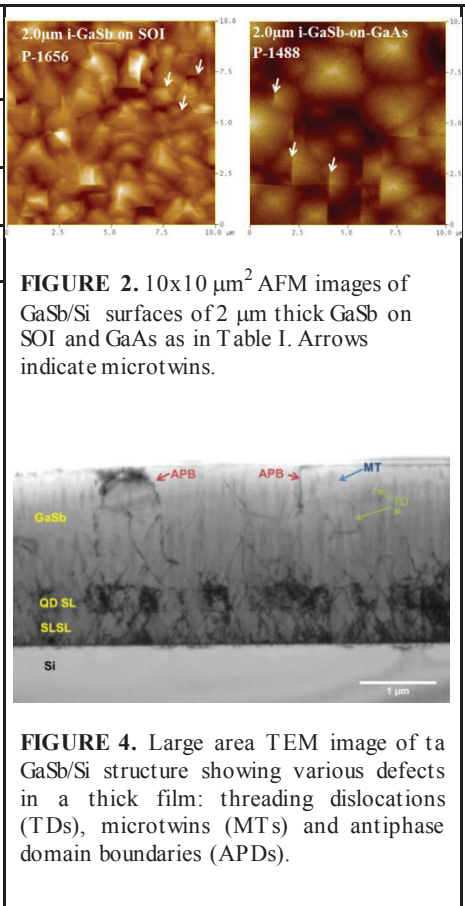
Table I. Bulk electrical properties of 2 μm thick undoped GaSb layers grown by MBE on SOI and GaAs

	Conc., (cm ⁻³)	μ (cm ² /V-s)
On SOI	1.2x10 ¹⁷	286
On GaAs	2.8x10 ¹⁶	813

P-1656, 2.0 μm i-GaSb-on-SOI

1.5 μm i-GaSb	} 3x
128nm i-(Al/Ga)Sb – HT buffer:	
8/8nm SL (8x) GaSb/Al _{0.5} GaSb	
200nm i-GaSb (HT)	
45nm i-GaSb	
1.1nm i-InSb (3.2ML) QDs	
1nm i-AlSb	
330nm i-(Al/Ga)Sb – HT buffer:	
8/8nm SL (8x) GaSb/Al _{0.5} GaSb	
200nm i-GaSb (HT)	
0.9nm i-AlSb QDs (3ML)	}
1-2nm (5min) Sb ₂ -soaking	
SOI-substrate	

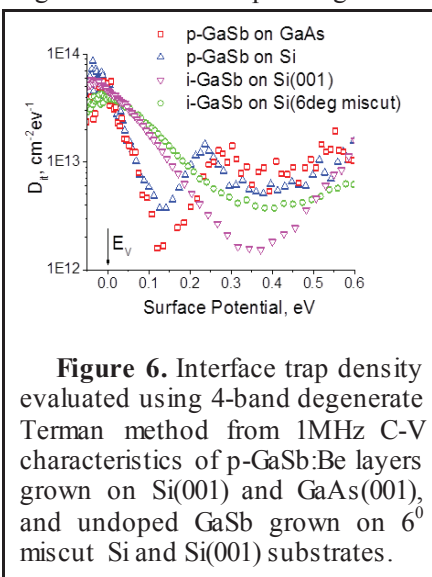
FIGURE 1. Schematic cross-section of a thick GaSb layer on SOI for bulk electrical properties measurements.



The presented electrical data in the Table I is averaged over the entire 2 μm structures. In order to evaluate the electrical properties at a specific depth, the sequential etching of the sample on SOI as in Fig. 1 was carried out using CH₄/Ar RIE/ICP process. Hall measurements were taken after each etch step and the depth of etching was confirmed by the profilometer. The results for hole concentration and mobility as a function of depth into the sample are shown in Fig. 3. The hole concentration increased at the deeper region. This is corresponding to the defects that were generated due to lattice mismatch between Si and metamorphic buffer layer.

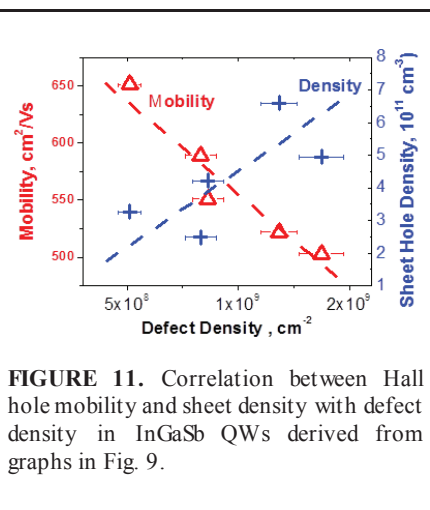
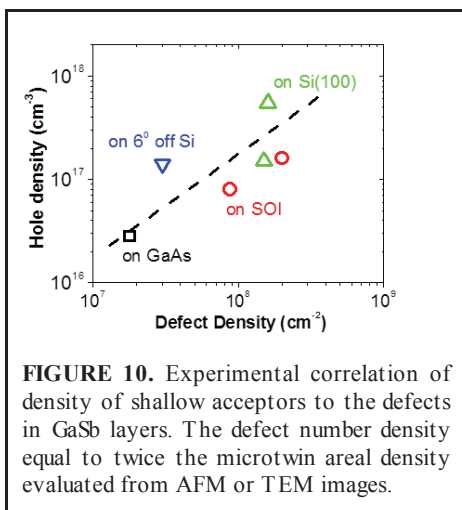
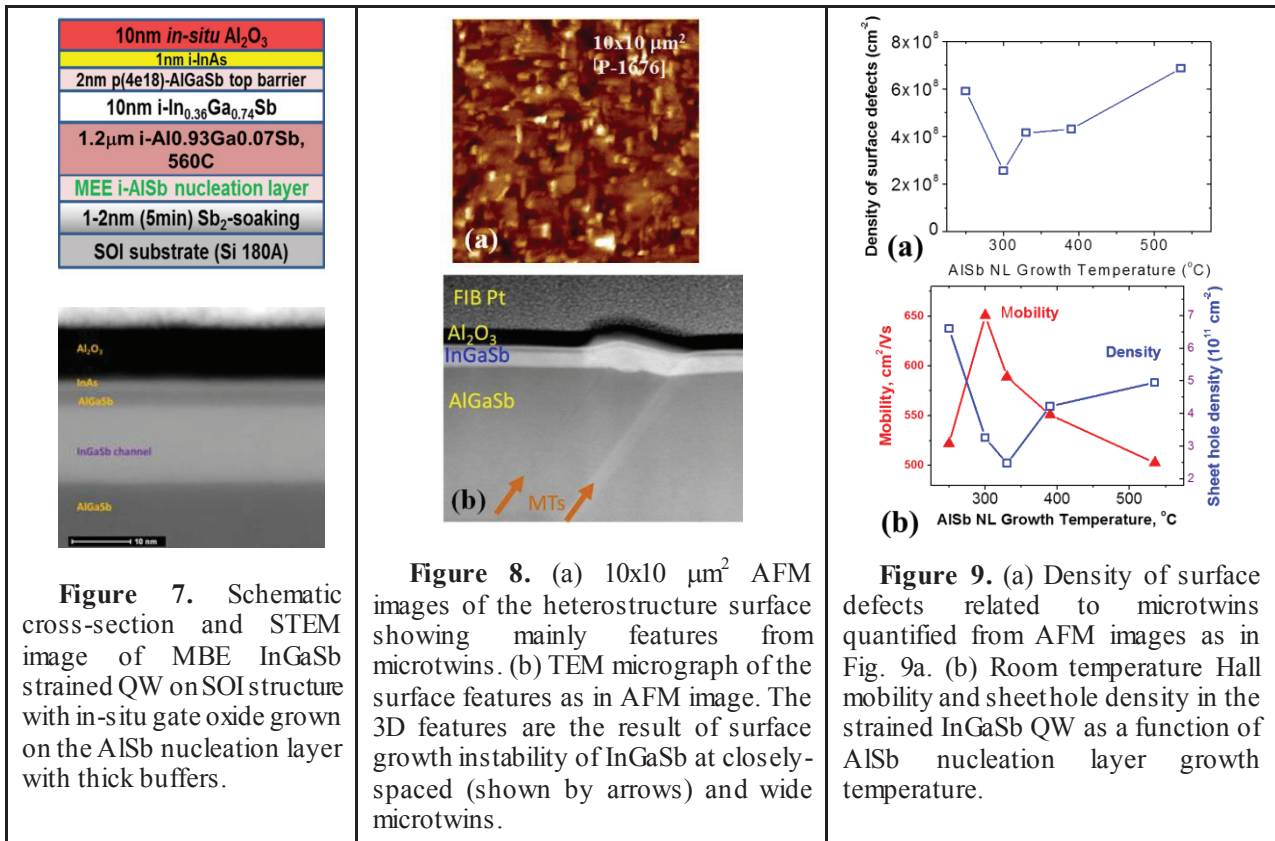
To further study the baseline bulk and interface electrical properties of GaSb grown on Si, 10 nm thick Al₂O₃ gate oxide was deposited by an in-situ reactive evaporation of Al in 10⁻⁶ Torr oxygen ambient. E-beam evaporated nickel was used as a gate metal to fabricate MOS capacitors. A cross-sectional TEM image of a typical structure is shown in Fig. 4. The defect densities extracted from the TEM images are shown in Fig. 5 and give the numbers just below 10⁸ cm⁻² for both TDs and MTs, the latter is assumed to give a 2x contribution to the areal defect density.

C-V characteristics of MOS capacitors were used to estimate acceptor concentration interface trap density D_{it}. The D_{it} extracted with Terman method is shown in Fig. 6. The trap density at the valence band edge is about 3 times higher in GaSb grown on Si than on GaAs but have a similar minimum D_{it} approaching 10¹² cm⁻² eV⁻¹ in the bandgap.



Strained InGaSb on Si

Previously we reported on optimization of nucleation of AlSb on Si, for growth of metamorphic buffers for strained InGaSb p-channels [2]. The electrical properties of defects were evaluated in 1.7% compressively strained 10 nm thick InGaSb QWs grown on AlSb nucleation layers deposited at different temperatures. All the samples had the similar structure (Fig. 7) with a 3nm buried channel. The major defects were found to be microtwins (Fig. 8). They caused the formation of rectangular bumps on the surface [2]. The MT density was quantified (Fig. 9a) and Hall mobility and concentration was measured for the samples (Fig. 9b).



Figs. 10 and 11 summarize the correlation between electrical properties and defect density in GaSb layers (Fig. 10) and strained InGaSb QWs (Fig. 11) that clearly reveals increase of unintentional acceptor doping and reduction of mobility with higher defect density. The hole concentration in QW (Figs 9 and 11) depends on modulation doping and surface band bending, and direct correlation with defects is difficult. However, the

tendency is clear, giving the range of defect-related p-doping of the QW of $(2-5) \times 10^{17} \text{ cm}^{-3}$. Effect on mobility is quantitative, and the reduction of defect density is clearly needed for the QW mobility increase to the values of $\sim 900 \text{ cm}^2/\text{Vs}$ as previously reported for similar structures on GaAs substrates [1].

REFERENCES

1. V. Tokranov, S. Madisetti, M. Yakimov, P. Nagaiah, and S. Oktyabrsky, *J. Crystal Growth* **378**, 631-5 (2013).
2. S. K. Madisetti, V. Tokranov, A. Greene, M. Yakimov, M. Hirayama, S. Oktyabrsky, S. Bentley, and A. P. Jacob, *J. Vac. Sci. Technol.* **B 32**, 051206 (2014).

KEYWORDS

Group III-Antimonide semiconductors, Metamorphic growth, Defects, Mobility, p-type defect levels, III-Vp-MOSFET

Analysis Of Defects In SiGe And Ge

Abhijeet Joshi & James Ewan

ACTIVE LAYER PARAMETERICS, Inc.

Los Angeles, CA 90024

INTRODUCTION

The DHE system provides direct measurements of the resistivity profiles and the mobility profiles and the calculated carrier profile. This is the only known way to obtain both carrier profile & mobility profile for activated samples without resorting to empirical models.

The primary equation behind the calculation of the activated carrier profile is,

$$N = \frac{1}{\rho \times \frac{\mu}{r} \times q_{electron}}, \quad (1)$$

Where, ρ is the layer resistivity, μ is the layer carrier mobility and $q_{electron}$ is the charge on an electron. The value r is assumed to be 0.8 for holes and 1.0 for electrons. The mobility profile was not previously available by any other technique.

From the primary data produced it may be possible then to further evaluate the impact of defect – either that has persisted after epitaxial growth/ re-growth or that has not been completely removed from the material after annealing.

Measuring the mobility distribution and comparing the measured mobility and the carrier distribution with the carrier mobility curve for undamaged and unstrained materials results in an important discovery. This is the identification of processes that result in the generation of significant concentrations of scatter defects. The DHE system and the following analysis allows for the quantification of the effects of these scatter defects on mobility.

There is a need for highly localized Ge and SiGe channels for 10nm nodes and beyond. Direct selective SiGe epi-growth followed by oxidation for Ge condensation and 100% selective Ge-epi are some of the methods used. Damage in SiGe and Ge channels may be analyzed for defects with the DHE system. These concerns are highly topical with the current industry thrust to fabricate devices with germanium high-mobility channels.

DEFECT MEASURE

A unified treatment of scatter defect contribution and strain effects in the material is achieved via application of Matthiessen's rule, which phenomenologically accounts for the deviation of ideal mobility in the presence of residual damage and strain effects.

In any material doped with an impurity, value of μ is affected by the presence of impurity scattering, lattice scattering, mobility scatter defects which are associated with the doping process and also strain effects,

$$\frac{1}{\mu} = \frac{1}{\mu_{IMP}} + \frac{1}{\mu_{LATTICE}} + \frac{1}{\mu_{SCATTER}} \dots, \quad (2)$$

Where, $\frac{1}{\mu_{IMP}}$, $\frac{1}{\mu_{LATTICE}}$, etc. are the contributions due to impurity scattering, lattice scattering, etc. The DHE

system measures the actual mobility μ , and material models provide the ideal mobility value μ_o (For silicon: the ASTM F723 Standard [2] & Cuttriss (1961)[3] for 100% Ge). Modification of Eqn. (1) provides us with,

$$\frac{1}{\mu} - \frac{1}{\mu_o} = \frac{1}{\mu_{SCATTER}} - \frac{1}{\mu_{STRAIN}} = \frac{1}{\mu_{DEF}} \quad (3)$$

The left hand side of the equation or the “defect measure” ($1/\mu_{DEF}$) quantifies the contribution of scattering defects and/or strain.

SILICON-GERMANIUM DATA

In recently reported literature [4], SiGe samples were measured. These were deliberately strained with addition of Ge in the silicon substrates. The study combined a very high dose Ge+B plasma implantation and selective surface laser melt annealing using short wavelength laser-anneals. Structural information provided by XRD and X-TEM analysis provided information about strain in the samples whose Ge content was 0%, 20% and 55%. DHE measurements showed an increase in mobility by 70% for the 20% doped sample (to 63 cm²/V-s), and a sizable 4.3X increase in the 55% Ge sample. Note that 0% Ge has a mobility value of 38 cm²/V-s.

The mobility profile as obtained from the DHE system for the 55% Ge sample is shown in Figure 1. The sample had a peak concentration of 55% around 1.7nm as seen by AR-XPS depth measurements. Complete damage recovery for the sample was seen at 2.0J/cm² as shown by ThermaWave [3].

The “defect-measure” profile for the same SiGe sample is provided in Figure 2. The marked region corresponds with the high Ge region as indicated by AR-XPS data[3] in the 0-200Angstrom range.

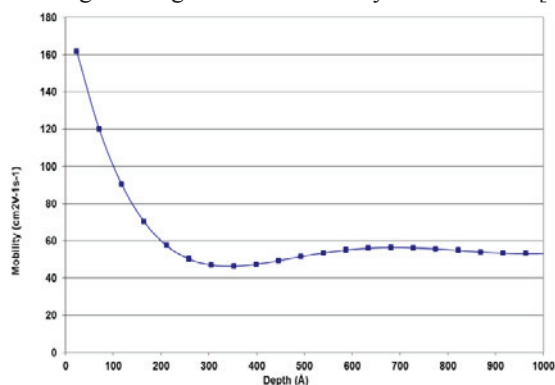


Figure 1: Data for sample 55% Ge (1E17/cm²) + B (4E16/cm²)

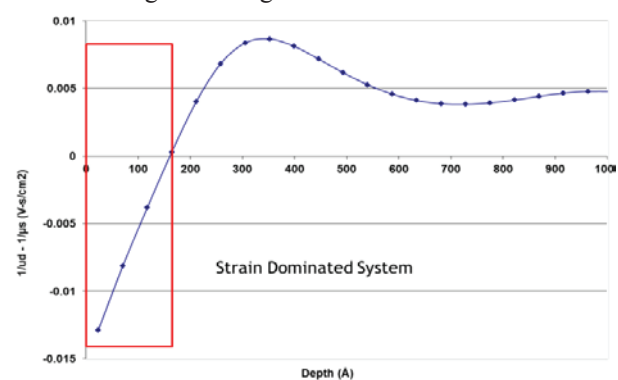


Figure 2: “Defect-Measure” for sample 55% Ge (1E17/cm²) + B (4E16/cm²)

CONCLUSION

The defect measure provides quantitative deviations from the ideal, defect-free, fully relaxed systems as described by idealized models. The target sample’s mobility profile data as provided by DHE system can be leveraged to conduct extensive defect and/or strain analysis via the “defect measure.”

References:

1. A Joshi, S.A. Prussin, “Determining defect & strain effects on active layer mobility”, 20th International Conference on Ion Implantation Technology (IIT), (2014).
2. W.R. Thurber, R.L. Matthis, Y.M. Liu, and J.J. Filliben, NBS Special Publication 400-64, May 1981.
3. Cuttriss, D. B. "Relation between surface concentration and average conductivity in diffused layers in germanium." Bell System Technical Journal 40.2 (1961): 509-521.
4. John Borland, Shu Qin, Peter Oesterlin, Karim Huet, Walt Johnson, Lauren Klein, Gary Goodman, Alan Wan, Steven Novak, Thomas Murray, Richard Matyi, Abhijeet Joshi, Si Prussin, “High mobility Ge-channel formation by localized/selective liquid phase epitaxy (LPE) using Ge+B plasma ion implantation and laser melt annealing”, Proc. 13th International Workshop on Junction Technology (IWJT), pp. 49 - 53. 6-7 June 2013.

Key words: Complete analysis of Activated Layers, Strain-Effects and Defect Analysis, Defect Analysis of Germanium, Germanium epi-layers.

In-Situ Real-Time Monitoring And Control Of Kinetic Processes In Atomic Layer Depositions By Spectroscopic Ellipsometry With 1.25 Hz Sampling Rate

Marcel Junige^{*1}, Varun Sharma¹, Ralf Tanner¹, Daniel Schmidt², Greg Pribil³,
Matthias Albert¹, Mathias Schubert⁴, Johann W. Bartha¹

¹ Technische Universität Dresden, Institute of Semiconductors and Microsystems, 01062 Dresden, Germany;

² Singapore Synchrotron Light Source, National University of Singapore, Singapore 117603, Singapore;

³ J. A. Woollam Co. Inc., 645 M Street, Suite 102, Lincoln, Nebraska 68508-2243, USA;

⁴ Department of Electrical Engineering, University of Nebraska-Lincoln, Lincoln, Nebraska 68588-0511, USA;

* telephone: 0163 5809233, e-mail: marcel.junige@tu-dresden.de

INTRODUCTION

All present as well as future strategies in semiconductor manufacturing for next-generation nanoelectronics, i. e. the continued miniaturization (“more Moore”), the integration of additional functionalities (“more than Moore”), and the implementation of novel device concepts (3D integration / “beyond CMOS”),^[1] will progressively implement ultra-thin films that scale no more than a few nanometers and still meet their application-specific functionality, especially, on highly complex three-dimensional (3D) structures and on large-area substrates. However, the reliable manufacturing and accurate control of such a film’s ultra-thin thickness in connection with its desired functional properties remains a critical challenge. This applies equally to the entire development chain from basic research to mass production.

Atomic Layer Deposition (ALD)

In order to overcome the coating challenges, Atomic Layer Deposition (ALD) has been established for the last decade due to its unique sub-nanometer thickness control, high uniformity (i. e. 3D conformality as well as large-area homogeneity), and comparatively better film quality at lower deposition temperatures, besides some other advantages.^[2] ALD is a special kind of chemical vapor deposition, which sequentially alternates the individual exposure of a material’s vaporized precursor and gaseous co-reactant(s), respectively, separated by purging steps of an inert gas. Hence, in an ideal case, each individual physicochemical (ALD-half-)reaction is confined to the sample’s solid-state surface and achieves timewise self-termination, provided that the precursor adsorbs with a saturating monolayer coverage and that the co-reactant completely removes the adsorbate’s ligands forming a saturating monolayer of functional surface sites for the next precursor adsorption, respectively. As a result, just a fraction of the condensed material’s monolayer is deposited by every cyclic repetition of the sequential ALD gas pulses until the desired nano-scaled film thickness is obtained.

In-Situ Real-Time Spectroscopic Ellipsometry (irtSE)

In order to face the characterization challenges of in-situ real-time monitoring and control for an efficient ALD process development and reliable manufacturing, Spectroscopic Ellipsometry (SE) is ideally suited^[3] as it provides a sub-ångström sensitivity, high accuracy, fast measurement rate, and non-destructive plus non-invasive access to the kinetic (growth or removal) processes at a sample’s surface. We have recently developed an irtSE algorithm that enabled the acquisition of entire ellipsometric (Ψ , Δ) spectra (250-1700 nm) with a sampling rate of ~ 1.25 Hz.^[4]

MATERIALS AND METHODS

The utilized FHR-ALD-300 reactor (by FHR Anlagenbau GmbH, Ottendorf-Okrilla, Germany) was equipped with a M 2000[®] FI Rotating Compensator Ellipsometer (RCE) (by J. A. Woollam. Co., Lincoln, Nebraska, USA). The ellipsometer windows were protected against the reactor's gas phase by purging the tubular view ports with a laminar Ar gas flow (no shutters were implemented). The ALD reactor chamber was also clustered to a Multiprobe[®] Ultra High Vacuum (UHV) system (by Omicron Nanotechnology GmbH, Taunusstein, Germany) for direct surface analysis like Photoelectron Spectroscopy (PES: XPS, UPS) or Scanning Probe Microscopy (SPM: AFM, STM) at the same sample surface without breaking a high vacuum of $\sim 10^{-5}$ Pa during in-vacuo sample transfer. This entire experimental setup has previously been described in more detail in the references [5, 6].

The benefits of irtSE with a sampling rate of ~ 1.25 Hz for the monitoring and control of kinetic processes in ALD is demonstrated here on the basis of four materials: aluminium(III) oxide (Al_2O_3), tantalum(V) oxide (Ta_2O_5), tantalum nitride (TaN_x), and ruthenium (Ru). The respectively used precursor and co-reactant was trimethylaluminum (TMA) – ozone (O_3), [(tert-butylimido)tris(ethylmethylamido)tantalum] (TBTEMT) – O_3 , TBTEMT – ammonia (NH_3), and [(ethylcyclopentadienyl)(pyrrolyl)ruthenium] (ECPR) – molecular oxygen (O_2). The Ru ALD process development has previously been published in more detail in Ref. [6].

RESULTS AND DISCUSSION

In-Situ Real-Time Monitoring Of Kinetic Processes In ALD

Fig. 1 shows the Al_2O_3 , Ta_2O_5 , TaN_x , and Ru optical layer thickness as determined by irtSE with a sampling rate of 1.25 Hz in the real-time course of one respective ALD cycle. In all the investigated cases, the optical thickness deviated from an average no more than 0.01 nm, fulfilling a noise level at least one order of magnitude below the ALD signal level. After completion of one entire ALD cycle, each thickness incremented with respect to the previous cycle, which can be interpreted as the amount of per-cycle-deposited film material (also commonly referred to as the growth per cycle, GPC). During each precursor's exposure (purple shadow), the optical thickness incremented rapidly at the beginning but then saturated with the exposure time, which indicated a self-terminating precursor adsorption. During each co-reactant's exposure (green shadow), the optical thickness decremented and was also saturated with the exposure time, which implied a self-terminating ligand removal, thus, forming the respective condensed film material. All the reactants exposures exhibited a different reaction kinetics, implying an individually associated activation energy. During all the Ar purges, each optical thickness remained practically constant neglecting some fluctuations, which suggested an irreversible precursor adsorption with negligible thermal self-decomposition.

Impact Of Process Parameters On ALD Growth Actions

As an example, Fig. 2 shows the impact of the actual deposition temperature (corrected according to SE of the pre-heated Silicon starting surface) during Al_2O_3 ALD on the thickness increment per cycle (also GPC) and on the pulsewise optical thickness changes. A rather constant GPC around 1 Å/cycle was revealed between 220 to 350 °C with fairly temperature-independent individual ALD-half-reactions, which featured an almost ideal ALD process.

CONCLUSIONS AND OUTLOOK

In conclusion, we investigated kinetic processes (precursor adsorption, ligand removal, and purging behavior) for the ALD of Al_2O_3 , Ta_2O_5 , TaN_x , and Ru, respectively, by applying a novel irtSE algorithm that enabled a sampling rate of ~ 1.25 Hz and thus a desired high time resolution in conjunction with a mean-averaged thickness deviation of < 0.01 nm. The capability to extend these studies, in order to reveal the impact of various process parameters as well as their interdependencies, was exemplarily outlined for the temperature (in)dependence of the Al_2O_3 ALD process. Consequently, our irtSE approach might be ideally suited for a much more detailed and at the same time more efficient ALD process development that could screen smaller amounts of innovative precursors in shorter time. In principle, this could even extend to other deposition or etch processes. Beyond a process development in basic research or industry, the use of SE for in-situ real-time process control in manufacturing was also possible as SE would detect even smallest deviations from a defined standard in less than one second.

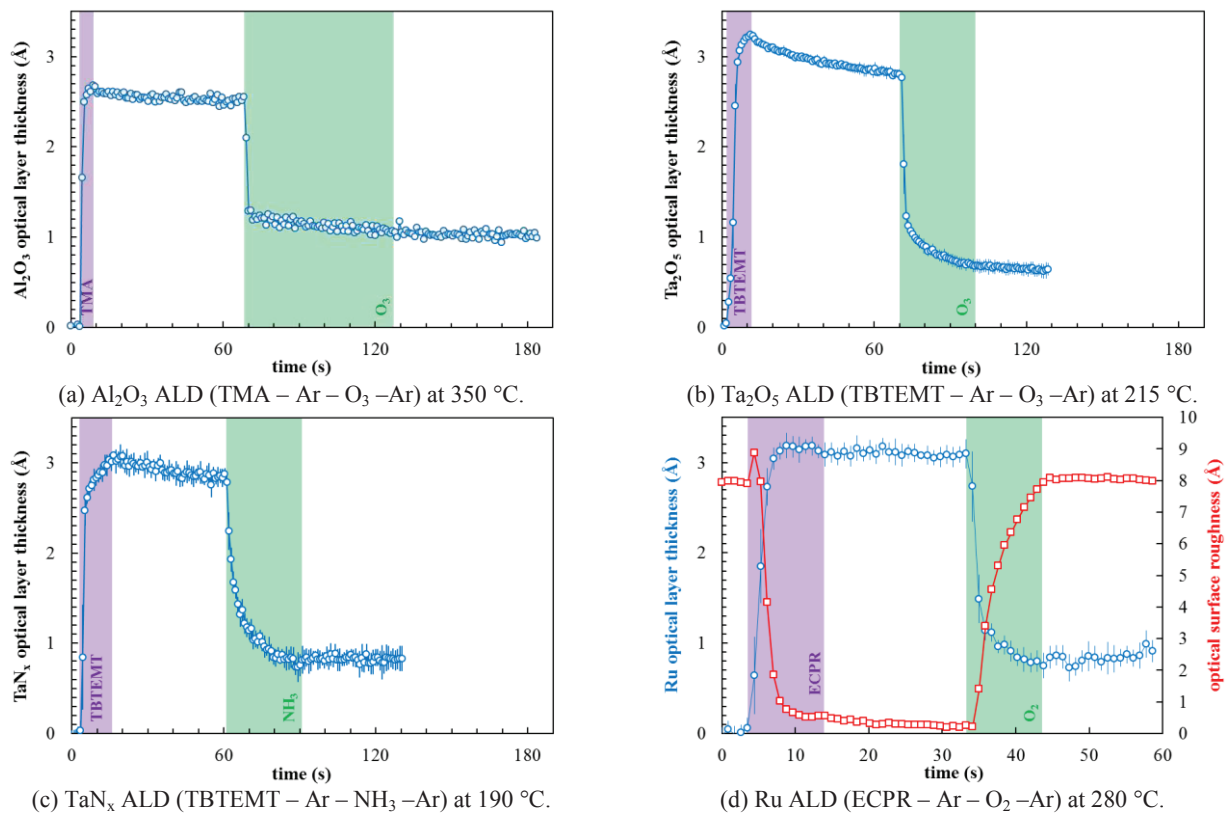


FIGURE 1. Optical layer thickness in the real-time course of one ALD cycle for Al_2O_3 , Ta_2O_5 , Ta_x , and Ru, respectively.

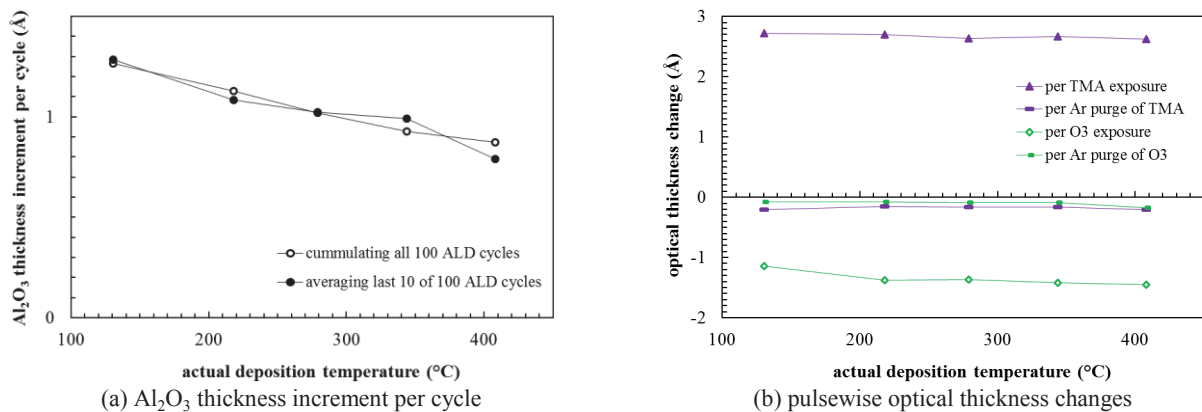


FIGURE 2. Per-cycle and pulsewise changes of the Al_2O_3 optical layer thickness in dependence on the deposition temperature.

REFERENCES

1. International Technology Roadmap for Semiconductors (ITRS), www.itrs.net (2013 ed.).
2. M. Leskelä, M. Ritala, O. Nilsen: *MRS Bulletin* **36** (2011), 877.
3. E. Langereis *et al.*: *J. Phys. D: Appl. Phys.* **42** (2009), 073001.
4. M. Junige *et al.*: *8th Workshop Ellipsometry* (Arbeitskreis Ellipsometrie – Paul Drude e.V., Dresden, 2012).
5. M. Junige *et al.*: *IEEE Semiconductor Conference Dresden* (IEEE, Dresden, 2011).
6. M. Knaut *et al.*: *J. Vac. Sci. Technol. A* **30** (2012), 01A151.

KEYWORDS

in-situ real-time Spectroscopic Ellipsometry (irtSE), Atomic Layer Deposition (ALD), Al_2O_3 , Ta_2O_5 , Ta_x , Ru

Characterization Of Plasma Process Induced Damage Near SiN/SiO₂/Si Interface By Room Temperature Photoluminescence

Jung Geun Kim,¹ Ho Jin Cho,¹ Sung Ki Park,¹ Seok-Hee Lee,¹
Byoung Gon Choi,² Jea Young An,² Young Il Cheon,² Young Ho Jeon,²
Toshikazu Ishigaki,³ Kitaek Kang³ and Woo Sik Yoo³

¹SK hynix, Icheon, Gyeonggi-do, 467-701, Korea

²SK hynix, Cheongju, Chungcheongbuk-do, 361-480, Korea

³WaferMasters, Inc., San Jose, California, 95112, USA

INTRODUCTION

All wafers go through multiple plasma processing steps (such as doping, deposition, etching, ashing, curing, hardening and treatment) during advanced complimentary metal-oxide-semiconductor (CMOS) device fabrication. Even in the metrology side, Corona discharge-based, non-contact capacitance-voltage (C-V) and current-voltage (I-V) measurements utilize atmospheric pressure, high voltage plasma to deposit charges onto dielectric films as non-contact electrodes.

Negatively affected plasma process induced material properties are generally referred to as plasma process induced damage (PPID). It has been known to modify the interface of dielectrics and Si. However, the characterization of PPID often requires special test device structures with arrays of antennae. Even small wafer-to-wafer and within wafer variations and hidden process induced damage on the test device structures complicates the sensitivity of measurement and handicaps the detection of subtle change of dielectrics/Si interface quality.

During the process development and tuning, the integrity of the gate dielectrics is mainly characterized by off-line electrical measurements and integrity of the dielectrics is routinely monitored. Since the subtle and unexpected integrity variations within the gate dielectric can negatively impact production device yield significantly, development of a non-contact in-line monitoring technique for gate dielectric integrity which is both effective and practical is strongly desired.

In this paper, the effect of the subsequent high density plasma-chemical vapor deposition (HDP-CVD) processes on the integrity of the stacked gate dielectrics/Si interface was investigated using room temperature photoluminescence (RTPL) under various excitation wavelengths. The applicability of RTPL spectroscopy for in-line PPID monitoring of gate dielectric integrity during subsequent plasma process steps was investigated.

EXPERIMENT

A dozen thin gate dielectric film stacks (SiN/SiO₂) were deposited on 300 mm-diameter Si wafers by low pressure thermal chemical vapor deposition (LPCVD) in a vertical furnace. The thicknesses of SiN and SiO₂ layers were 20 and 50 nm, respectively.

Fig. 1 shows the schematic cross-sectional views of the wafers. One wafer (Wafer 01) was kept as a reference wafer for RTPL characterization. The other 11 wafers (Wafer 02 ~ 12) received 500 nm thick HDP-CVD SiO₂ deposition process steps under various process conditions. Radio frequency (r. f.) power, r. f. power ratio, process gas flow rate, gas flow direction, deposition pressure and deposition time during the HDP-CVD were varied for the 11 wafers (Wafer 02 ~ 12).

RTPL spectra of all wafers were measured in the wavelength range of 900 ~ 1400 nm under 650 and 827 nm focused laser beam excitation. The spot size of the excitation laser beam was in the range of 50 ~ 100 μm in diameter. The beam probing depths for 650 nm and 827 nm are estimated to be ~4.0 μm and ~10 μm in Si. [1,2] Laser power in the range of 20 ~ 50 mW at the wafer surface was used for RTPL measurements. The RTPL signal was integrated for 10 ms per measurement point under 650 nm and 827 nm excitation, respectively. For wafer mapping, up to 15,101 points (2 mm intervals with 10 mm edge exclusion) were measured. Due to space limitations, only five wafer results are shown in this paper.

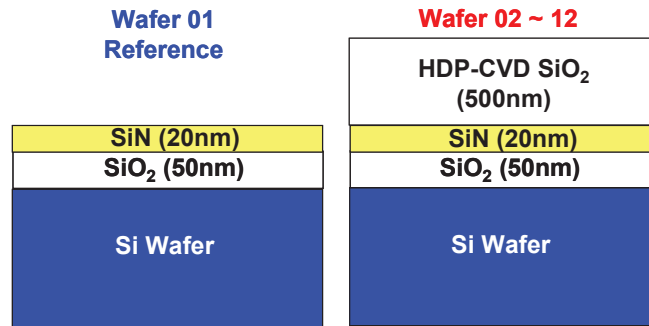


FIGURE 1. Schematic cross-sectional views of wafers.

RESULTS AND DISCUSSIONS

RTPL spectra of the center of five wafers (Wafer 01 ~ 05) and the range of RTPL intensity at five points (wafer center and four points 10 mm away from the wafer edge) under 650 and 827 nm excitation were plotted in Fig. 2 (a) ~ (c).

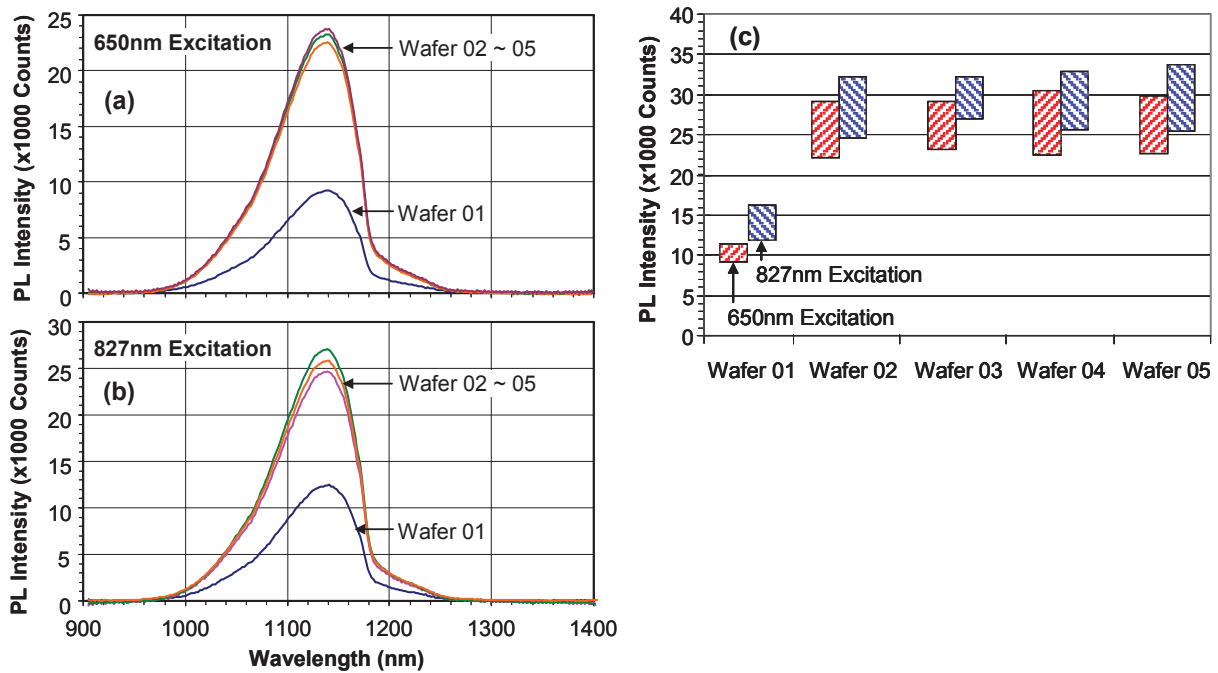


FIGURE 2. RTPL spectra under 650 nm (a) and 827 nm (b) and intensity ranges of five point measurements (c).

Strong RTPL signals were measured from all wafers before and after HDP-CVD SiO₂ film deposition under both 650 nm and 827 nm excitation. Typical asymmetric interband RTPL spectra, with a peak wavelength at ~1140 nm, were measured. The wafers with HDP-CVD SiO₂ films (Wafer 02 ~ 05) showed stronger RTPL intensities than the reference wafer (Wafer 01 - without an HDP-CVD SiO₂ layer) due to the passivation layer. However, the RTPL intensity variation over 5 measurements per wafer became larger for wafers with the HDP-CVD SiO₂ film deposition.

In Corona charging experiments, field effect correlation with RTPL intensity from a SiO₂/SiN_x stack passivated Si has been verified. [3] Positive fields enhance RTPL intensity while negative fields reduce RTPL intensity. RTPL intensity change is proportional to the applied field and polarity.

RTPL is very sensitive to oxide/Si interface quality and in this experiment successfully detected (or found) UV radiation damage caused by routine interferometry-based film thickness measurement. [4]

Figure 3 shows 2D and 3D RTPL intensity maps of Si wafers with and without HDP-CVD SiO₂ (500 nm) films on stacked SiN (20 nm)/ SiO₂ (50 nm) gate dielectric films, measured under 827 nm excitation. As seen from the RTPL wafer maps, RTPL intensity from the HDP-CVD SiO₂ films are significantly enhanced at the wafer edge. The difference in RTPL intensity patterns of the wafers with HDP-CVD SiO₂ films can be interpreted as the signature of PPID patterns of particular plasma conditions during the HDP-CVD step.

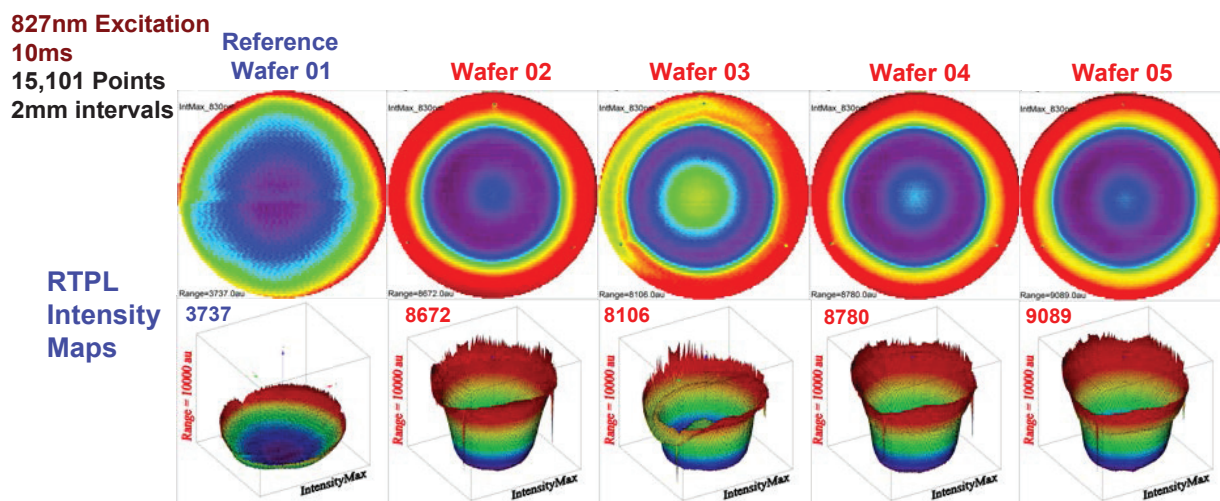


FIGURE 3. 2D and 3D RTPL intensity maps of Si wafers with and without HDP-CVD SiO₂ (500 nm) films on stacked SiN (20 nm)/SiO₂ (50 nm) gate dielectric films.

SUMMARY

Multiwavelength RTPL measurements were performed to visualize and monitor HDP-CVD conditions on the integrity of stacked gate dielectrics/Si interface. Room Temperature Photoluminescence can be very useful for in-line monitoring of PPID as well as gate dielectric integrity compromised during subsequent plasma process steps.

REFERENCES

1. W. S. Yoo, T. Ueda, T. Ishigaki, and K. Kang, Ion Implantation Technology, *AIP Conf. Proceedings*, **1321**, 204 (2010).
2. W. S. Yoo, T. Ueda, T. Ishigaki, K. Kang, M. Fukumoto, N. Hasuike, H. Harima and M. Yoshimoto, *J. Electrochem. Soc.*, **158** (1), H80 (2011).
3. M. Wilson, J. Lagowski, P. Edelman, F. Korsos, G. Nadudvari, Z. Kiss, J. Schmauder, V. Mihailetchi and S. Olibet, *Energy Procedia*, **38**, 209 (2013).
4. J. G. Kim, H. J. Cho, S. K. Park, S. H. Lee, B. G. Choi, J. Y. An, Y. I. Cheon, Y. H. Jeon, T. Ishigaki, K. Kang and W. S. Yoo, *ECS Solid State Lett.*, **3** (3), N11 (2014).

Application of Raman Spectroscopy for Local Stress Methodology and Characterization of Amorphous Carbon and SiGe Films in Semiconductor Process Development

Jae Hyun Kim^{1,2*}, Chang Hwan Lee², Koon Ho Bae², Seung Min Han¹

¹Graduate School of EEWS, Korea Advanced Institute of Science and Technology,
291 Daehak-ro, Yuseong-gu, Daejeon 305-701, Korea
jhkim76@kaist.ac.kr, +82 42 350 1756

²SK Hynix, 2091, Gyeongchung-daero, Bubal-eub, Icheon-si, Gyeonggi-do, South Korea

INTRODUCTION

Micro Raman spectroscopy can be effectively measured as the process control of semiconductor device materials. Due to small beam size, the light is penetrated into active silicon area on patterned wafer, and then scattered Raman signal give a stress state information. Also, it have effectively used for characterization of composition analysis on unknown thin film. In Raman spectroscopy, non-contact optical metrology offers a fast and cost saving monitoring of dielectrics in IC manufacturing process.

LOCAL STRESS METROLOGY USING RAMAN FREQUENCY

Stress control in silicon and other semiconductor devices is a primary importance in order to prevent problems related with the nucleation, propagation of dislocations and the formation of cracks and voids. Raman spectroscopy is able to measure the stain of micro and nano size structure with spatial resolution down to $<1 \mu\text{m}$ with a wide range of depth resolution. Therefore, it is suitable for non-destructive, high speed screening.

Figure 1 shows schematic diagrams on a Cross section image of the shallow trench isolation fabricated on the silicon wafer is shown in the schematic diagram in Figure 1. The stress state in Si is expected to be different after the oxidation and/or amorphous silicon deposition processing of the side walls in silicon structure. The spin-on dielectric (SOD) material of gap-filled isolation can contract significantly upon thermal annealing. The Raman can be effectively used to characterize the local mechanical stresses in the trench structures as a function of the processing parameters. Figure 2 shows the converted stress from the Raman frequency change as a function of the position on the active silicon area. Raman spectroscopy will be a measure of the out-of plane stress, where a positive shift in frequency is translated into a tensile stress state. Specimens with the oxidation sample of sidewall have out-of plane compressive stress (negative shift) within the measured active silicon area, otherwise, Deposited amorphous silicon sample of side wall showed tensile stress in the measured area, because the volume of deposited amorphous silicon to active silicon almost increased twice as many as.

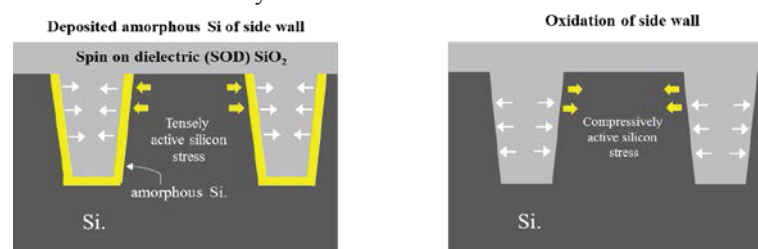


FIGURE 1. Schematic diagrams on a cross section image of the shallow trench isolation

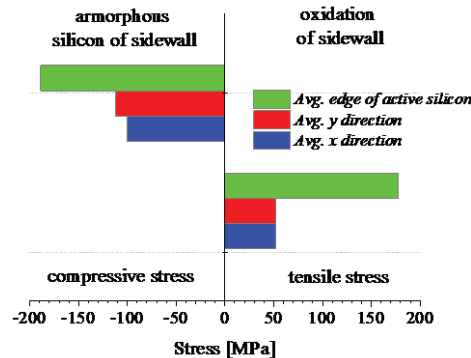


FIGURE 2. Measurement Area on the pattern wafer and the results of Raman shift at each process conditions

RAMAN FREQUENCY OF AMORPHOUS CARBON AND SiGe FILMS

Carbon materials are used as a passivation layer in a semiconductor device. Gate etching processes rely on the formation of a thin diamond like a carbon layer on the sidewalls to achieve profile control. The final gate profile is determined based on competition between lateral etch rate, deposition rate and vertical etch rate.

Raman spectra of the carbon material is well-known that allows for a very sensitive analysis. For carbon films, the Raman spectrum of G band usually occurs between 1480 and 1580 cm⁻¹, while the D band position appears between 1320 and 1440 cm⁻¹. Figure 3 shows that the G band position changes depending on the type of source and deposition temperature gas. In order to obtain diamond-like carbon (DLC) film, a C₃H₆ gas is used for deposition at 300 °C. It was possible to obtain the proper gate sidewall profile after etch process.

Raman spectroscopy can also be used to probe the lateral strain in the underlying SiGe layer in a strained Si on Si_{1-x}Ge_x substrate system. It is found that there are clear differences on Raman spectrum of silicon germanium between samples. Especially, for Si-Si band in SiGe (Band 1), all spectral parameters (Peak shift, Amplitude, Width) changed in each samples. Raman spectroscopy has a possibility to monitor Ge concentration and the degree of relaxation of SiGe layer in the manufacturing process.

Deconvolution of the SiGe bands was more difficult due to the low signal intensity, asymmetrical shape of the SiGe bands, and overlapping spectra from the presence of amorphous phases. Also, the formula used to calculate Ge% are empirical formulas determined by Tsang et al. in 1993 based on a set of samples of thick SiGe layers and poor quality crystals than the ones measured here. Degree of relaxation in the SiGe layer, and Ge content are defined by the relationship.

$$\omega_{SiSi} = 520.5 - 62x - 815\epsilon$$

$$\omega_{SiGe} = 400.5 + 14.2x - 575\epsilon$$

The table indicates Ge concentration calculated from measurement results (average) and above formulas. The coefficients in formulas should be determined with based on reference data of Ge concentration for each samples. This is the standard font and layout for the individual paragraphs.

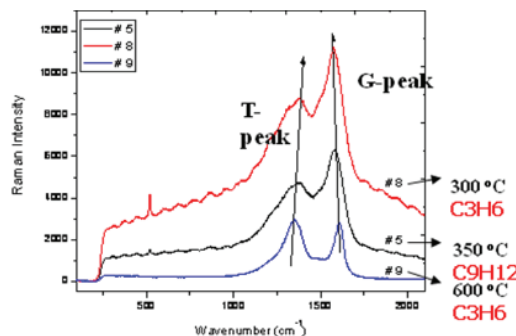


FIGURE 3. The results of Raman shift as deposition temperature and gas source

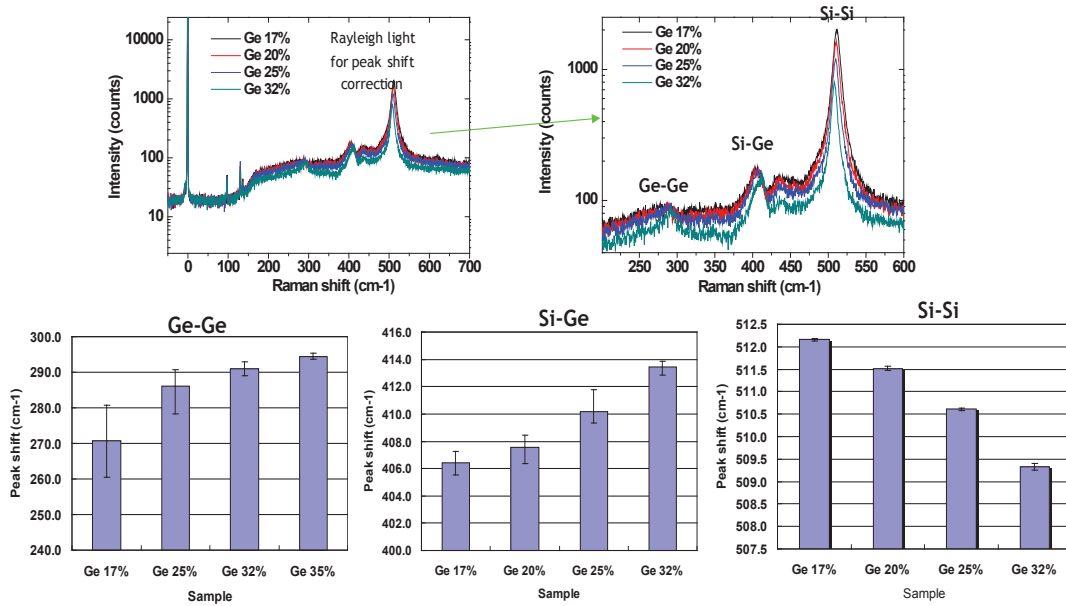


FIGURE 4. Raman results of SiGe film on silicon substrate

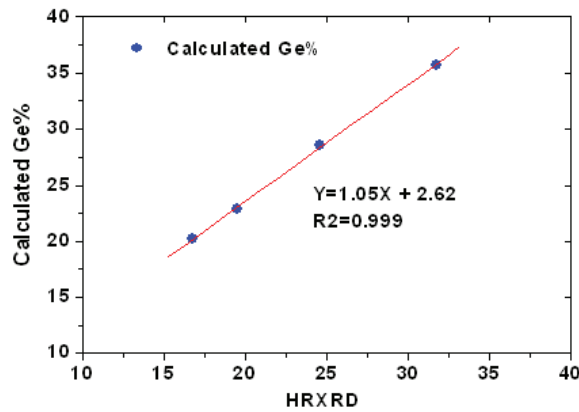


FIGURE 5. The comparison results of calculated Ge contents and HDXRD

REFERENCES

1. De Wolf and Ingrid, Semiconductor Science and Technology 11.2 (1996): 139.
2. Lucazeau and G. Abello, 1995 Raman spectroscopy in solid state physics and material science. Theory, techniques and applications. 23, pp.301-3111

KEYWORDS

Raman Shift, amorphous silicon, SiGe, amorphous carbon, local stress, semiconductor process

Positron annihilation lifetime spectroscopy (PALS) on advanced, self-assembled porous organosilicate glasses

M. Kraatz¹, A. Clausner¹, M. Gall¹, E. Zschech¹, M. Butterling², W. Anwand³, A. Wagner³, R. Krause-Rehberg², K. Pakbaz⁴

¹*Fraunhofer Institute for Ceramic Technologies and Systems – Materials Diagnostics, Maria-Reiche-Str. 2, 01109 Dresden, Germany*

²*Department of Physics, Martin Luther University Halle-Wittenberg, Von-Danckelmann-Platz 3, 06120 Halle Germany*

³*Institute of Radiation Physics, Helmholtz-Zentrum, Dresden-Rossendorf, P.O. Box 510119, 01314, Dresden, Germany*

⁴*SBA Materials, Inc., Albuquerque, 9430-H San Mateo Blvd. NE, New Mexico 87113, USA*

INTRODUCTION

The dielectric material, necessary for insulation and packaging of on-chip wiring in microelectronics, causes capacitances and signal delays, which ever increase with continuing minimization down to the nanoscale. The root cause for the capacitance is the permittivity, also called dielectric constant or k-value. The aim is to reduce the permittivity to a minimum in order to make further down-scaling possible and keep up the pace of structure integration. It seems that the only viable approach to decrease the k-value below 2.2 is to introduce a significant amount of porosity into the dielectric material. Porous organosilicate glasses (OSGs) are promising materials to serve these requests. Concurrent with the introduction of porosity, the mechanical properties substantially deteriorate and are a great concern for chip reliability. In this work, self-assembled organosilicate glasses with varying k-values down to 1.8 are investigated by positron annihilation lifetime spectroscopy (PALS) to assess the pore size. By self-assembly, the pore structure is ordered and allows higher mechanical strength at the same porosity level compared to non-ordered pores. For further characterization, the PALS study is accompanied with Monte Carlo simulation of the positronium trace in the pores of the OSGs.

MATERIAL AND METHOD

The organosilicate glass is prepared by a sol-gel template synthesis [1]. Silane precursor sols are deposited by spin coating on a silicon substrate. The porogen consists of amphiphilic triblock copolymers which act as labile blocks and are evaporated upon thermal curing. The self-assembly process forms uniform nanopores with a narrow pore size distribution. Films with thickness of about 500 nm were produced with varying porogen loading, leading to varying porosity from upper limits of 25% to 50% and k-values from 2.4 to 1.8.

The PALS measurements were performed at the positron laboratory EPOS at the electron linear accelerator with high brilliance and low emittance ELBE at the Helmholtz-Zentrum Dresden-Rossendorf. The monoenergetic positron beam is pulsed and has a high repetition rate and intensity. The positrons are created by pair-production at a tungsten target. During the monoenergetic positron spectroscopy (MEPS) measurements, the energy of the positrons was tuned between 0.5 and 12 keV with corresponding penetration depths up to 2 microns, ideal for the study of the thin films.

In insulators such as the organosilicate glass, the positrons can form positronium (Ps), which is a bound state of a positron and an electron with hydrogen-like electronic structure. A part from the positrons form para-Ps, the singlet state with antiparallel spin. The para-Ps annihilates very quickly in 125 ps. Interesting for the pore size study

is the ortho-Ps, the triplet state with parallel spin and a long lifetime up to 142 ns in vacuum. Depending on pore size, the thermalized ortho-Ps can be reflected up to millions of times, and if the pores are connected, can diffuse several microns in the material. Upon every reflection, there is a chance to exchange the electron of the Ps with an electron of the pore wall material. If the new electron has an antiparallel spin, the Ps annihilates almost instantly, called pick-off annihilation, and the annihilation radiation event can be recorded relative to the positron pulse, thus determining the lifetime. The PALS lifetime corresponds to a mean free path of the Ps in the pore structure. A longer lifetime is attributed to a longer mean free path, which can be interpreted as a pore size. The extended Tao-Eldrup model [2,3] was used to convert the lifetime to pore sizes.

Results

The results of the PALS measurements are shown in FIG. 1. In part a), the derived intensities for the pore components are shown for the sample with k-value of 2.05, representative for the porous OSG samples. The pore component intensities were derived from the PALS spectra with a routine called MELT (maximum entropy lifetime). The pore components below 1 nm are attributed to matrix effects and open volume in the glass matrix. The stacked plot shows the intensities for different positron penetration depths. The interesting peaks are between 2 and 4 nm, which are interpreted as the signal for the intentionally generated pores. The film thickness is 500 nm and the peaks beyond 500 nm depth can be explained by the broadened profile of positron penetration, where the broadening widens with increasing depth. The penetration depths shown in the stacked plot correspond only the maximum of the profile and a considerable amount of positrons form Ps in still shallower regions. In part b), the average pore sizes for all samples are plotted. The average was taken for depths from 200 nm to 500 nm. For the porous OSGs, only the component 4 corresponds to the actual, relevant pores. The pore size is in between 3 and 4 nm, as expected from the chemistry of the films. The component 4 for the dense reference samples (k-value 2.9 and 3.0) can only be explained by another open volume component in the glass matrix. Interestingly, the component 3 densifies from the dense to the porous material.

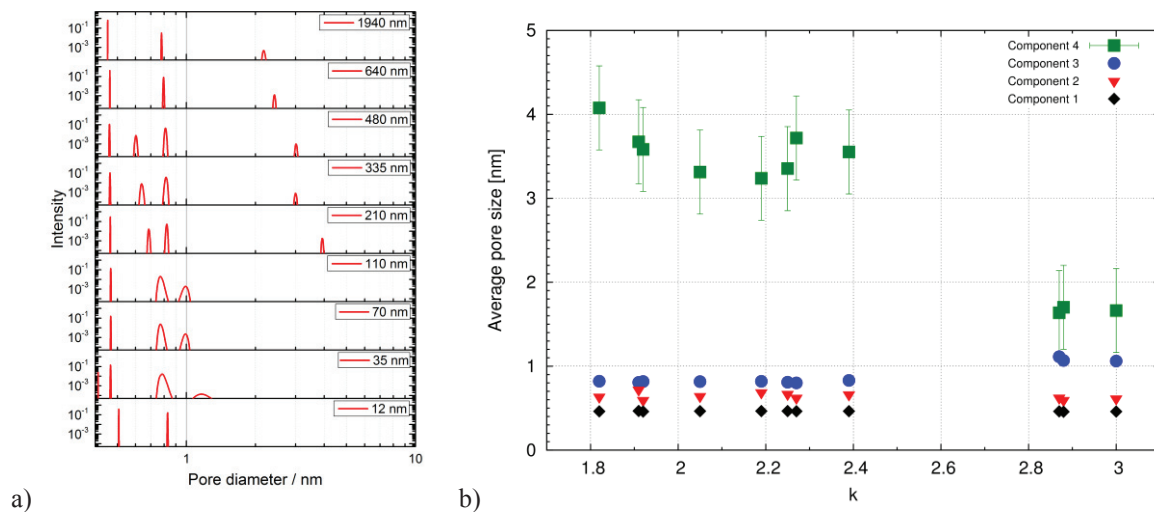


FIGURE 1. a) Intensity of the pore components as derived from the PALS measurements, representative for the porous OSG samples. The plot is stacked for different positron penetration depths. The particular sample has a k-value of 2.05. Pore components below 1 nm are attributed to matrix effects and open volume in the glass matrix and carry no information about the pore structure. The peaks between 2 and 4 nm correspond to the intentionally put in pores. b) Results of the pore size measurement. The average pore size (component 4) is between 3 and 4 nm for the porous samples. As reference, also dense OSG with k-values of 2.9 to 3.0 was measured. Here the component 4 is attributed to another open volume in the glass matrix.

Simulation Of The Ps Trace

For further characterization of the PALS method, a Monte Carlo routine has been programmed to simulate the trace of the Ps inside the pore structure. Since the pore structure is ordered and to save computational resources, a single pore was modeled in three spatial dimensions (3D) with periodic boundary conditions and regular pore connections to front, back, to the left, right, top and bottom. To estimate how far the Ps will diffuse, the border transitions were recorded. An image of a modeled pore with 500 reflections is shown in FIG. 2. The pore diameter is 3.5 nm, the pore connection length is 1 nm and the connection diameter is 1 nm.

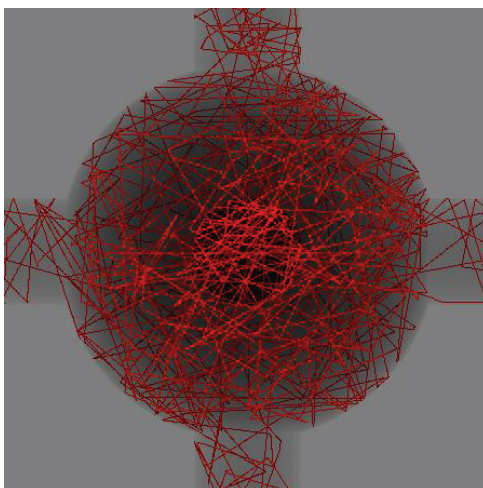


FIGURE 2. Modeled Ps trace in a single 3D pore with periodic boundary conditions and connections to the front, back, bottom, left and right. For practical reasons, only 500 reflections are shown. The pore diameter is 3.5 nm and the total connection length is 1 nm. The diameter of the connection is 1 nm.

The reflections of the Ps inside the pore are modeled with isotropic scattering and the scattering angle is randomly chosen. As a first result from the simulation, it can be stated that the Ps - during its lifetime of tens of ns - visits tens of thousands of different pores if the pores are connected with the above stated geometrical assumptions. The visited pores can cover a space with several microns in diameter. For an isolated pore, the mean free path of the trace was compared to the theoretical value of $4*V/S$, where V is the volume and S the surface area. The theoretical value for a 3.5 nm pore is about 2.3 nm. From the simulation, this value is smaller, about 1.9 nm, which can be explained by slight discretization errors. The simulation can be used to assess mean free paths in connected pore structures in order to correlate these with PALS lifetimes and derive conclusions about the topology of pores in the real material.

REFERENCES

1. D. Y. Zhao, J. L. Feng, Q. S. Huo, N. Melosh, G. H. Fredrickson, B. F. Chmelka, G. D. Stucky, *Science* 279, 548 (1998).
2. S. J. Tao, *J. Chem. Phys.* 56(11), 5499 (1972).
3. M. Eldrup, D. Lightbody, J. N. Sherwood, *Chemical Physics* 63(1-2), 51 (1981).

KEYWORDS

OSG, ULK, PALS, pore size, positronium, Monte Carlo

Terahertz Time-Domain Spectroscopy for Characterization of Doping Profiles in Semiconductors

Santosh Kurinec¹, Chih Yu Jen¹, Gaurav Tulsyan², Christiaan Richter³

¹*Microsystems Engineering*, ²*Materials Science & Engineering*, ³*Department of Chemical Engineering*
Rochester Institute of Technology
Rochester, NY 14623, USA

INTRODUCTION

Various methods currently used for determining doping profiles in semiconductors are secondary ion mass spectroscopy (SIMS), spreading resistance profiling (SRP), and capacitance-voltage measurements. SIMS is a physical characterization technique that counts all dopant atoms, whereas SRP and CV are electrical characterization techniques that measure only the electrically active ones. All these techniques have their strengths and limitations. In this paper, we present the use of terahertz spectroscopy to monitor dopant profiles in silicon.

Rapid progress in ultrafast fiber laser technology in recent years has enabled the emergence of several robust commercial terahertz metrology systems suitable for use in a manufacturing environment. Terahertz time-domain spectroscopy (THz-TDS) can accurately and rapidly measure the attenuation and phase delay for every frequency in the pulse bandwidth of the terahertz pulses generated and detected (by taking the Fourier transform of the pulse waveform). Over the last few decades, this technique has been developed, refined, and used mostly in the laboratory for scientific research [1]. It has been used to track the dynamics of electrons in nanomaterials on subpicosecond timescales, to reveal the fundamental behavior of electrons and holes, and to unlock the science of new materials like graphene or superconductors [2]. In all of these applications, the sample either has to be, or is, modeled as being a uniform film or a film having at most two or three uniform layers. Here, we have attempted to extend the use of terahertz spectroscopy to monitor continuously varying depth profiles as opposed to merely monitoring the thickness of one or more uniform layers. Phosphorus doped profiles in p type silicon wafers have been investigated to reconstruct doping profiles from terahertz transmission using THz-TDS. The results demonstrate the potential use of this technique for rapid, non-destructive determination of diffusion profiles with a potential for in situ profile monitoring.

PRINCIPLE OF THz-TDS

In the UV-Vis, NIR and MIR spectral regions of the EM spectrum free carrier absorption in doped Si is either negligibly weak and/or obscured by other optical features like impurity absorption, phonons or inter-band absorption [2]. This leaves only the terahertz and microwave regions as candidates for clear unambiguous optical probes of free carrier properties (density, mobility and as proposed here also doping profiles) in materials like doped silicon. The microwave region, although suitable, has much less dispersion (different velocity/phase shift and absorption of different frequencies) compared with the terahertz region and relatively less contrast between doped and undoped samples. These fundamental facts about the optical physics of doped silicon renders terahertz light the optimal probe for directly and nondestructively determining the free carrier distribution throughout a junction in doped silicon. Predicting doping profile relies on the interaction of THz radiation with free carriers. THz-TDS can accurately measure the attenuation and phase delay for every frequency in the pulse bandwidth of the terahertz pulses generated and detected (by taking the digital Fourier transform (DFT) of the pulse waveform) as depicted in the schematic of Fig.1. The difference of complex THz transmission between the measurement and simulation from the transfer matrix is utilized to map an electrical doping profile in the semiconductor.

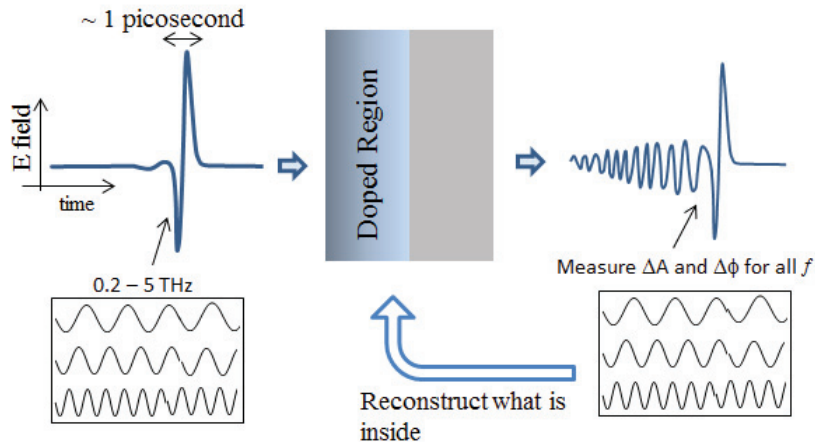


FIGURE 1. Schematic describing the working principle of THz-TDS in the determination of doping profile

EXPERIMENTAL & RESULTS

The THz-TDS system used in this work has a conventional configuration as shown in Fig. 1 and described in detail in reference [2]. Photoconductive antennae (PCAs) are utilized to generate and detect free-space broadband terahertz pulses. In our system, a Ti:sapphire laser (Coherent Mira) with pulse width 150–200 fs, 80 MHz rep rate, and average power ~ 1.3 W along with an optical delay (a moving mirror) was used to photo-excite carriers in two identical PCAs and map out terahertz pulses on a subpicosecond timescale. The pulse width is relatively long compared to the down to ~ 30 fs pulses that can be obtained with state-of-the-art laboratory laser systems. The PCA's consisted of an array of Au stripline antennae (78 striplines) on semi-insulating GaAs (BATOP iPCA-21-05-1000-800-h). The signal from the detector PCA's was amplified directly through a Lockin amplifier (SRS830) without any pre-amplification.

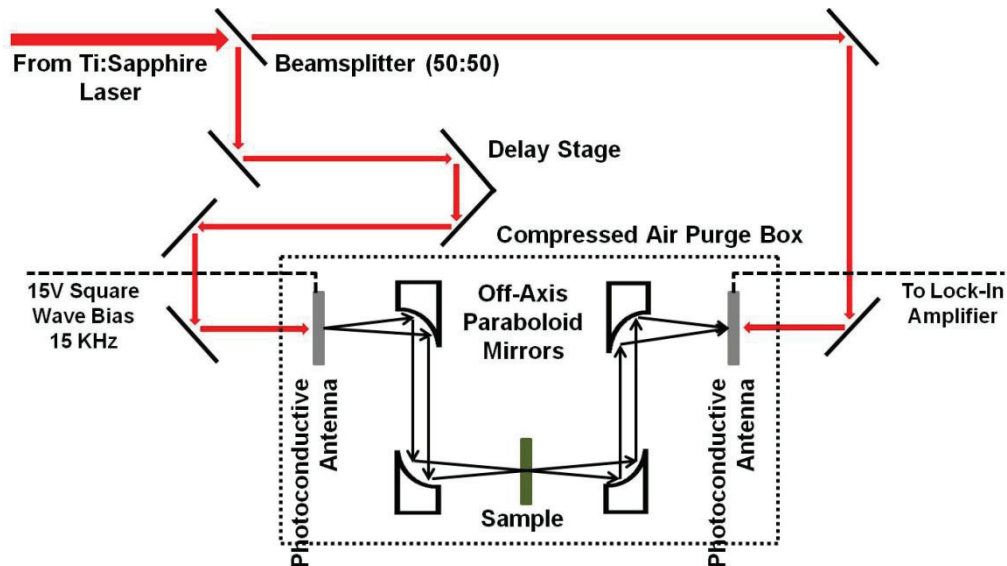


FIGURE 2. Configuration of the experimental laboratory setup of the transmission-type THz-TDS

Several phosphorus doping profiles were created in silicon wafers (boron-doped, (100), 10-25 Ω -cm) in house in the RIT's cleanroom facilities using ion implantation and thermal (rapid sand regular furnace) diffusion. Results

on two of the samples are included in this abstract as examples. Once the power ratio and phase shift are obtained from a THz measurement, the reverse fitting process is implemented to predict a doping profile. Figure 3 shows the initial guess profiles and final fitting results compared with the SIMS profiles for an ion implanted rapid thermally annealed and a thermally diffused profile. Further work is being done to investigate the application range of this technique and in other semiconductors.

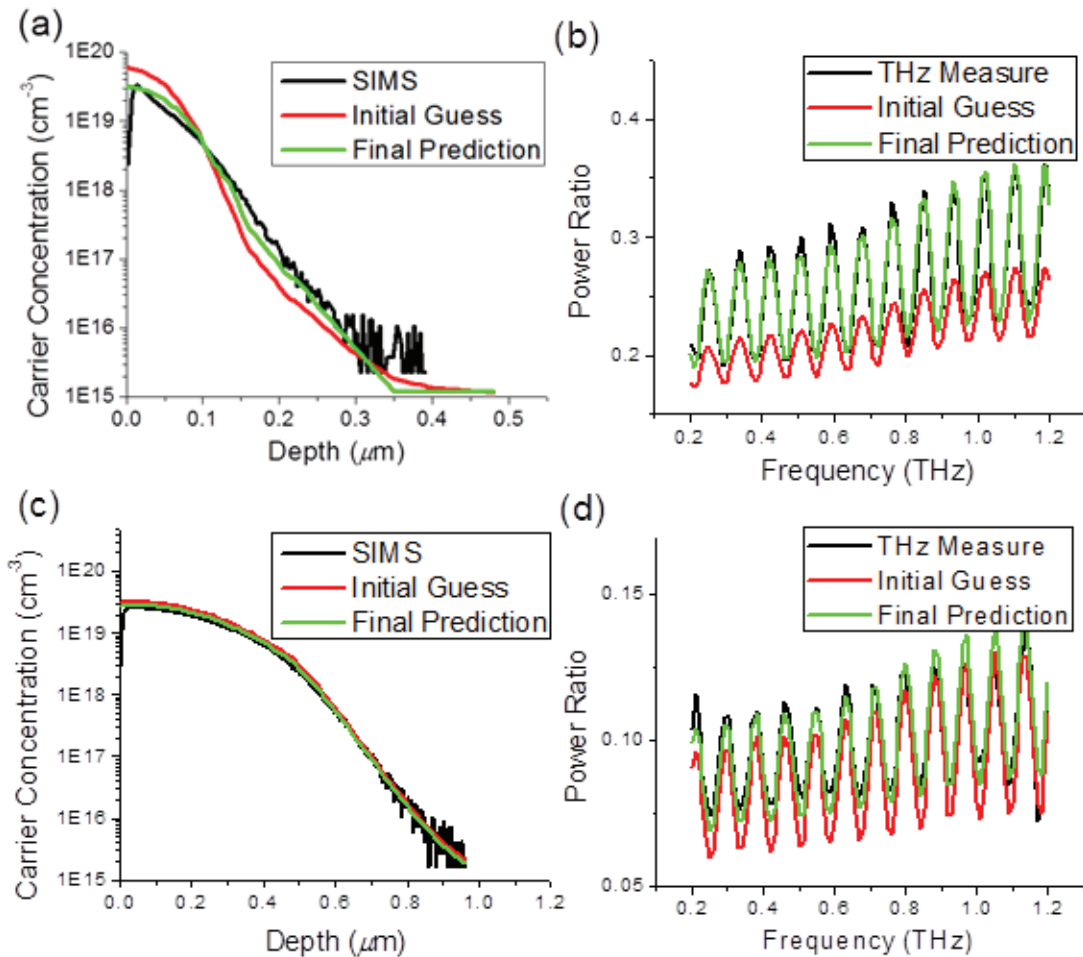


FIGURE 3. Demonstration of doping profile prediction with initial guess profiles from TCAD and its comparison with the SIMS measurements for (a,b) ion implanted, rapid thermally annealed with a dose of $1 \times 10^{15} \text{ cm}^{-2}$; (c,d) thermally diffused with a dose of $2 \times 10^{15} \text{ cm}^{-2}$.

In conclusion, we have experimentally demonstrated that the transmission mode THz-TDS can be used to map the electrically active doping profile in a non-contact manner with a potential to be an in situ monitoring technique.

REFERENCES

1. C. Richter and C. A. Schmuttenmaer, *Nature Nanotechnol.*, vol. 5, pp. 769-772, 2010
2. C.Y. Jen and C. Richter, *IEEE Transactions on Terahertz Science and Technology*, PP99, 1 - 8, (2014)

KEYWORDS

Doping profile, terahertz time-domain spectroscopy (THz-TDS)

Real-Time Monitoring of Thin-Films Using Temperature-Controlled Ellipsometry for Nanotechnology Applications

C. Licitra, F. Piegas Luce, F. Mazen, P. Noé, J. El-Sabahy, V. Jousseume, E. Beche, L. Vignoud

*Univ. Grenoble Alpes, F-38000 Grenoble, France.
CEA, LETI, MINATEC Campus, F-38054 Grenoble, France.*

INTRODUCTION

Some materials show an interesting shift of their properties with temperature allowing them to be integrated in active devices, such as phase-change memories, or to be involved in crucial process steps, such as solid phase epitaxial regrowth. On the contrary, some materials show a detrimental loss of their properties when exposed to high temperatures. The characterization of such variations is important for materials integration. It is generally done at room temperature by measuring pre-annealed samples but it requires a lot of sample preparation and it generally does not detect sharp transitions. In addition some materials present reversible properties when cooled back to their initial temperature. Temperature-controlled ellipsometry can therefore be a useful technique to characterize the change of properties along with temperature as it allows the fast detection of phase transitions and refractive index or thickness variations. In this study we will detail the use of temperature-controlled ellipsometry for the characterization of various materials. Applications are ranging from the determination of the solid phase epitaxial regrowth rate of amorphous silicon layers, the detection of the amorphous to crystalline phase transition of chalcogenides, the porous properties variations of porous SiOCH materials, and finally the measurement of the glass transition of polymers used for 3D integration.

EXPERIMENTAL APPARATUS

This work was performed using an Instec heat cell (FIG. 1) mounted on a Woollam M2000 ellipsometer in the ultraviolet to near infrared region (193-1700 nm).

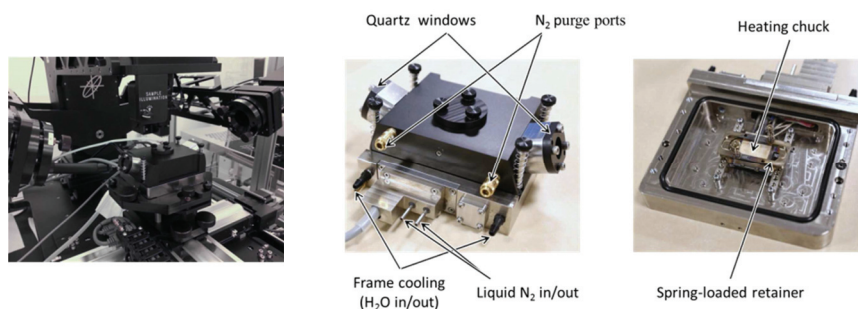


FIGURE 1. Left, heat cell mounted on the ellipsometer. Right, heat cell details.

The angle of incidence is set to 70° because of the windows orientation. The temperature can be regulated from -80°C to 600°C thanks to a resistive heating and liquid nitrogen cooling. The ellipsometric acquisition time is less

than 2 seconds enabling the use of relatively fast temperature profiles. The maximum ramping speed has been measured at around 50°C per minute and was used for the experiments at constant high temperatures. Temperature profiles with lower speed were used for the observation of phase and glass transitions.

CALIBRATION, RESULTS AND DISCUSSION

Some calibration aspects will be discussed regarding the different issues associated with heat cells. Indeed some care has to be taken to perform reliable experiments. Sources of errors can come from the windows-induced birefringence, from the substrate optical constants that can vary with temperature, from the sample oxidation or from temperature differences between the chuck and the sample's surface.

A first example of Solid Phase Epitaxial Regrowth (SPER) will be discussed. SPER is a crystallization technique used for dopant activation at low temperature in CMOS 3D sequential integration [1]. An amorphous film is formed on top of a crystalline seed and then doped. In some conditions, the annealing below 600°C allows the amorphous film to be recrystallized from the bottom seed and the dopants to be activated, enabling the thermal budget of dopant activation to be reduced. Different process conditions and different stacks will be studied showing that temperature-controlled ellipsometry is quite well adapted to monitor the SPER process. An example of recrystallization is shown in FIG. 2.

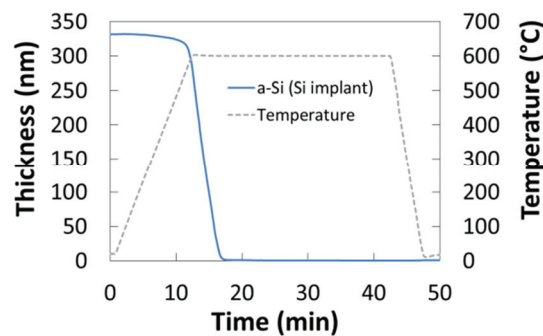


FIGURE 2. Thickness evolution of an amorphous silicon film on a silicon substrate during annealing at 600°C.

A second example of chalcogenides used for memory applications will be discussed. GeTe is a promising candidate for memory applications [2]. Real-time ellipsometry gives access to the crystallization temperature (~180°C in that case) and to different parameters variations (thickness, bandgap, drift of the refractive index vs. time). We can also easily access to the optical constants of the 2 phases. An example of amorphous to crystalline phase transition is shown in FIG. 3.

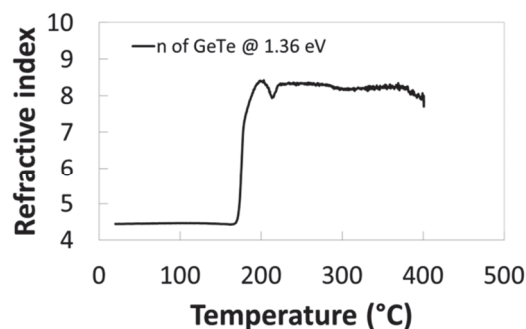


FIGURE 3. Amorphous to crystalline phase transition of GeTe observed using real-time ellipsometry.

Finally other examples will be detailed such as the measurement of the foaming of porous SiOCH materials (e.g. a film expansion associated with a porosity increase) which are used for MEMS sensors applications, the

characterization of the temperature resistance of porous SiOCH films used in the CMOS back end of the line and the characterization of polymers used for 3D integration.

CONCLUSION

Real-time monitoring using spectroscopic ellipsometry is a very powerful tool for many nanoelectronics and nanotechnology applications. It is becoming a more accessible technique since commercial heat cells can be easily adapted on existing ellipsometers. It is however still limited to small samples because of the difficulty to heat large wafers unless one mounts the ellipsometer directly on a wafer-compatible furnace. Combined with the power of spectroscopic ellipsometry, real-time monitoring can therefore accelerate the process developments of new materials by reducing the time-consuming preparation and measurement of multiple pre-annealed samples.

ACKNOWLEDGMENTS

This work was supported by the National Research Agency (ANR) through the French "Recherche Technologique de Base" Program. The experiments were performed on the Nanocharacterisation platform (PFNC) at MINATEC.

REFERENCES

1. C. Xu *et al.*, VLSI Technology, Systems, and Applications (VLSI-TSA), 2012 International Symposium on , vol., no., pp.1,2, 23-25 (2012)
2. G. W. Burr *et al.*, J. Vac. Sci. Technol. B 28 (223), (2010).

KEYWORDS

Ellipsometry, in-situ, real-time, temperature

High Precision X-Ray Multilayer Mirrors For Customized Solutions

S. Niese¹, M. Krämer¹, T. Holz¹, P. Krüger², S. Braun³, E. Zschech² and
R. Dietsch¹

¹AXO DRESDEN GmbH, Gasanstaltstr. 8b, 01237 Dresden, Germany; contact@axo-dresden.de

²Fraunhofer IKTS-MD, Maria-Reiche-Str. 2, 01109 Dresden, Germany

³Fraunhofer IWS Dresden, Winterbergstr. 28, 01277 Dresden, Germany

INTRODUCTION

The analysis of materials with X-rays is well introduced to science and industry. Two major applications are the characterization of thin films by various kinds of X-ray diffraction methods, and non-destructive imaging of heterogeneous structures with X-ray imaging methods, in particular X-ray microscopy to visualize microscopic features non-destructively. In most cases, the X-ray beam needs to be tailored with suitable X-ray optics to enhance the performance and to allow for suitable working distances. X-ray multilayer mirrors are often first choice for the application at typical laboratory X-ray sources since a beam with a requested dimension and divergence can be provided and a sufficient monochromatization is achieved. We show a typical workflow of the optimization and examples from the fabrication of X-ray multilayer mirrors for specific applications.

SYSTEM DESIGN

Several aspects have to be considered regarding the design of the entire X-ray system. This includes the choice of an appropriate X-ray source (e.g. type and size of the X-ray focus, anode material) and mirror type (e.g. one- or two dimensional operation, focusing or collimating behavior, monochromaticity/bandwidth). These conditions define the general shape of the X-ray mirror that is coated with a high precision multilayer stack of alternating materials to permit Bragg diffraction. The parameters of the multilayer vary along the length of the mirror, e.g. a gradient of the multilayer period is applied to compensate for the changing angle of incidence. Furthermore, different multilayer systems are available to achieve a narrow-band or broad-band behavior, or to tune the reflectivity. These specular properties can be predicted by respective simulations. The influence of the finite size of the X-ray source, imperfections of the curvature of the X-ray mirror, or effects due to non-negligible energy difference between the characteristic $K\alpha_1$ and $K\alpha_2$ photon energy at higher photon energies can be studied with raytracing simulations of the entire optical path, taking the specular behavior into account. Thus, a complementary optimization of the geometry of the X-ray mirror, the choice of appropriate substrate parameters, and the properties of the multilayer is possible.

EXAMPLES

In this section, some customized solutions of high precision X-ray multilayer mirrors are presented.

Condenser Optics For Full-Field Hard X-Ray Microscopy With Multilayer Laue Lenses

Multilayer Laue lenses (MLL) are a novel type of X-ray lenses fabricated by thin film deposition and subsequent micromachining. Thus, they circumvent some technological limitations of Fresnel zone plate fabrication

and aim for better efficiencies and enhanced resolution in particular for point focusing of hard X-rays at synchrotron radiation facilities [1]. Recently, we demonstrated that crossed partial MLLs can be used for full-field X-ray microscopy as well [2]. For the latter study, MLLs were integrated into a commercial X-ray microscope using the rotationally symmetric hollow-cone illumination of a capillary condenser. However, this illumination is not assumed to be optimal for MLLs, because they generate the image aside the optical axis. We present the design and first experimental results of an optimized condenser system, which takes advantage of multilayer mirrors. This configuration is characterized by a better matching of the numerical apertures of condenser and MLL, and of the size of the illuminated region to the field of view of the X-ray lens. Direct beams, Bremsstrahlung and $K\beta$ radiation are efficiently suppressed to improve imaging conditions. In addition, this configuration enables the application of photon energies $E > 10$ keV for full-field X-ray microscopy at high spatial resolution using laboratory X-ray sources. Thus, future applications are in particular seen in high-resolution and non-destructive analysis of microelectronics processes and products [3] or iron-based and related materials. First experimental results were achieved with a demonstrator setup, using a commercial Cu-K microfocus X-ray source and an ordinary X-ray camera. Though the performance of source and detector limit the imaging capabilities, the influence of the illumination was studied and radiographs were acquired (Figure 1).

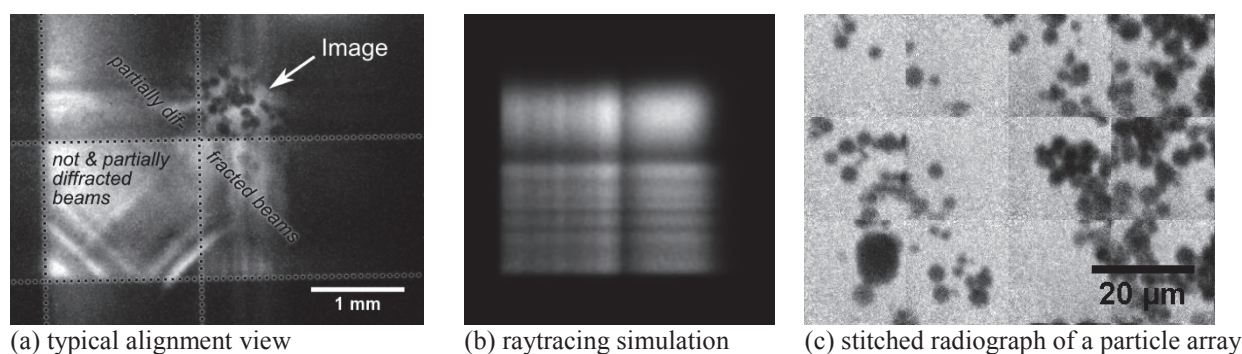


FIGURE 1. (a) and (c) Detector images acquired with the demonstrator setup. (b) Raytracing simulation of the alignment view only considering first and zero order diffraction of the X-ray lens. The general shape of the illumination expected in the image plane is well predicted.

Mirror optics for special demands

Some aspects become more important, if high photon energies, large working distances, or small X-ray sources are present. A comprehensive example is the design of a focusing mirror optics for Ag- $K\alpha$ radiation. In this case, the splitting of both $K\alpha_1$ and $K\alpha_2$ lines ($\Delta E = 0.17$ keV) as well as the lateral extent of a typical microfocus X-ray source have to be considered. Depending on the choice of the multilayer system and the dimensions, the secondary focus might be characterized by two overlapping areas of both energies, since the bandwidth of the multilayer is too small to image the entire area of the X-ray source. Some further examples of similar issues will be shown.

This work is partly supported by the German Ministry for Education and Research (BMBF) under the Program "IKT 2020 - Research for Innovations", Project No. 16ES0069.

REFERENCES

1. J. Maser, G. B. Stephenson, S. Vogt, W. Yun, A. Macrander, H. C. Kang, C. Liu and R. Conley, *Proc. SPIE*, **5539**, 185-194 (2004).
2. S. Niese, P. Krüger, A. Kubec, S. Braun, J. Patommel, C. Schroer, A. Leson and E. Zschech, *Optics Express* **22**, 20008-20013 (2014).
3. E. Zschech, S. Braun and W. Yun, *Proc. 2nd European Conf. and Exhibition on Integration Issues of Miniaturized Systems*, pp. 1-7 (2008).

KEYWORDS

X-ray optics, X-ray microscopy, X-ray mirror, X-ray diffraction, Multilayer

Analysis of Surfaces for Immobilization of Biomolecules using Soft X-Ray Spectrometry

A. Nutsch^{1*}, C. Streeck¹, J. Weser¹, B. Beckhoff¹, D. Grötzsch², W. Malzer², P. Dietrich³, T. Fischer³, C. Nietzold³, K. Rurack³ and W. Unger³

¹ *Physikalisch-Technische Bundesanstalt (PTB), Abbe Strasse 2-12, 10587 Berlin, Germany*

² *Technische Universität Berlin, Hardenbergstr. 3610623 Berlin, Germany*

³ *Bundesanstalt für Materialforschung und -prüfung (BAM), Unter den Eichen 87, 12205 Berlin, Germany*

*Corresponding author: andreas.nutsch@ptb.de

INTRODUCTION

Immobilization of biomolecules on functionalized surfaces from a liquid is essential in life science and nanotechnology. The metrology for immobilized biomolecules poses challenges such as the reliable quantification of light elements or the detection and identification of biomolecules at solid liquid interfaces. This paper addresses the capability of synchrotron radiation based instrumentation and in-situ characterization technologies to perform elemental quantification on surfaces and to identify immobilized biomolecules. X-Ray Fluorescence (XRF) analysis allows for the quantification of functional groups containing light elements such as C, N and O in a first-principles based or reference-free approach. Near Edge X-Ray Absorption Fine Structure (NEXAFS) spectroscopy is suitable to identify proteins at liquid solid interfaces using characteristic π^* resonances of amide bonds. Samples studied were amino-functionalized surfaces and Concanavalin A, a lectin originally extracted from the jack bean, immobilized from a liquid on a thin SiC membrane.

EXPERIMENTS

The analysis of immobilized biomolecules using soft X-Ray Spectrometry (XRS) was performed at the PTB plane grating monochromator (PGM) beamline for undulator radiation at the synchrotron radiation facility BESSY II. The beamline provides excitation photon energies in the range from 78 eV to 1860 eV with both high spectral purity and high photon flux. The UHV-compatible XRS instrumentation of PTB allows for the adjustment of 9 axes for the sample positioning, the recording of incident and reflected photon fluxes, as well as the insertion of a beam geometry and solid angle of detection defining aperture system. This is the enabler to apply different analytical XRS techniques such as XRF, GIXRF, XRR and NEXAFS in one set-up [1]. The accurate knowledge of relevant experimental and instrumental measurement parameters such as the beam geometry, detector response functions and efficiency, as well as incident photon energy and flux allow for reference-free quantification in XRS and, thus, for the elemental composition, and mass deposition related dimensions [2-4]. Especially, the tunable soft X-ray radiation allow for the probing of chemical states and bonds of light elements such as B, C, N, O, and F relevant for bio-technology, nano-technology and biomedical applications.

Samples for the study of functionalized surfaces were prepared on $75 \times 25 \text{ mm}^2$ glass slides. The surface was pre-conditioned (e.g. by piranha etching) and subsequently functionalized (e.g. with APDIPES or CPDMMS). Fluorescence markers containing B and F were used to probe for the efficiency of the functionalization.[5,6]

Samples used for in-situ studies of immobilized biomolecules were ultra-thin windows of either SiC or SiN that were functionalized with epoxy and sugar on one side. During exposure to a liquid containing Concanavalin A, this protein was immobilized and detected in-situ by the characteristic amide resonance at 402 eV in NEXAFS studies.

Results and Discussion

The analytical techniques XRF and NEXAFS allow for complementary characterizations of the sample surface with respect to elemental composition and contamination using XRF as well as to statements regarding chemical bonds by evaluation of characteristic features of NEXAFS spectra. Elements of interest during the analysis were O, C, N, and F.

Figure 1 shows the TXRF spectra of the samples with different surface functionalization made from different mixtures of APDIPES and CPDMMS. Figure 1 shows the respective XRF spectra. The N fluorescence line at 396 eV was deconvoluted using the physical detector response function at a calibrated energy scale. Taking into account all experimental parameters as well as x-ray fundamental parameters, the silane density on the surface was calculated as 2.3 ± 0.1 molecules/nm². A NEXAFS spectra of a silanized surface labelled with a specific fluorescence marker [5,6] was obtained by tuning the excitation energy across the absorption edge of interest. The NEXAFS resonances could be assigned to different bonds in the thin organic layer on the surface according to NEXAFS resonances as described, e.g., by Stöhr [7].

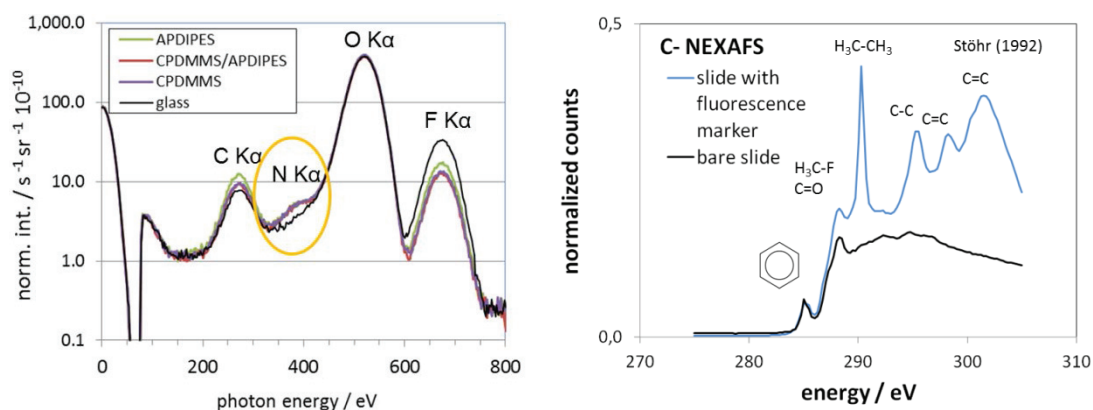


FIGURE 1. On the left side, the XRF spectra for different silanized samples and a bare glass slide are shown. The right spectra shows the NEXAFS spectra of a glass slide compared to a slide with a functionalization involving a fluorescence marker.

Figure 2 shows the principle for in-situ detection of immobilized biomolecules at the solid-liquid interface. An ultra-thin window transparent for the exciting x-ray beam and the x-ray fluorescence lines is functionalized and able to immobilize biomolecules out of a liquid. For this purpose, a new instrumentation was developed to perform these experiments in ultra-high vacuum with soft x-ray radiation. Tuning the energy across the N-K absorption edge and detecting the respective N-K fluorescence lines allows for probing the interface with respect to characteristic NEXAFS resonances of immobilized biomolecules. For the experiments the amide resonance at 402 eV was used to demonstrate the detection of the Concanavalin A in a 100 ppm solution and immobilized attached at the solid-liquid interface.

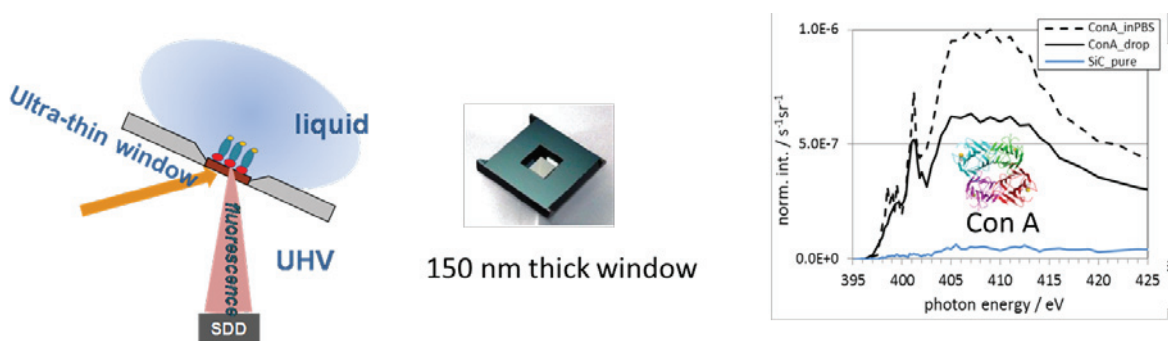


FIGURE 2. The left part shows the experimental setup using a thin window functionalized on one side. The right figure shows the N K – NEXAFS of the blank window and the NEXAFS with Concanavallin A in solution and attached to the functionalized surface of the window.

Conclusion

The surfaces used in the above presented studies are used in nanoelectronics, too. The use of similar surfaces enhances the transfer of methodologies developed in nanoelectronics to metrology applied in life science. Nanoelectronics demand for ultra sensitive and accurate metrology. Furthermore, quantification and qualification has to be traceable. In life science the application of metrology benefits from the developments and state of the art in nanoelectronics. TXRF using soft X-rays was successfully implemented for the quantification of functionalized glass slides. NEXAFS based on fluorescence detection was deployed to detect in-situ the amide bonds of proteins in liquids and at solid liquid interfaces.

Acknowledgment

This work is funded by the European Union through the European Metrology Research Programme (EMRP). The EMRP is jointly funded by the EMRP participating countries within EURAMET and the European Union.

- [1] J. Lubeck, B. Beckhoff, R. Fliegauf, I. Holfelder, P. Hönicke, M. Müller, B. Pollakowski, F. Reinhardt, and J. Weser, *Rev. Sci. Instrum.* 84, 045106 (2013)
- [2] B. Beckhoff et al. *Analytical Chemistry* 79, 7873 (2007)
- [3] M. Mantler, J. P. Willis, G. R. Lachance, B. A. R. Vrebos, K.-E. Mauser, N. Kawahara, R. M. Rousseau, and P. N. Brouwer, in *Handbook of Practical X-Ray Fluorescence Analysis*, edited by B. Beckhoff, B. Kanngießner, N. Langhoff, R. Wedell, and H. Wolff, Springer-Verlag, Berlin Heidelberg, 309, 2006
- [4] B.L. Henke, E.M. Gullikson, and J.C. Davis, *Atomic Data and Nuclear Data Tables*, 54, 181 (1993).
- [5] Hecht, M.; Fischer, T.; Dietrich, P.; Kraus, W.; Descalzo, A. B.; Unger, W. E. S.; Rurack, K. *ChemistryOpen* 2013, 2, 25-38
- [6] Fischer, T.; Dietrich, P. M.; Streeck, C.; Ray, S.; Nutsch, A.; Shard, A. G.; Beckhoff, B.; Unger, W. E. S.; Rurack, K. *Anal. Chem.* 2015
- [7] J. Stöhr, *NEXAFS Spectroscopy*, Springer Series in Surface Science, 25 (1992).

KEYWORDS

bioanalysis, synchrotron instrumentation, soft X-rays, XRF, NEXAFS

Application of helium ion microscopy to direct nano-patterning of graphene

Shinichi Ogawa and Yuichi Naito

*Nanoelectronics Research Institute, National Institute of Advanced Industrial Science and Technology (AIST)
West 7A, 16-1 Onogawa, Tsukuba, Ibaraki 305-8569 Japan.*

ABSTRACT

Graphene, which refers to allotropes of two-dimensional carbon crystals, has been intensively studied because of its unique physical and electrical properties.^{1, 2} Electron-beam (EB) lithography followed by a plasma etch³⁻⁶ has been widely used for fabricating graphene-based devices, and a lithographic technique of making graphene patterns through atomic force microscopy (AFM)-based local anodic oxidation (LAO)⁷⁻¹⁰ has been reported. However, these two methods have drawbacks. EB lithography requires photoresist processing, which might leave resist residue on the graphene surface and the residue degrades its transport properties. The AFM-based LAO is a traversal technique of time-consuming, and degradation of the AFM probe tip might occur. This study shows an impact of accelerated helium ion (He^+) beam irradiation onto the graphene using a helium ion microscope (HIM)^{11, 12} and demonstrated nanoscale direct patterning of the graphene.

Helium ions (He^+) beams of 0.3 nm diameter were scanned on single-layer graphene (SLG) films on Si/SiO₂ substrates for direct nano-patterning. The He^+ irradiated square test patterns indicated that doses of $2.0 \times 10^{16} \text{ cm}^{-2}$ at 30 kV induced a metal-insulator transition in the SLG. (Fig.1 – Fig.4) A resolution of the HIM patterning on the SLG was investigated by fabricating nano-ribbons. Scanning capacitance microscopy (SCM) measurements revealed that a spatial resolution of the HIM direct patterning non-monotonically depended on the dosage of the He^+ . Increasing the dose to $5.0 \times 10^{16} \text{ cm}^{-2}$ improved the spatial resolution to several tens of nanometers. However, doses of more than $1.0 \times 10^{17} \text{ cm}^{-2}$ degraded the patterning characteristics.

The direct patterning process using the HIM can be a versatile approach for controlling the physical and electrical properties of the graphene film and be applied to graphene-based devices.

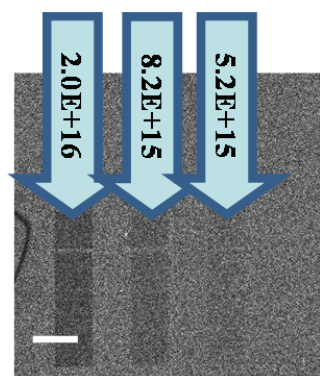


Fig.1 HIM image of SLG irradiated with 2.0×10^{16} , 8.2×10^{15} , and 5.2×10^{15} cm^{-2} dosages of He^+ . A scale bar is 500 nm

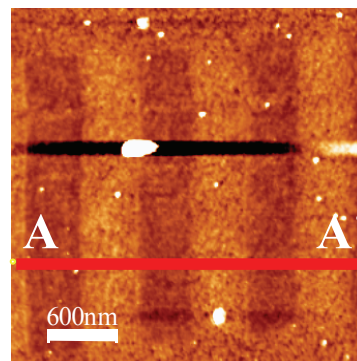


Fig2. AFM topography image of Fig. 1

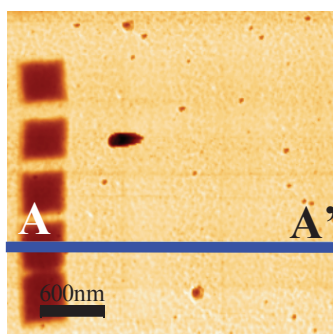


Fig.3 SCM ΔC image of Fig. 1. Scale bars in Figs. 2 and 3 are 600 nm.

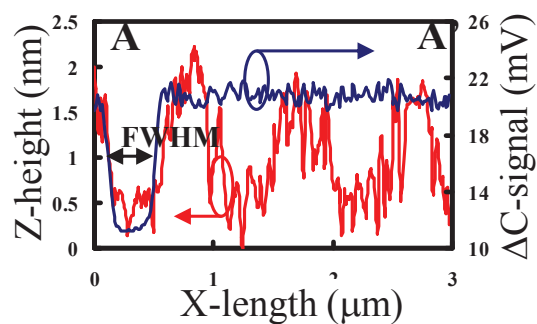


Fig.4 Line profiles along A-A' in Figs. 2 and 3.

REFERENCES

- ¹ A. K. Geim and K. S. Novoselov, Nat. Mater. **6**, 183 (2007).
- ² A. H. Castro Neto, F. Guinea, N. M. R. Peres, K. S. Novoselov and A. K. Geim, Rev. Mod. Phys. **81**, 109 (2009).
- ³ C. Stampfer, J. Güttinger, F. Molitor, D. Graf, T. Ihn, and K. Ensslin, Appl. Phys. Lett. **92**, 012102 (2008).
- ⁴ S. Schnez, F. Molitor, C. Stampfer, J. Güttinger, I. Shorubalko, T. Ihn, and K. Ensslin, Appl. Phys. Lett. **94**, 012107 (2009).
- ⁵ F. Molitor, S. Dröscher, J. Güttinger, A. Jacobsen, C. Stampfer, T. Ihn, and K. Ensslin, Appl. Phys. Lett. **94**, 22217 (2009).
- ⁶ Lin-Jun Wang, Gang Cao, Tao Tu, Hai-Ou Li, Cheng Zhou, Xiao-Jie Hao, Zhan Su, Guang-Can Guo, Hong-Wen Jiang, and Guo-Ping Guo, Appl. Phys. Lett. **97**, 262113 (2010).
- ⁷ Lishan Weng, Liyuan Zhang, Yong P. Chen, and L. P. Rokhinson, Appl. Phys. Lett. **93**, 093107 (2008).
- ⁸ S. Masubuchi, M. Ono, K. Yoshida, K. Hirakawa, and T. Machida, Appl. Phys. Lett. **94**, 082107 (2009).
- ⁹ R. K. Puddy, P. H. Scard, D. Tyndall, M. R. Connolly, C. G. Smith, G. A. C. Jones, A. Lombardo, A. C. Ferrari, and M. R. Buitelaar, Appl. Phys. Lett. **98**, 133120 (2011).
- ¹⁰ S. Masubuchi, M. Arai, and T. Machida, Nano Lett. **11**, 4542 (2011).
- ¹¹ B. W. Ward, J. Notte, and N. P. Economou, J. Vac. Sci. Technol. B **23**, 877 (2005).
- ¹² S. Ogawa, W. Thompson, L. Stern, L. Scipioni, J. Notte, L. Farkas, and L. Barriss, Jpn. J. Appl. Phys. **49**, 04DB12 1-4 (2010)

KEYWORDS

1. helium ion microscopy, 2. patterning, 3 graphene

Sensitive Nanomaterials Detection and Analysis in Solution

Janahan Ramanan, Basil G. Eleftheriades, Bhagrava Ravoori,[§] Marie Tripp,[§]
Tuyen K. Tran,[§] and Amr S. Helmy

Department of Electrical and Computer Engineering, University of Toronto, Toronto M5S 3G4, Canada.

[§]Intel Corporation, Hillsboro, OR, USA

e-mail: a.helmy@utoronto.ca

INTRODUCTION

In semiconductor manufacturing, wafers are often exposed to aqueous solutions/liquid chemicals at various stages of the process line. Any contamination of these process liquids could lead to secondary particle contamination of the wafers and/or improper processing leading to lower yields. The maximum tolerable contaminant particle size scales roughly as the half-pitch dimension of a given technology node, which is in turn defined according to the road map of the International Technology Roadmap for Semiconductors (ITRS). When they already reside on the semiconductor surface, there are established approaches that aide in detecting these particles, albeit the revelation of the chemical makeup of the particles requires expensive EDS analysis. The key to high yield is to avoid particles getting onto the wafer in the first place. In conjunction to detecting particles on wafers, particle detection in process liquids can play an important role to impact the yield.

Being able to detect the particles in solution (aqueous or otherwise) with chemical specificity to prevent their inclusion on wafer surfaces is an issue of great concern to the semiconductor industry. Thus far there has been a significant body of work outlining the implications of particle inclusion, however there are less viable solutions reported to address these concerns [1]. It is equally challenging to be able to analyze nanomaterials on the wafer surface and within solution with chemically specificity. One promising work-around is to chemically modify a CMOS transistor gate using a material that can immobilize a given contaminant. This approach is more sensitive but such a chemical detection-based approach is prohibitively expensive and is impractical: It has short lifetimes (minutes) and requires a priori knowledge of the particle attributes to be able to immobilize it selectively.

At present, there is no known sensitive means of identify nanomaterials in liquids (water based or other chemicals) without a prior knowledge of the type/nature of the materials and the need to concentrate these contaminants to be able to get a detection signal [2]. As such, there is no means for in-situ monitoring of such materials. Optical spectroscopy techniques can be optimal candidates to monitor and quantify nanomaterials in water when their sensitivity is enhanced. We have demonstrated that one can use Photonic Bandgap optofluidics to achieve 3-4 orders of magnitude enhancement in FTIR and Raman spectroscopy. We believe that this enhancement can be further improved by design and enhanced instrumentation to make Raman and FTIR an ideal tool to monitor contaminant nanomaterials in solution with sufficient sensitivity.

This approach is different as it utilizes techniques with inherent chemical specificity (Raman and FTIR) to carry out the detection. The limitation of these techniques is their low sensitivity, which the enhancement associated with the optofluidic designs we discuss here alleviate significantly to render the system of practical use with a practical technological approach that provides it with a competitive cost structure.

RAMAN SIGNAL ENHANCEMENT USING OPTOFLUIDICS

Standard Raman instrumentation is severely limited in sensitivity for the analysis of liquids gasses and aerosols, requiring large samples, due to their inefficient optical designs. These limitations prevent the technology from being more widely adopted in industries such as environmental monitoring [3,4] defense [5], biotechnology and pharmaceutical [6], where the majority of samples are gasses, liquids or aerosols. On the other hand, the new commercially available high-resolution and high-sensitivity Raman systems are bulky and, most importantly, extremely expensive.

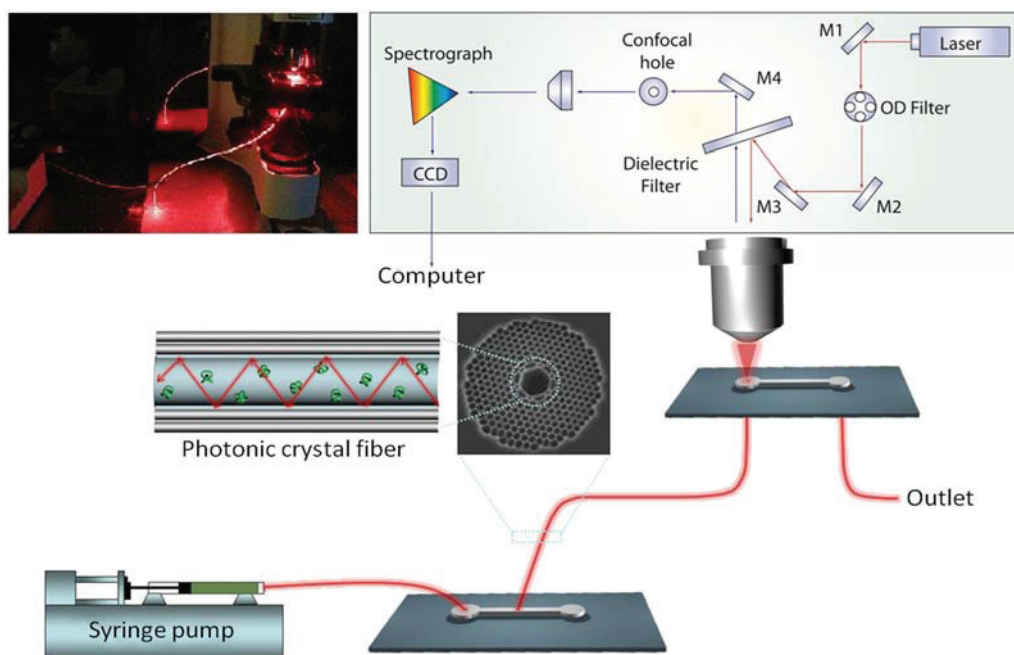


Figure 1 Schematic of the Raman setup used with the assistance of microfluidics and optofluidics.

There are many variations of Raman spectroscopy developed with the aim of improving its sensitivity for samples in the liquid and gaseous state. For example, resonant Raman spectroscopy (RR) can be used to enhance the intensity of the Raman signal by tuning the pump laser frequency to match the excited electronic state of the molecules in question. As such it is not conducive to portable systems. Surface enhanced Raman spectroscopy (SERS) and tip-enhanced Raman spectroscopy (TERS) are two other techniques in which metallic nanostructures in close proximity, or adsorbed, to the analyte can improve the Raman signal through electromagnetic and chemical enhancement. However, special substrates or metallic nanostructures that are attached to the material of interest are needed. As such these approaches are not conducive to portable systems.

A relatively new approach to increase the received Raman signal (and thus the sensitivity) for all generated Raman modes without altering the bonds of the native analyte is to incorporate optofluidic devices into the Raman spectroscopy setup as the interaction medium. Optofluidic constructs enable an increased interaction length through the confinement of both the laser light and the liquid of interest into the same cavity, enabling a strong and efficient process of light-matter interaction. Fig. 1 shows an example of a Raman spectroscopy setup utilizing an optofluidic fiber as the light-matter interaction medium in the backscattering configuration. In this example, the analyte is filled into the central core of the optofluidic fiber from the bottom end through capillary action. At the other end the pump laser light is focused into the same central core through the objective to generate Raman scattering signals from the analyte. Due to the strong confinement of the pump laser light in the optofluidic fiber, the pump laser light maintains a strong power density in the central core. As both the pump laser light and the analyte are confined within the same central core of the optofluidic fiber, the strongly confined pump laser can interact with the analyte throughout the entire fiber length. Thus, Raman signals are scattered throughout the entire length of the fiber as opposed to just the depth of field of the objective in the conventional scheme. Since Raman signals are mostly shifted by less than several tens of nanometers from the wavelength of the pump laser, they will also be confined inside the liquid core and collected throughout the fiber. As a result, the output signal from the fiber end will be collected more efficiently by the objective for detection; thus an enhanced Raman scattering signal could be retrieved at the detector.

RAMAN SIGNAL ENHANCEMENT USING OPTOFLUIDICS

The approach described above has been used to verify its efficacy to detect nanoparticles that are dispersed in UPW. Various nanomaterials including Al_2O_3 , SiO_2 and TiN have been studied. They were dissolved in UPW and the Raman spectra of these solutions are then obtained using the aide of opto-fluidics. As an example the spectrum

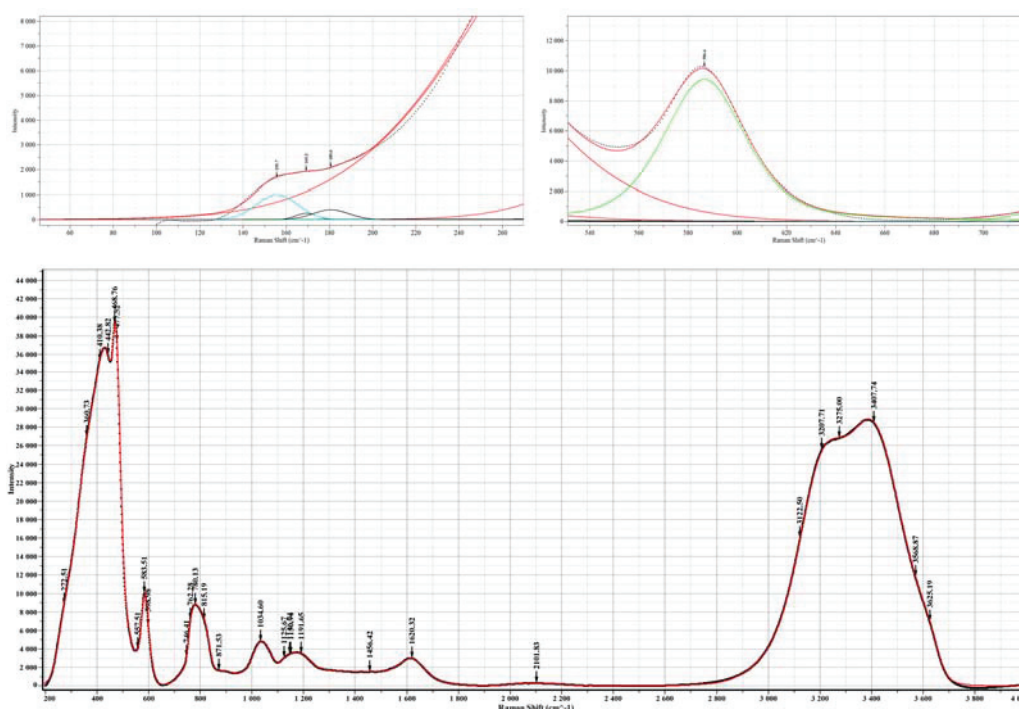


Figure 1 Raman spectra of UPW with Al_2O_3 obtained using optofluidics. The two inset focus on two regions of the spectrum where Al_2O_3 Raman modes reside.

of UPW with Al_2O_3 incorporated is shown in Fig. 2. In this example, Al_2O_3 is incorporated at a calculated molar concentration of 1.3×10^{-11} molar assuming that the mobility diameter \sim physical diameter. As can be seen in the figure Raman spectra with exquisite signal to noise ratio can be obtained using this approach. As obtained from the literature Raman modes for Al_2O_3 are located at: 184.88, 252.81, 381.87, 419.23, 484.90, 538.11, 578.87, 646.80, 675.10, 710.20, 753.22, 815.49 and 852.85 cm^{-1} . In the obtained spectrum, peak fitting for modes at 161.28 & 372.69 cm^{-1} accurately matches what is expected for Al_2O_3 after the background is subtracted. The Raman modes $> 100\text{-}400$ cm^{-1} region cannot be accurately analyzed due to the presence of strong silica modes that coincide with those belonging to Al_2O_3 . The silica modes can be attributed to the silica fibre used to obtain the Raman spectra.

KEYWORDS

Nanomaterials detection, Chemically Specific Sensing, Optical Spectroscopy, Optofluidics, Handheld Sensors.

REFERENCES

- 1 Abbas Rastegar, Martin Samayoa, Matthew House, Huseyin Kurtuldu, Sang-Kee Eah, Lauren Morse, and Jenah Harris-Jones, Particle Control Challenges in Process Chemicals and Ultra-pure Water for sub-10 nm Technology Nodes, Extreme Ultraviolet (EUV) Lithography V, Proc. of SPIE, 9048 (2014).
- 2 Wibowo, J., Shadman, F., Blackford, D., "Measuring and removing dissolved and colloidal silica in ultrapure water". MICRO, Ultrapure Fluids (1997)
- 3 U. Villanueva, J.C. Raposo, K. Castro, A.d. Diego, G. Arana, J.M. Madariaga, Raman spectroscopy speciation of natural and anthropogenic solid phases in river and estuarine sediments with appreciable amount of clay and organic matter, J. Raman Spectrosc. 39 (2008) 1195-1203.
- 4 A. Sarmiento, M. Maguregui, I. Martinez-Arkarazo, M. Angulo, K. Castro, M.A. Olazábal, L.A. Fernández, M.D. Rodríguez-Laso, A.M. Mujika, J. Gómez, J.M. Madariaga, Raman spectroscopy as a tool to diagnose the impacts of combustion and greenhouse acid gases on properties of Built Heritage, J. Raman Spectrosc. 39 (2008) 1042-1049.
- 5 M.D. S., S.R. J., Portable Raman explosives detection, Anal. Bioanal. Chem. 393 (2009) 1571-1578.
- 6 R.M. Abu-Ghazalah, S. Rutledge, L.W.Y. Lau, D.N. Dubins, R.B.M. J., A.S. Helmy, Concentration-dependent structural transitions of human telomeric DNA sequences, Biochem. 51 (2012) 7357-7366.

In-Die high resolution nanotopography data, impact in the CMP process monitoring for advanced nodes

N. Ruiz¹, F. Dettoni², M. Rivoire^{1,2}, V. Balan¹, C. Beitia¹

¹ Univ. Grenoble Alpes, F-38000 Grenoble France

CEA, LETI, MINATEC Campus, F-38054 Grenoble, France

² STMicroelectronics, 850 rue Jean Monnet, 38926 Crolles, France.

a e-mail: carlos.beitia@cea.fr, Phone: +33 (0)4 38 78 20 69, Cell: +33 (0)6 89 79 84 65

INTRODUCTION

Today semiconductor industry trends are toward complexity, 3D integration and miniaturization. Thus, in the more Moore classical approach, the number of process steps and new materials has increased making advanced nodes technology very complex. On the other hand, 3D integration has appeared in the More than Moore approach as an alternative to improve functionality and/or performances (stacking different devices in a whole system or stacking transistor layers in the 3D monolithic approach). A common and key process appears in this context, Chemical mechanical planarization (CMP). Nanotopography in all these technologies is crucial in order to achieve proper process due to its impact on CMP.

Recently nanotopography data has been made available at wafer and die level, through different flavors of interferometry techniques with and without stitching and different lateral and axial resolution [1, 2, 3]. This considerable amount of data gives access to local and global information in-die and over the wafer in a statistical way which can be very useful for improving CMP process.

The present study deals with high resolution nanotopography data (μm scale) at die level across the wafer. In previous work the challenges to access to this data have been solved [4, 5]. However, the next step of analyzing the data is also important, the present work will show that classical parameter are not enough and new areal analysis combined with local statistical zone comparisons will give new insight to CMP process optimization.

EXPERIMENTAL

In this study we have used an interferometer WYKO NT9300 from Bruker. The interferometer operates in a phase shifting mode ($\lambda = 533 \text{ nm}$) using a Michelson configuration. The field of view is $2.4 \text{ mm} \times 1.8 \text{ mm}$, the vertical resolution is 1 nm and the lateral resolution is $3.6 \mu\text{m}$. Stitching measurements were performed in order to have die level maps.

The wafers studied are of two types, to underline the general problem: Front end of line at STI and PMD CMP process steps and Back end of line wafer with several metal layers for 28 nm technological nodes.

RESULTS AND DISCUSSION

Die level nanotopography maps of the BEOL wafer are displayed in Figure 1. They show the different zones of the die and the difference between center and edge dies. It is important to underline the quantity of data available in such a map. Under the actual acquisition conditions a cm^2 die with a μm level resolution represents more than 64 million points. For confidential reasons all data have been normalized, this do not avoid the analysis and study of the nanotopography variations. This data gives a unique statistics information over the wafer and allows representative comparison inside die and between dies. This it is well illustrated in Figure 1 where it can clearly be observed both contributions to the nanotopography variation over the wafer. The first information that the high resolution maps gives is a global view of the total area of the die and an indication of potential problematic zones as well as their position in the die and over the different die in the wafer. This is a big advantage when comparing to

traditional test box measurement, for two reason, first there is not point to compare one profile data to the amount of data in the nanotopography maps and second given the dependency between CMP and local variation of structures densities and materials in the die, the representativity of the local profile respect to the global die information is a real added value.

In order to go further in the analysis of the information inside the data, the FEOL wafers have been measured after CMP at three different dies on the wafer positions (center, middle and edge) and a distribution heights analysis was carried out in the data.

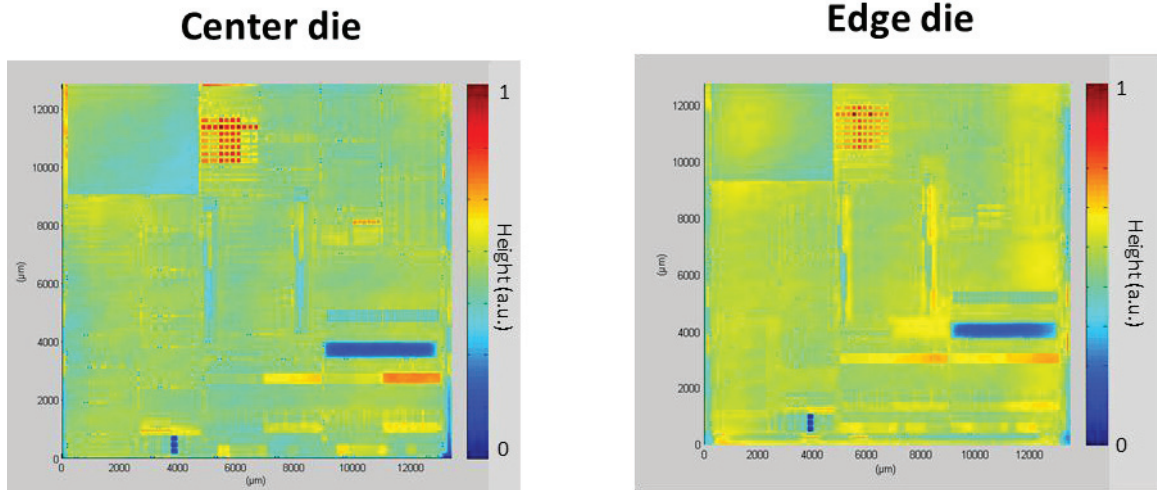


Figure 1 Nanotopography map after CMP at BEOL wafers center and edge die.

Figure 2 shows the nanotopography maps of both process steps after CMP as in figure 1. Given the amount of data, the height distribution was calculated in a histogram by using a 1000 bin partition. The minimum height value was defined as the zero class value and the values were normalized respect to the maximum value of the different dies of each process step. This allows comparison of relative height center position of the distributions easily. This information is representative of the whole die (contrary to classical profile local data) and gives a good indication of the efficiency of CMP process.

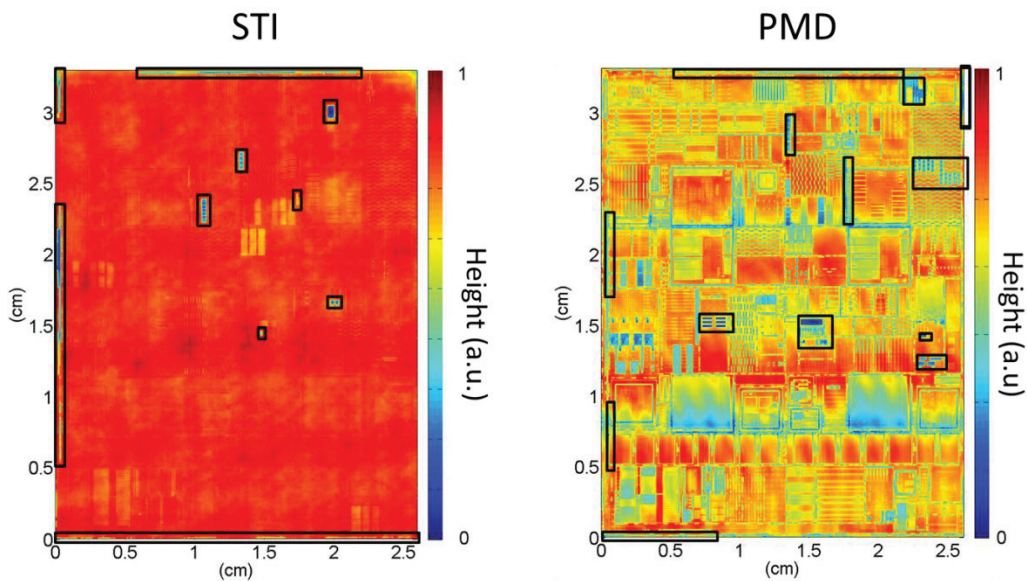


Figure 2 Die nanotopography at STI and PMD process steps just after CMP and position of problematic zones

Indeed, in the case of an ideal perfect CMP processed flat surface, a Dirac distribution will be expected. For real processes we can consider that a unique and narrow Gaussian distribution will represent an optimized CMP process. So the appearance of different populations in the height distribution and the increase of its middle height half width value will be good indicators of CMP limitations. Figure 3 shows the results for the height distribution for both processes.

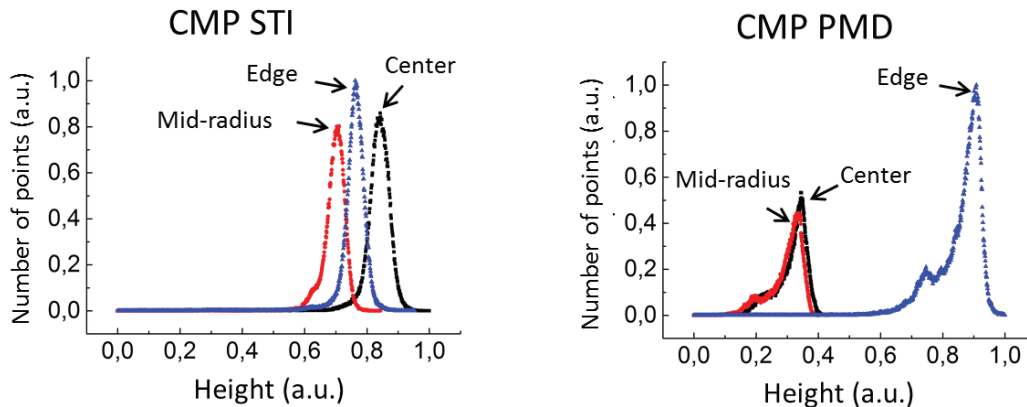


Figure 3 Normalized heights distributions for CMP STI and CMP PMD processes.

It is easy to see the differences in figure 3 and a process signature in the distribution can be observed. The CMP STI process can be well described by a Gaussian distribution with a negligible secondary population in the lower values side of the distribution, so we can consider that they represent mostly a unique population. In addition all distributions are centered about 0.8 with 0.1 variations. This CMP process is selective. The heights distribution analysis coupled with the traditional local profile approaches, which still possible in the same data, indicates that spite of some dishing introduced between materials, CMP is efficient for the die level uniformity (independent of the different in material and densities inside the die) and this across the wafer. At the contrary, the CMP PMD process has a clear different signature with an important secondary population in the lower values side of the distribution. In this case it cannot be assumed a unique population. Also the mean heights between dies are different. Thus, the distribution center value in the edge die is about 0.9 while middle and center die are at about 0.3. This double population may be attributed to the non-selective nature of this CMP process. Again, this analysis coupled with the standard profile analysis, shows that even if the process does not present dishing at the die level it is not uniform over the die and differs from edge respect to middle and center position of the wafer.

CONCLUSION

This work demonstrates that high resolution nanotopography data gives new insights to CMP impact analysis in the surface of the wafers. The results show that nanotopography maps, gives access to information from cm to μm scale at die and wafer level. Such detailed information was not possible to gather with classical profiles and test box measurements. These maps are a quick way to detect problematic zones and have an idea of the global variation over the whole die and are complementary to local profile measurements. Finally, given the amount of data, statistical analysis considering die level height distribution is possible. The distribution parameters (position and half width) are shown to be pertinent to monitor and evaluate CMP efficiency and opens news ways for CMP metrology. Finally this kind of measurement and analysis are expected to be useful for other technological brick as 3D integration, 3D monolithic integration and substrate bonding.

REFERENCES

1. F.Dettoni et al, Frontier of Characterization and Metrology for Nanoelectronics, (FCMN), 221-223 (2013)
2. R. O. Topaloglu et al, International Conference on Planarization/CMP Technology, 98- 101 (2013)
3. D.Lewke et al, Advanced Semiconductor Manufacturing Conference, (ASMC), 243-248 (2013)
4. F.Dettoni, PhD thesis, October (2013)
5. F.Dettoni et al, Microelectronic Engineering **113**, 105-108 (2014)

KEYWORDS

Nanotopography, interferometry, CMP, die-level

High Resolution X-ray Diffraction For In-line Monitoring Of Ge MOSFET Devices

Paul Ryan¹, Matthew Wormington², Jianwu Sun^{3,4}, Andriy Hikavy³, Yosuke Shimura^{3,5,6}, Liesbeth Witters³, Hilde Tielens³, and Roger Loo³

¹Jordan Valley Semiconductors UK Ltd, Belmont Business Park, Belmont Durham, DH1 1TW, UK

²Jordan Valley Semiconductors Inc, 3913 Todd Lane, Suite 106, Austin, TX 78744, USA

³IMEC, Kapeldreef 75, B – 3001 Leuven, Belgium

⁴ Currently at The Department of Physics, Chemistry and Biology (IFM), Linköping University, Linköping 58183, Sweden

⁵ Instituut voor Kern- en Stralingsfysica, KU Leuven, 3001 Leuven, Belgium

⁶ FWO Pegasus Marie Curie Fellow

INTRODUCTION

With the proposed introduction of new materials for the channel of Si semiconductor transistors at the sub-10 nm technology nodes there is the associated challenge of providing in-line characterization and metrology of material quality and properties. Strained and relaxed Ge channels are leading candidates for the channel material in for the NFET and PFET transistors required for CMOS technology. In this paper, we demonstrate the use of high-resolution X-ray diffraction (HRXRD) for both research and in-line monitoring of such devices. HRXRD has been used for many years for the characterization of epitaxial layers, for the development of new epi. processes, with the emphasis on materials characterization in the research phase rather than the on-going metrology required during production of devices¹. However, with the strain state and crystal quality of these structures being of increasing importance in future generations of transistors, HRXRD is already being used as a non-destructive in-line technique for development, integration and monitoring of these relaxed and strained epitaxial layers.

FABRICATION OF SAMPLES

Three different sample types were produced, a relaxed Ge layer², a strained Ge layer³ deposited on a single strain relaxed SiGe layer and a strained Ge layer deposited on a SiGe strain relaxed buffer structure (SRB)⁴. Samples were fabricated with different trench sizes and spacing to investigate the strain relaxation of layers as a function of trench size and processing conditions as well as on blanket wafers:

1. Relaxed Ge was grown selectively into trenches in shallow trench isolation after a Si recess. To reduce threading density, thick Ge layers were grown exceeding STI surface. Before making devices, the Ge layers were then made smooth using a CMP process.
2. The growth of strained Ge was more complex, and involved the integration of a single strain relaxed SiGe layer within the STI trenches after Si recess, with a Ge layer deposited on top of the buffer. The top Ge layer was strained with respect to the relaxed SiGe buffer layer.
3. Commercially available strain relaxed buffers consisting of 5 relaxed SiGe layers of increasing Ge content were used on which we deposited a Ge channel strained to the top SiGe layer. This was deposited as a blanket film with no patterning.

CHARACTERISATION

HRXRD measurements were performed using a Jordan Valley JVX7300LM X-ray metrology located in IMEC 300 mm fab. The system is equipped with both a large X-ray beam for measurements on blanket wafer and larger arrays of structure, and a smaller beam suitable for measurements on patterned wafers. Switching between sources is fully automated within recipes, and both sources were used. For standard monitoring of samples, standard ω -2 θ scans and Omega rocking curves were used, with the ω -2 θ scans giving information about the strain / relaxation states of the Ge layers within the samples, and rocking-curves giving defect information. For more detailed analysis, reciprocal

space maps were collected which can provide unambiguous relaxation and composition values from the different SiGe layers within the structure.

HRXRD scans were performed both along and across the lines to determine any anisotropy in the strain state of the epitaxial structures due to the trench dimensions. Electron microscopy (SEM and STEM) measurements were also performed to compare the uniformity and quality of the deposition of the layers within the trenches.

Relaxed Ge on STI Patterned Wafer

To determine quality of the relaxed Ge layer, SEM and HRXRD (ω -2 θ and ω scans) were performed.

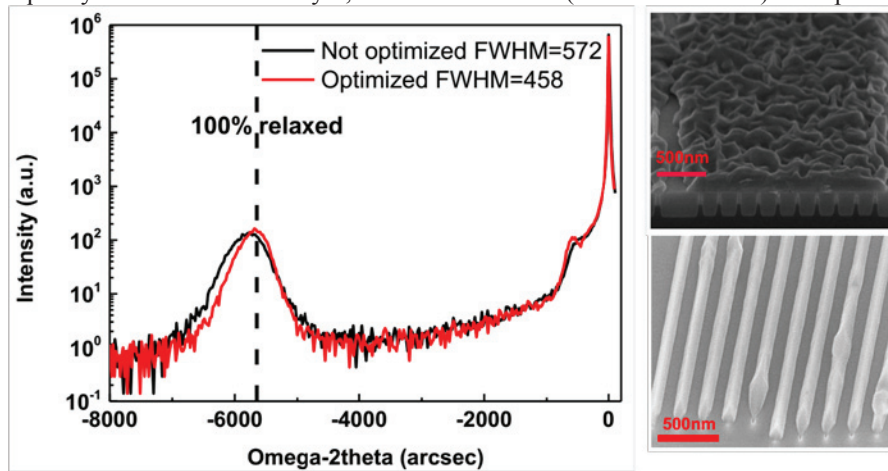


FIGURE 1. HRXRD (left, 004 reflection) and SEM (right, non-optimal on top and optimized on bottom) of relaxed Ge layers.

The position of the peak within the ω -2 θ scans indicates the layers are fully relaxed, and the widths of both the ω -2 θ and ω scans (for constant thickness) is an indication of the layer quality. For an optimized growth process, the full width of the peak is reduced from $\sim 572^\circ$ to 458° , with the corresponding improvement illustrated in the SEM images.

Strained Ge / relaxed SiGe on STI Patterned Wafer

To assess the strain state of the strained Ge and relaxed SiGe buffer structure requires more detailed measurements than in the relaxed Ge case above.

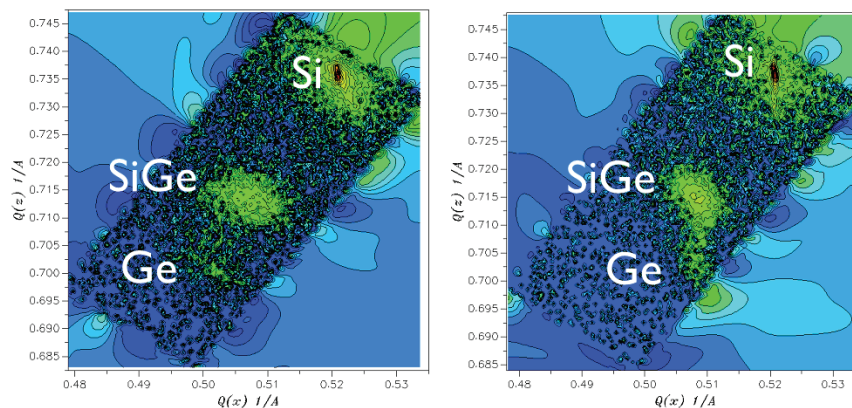


FIGURE 2. RSMs of the asymmetric 224GE reflection across and along the fins.

Unlike in the above case, where the only variable in the lattice parameter determined from the ω -2 θ was Ge relaxation, in the case of SiGe buffer layers either Ge content changes or relaxation changes can affect the peak position in the ω -2 θ scan. In this case, measurements collected at two different reflections are required to separate the effects, and give accurate values for both the composition and relaxation.

To investigate in more detail reciprocal space maps (RSMs) were performed both along (longitudinal) and across (transverse) the fins. From the RSMs, it is clear that the SiGe strain relaxed buffers are relaxed with respect to the Si substrate. Detailed analysis gives a Ge content of 70%, with relaxation values of 88% both along and across the fins.

However, the Ge layer is uniaxially strained along the fins, with some relaxation occurring across the fins. The relaxation of the SiGe and Ge layers across the fins varies with processing conditions.

Strained Ge / multiple relaxed SiGe layers on Blanket Wafer

Omega-2Theta scans and reciprocal space maps were performed on the samples containing multiple buffer layers.

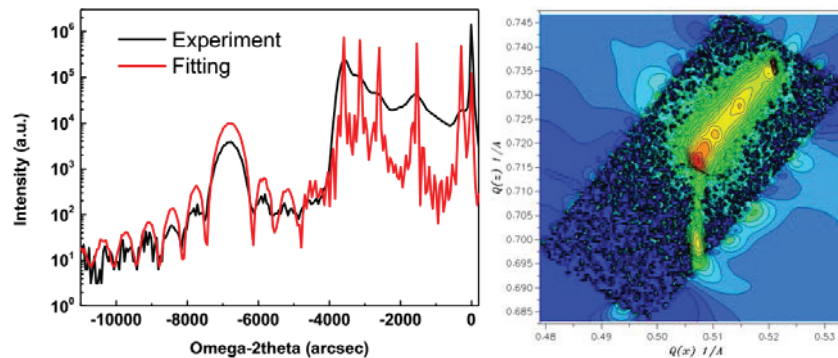


FIGURE 3. (004) Omega-2Theta scan (left) (224) RSM right, showing high quality Ge layer on fully relaxed SiGe buffer.

The ω -2 θ scans from the 004 measurements show clear peaks from each of the buffer layers (sharp peaks in the simulation) and a clear peak with fringes from the top Ge layer. The presence of fringes indicates the Ge layer is strained and of good crystal quality. It also allows the simulation of the structure using Jordan Valley RADS software⁵ to obtain the relaxation and thickness of the Ge layer, giving values of 29.6nm for the thickness.

The ω -2 θ scan can give compositions of all layers assuming the relaxation of the buffer layers is known. The RSM gives confirmation that the SiGe layers are indeed all fully relaxed. This approach has recently been extended to patterned STI wafers.

SUMMARY

Differences in the relaxation of the Ge layer deposited on the SiGe buffer layer has been observed across and along the trenches, with uniaxial strain along the fins and with the magnitude of the relaxation across the fins being dependant on the width of the trenches⁶, which is preferred for device performance. In addition, the epilayer quality can be influenced by process conditions, and monitored using HRXRD.

HRXRD has been used to non-destructively characterize relaxed and strained Ge layers and SiGe strain relaxed buffer layers and allows the monitoring of strain levels and relaxation during post epi device processing. The measurements were performed in a fully automated environment suitable for production monitoring of the thickness, composition and relaxation state of epilayers on both blanket and product wafers.

REFERENCES

- 1 D. K. Bowen, B.K. Tanner, X-ray Metrology in Semiconductor Manufacturing, Taylor & Francis (2006).
2. G. Wang, E. Rosseel, R. Loo, P. Favia, H. Bender, M. Caymax, M. M. Heyns, and W. Vandervorst, *Journal of Applied Physics* 108, 123517 (2010)
3. R. Loo, J. Sun, L. Witters, A. Hikavy, B. Vincent, Y. Shimura, P. Favia, O. Richard, H. Bender, W. Vandervorst, N. Collaert, and A. Thean, 7th International Silicon-Germanium Technology and Device Meeting (ISTDM), Book of Abstracts, p. 27, 2014
4. R. Loo, L. Souriau, P. Ong, K. Kenis, J. Rip, P. Storck, T. Buschhardt, M. Vorderwestner, *Journal of Crystal Growth* 324 (1), 15 (2011)
5. M. Wormington, C. Panaccione, K.M. Matney, D.K. Bowen *Phil. Trans. Roy. Soc. Lond. A* **357**, 2827 (1999).
6. J. Mitard et al. *Symposium on VLSI Technology*, p. 138 (2014)

KEYWORDS

X-ray, metrology, SiGe, Ge channel, diffraction, strain, relaxation

Advanced Metrology For Beyond Silicon Semiconductor Device Structures

Andreas Schulze^{1,*}, Roger Loo¹, Johan Meersschaut¹, Dennis van Dorp¹, David Gachet², Jean Berney², Wilfried Vandervorst^{1,3} and Matty Caymax¹

(1) imec, Kapeldreef 75, 3001 Leuven, Belgium

(2) Attolight AG, EPFL Innovation Park Building D, 1015 Lausanne, Switzerland

(3) KU Leuven, Dept. of Physics and Astronomy, Celestijnenlaan 200D, 3001 Leuven, Belgium

(*) Andreas.Schulze@imec.be

INTRODUCTION

In order to continue CMOS scaling for the 7 nm node and below, the integration of advanced semiconductor materials such as Germanium (Ge) and III-V compound semiconductors (InP, InGaAs, InAlAs) is indispensable [1]. This is mainly due to the fact that charge carriers inside the latter materials exhibit significantly lower effective masses and hence offer enhanced mobility and injection velocity values in comparison with silicon (Si). This in turn facilitates the fabrication of transistors with increased performance. Although Ge and III-V compound materials can be grown epitaxially on Si substrates to date, the large differences in lattice constant and material characteristics typically lead to very high defect densities in these layers, causing a degradation of the material properties and hence device performance. For this reason, a qualitative and quantitative assessment of the defectivity of such layers is of utmost importance. Moreover, controlling layer parameters such as thickness, composition, crystalline quality and strain becomes more and more difficult but at the same time also more demanding. Although transmission electron microscopy (TEM, in combination with EDX, NBD) has emerged as a very sophisticated metrology tool capable of determining the above mentioned parameters, the complexity (i.e. measurement time) as well as the destructive nature of the technique limit its application during process development and in an actual fab environment. Moreover, it is important to note that due to its high spatial resolution TEM can visualize individual crystalline defects in great detail, however, the reduced specimen size and the limited field of view hamper the assessment of defect densities below $\sim 1e8 \text{ cm}^{-2}$.

The aim of this project is therefore to explore various metrology concepts and assess their applicability towards characterizing heteroepitaxial device structures with respect to their material properties as stated above, thereby focusing mainly on techniques that can cope with increased demands in terms of precision, repeatability, selectivity, massive data processing and better turn-around-times. Although non-destructive and fast techniques are highly desired for this purpose, the indirect nature inherent to most of these techniques makes a cross correlation and calibration using a direct technique providing an absolute number inevitable.

In the first part of this conference contribution we will focus on defect characterization. We will start with reporting our latest results on direct metrology providing absolute numbers for the defect density in (Si)Ge and III/V-based structures grown on Si. Our method of choice for this purpose is defect decoration by chemical etching and subsequent etch feature inspection and counting. We apply the latter technique to blanket strain-relaxed buffer layers (SRB, suited for STI-last integration schemes) as well as layers grown selectively in narrow trenches resulting in fin-shaped structures (fin replacement). We will then present results obtained using indirect defect metrology techniques such as RBS and CL on the very same samples. This allows us to properly study the sensitivity and the dynamic range of the respective techniques and eventually achieve calibrated quantification procedures. In the last part we will demonstrate the use of small spot size XRD as an in-line metrology tool for monitoring composition and strain relaxation in narrow fin structures by means of dedicated metrology arrays.

DIRECT OBSERVATION OF EXTENDED CRYSTALLINE DEFECTS

While TEM can be used to quantitatively determine the defect density in structures containing many defects, the technique fails once the defect density drops below $\sim 1e8 \text{ cm}^{-2}$ due to the small sampling volume and the limited field of view, respectively. Chemical etching, on the other hand, can be used to decorate (i.e. visualize) crystalline defects such as threading dislocations and stacking faults and hence allows inspection and counting of these etch features at lower magnification, i.e. larger field of view. This in turn allows for improved statistics and moreover enables the characterization of lowly defective structures. We will show that in case of blanket SiGe SRB layers, vapor phase HCl etching [2] can be used to reveal aforementioned defects as etch pits or etch lines on the layer surface. Gas phase defect etching, although less well known than classical wet etching techniques based on solutions of Cr(VI) compounds, has several advantages such as no ES&H concerns and full wafer capability. Due to the thickness of SRB layers ($> 500\text{nm}$), relatively large etch pits can be generated (assuming the defect density is not too high which would otherwise lead to etch pit overlap). Using optical microscopy and defect inspection tools (e.g. haze measurements) we are able to map the distribution of isolated threading dislocations as well as pile-ups of dislocations across 300mm wafers. In case of thin layers or confined volumes such as narrow fins, the maximum size of the generated etch features is limited by the dimensions of the structure under test. We will demonstrate that under such circumstances automated inspection using a SEM review tool is required. Etch pits of $\sim 10\text{-}15\text{nm}$ in diameter generated by vapor phase HCl etching on a highly defective blanket $\text{Si}_{0.25}\text{Ge}_{0.75}$ layer are shown in Figure 1a. We are currently extending the procedure towards decorating defects in $\text{Si}_{0.25}\text{Ge}_{0.75}$ fins as well (Figure 1b). We will demonstrate that due to loading effects leading to an increased and non-uniform etch rate across the fin (Figure 1c) a careful adjustment of the process parameters is required in order to make it applicable to narrow fins as well.

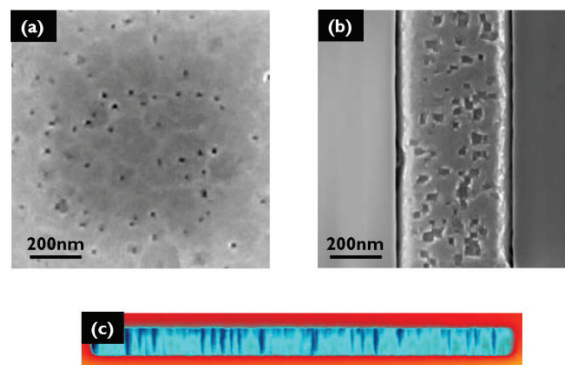


FIGURE 1. Etch pits as observed by SEM on (a) blanket $\text{Si}_{0.25}\text{Ge}_{0.75}$ layer and (b) $\text{Si}_{0.25}\text{Ge}_{0.75}$ fin generated by in-situ gas phase HCl etching. (c) AFM image obtained on a 200nm wide InP fin after etching in HBr solution. The presence of $\{111\}$ defects in the fin leads to preferential etching and hence to the formation of grooves on the surface.

Defect etching of III-V semiconductor materials is less well developed. We choose to start with wet defect etching techniques, focusing on InP selectively grown in narrow trenches. InP is an attractive buffer layer for the actual (e.g. InGaAs) channel layer. We will demonstrate that diluted HBr solutions can be used to reveal $\{111\}$ defects such as stacking faults and twins in nanoscale InP fins (Figure 1c).

The progress reported on chemical defect etching for (Si)Ge and InP constitutes an essential advancement in defect metrology providing absolute numbers on defect levels and is therefore of crucial importance for the understanding and calibration of indirect (and potentially nondestructive) measurement techniques.

INDIRECT DEFECT METROLOGY

Defect Characterization Of SiGe Using Rutherford Backscattering

To derive information on crystal quality using Rutherford backscattering (RBS), one first directs a high-energy He^+ ion beam in random orientation on the layer structure of interest and detects the backscattered ions as a function of their energy. Next, the sample is tilted with respect to the incoming ion beam such that the channeling condition is

achieved. Under such circumstances the backscatter yield drops significantly (Figure 2a). However, crystalline defects present in the layer block the channels in the crystal lattice and hence give rise to de-channeling or an increased backscatter probability. Using blanket SiGe layers of different defect densities (calibrated using chemical defect etching) we will demonstrate that the channeling yield (ratio of backscattered ions in channeling and random condition) provides valuable information on the defectivity of the material under test (Figure 2b). Moreover, the technique's applicability towards SiGe fin structures will be discussed.

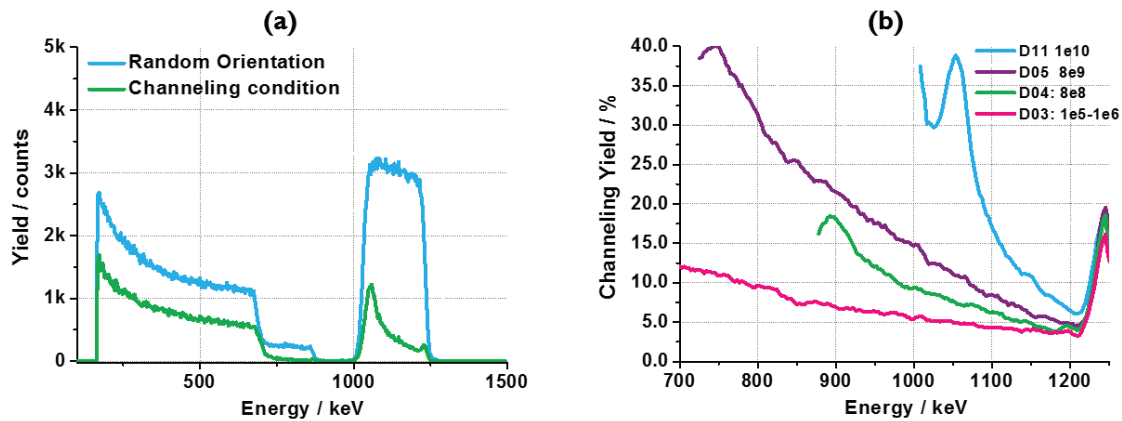


FIGURE 2. (a) RBS spectrum under random and channeling orientation obtained on a 300nm thick SiGe75% layer epitaxially grown on Si. (b) Channeling yield within various SiGe layers of different defectivity. Sensitivity over a wide range of defect densities becomes apparent.

Defect Characterization Of SiGe Using Cathodoluminescence

Cathodoluminescence is a non-destructive metrology technique whereby excess carriers are generated by a focused electron beam in a SEM setup while the luminescence as a function of photon energy or wavelength is recorded. The spatial resolution of the technique is determined by the diffusion length and thus by the life time of the generated excitons. We will first demonstrate on the example of blanket SiGe layers that CL spectra clearly reflect variations in layer defectivity (Figure 3a). We observe a reduced CL intensity in case of increasing defect densities, suggesting the introduction of additional non-radiative recombination channels. By mapping the CL intensity across a SiGe_{0.7} SRB it is possible to visualize a cross-hatch pattern (Figure 3b) which is linked to the misfit dislocation network in the underlying layer.

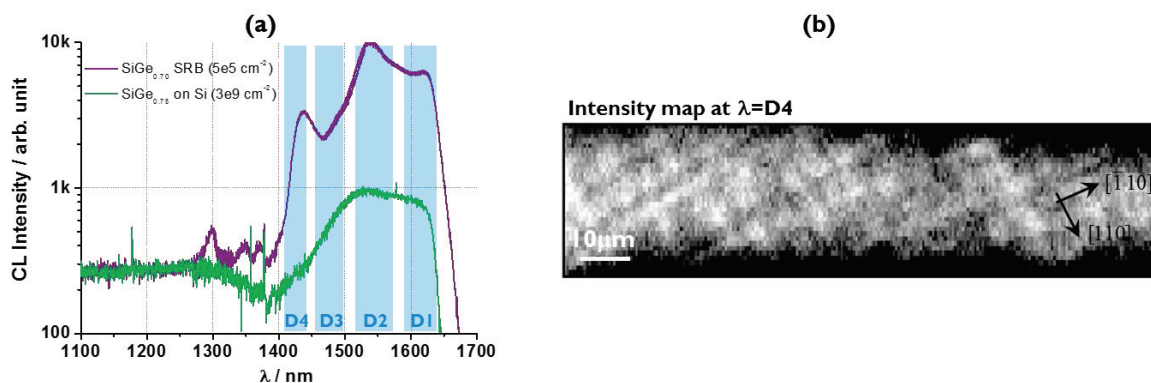


FIGURE 3. (a) CL spectra obtained on a highly defective SiGe_{0.75} layer as well as a SiGe_{0.7} SRB. (b) Intensity distribution map acquired on SiGe_{0.7} SRB at the wavelength corresponding to the D4 band.

It is important to note that in case of indirect bandgap semiconductors the diffusion length of the excitons cannot be neglected due to their inherently long life times. This hampers a direct visualization of an individual threading dislocation as a non-radiative recombination center (i.e. dark spot) in a CL intensity map as demonstrated earlier for GaN. Moreover, the recombination of excitons at surfaces and interfaces becomes crucial. Hence, we will discuss the importance of surface passivation, which is particularly crucial for fin structures with their large surface-to-volume ratio.

NON-DESTRUCTIVE STRAIN AND COMPOSITIONAL ANALYSIS

The composition (e.g. Ge content of a SiGe buffer) as well as the degree of strain relaxation (e.g. in a strained Ge channel layer of a p-FET device) can severely impact the device performance and hence represent crucial material properties which need to be monitored during process development and device fabrication. We will demonstrate how in-line XRD tools equipped with a small spot size x-ray source can be used to determine the composition and strain (longitudinal and transversal direction) in narrow fin structures. The obtained data will be compared with those derived from Raman spectroscopy. The possibility of extracting geometrical information (fin pitch, sidewall angle, layer thickness) from regular reciprocal space maps (x-ray scatterometry) will be discussed.

REFERENCES

- [1] M. M. Heyns, M. M. Meuris, and M. R. Caymax, "Ge and III/V as Enabling Materials for Future CMOS Technologies," *ECS Trans.*, vol. 3, no. 7, pp. 511–518, 2006.
- [2] Y. Bogumilowicz, J. M. Hartmann, R. Truche, Y. Campidelli, G. Rolland, and T. Billon, "Chemical vapour etching of Si, SiGe and Ge with HCl; applications to the formation of thin relaxed SiGe buffers and to the revelation of threading dislocations," *Semicond. Sci. Technol.*, vol. 20, no. 2, pp. 127–134, Feb. 2005.

KEYWORDS

Heteroepitaxy, Metrology, Defectivity, Strain, Composition, RBS, CL, XRD

Advanced Broadband Optical Inspection on Complex Logic Structures using NanoPoint at 28nm Design Nodes

Robert Teagle, Hoang Nguyen, Ralf Buengener, Peter Lin
GLOBALFOUNDRIES, 400 StoneBreak Road Extension, Malta, NY - 12020

Ankit Jain, Sumanth Kini, Rahul Lakhawat, Ravi Sanapala
KLA-Tencor, 2 Bayberry Drive, Malta, NY -12020

Abstract

For many years, as the design rules shrink, optical wafer inspection for detection of yield-killer defects has become more and more challenging. Detection of Defects of Interest (DOI) in logic structures has been limited by very strong wafer noise. A novel, patented technology called NanoPoint from KLA-Tencor extends optical inspection, enabling IC manufacturers to perform highly sensitive optical patterned wafer defect inspections. This paper will discuss the background, principles and present fab use cases in back end-of-line (BEOL) process modules, enhancing the optical inspection sensitivity in logic regions to better detect line end voids at Copper chemical mechanical polish (CuCMP). This sensitivity is achieved by inspecting only very small areas (Care Areas) that are derived using design files. Figure (a) explains in detail how surgical design based care area definition can help enhance the optical inspection tool's ability to detect signal from killer DOI buried in noise background. This technology uses two different techniques to isolate killer defects from the noise:

1. CBI (Context Based Inspection) utilizes design information to generate targeted care areas surrounding critical regions based on intelligent, user-defined rules.
2. TBI (Target Based Inspection) utilizes the optical properties of the pattern on the wafer to find similar patterns and creates small care areas.

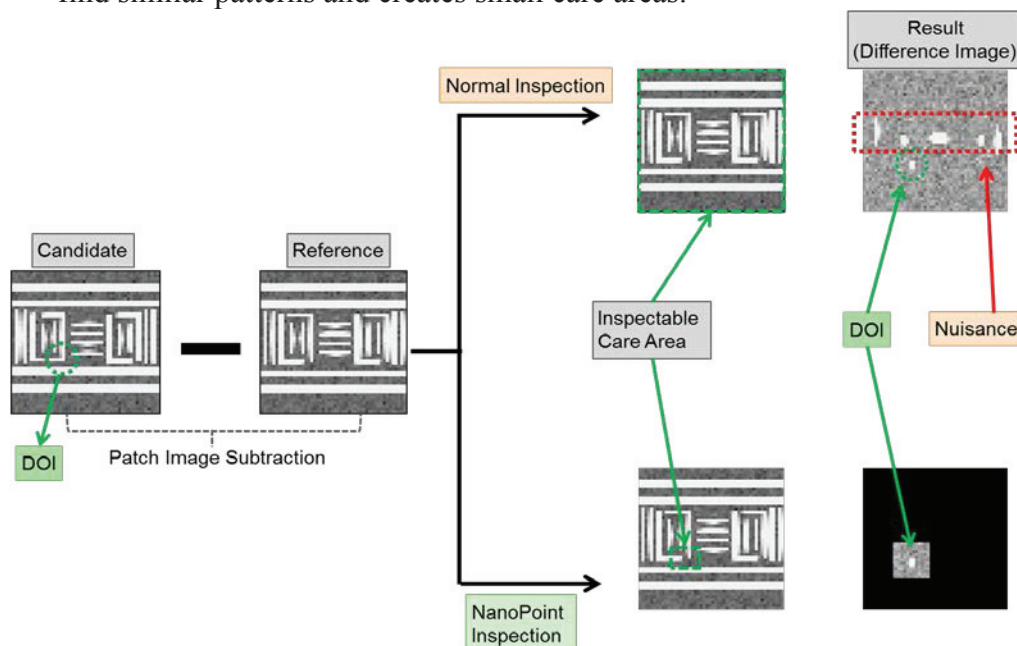


Figure (a): NanoPoint enables generation of very small specific and targeted care areas which allows for removal of nuisance generating patterns and inspection of yield-critical patterns.

These surgical inspection areas can be generated from multiple sources. Rule based search (RBS) is one of the techniques used where specific rules are applied to the design file to isolate critical patterns of interest. Another way to insert these inspection regions is by getting inputs from the design team on pre-determined weak spots known from prior design characterization techniques.

Below is a drawing of how RBS is used to define surgical care areas. Using traditional optical defect inspection detection, noise coming from region other than the critical pattern of interest overcomes the signal from defects of interest. There are different noise sources in metal CMP. Some of the typical noise sources are prior level defectivity, line edge roughness, tiny non killer voids. Surgical NPDCA (Nanopoint design care area) can be generated using RBS (Rule based search) on the design file. This eliminates the noisy area from being inspected and focuses on critical pattern. Multiple layer information can be used to define rules to generate specific care area for detection of killer line end voids.

Example: Dense and isolated thin line rule: By defining the line thickness and the spacing between the dense line, user can generate custom regions on the chip that are critical for inspection. These regions typically have smaller process margin and tend to fail for opens and shorts. By setting up this care area, we can eliminate open area which is typically the primary source of noise. With this rule, significant enhancement in sensitivity can be achieved at low nuisance rates

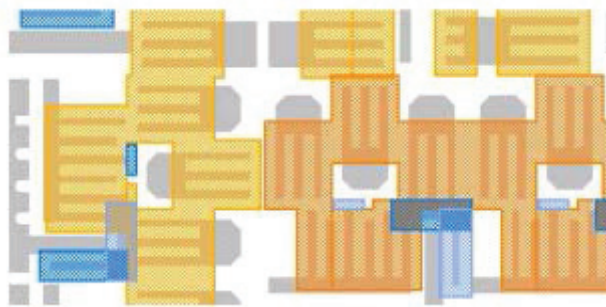


Figure (b): 1. Dense thin line rule at M1 CuCMP

Key Point:

The ability to inspect Key Pattern of interest, thus eliminating non critical/ noisy areas in your inspection area.

Key words: Broadband plasma inspection, care area, NanoPoint, CBI (Context Based Inspection), TBI (Target Based Inspection), NPCA (NanoPoint care area), PWQ (Process window qualification)

Conductive Diamond Probes for Advanced Atomic Force Microscopy

V. Usov^{1,2,3,*}, N. O'Hara^{2,3}, Z. Xiapu^{1,2}, D. Scanlan^{2,3}, A. Potie^{1,2}, J. Boland^{1,2},
G.L.W. Cross^{1,2,3}

¹*School of Physics, Trinity College, Dublin 2, Ireland*

²*Advanced Materials and BioEngineering Research Centre (AMBER), Trinity College, Dublin 2, Ireland*

³*Adama Innovations Ltd., CRANN, Trinity College Dublin, Dublin 2, Ireland*

**Corresponding author: dscanlan@tcd.ie*

INTRODUCTION

We report on the fabrication and performance of 3D diamond probes for high resolution atomic force microscopy (AFM). Our unique fabrication process, a combination of Ga ion 'mask' implant, followed by ICP etch, enables the highly flexible but tightly controlled synthesis of high resolution tips into shapes which are most required in contemporary AFM. In particular we show (i) 400nm high conical probes with the tip diameter as small as 2 nm and demonstrate the ultra high resolution imaging achieved on Si <111> surface; (ii) 650 nm high pillar shaped probes with the 250 nm pillar height, 15 nm pillar diameter and the aspect ratio of 17 and demonstrate significantly improved depth profiling on Via's and Trenches; (iii) Flare shaped CD probes, with leading Overhang and Vertical Edge Height dimensions.

Harnessing the conductivity of the highly doped diamond, we demonstrate the electrical performance of the probes. In addition, the diamond probes are shown to exhibit low wear compared to the other commercially available columnar probes, and as such would be applicable for video rate AFM imaging considering low wear and high finesse tracking and imaging qualities.

REFERENCES

1. W. McKenzie, J. Pethica and G.L.W. Cross. "A direct-write, resistless hard mask for rapid nanoscale patterning of diamond", *Diamond and related Materials* (2011) **20**, 707

KEYWORDS

Atomic force microscopy, AFM probes, diamond AFM probes, CD AFM

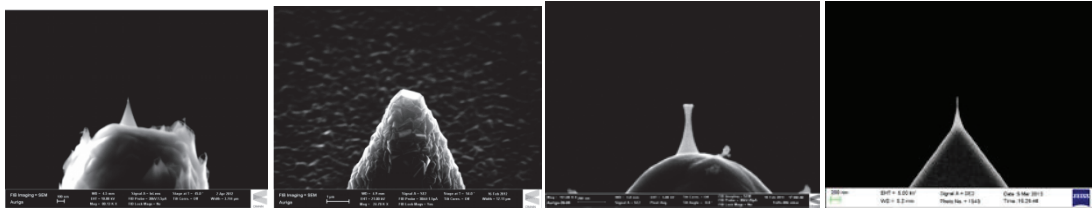


FIGURE 1. SEM images of various Diamond Probe Types.

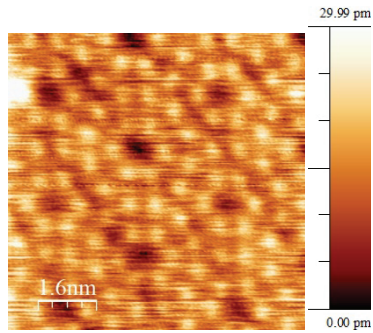


FIGURE 2. AFM topography image of Si (111)-(7×7) surface obtained at 77 K in the frequency modulation mode and oscillation amplitude $A=9\text{nm}$.

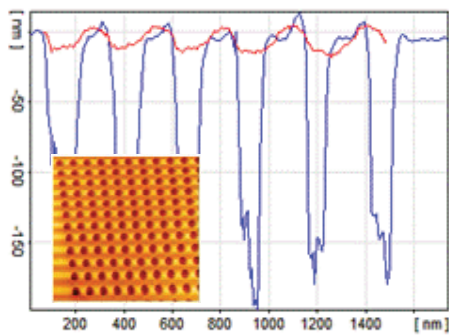


FIGURE 3. Topography profile of high aspect nanopatterned steel, comparing typical SiN AFM probes (red) and our diamond probes (blue)

Sub 20 nm Particle Inspection On EUV Mask Blanks

Peter Bussink, Jean-Baptiste Volatier, Peter van der Walle, Erik Fritz and Jacques van der Donck

TNO, P.O. Box 155, 2600 AD, Delft, The Netherlands

INTRODUCTION

The Rapid Nano is a particle inspection system developed by TNO for the qualification of EUV reticle handling equipment [1]. The detection principle of this system is dark-field microscopy. The performance of the system has been improved via model-based design. Via our model of the scattering process we identified two key components to improving the inspection sensitivity [2]. The first component is to illuminate the substrate from multiple azimuth angles. This illumination mode averages out the variance in the background scattering, allowing for a lower detection threshold to be used. Two years ago, this illumination mode was implemented in our existing inspection system [3].

The second component to improve the sensitivity is to decrease the wavelength of illumination. A shorter wavelength increases the total scattering and reduces the background scattering relative to the defect signal. A new Rapid Nano inspection system will be completed in the beginning of 2016, which combines the multi-azimuth illumination with a 193 nm source. This system will have a sensitivity in-line with the ITRS roadmap for defects on EUV masks.

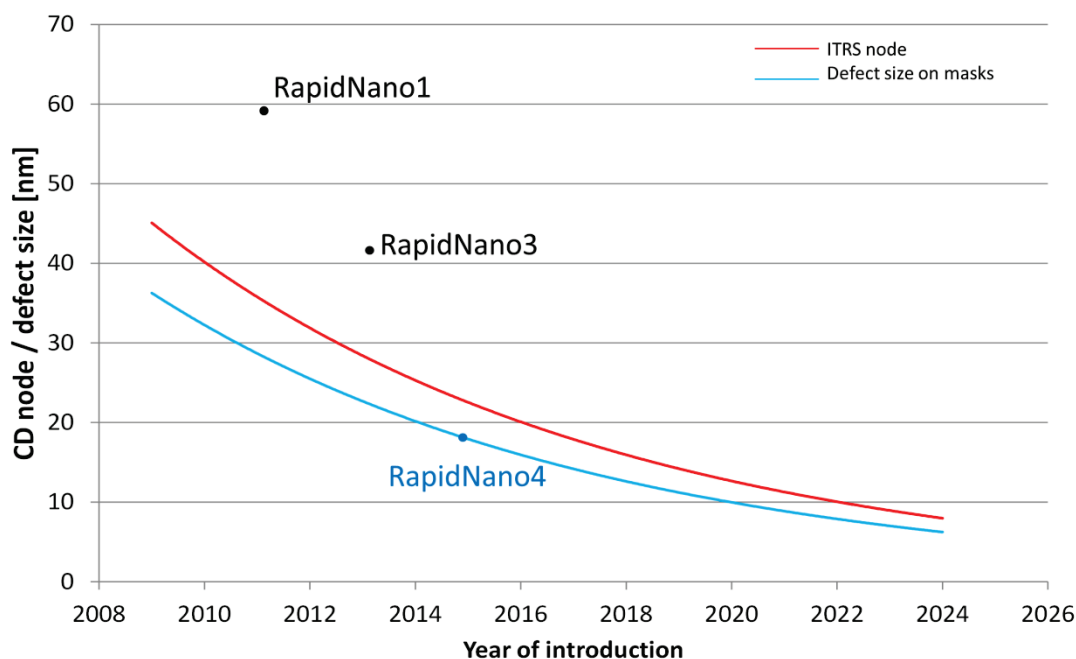


FIGURE 1. The lower detection limit of the RN1 (532 nm, 1 azimuth), RN3 (532 nm, 9 azimuths) and the RN4 (193 nm, 9 azimuths) plotted on the ITRS roadmap for defects on masks.

DESIGN CHALLENGES FOR A DUV INSPECTION SYSTEM

Redesigning the Rapid Nano system for DUV illumination comes with some technical challenges particular to this wavelength regime. First, an objective lens with a large field of view and wavefront error contribution below diffraction limit was not commercially available. Therefore, such a lens was designed and fabricated at TNO.

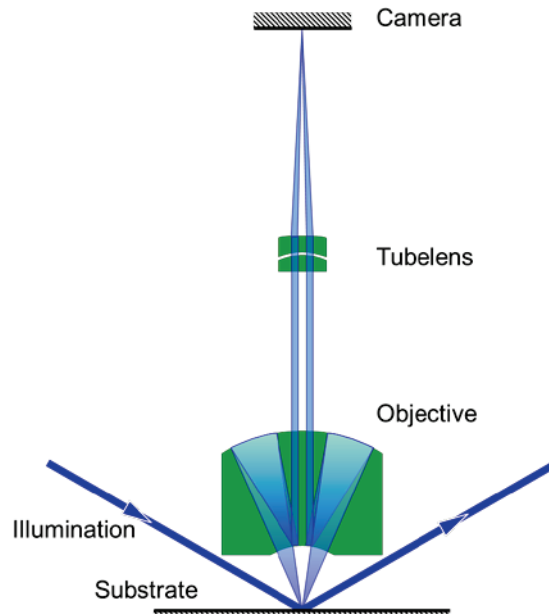


FIGURE 2. Schematic of the Rapid Nano 4 system. The substrate is illuminated at a grazing angle, while scattered light is imaged on a camera.

The second design challenge is the high peak power of the illumination system. Due to high transmission losses, the low scattering cross-section of nano-particles and the high throughput requirements of the semicon industry, a high illumination intensity is required. The short pulse length of DUV lasers makes the peak power exceeds the damage threshold of the optics and substrate at the required average power. To solve this problem, the Rapid Nano 4 is designed with a pulse stretcher that increases the pulse length and reduces the peak power by a factor of 4.

A final consideration when designing a DUV system is the optics lifetime. The high energy photons can crack contamination present in the surrounding air and deposit it e.g. in the form of carbon on the optics. For this reason the purging of the optics with ultra clean N_2 gas has to be carefully designed.

TABLE 1. Predicted and measured performance of the different Rapid Nano generations

	PSL on Si [nm]	Al on Si [nm]
RN1: 532 nm, 1-azimuth		
Predicted	59	35
Measured	59	35
RN3: 532 nm, 9-azimuth		
Predicted	43	25
Measured	42	
RN4: 193 nm, 9-azimuth		
Predicted	18	18

REFERENCES

1. Donck, J.C.J. van der, Snel, R., Stortelder, J.K., Abutan, A., Oostrom, S., Reek, S. van, Zwan, B. van der, Walle, P. van der, "Particle detection on flat surfaces", Proc. SPIE 7969, 1S (2011).
2. Walle, P. van der, Kumar, P., Ityaksov, D., Versluis, R., Maas, D.J., Kievit, O., Janssen, J., Donck, J.C.J. van der, "Nanoparticle detection limits of TNO's Rapid Nano: modeling and experimental results", Proc. SPIE 8522, 2Q (2012).
3. Walle, P. van der, Kumar, P., Ityaksov, D., Versluis, R., Maas, D.J., Kievit, O., Janssen, J., Donck, J.C.J. van der, "Increased particle detection sensitivity by reduction of background scatter variance", Proc. SPIE 8681, 16 (2013).

KEYWORDS

Particle, defect, inspection, EUV, mask blank, equipment qualification

Three-Dimensional SEM Metrology for Nanoelectronics

András E. Vladár and John S. Villarrubia

*National Institute of Standards and Technology
Semiconductor and Dimensional Metrology Division
Physical Measurements Laboratory
Gaithersburg, MD 20899 USA
andras@nist.gov*

INTRODUCTION

Our world is three-dimensional, and so are the integrated circuits (ICs) and the devices of nanoelectronics. In the past, for a long time, we have been very fortunate, because it was enough to measure a simple critical dimension (CD), the width of the resist line, to keep IC production under acceptable control. In the last few years with complex chip architectures this requirement has changed to contour and now to three-dimensional (3D) measurements. At some point in the future it will be necessary to know where individual atoms are and what are the electrical properties of only a few of them. While this today seems bordering impossibility, the latest results obtained by NIST researchers using sophisticated modeling combined with high-quality scanning electron microscope (SEM) imaging show promise, at least a significant step forward. 3D simulation and model-based assessments of the possibilities indicate that measurements of at least 5 nm size structures will not pose an insurmountable obstacle. Results of SEM measurements and Monte Carlo modeling and simulation presented here identify the ways instrument and measurement method development should move to be able to provide indispensable 3D dimensional and compositional information on various current and future devices of nanoelectronics.

THREE-DIMENSIONAL NANOMETER-SCALE SEM METROLOGY

The current IC industry practice, the use of mostly arbitrary (fudge factor) edge algorithms lead to unpredictable biases, partly due to the neglect of the 3rd dimension, i.e., the shape of the structures [1,2]. Carefully optimized SEM measurements combined with matching the measured images with model-based library results have proven to provide excellent results. The shape cross-section determined by this method was compared to transmission electron microscopy (TEM) and critical dimension small angle x-ray scattering (CD-SAXS) measurements of the same sample with good agreement within a few atoms-worth of exactness [3,4], see Figure 1 left. Future development for sub-10 nm nanoelectronics devices will require better instrumentation, better analytical methods and likely the combination of the results of more than one measurement methods.

Three-Dimensional Nanometer-Scale SEM Measurements

SEM images contain useful 3D information on 10 nm and smaller structures. Model-based interpretation of the image or simple color coded visualization using image pairs could reveal this 3 D information otherwise not recognizable for human vision and comprehension, see Figure 1 middle and right. Further efforts are needed and some are already underway to explore the possibilities and to find production-worthy solutions. Based on the results of the current work at NIST, it likely that some kind of SEM-based 3D metrology will be possible even for all those structures at the very end of the International Technology Roadmap for Semiconductors (ITRS).

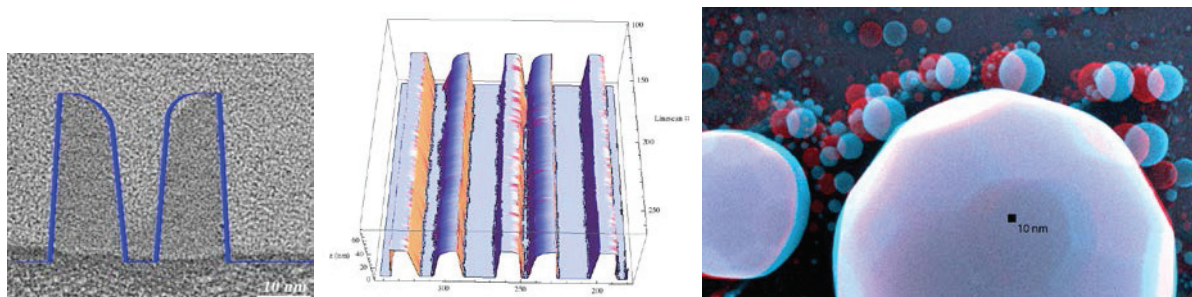


FIGURE 1. The average cross sectional shape by the SEM measurements compared to a TEM image (left), and area of an IC rendered into a 3D plot by the NIST model-based method (middle), anaglyph 3D image of an gold-on-carbon sample showing as small as 3 nm size particles (right).

Three-Dimensional Nanometer-Scale SEM Modeling and Simulation

There are excellent examples for the rewards of sound metrology: substantial improvements, solutions for almost all of the shortcomings of current SEM metrology tools in data acquisition, processing, and shape and size determination. Putting good physics to work—just like in crafting the integrated circuits—pays handsomely in metrology as well. Sophisticated modeling and simulation could predict the feasibility of SEM-based 3D measurements, and help in the development of measurement methods, and the instrumentation. Figure 2 shows a simulated SEM image of nanometer-size particles. The varying secondary electron yield differences at edges and facets allow for 3D reconstruction of the true shape, and a pair or more of these images simulated at various angles allow for the development and testing 3D reconstruction software.

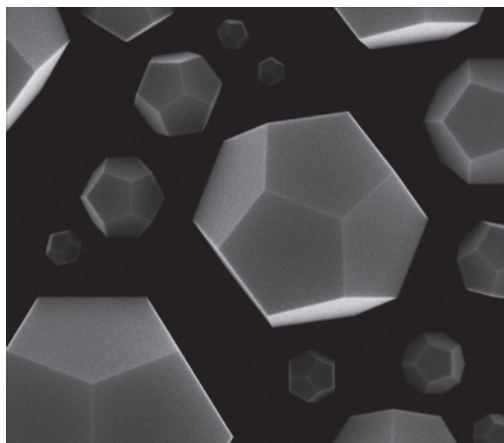


FIGURE 2. Simulated SEM image of nanometer-size particles. Note the varying secondary electron yield differences at edges and facets.

The future of 3D CD metrology is bright and it depends on us to make it as good as it can and must be. Further improvements in size and shape determination in this study are still possible, but likely the values and information obtainable by the NIST model-based method are already useful for process development and control on 10 nm and likely 7 nm size IC structures. For smaller size 3D SEM metrology more work is need, including the use of laser-interferometry sample stage in the acquisition of the images, and further advancements in the accuracy of modeling and simulation.

REFERENCES

1. J. S. Villarrubia et al., *Simulation Study of Repeatability and Bias in the CD-SEM*, J. Microlith., Microfab., Microsyst. 4(3) (2005)

2. A. E. Vladár et al., *Can we get 3D-CD metrology right?* Proc. of SPIE Metrology, Inspection, and Process Control for Microlithography Vol. 8324 832402-1 (2012)
3. A. E. Vladár et al., *10 nm Three-dimensional CD-SEM Metrology*, Proc. of SPIE Metrology, Inspection, and Process Control for Microlithography Vol. 9050 90500A-1 (2014)
4. J. S. Villarrubia et al., *Scanning electron microscope measurement of width and shape of 10 nm patterned lines using a JMONSEL-modeled library*, Ultramicroscopy (2015)

KEYWORDS

nanometer-scale, SEM, modeling, simulation, measurement, three dimensional, 3D, critical dimension, scanning, transmission, electron microscope, TEM, small angle x-ray scattering, CDSAXS, matching

Grazing Incidence X-ray Fluorescence (GI-XRF) For Thin Film And Ultra-thin Film Thickness Metrology

Charles C Wang, Nimoal Sun, Jiang Lu, Weifeng Ye, Chi Ching, Yuri Uritsky

Applied Materials, Inc., M/S 0203,3100 Bowers Ave, Santa Clara, CA 95054

INTRODUCTION

Metal based thin films and ultra-thin films have many applications in the critical semiconductor structures in IC fabrication beyond the 1X node. Prominent examples include Ti and Ta containing material used in metal gates, Co based capping layer and liner in interconnect applications and the variety of metal films for MRAM and other advanced memory devices. Depending on the applications, the thicknesses of these thin films are typically in the range of several hundred Å to a few Å. In order for these metal films based devices to perform successfully, strict thickness and composition control is needed [1, 2]. All these demand higher sensitivity/throughput and more versatile metrology tools in the wafer fab for the monitoring of the uniformity of film thickness and composition over the surface of a wafer to ensure the performance of the deposition tools meeting the manufacturing specifications. Traditionally, thickness monitoring of metal films in the wafer fab is carried out by stand-alone tools based either on sheet resistance measurements or on ultra-sonic principles. If the metal films are thin enough to be penetrated by visible light, then optical based tools such as ellipsometer or reflectometer can also be used. However, all these traditional thickness metrology tools have difficulties in measuring ultra-thin films with thickness less than 100 Å. Sheet resistance and ultrasonic based tools are lacking the sensitivity due to the minute quantity of material in ultra-thin films. In the case of optical based tools, a decrease in data accuracy is encountered due to the interfering signals arising from surface contamination/oxidation and variations of substrate surface conditions. Besides, all the above mentioned metrology tools do not have the composition measurement capability. To overcome these limitations, grazing incidence X-ray fluorescence (GI-XRF) based technique is considered. Because the typical X-ray energies used in XRF measurement are in the range of 1.5 keV to 20 keV, the attenuation lengths of X-rays in the material are in the micron scale. Hence the attenuations of the primary excitation X-ray and the excited fluorescence X-rays from the elements of interest inside the thin film sample are negligibly small. Consequently, the fluorescence X-ray signal from a particular element in the thin film is not affected by the disturbance caused by surface oxidation and contamination of the thin film and any interface effect and is proportional to the surface dose (number of atoms per unit area) of the element. Thus it is easy to calibrate the fluorescence X-ray signals for thickness and composition measurement. To overcome the difficulty of low sensitivity due to the minute quantity of thin film material on surface, grazing incidence (GI) of the primary excitation X-ray can be used to amplify the fluorescence X-ray production. Because the X-ray attenuation in the thin film is negligible, the amount of the thin film material illuminated by the primary X-ray is proportional to $1/\sin(\theta)$, θ being the incidence angle relative to the sample surface, hence the fluorescence X-ray signal is amplified by the same factor. Comparing to normal incidence, where the θ is 90° , at a grazing incidence angle of 5° , the amplification factor is 11.4 and at even smaller incidence angle of 2° , the amplification factor is 28.7. Therefore, the GI-XRF has the advantages of much higher sensitivities and without subjecting to the interfering effect of the surface and interface reactions and contamination. Based on GI-XRF principle, a stand-alone thickness metrology tool is being developed and implemented. Its performance evaluation data are being discussed.

GI-XRF DEVELOPMENT/ IMPLEMENTATION

Traditional XRF tools are usually implemented with a polychromatic X-ray source and a primary X-ray incidence angle larger than 10° . The higher incidence angle allows for easy focusing of the primary X-ray to a small spot size with large convergence angle and for less effect of the local variation of the primary X-ray incidence angle on the fluorescence X-ray intensity. The small spot size is required for both pattern wafer monitoring and for small edge exclusion during blanket film wafer monitoring. However, the use of the polychromatic X-ray source has the

disadvantage of high continuous bremsstrahlung radiation induced background signal [3] that can overwhelm the weak fluorescence signal from ultra-thin films and cause the data precision to drop considerably.

To realize the signal amplification advantage of the GI-XRF at the very low incidence angle for ultra-thin film thickness metrology, stringent requirements are being placed on the X-ray source design: (1) The source X-ray convergence angle has to be small (all incidence X-rays have to be parallel to each other), else at very low incidence angle, part of the X-ray beam would be blocked by the sample surface; (2) High intensity micro-beam monochromatic X-ray sources have to be used to allow for the measurements of small features and to avoid the bremsstrahlung radiation caused background. The major difficulty with the use of monochromatic source is the fluorescence X-ray production efficiency decreases exponentially as the energy of the fluorescence X-ray becomes far below the primary X-ray energy. To overcome this problem, multiple X-ray sources with different primary X-ray energies need to be used. To cover the X-ray spectrum range of interest from 1.5 keV to 17.5 keV, three high-intensity micro-beam monochromatic X-ray sources (see details in Table 1) are developed with small enough convergence angle to allow for incidence angle to be as low as 2° , which results in a signal amplification of 28.7.

TABLE 1. GI-XRF X-ray source information

Target material – X-ray line	Source Energy (keV)	Convergence angle	Beam width (μm)
Cu – $K\alpha$	8.1	$< 1^\circ$	~ 70
Au – $L\beta$	11.4	$< 2^\circ$	~ 70
Mo – $K\alpha$	17.5	$< 2^\circ$	~ 70

Accompanying the high magnification factor of the GI is the disadvantage of the fluctuation of fluorescence X-ray production due to the variation of primary X-ray incidence angle induced by the local height and angle variation of the wafer surface. To avoid this issue, the local variation of the incidence angle of the primary X-ray has to be extremely small. In the case of 2° incidence angle, the variation has to be less than 0.01° in order to maintain the variation of the X-ray signal to less than 0.5% (1σ); this requires that the local height variation be less than 0.17 μm for a length scale of 1mm and the edge-to-edge height difference resulting from the tilt of a 300 mm wafer stage be less than 50 μm . Initial design of the wafer stage used a 3-point edge support, which resulted in a maximum wafer height variation of 70 μm . This caused a metrology tool imperfection induced periodical variation of the X-ray intensity of silicon $K\alpha$ line from the edge of a bare silicon wafer and an inherent imprecision of 1.13% (1σ). To solve this problem, a full surface support extremely smooth and flat wafer stage was developed. As can be seen in Figure 1, the signal variation was reduced to a mere 0.28% (1σ). Additional improvement is realized by incidence angle adjustment at each sampling point with a bit reduction of the throughput.

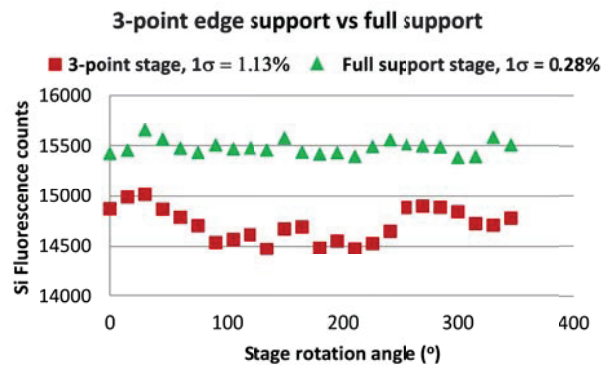


FIGURE 1. Red dots are silicon X-ray data from a bare Si wafer on a 3-point edge support stage. Green dots are Si data from a full-surface support flat stage. All the data were acquired from locations evenly spaced on the circumference which was 2mm from the wafer edge.

EVALUATION OF THE GI-XRF PERFORMANCE

The new GI-XRF tool was tested for its ultra-thin film measurements capability. Single point repeatability test results are shown in Table 2. For majority of the films with thickness larger than 10 Å, relative standard

deviations (1σ) close to 0.5% can be achieved in a short measurement time. The ultra-thin (~ 2 Å thick) Co, Ta and Pt tested are for STT-MRAM application. In the case of ultra-thin Ta and Pt, less than 1% (1σ) is obtained with a 20 seconds measurement time and an incidence angle of 2° , which is the lowest angle available for the current tool. For ultra-thin Co, less than 0.5% (1σ) should be achievable by decreasing the incidence angle further to 4° and with a measurement time of 10 seconds per point.

TABLE 2. GI-XRF tool single point repeatability test results

Thin Film Material	Thickness (Å)	X-ray source Material	Source X-ray incidence angle	Counting time (s)	Precision (relative standard deviation)
TiN	40	Cu	4	10	0.47%
Co	12	Cu	5	2	0.57%
Cu	70	Au	5	5	0.58%
Pt	17	Mo	2	20	0.28%
Ru	8.8	Cu	2	20	0.68%
Pt	2.6	Mo	2	20	0.97%
Co	2.1	Cu	5	10	0.61%
Ta	2.1	Au	2	20	0.83%

The high sensitivity of the new GI-XRF tool has been applied to the study of the substrate dependence of the selective CVD Co (for Cu capping to improve EM performance) deposition. The Co X-ray intensity is determined to be 1000 counts per second (cps) per angstrom, while the background X-ray intensity on a bare substrate is 250 cps. The Co detection limit was calculated to be 0.02 Å with a counting time of 10 seconds. As illustrated by the data in Table 3, GI-XRF can easily differentiate the deposition rates on different substrates – data from Co deposition show that the Co thicknesses on copper and on low-k are 28.63 Å and 0.05 Å, respectively; therefore, the selectivity of 573 to 1 on copper versus on low-k has been demonstrated.

TABLE 3. Selectivity measurements of selective Co deposition process on copper and Low-k

Deposition thickness (Å)	Co thickness on Cu (Å)	Co thickness on Low-k (Å)	Selectivity Cu:Lowk
0	0.00	0.00	NA
Thickness 1	28.63	0.05	573:1
Thickness 2	51.97	0.14	371:1

CONCLUSIONS

A high sensitivity GI-XRF tool has been demonstrated; thickness data from ultra-thin films with thicknesses from 40 Å down to 2 Å can be obtained, with relative standard deviation less than 1%, in a reasonably short measurement time. This new tool has been used for the thickness and composition metrology of many ultra-thin films. Examples include CVD Co liner and capping layers; ALD TiN, TaN and other metal compounds/alloys used in metal gate applications; the various MRAM films, CoFe, NiFe, Ta, Pt, Ru and Co. It is desirable to improve the precision and throughput further especially in the cases of less than 10 Å ultra-thin films. To realize that, more intense X-ray source and more efficient X-ray deliver system need to be developed. It is also possible to double the X-ray intensity by lowering the incidence angle to 1° by developing even smaller convergence angle X-ray sources together with more efficient incidence angle adjustment mechanisms.

REFERENCES

1. X. Ma *et al*, *J. Semicond.* **35**, 096001-1-096001-4 (2014)
2. A. H. Simon *et al*, *Reliability Physics Symposium (IRPS)*, 3F.4.1 - 3F.4.6, 2013 IEEE International
3. W. Gibson and G. Havrilla, *Handbooks of Optics*, Vol. 5, New York, McGraw-Hill, pp. 29.1 – 29.13

KEYWORDS

GI-XRF, ultra-thin film, CVD Co, MRAM, metal gate

Robust Optical Modeling of SiGe Layers

Martin Weisheit, Robert Melzer, Henry Bernhardt, Adam Urbanowicz¹

GLOBALFOUNDRIES Module 1 LLC & Co. KG, Wilschdorfer Landstraße 101, D-01109 Dresden
¹*now at Nova Measuring Instruments*

INTRODUCTION

Epitaxial Silicon Germanium layers are commonly used in the semiconductor industry to compress the P-FET transistor channel and thus increase its drive current. Accurate metrology of SiGe thickness and Ge content is required, preferably by a fast and nondestructive method, such as spectroscopic ellipsometry. In principle, an optical measurement of Ge concentration is possible, since the composition of a single-crystalline SiGe alloy determines its optical properties. However, the complex nature of this relationship makes the analysis difficult in general. In addition, more than a single SiGe layer is often present due to manufacturing constraints, which complicates the analysis of ellipsometric spectra even further. An analytical description for the dielectric function of SiGe is developed that enables robust and accurate analysis of ellipsometric data for Ge concentrations up to 50%.

SIGE DIELECTRIC FUNCTION PARAMETRIZATION

The fundamental basis for accurate ellipsometric measurements of SiGe layers is a precise mathematical model for the optical properties (dielectric function, DF) of SiGe, for all Ge concentrations up to the maximum amount encountered in production. Commonly, a series of SiGe layers, which cover the needed composition range, are analysed by Spectroscopic Ellipsometry, and a reference method, such as Auger Electron Spectroscopy, is used to measure the true Ge concentration. The SiGe DF extracted for each individual composition is then stored in a lookup-type model along with the reference Ge concentration. A spectroscopic ellipsometry measurement of an unknown SiGe alloy is then matched to the best-fitting database entry. Some kind of spectrum interpolation is employed to find best fits for intermediate compositions.

The problem with this approach is that there are never enough reference spectra to densely cover the needed composition range and that even with smart interpolation approaches (critical point shift, for example), the results are not optimal. Therefore, we take a different approach, which extracts from a series of reference measurements an analytical formula for the SiGe DF that depends solely on the Ge concentration.

The imaginary part of the SiGe DF is shown in figure 1. It is composed of a number of peaks, whose shape in the vicinity of the critical points is described in the literature by various functions [1]. These are based on the physical absorption processes at those specific critical points. In order to describe the DF over the whole spectrum with as few parameters as possible, we use a superposition of N Tauc-Lorentz oscillators [2], which is a very good approximation to the true SiGe DF for $N > 4$. (The complex TL oscillator is inherently Kramers-Kronig consistent, i.e. the real part of the DF is described correctly as well). Each TL oscillator is a function of 4 parameters: amplitude A , energy E , width C , and gap energy E_g . Thus, a set of $4N$ parameters describes the DF for each SiGe composition. Figure 1 shows how the DF varies with Ge concentration: the first peak shows the strongest shift in energy and amplitude, but in fact all $4N$ peak parameters vary more or less strongly with the Ge content.

Since the SiGe layer is single crystalline due to the epitaxial matching to the underlying Si substrate, its crystal structure and thus optical properties are uniquely defined by the Ge concentration (assuming statistical distribution of Si and Ge atoms on the lattice). This means that $4N-1$ peak parameters are perfectly correlated to each other. Only one parameter is truly free, and each peak parameter can thus be written in principle as a unique function of the Ge concentration. The challenge is to find those functions. In an iterative approach, similar to the one described in detail in [3] for the DF of mechanically stressed Si, a polynomial relationship to the Ge concentration is first assumed for

the most sensitive peak parameters, which constrains the functional dependence for the others. This is repeated until a functional relationship is established for all peak parameters. As a result, the SiGe DF is fully parameterized to the Ge concentration as a single parameter, but to a rough approximation only. In the final step, the polynomial constants (up to 3 per peak parameter) are determined in a multi-sample fit involving the ellipsometric spectra of all reference samples [4]. We used 10 reference Ge concentrations, spaced roughly equally from 0 to 47% (i.e., including pure Si). This results in a large, highly non-linear optimization problem to simultaneously find a fit optimum for a set of up to $3 \cdot 4N$ (typically 30 to 100) free parameters.

In this way we were able to describe the DF of fully strained SiGe alloys by a self-contained analytical function with Ge concentration as the single dependent parameter, valid in the range of 0 to 50% Ge. With this functional approach, the fitted Ge concentration smoothly follows the true Ge content and avoids problems related to the reference concentration points in the conventional lookup & interpolate approach (e.g., fit trending toward the reference points, since interpolated spectra have inherently higher fit error). Figure 2 illustrates this point for a very simple interpolation model.

Comparing Ge concentration fit results to reference measurements for a large number of samples of various thicknesses and concentrations shows that the accuracy is about 1% (percentage point), precision and repeatability are $<0.1\%$ (single SiGe layer with native oxide). This accuracy is achieved if all model assumptions are fulfilled, i.e., epitaxial SiGe film on Si(100), fully strained and homogeneous. Non-ideal conditions can be detected by an increase in the mean-squared error of the fit.

FIT STRATEGY

In order to find the true thickness and Ge concentration for an unknown SiGe film, a robust fit strategy is needed to avoid getting trapped in local optimization minima of the fit error landscape. The fit error landscape can be visualized in this case as a 2-dimensional function of SiGe thickness and Ge concentration (the native oxide on top, which is also a fit parameter, can be safely ignored due to its low thickness). A number of local minima will be evident, which must be avoided by choosing starting values close enough to the true global minimum. By analyzing a number of such fit error landscapes for samples of different thicknesses and concentrations, a robust fit strategy can be established: start with a gridded global fit of Ge concentration in 15% steps, SiGe thickness in 20nm steps, to find the best starting value, and finish with Levenberg-Marquardt iterations to the minimum. This procedure will always find the global optimum. SiGe films up to 200nm thickness and up to 50% Ge concentration are thus fitted reliably in a few seconds with a single recipe. A number of examples for single- and multi-layer stacks will be shown in the presentation.

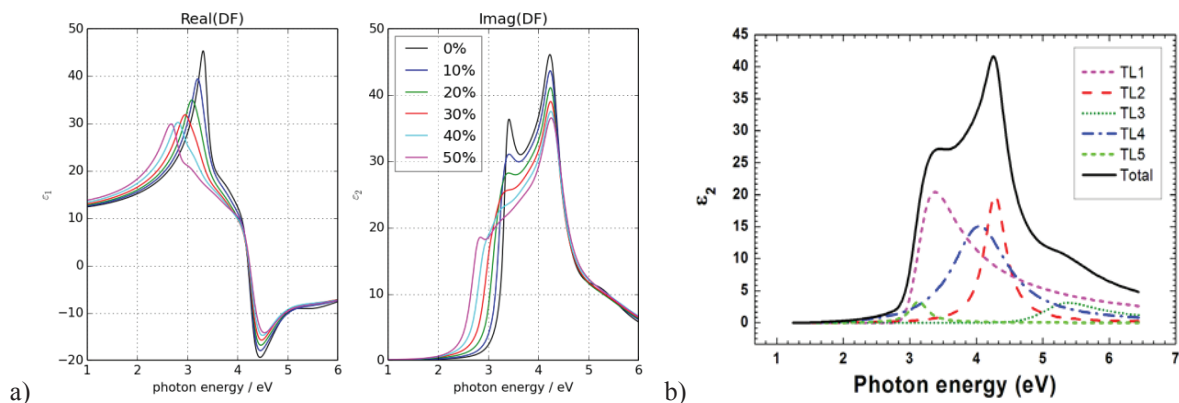


FIGURE 1. Real and imaginary part of the dielectric function of fully strained epitaxial SiGe layers on Si (a) and functional description by superposition of Tauc-Lorentz oscillators (b)

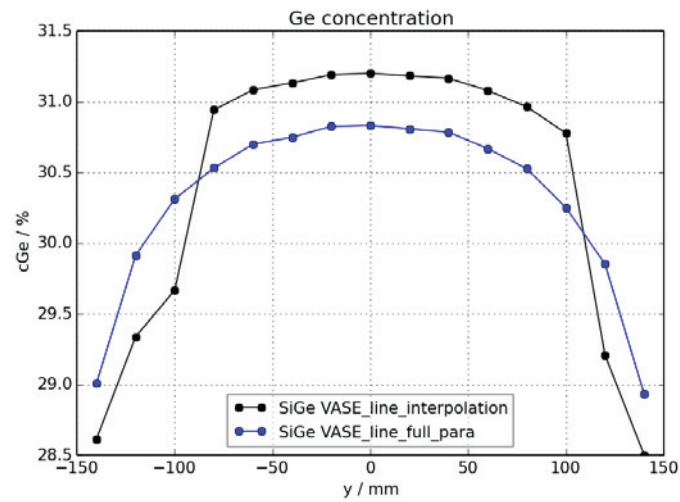


FIGURE 2. Fitted Ge concentration of a 4nm thick epitaxial SiGe film along the wafer diameter for a simple interpolation model (black curve) and the fully parameterized SiGe model described here (blue curve). The discontinuous Ge concentration jump at 100mm radius in the interpolation model is an artifact of the large discrete spacing of reference spectra.

REFERENCES

1. C. C. Kim, J. W. Garland, H. Abad, and P. M. Racciah, *Phys. Rev. B* **45**, 11749-11767 (1992)
2. G. E. Jellison and F. A. Modine, *Appl. Phys. Lett.* **69**, 371-373 (1996)
3. Z. Chong, M. Weisheit, M. Hecker, and E. Zschech, *Semicond. Sci. Technol.* **24**, 045013 (2009)
4. B. Johs, C. Herzinger, B. Guenther, WVASE32 Version 3.686 (2008)

KEYWORDS

SiGe, spectroscopic ellipsometry, dielectric function, metrology

Effects of Image Processing on Electron Diffraction Patterns Used for Nanobeam Diffraction Strain Measurements

Mark Williamson¹, Piet van Dooren¹, and John Flanagan²

¹FEI Company, Achtseweg Noord 5, 5651 GG Eindhoven, The Netherlands

²FEI Company, 5350 NE Dawson Creek Drive, Hillsboro, OR 97124

INTRODUCTION

For more than 60 years it has been known that mechanical strain can increase carrier mobility in semiconductor materials, [1]. More recently strained silicon has been introduced into the manufacturing of electronic and optical devices. Strain engineering has helped semiconductor manufacturers keep up with Moore's scaling [2]. Moving forward the International Technology Roadmap for Semiconductors suggests that both technological and manufacturing benefits could come from the use of strained germanium or III-V materials [3]. Motivated by the benefit of strain engineering strain measurement at the nanometer level is also a topic of interest in the semiconductor industry.

Typically strain in nanometer scale devices is measured with the transmission electron microscope (TEM). Several techniques are available for strain measurements in the TEM including but not limited to, nanobeam electron diffraction (NBD) [5,6], dark-field electron holography (DFEH) [7-9], convergent beam electron diffraction (CBED) [10], and HRTEM geometric phase analysis (GPA) [11]. Of these techniques nanobeam electron diffraction is generally considered the easiest technique to perform and produces the most direct data to analyze.

The positions of the reflections in an electron diffraction pattern (DP) are inversely proportional to the spacing of the lattice planes which produce the reflection. Therefore, by measuring the shifts in diffraction pattern reflections it is possible to measure the changes in the spacing of lattice planes. For the past 8 years the FEI Company has offered a package, True Crystal, for recording and analyzing NBD data. Over the last 18 months FEI has been testing and coding a new software package (Epsilon) to replace the software component of True Crystal. In doing this engineers have reviewed the algorithms and image processing techniques used for NBD measurements. In particular significant effort has been invested in looking in the peak fitting algorithms and image processing associated with this analysis. This poster will show the results of this analysis.

NBD ALGORITHM

As stated above, the algorithm for computing strain from electron diffraction data involves determining the positions of the reflections in the diffraction pattern very accurately. Typically the diffraction patterns are filtered in some method to strengthen the signal in the image. After this filtering the reflections in the DP are grossly determined based on some known basis vectors. Then the reflections are fit using a more accurate method including linear least squares fitting to a surface or various methods of fitting cross-sections of the reflections. The peak positions are then used to determine the best two vectors capable of reproducing the entire diffraction pattern. These two new vectors are then used to recreate the diffraction pattern for the strain calculation. The strain is calculated by comparing the refined reflections in reference diffraction patterns and the diffraction patterns to be measured.

In order to measure strains of 0.05% from a single [111] reflection in a (110) Si diffraction pattern with a typical camera length and binning it is necessary to determine the reflection position within 1/20th of a pixel. In order to

achieve this accuracy in strain it is often required to preprocess the diffraction patterns prior to determining the peak positions as well as applying more advanced algorithms.

Image Processing

Several image processing routines were implemented in the Epsilon software package including: diffraction pattern autocorrelation, background subtraction, and edge detection routine. The autocorrelation correlates each diffraction pattern with itself. The background subtraction routine models the image as a series of strong high resolution, high intensity peaks surrounded by flat low resolution background. The latter is modeled by blurring the image. The blurred image is then subtracted from the un-blurred image to remove the background. The blurring parameter is the width of the Gaussian kernel used for image blurring. Larger numbers induce more blurring; hence stronger background subtraction. To further improve the peak contrast an edge detection routine is also employed. In this routine the Laplacian of Gaussian is utilized to bring out sharp peaks.

Of the three image processing techniques described above the one with the largest effect on resulting strain data is the autocorrelation. Figure 1 is a plot of reflection positions in a diffraction pattern as a function of the reflection (Miller indices). The image shows several imaging processing conditions. The agreement between theory and experiment is quite good though the (224) type reflections. In the diffraction patterns without the autocorrelation the agreement with theory starts to deviate significantly after this point. The best fit to the theoretical data is with the autocorrelation only and is 0.07% and increases to 5% when measuring all points without the autocorrelation.

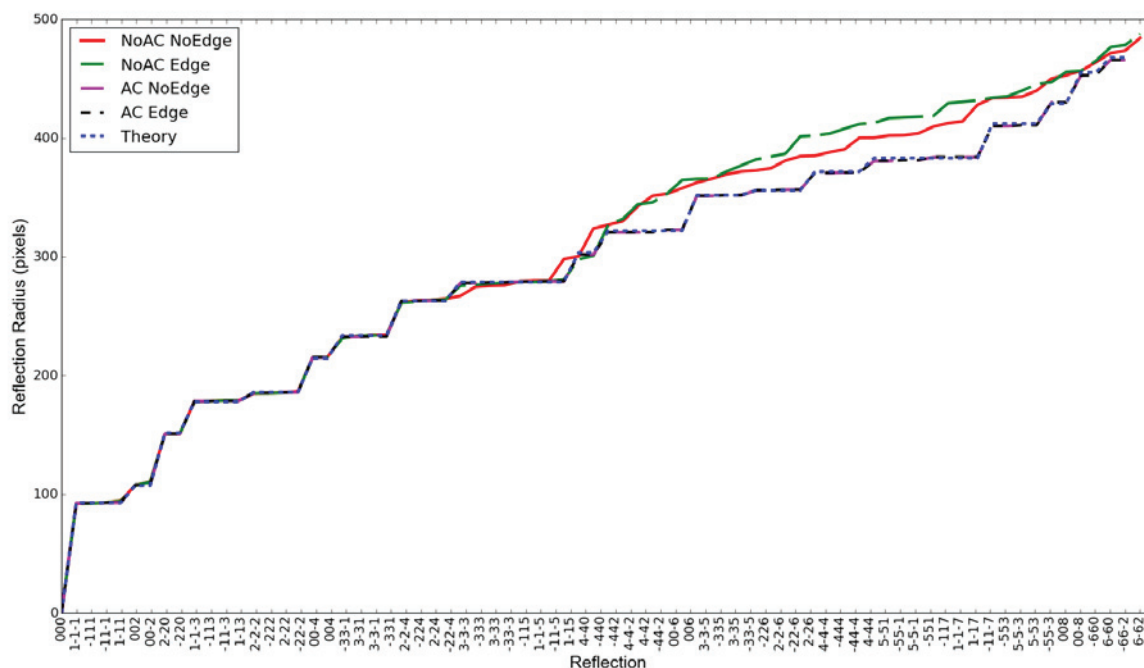


FIGURE 1. Plot showing the reflection positions in pixels as a function of reflection in the diffraction pattern. Five image processing conditions are shown including combinations of with and without autocorrelation and edge detection and a theoretical line. The theoretical line is computed by assuming that the average pixel distance for the (111) reflections is correct and then the subsequent pixel distances are computed from the known interplanar spacing of Si.

Peak Fitting Routine

The four peak fitting routines implemented in the Epsilon software are described below.

Paraboloid: Fits a paraboloid to the peak over a radius, Peak interpolation radius, defined in the UI.

- **Circle Fit:** Fits a circle to the peak edges. The peak maximum and peak background (a two-pixel wide annulus touching the border) are computed and a value between these two values is taken to threshold the ROI. The threshold value is available as an input parameter in the software. Once the ROI threshold is taken, the threshold border is obtained and fit to a circle in a least squares sense. The circle center is defined as the peak position.
- **Ellipse Fit:** Operates much the same as the circle fitter except, instead of a circle, an ellipse is fit and the ellipse center is taken as the peak position.
- **Disk Fit:** Fits a circular disk of disk radius to the diffraction peaks. A binary image of disk radius is created in a box whose size is equal to the peak containing box. Then the box (image) containing the diffraction peak is thresholded as described in the circle fit section. The synthetic disk is then matched to the thresholded peak to sub pixel precision. To obtain proper results, it is critical for the synthetic disk size to match the actual peak size.

An experiment was designed to determine which algorithm provided the best fit to the data. Data was recorded on a {110} silicon substrate with an approximately parallel electron beam. Various combinations of the peak algorithms and image processing were analyzed to determine their effect on the strain data. In particular, the parameter optimized was the variance of the strain in the [220] direction. These tests showed again that the autocorrelation was important with a P value of 0.0 and also that the fitting routine had a significant influence on the result with a P value of 0.014. The results show that the disk fitter as implemented results in a significantly higher variation in the strain data than any of the other fitting algorithms.

CONCLUSIONS

Typical algorithms used for NBD analysis have been examined using statistical analysis in order to produce strain results with the lowest variance in a sample assumed to be at constant strain. Performing an autocorrelation of the incoming diffraction patterns has a strong effect on the strain. Paraboloid, circle, and ellipse peak fitting routines produce similar strain results.

This poster further details the statistical analysis of the image processing and peak fitting routines on the strain results. In addition, it will show the results for diffraction data recorded with more convergent electron beams and thus greater spatial resolution.

REFERENCES

1. C.S. Smith, *Phys. Rev.* **9**, 42-49, (1954).
2. S.E. Thompson et. Al., *IEEE Transactions on Electron Devices*, **51**(11), 1790-1797, (2004).
3. S.E. Thompson et. Al., *IEEE Transactions on Electron Devices*, **56**(5), 1010-1020, (2006).
4. www.ITRS.net
5. A. Beche et al. *Applied Physics Letters*, **95** 123114 (2009).
6. P. Favia et al. *Journal of the Electrochemical Society*, **158**(4) H438-H446 (2011).
7. F. Hue et al. *Applied Physics Letters*, **95**, 073103, (2009).
8. Cooper et Al. *Applied Physics Letters*, **96**, 113508, (2010).
9. Y.Y. Wang et. Al. *Ultramicroscopy*, **124**, 117-129 (2013).
10. *Applied Physics Letters*, **86**. 063508, (2005).
11. M.J. Hytch, *Ultramicroscopy* **74**, 131-146 (1998).

KEYWORDS

Automation, Transmission Electron Microscopy, Nanobeam Electron Diffraction, Strain, Image Processing, Autocorrelation

Measurement Range Induced Electron Density Perturbations in X-Ray Reflectometry

Donald Windover

*Materials Measurement Science Division, Materials Measurement Laboratory,
National Institute of Standards and Technology, Gaithersburg, MD 2089, USA*

INTRODUCTION

X-ray reflectometry (XRR) is a method of choice for non-destructive thickness determination of thin films and provides a direct metrology pathway between electron density contrast features (interfaces between dissimilar thin films) and realization of the meter. However, there are many subtleties within both modeling and refinement of structural information from XRR. X-rays impinging on a smooth surface at glancing angles will either reflect off from or refract into a material; as this angle changes, so does the intensity of reflection and refraction from materials based on the index of refraction (more specifically, electron density) of the material. A stack of different layers will exhibit index contrast at interfaces causing interference phenomena, which are readily modeled from a first-principles treatment of Maxwell's Equations. The process is typically modified to represent the structure under study as a stack of layers of constant index of refraction and a refinement of reflection, attenuation, and refraction which are computed for each layer of the stack (starting from the substrate) and each term is recursively coupled with layers above and below within the stack; this approach is known as a Parratt method.[1] Unfortunately, real structures are not idealized perfect slabs of constant index of refraction separated by perfectly smooth interfaces; real structures will vary in composition, densification, and will have both interface roughness and often interdiffusion to muddle the modeling. The most common method to deal with real life structures is to compose a model with a Gaussian gradient (electron density gradient) at interfaces which to first-order describes both roughness and interdiffusion phenomena. In this work, we use another method, referred to as the groove track method (GTM), which breaks a complex stack into a series of thin, uniform thickness slabs and allows for varying electron density within each slab to model both uniform density layers and roughness and interdiffusion gradients in a non-Gaussian constrained way.[2] The advantage of this method is that it provides a truly model independent measure of electron density variation within a layer stack.

APPROACH

In this study, we demonstrate the impact of changes in the angular measurement range on the GTM model independent electron density profile analysis method. We chose the simplest structure possible, a single high-density layer on a smooth, flat substrate. We used measurements from a Certified Reference Material (CRM) developed by the Physikalisch-Technische Bundesanstalt (PTB) [sample #25].[3] This CRM consists of a single, smooth, nominally 10 nm Pt layer, deposited by pulsed laser deposition onto an atomically smooth quartz substrate. XRR measurements were modeled with a structure consisting of a single electron density with some surface contamination layer and a slight interface with the quartz substrate. Data was collected using a Rigaku SmarLab* diffractometer configured with a Cu characteristic sealed tube source, a graded parabolic multilayer mirror, and a Ge 220 2-bounce monochromator; a typical configuration for XRR measurements in industry and research. Ten specular reflectivity measurement repeats were performed at $0^\circ - 7^\circ$ in 2θ and with a 0.005° step width and 10 s per point statistics. Five more specular reflectivity measurement repeats were performed similarly but with a wider angular data range ($0^\circ - 10^\circ$ in 2θ). The data was refined using a strategy under development at NIST, where multiple genetic algorithm (GA) refinements are run on each XRR data set and the statistical variance of parameters are used to demonstrate the robustness of model parameters. Preliminary single layer refinements using a single, layer with surface and interface

roughness could fit the data well, and provided a Pt thickness of ~ 10.15 nm. We then introduced a model with ten, 1 nm Pt layers and one surface layer which was allowed to refine between 0.1 nm and 1 nm thickness. Density was allowed to range between 5 g/cm^3 and 25 g/cm^3 for each of the Pt layers.

RESULTS

Figure 1 shows the results of refining ten, 1 nm fixed width slabs of Pt (with no applied Gaussian interface roughness) for the $0^\circ - 10^\circ$ 2θ data range (left) and the $0^\circ - 7^\circ$ 2θ data range (right). The $0^\circ - 10^\circ$ 2θ data range clearly shows a uniform electron density, Pt layer, 10 nm wide, on the substrate (all densities of the individual layers nearly agree) with slight changes in density at both interfaces. The weak horizontal lines represent the electron density result from each of 100 separate GA simulations and the dotted line is the electron density for bulk Pt. The corresponding box plots are nearly hidden within lines as well, indicating a very low variance in electron density between refinements. Although measuring the same structure and merely hours apart, the $0^\circ - 7^\circ$ 2θ data range (right) shows several very different electron density profile. We clearly see a pronounced oscillatory feature in the profile which is non-physical artifact. We also see a much higher degree of refinement-to-refinement variance, which is indicative of an under-constrained refinement model (large boxes in the box plot overlay). Too many different structural solutions to the same data can satisfy the same goodness of fit for this data range. The periodicity of the oscillation is on the same reciprocal length scale as the data truncation, suggesting we are seeing a perturbation phenomenon within the XRR analysis, a feature as yet unobserved in XRR theory.

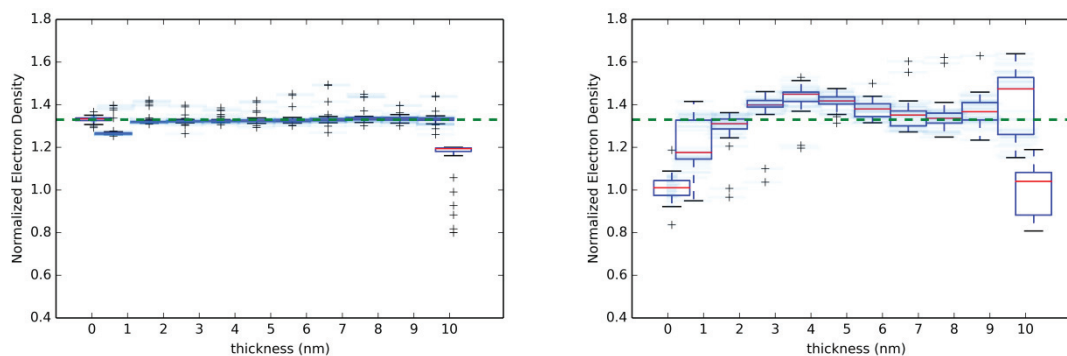


FIGURE 1. (left) Electron Density profile for XRR measurement of a 10 nm Pt on Glass reference material (PTB #25) measured from $0^\circ - 10^\circ$ in 2θ using Cu radiation. (right) Electron Density profile of same the sample fit using $0^\circ - 7^\circ$ in 2θ .

To better understand this anomalous electron density oscillation, we cut the five, the $0^\circ - 10^\circ$ 2θ data range measurements into shorter ranges from $0^\circ - 4^\circ$ in 2θ to $0^\circ - 8^\circ$ in 2θ and repeated our GA analysis approach for each of these truncated data sets. Figure 2 shows the best fit for four of these XRR ranges from $0^\circ - 4^\circ$ 2θ (top profile) to $0^\circ - 10^\circ$ 2θ (bottom profile). The plots are normalized and separated by factors of 10^2 to separate refinements for observation of trends. Three horizontal lines are included to show where the 4° , 6° , and 8° 2θ data sets end. For each measurement range, the best fit model (dotted line) is shown overlay the $0^\circ - 10^\circ$ 2θ to illustrate where the refinement model starts to dramatically deviate from the ground truth data. For the $0^\circ - 4^\circ$ 2θ case, the best fit model has a clearly false increase in intensity in a large range periodicity. The other cases also contain sharp spikes which would be disqualified if the measured data used were over the full $0^\circ - 10^\circ$ in 2θ .

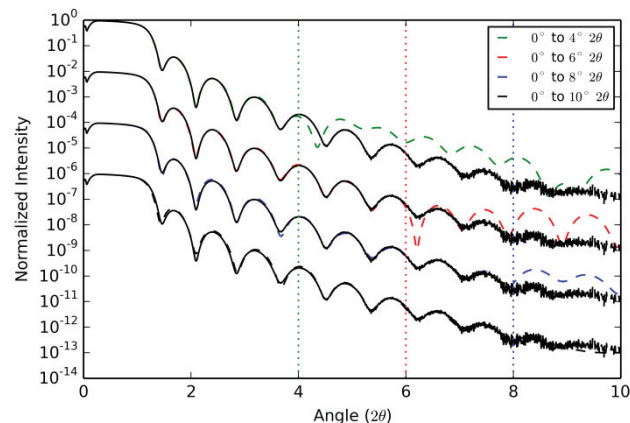


FIGURE 2. XRR Measurement of a 10 nm Pt on Glass reference material (PTB # 25) (black lines) and XRR model fits a measurement range of: $0^\circ - 4^\circ$ in 2θ (top), $0^\circ - 6^\circ$ in 2θ (2nd down), $0^\circ - 8^\circ$ in 2θ (3rd down), and $0^\circ - 10^\circ$ in 2θ (bottom).

CONCLUSIONS

Refining XRR electron density profiles using unconstrained methods, such as GTM may be subject to the introduction of oscillatory artifacts derived from the limited sampling Q-space present in a measurement. Note that in our example, the cause of introduction was stopping data collection prematurely (at $< 10^\circ 2\theta$). However, having an inadequate signal to noise ratio caused by either bad sample alignment, instrument alignment, or weak X-ray tube, too aggressive of a monochromator, or lack of a parabolic optic could lead to such oscillations being present even with large data collection ranges.

REFERENCES

1. L. G. Parratt, *Appl. Phys. Physical Review*, **95**, 359-369 (1954).
2. X. -L. Zhou and S. -H. Chen, *Physical Reports*, **257**, 223-348 (1995).
3. Hasche, et al., *SPIE Recent Developments in Traceable Dimensional Measurements II*, **5190**, 165-172 (2003).

KEYWORDS

X-Ray Reflectometry, Metrology, Density, Thin Films, Platinum, Reference Materials

2D and 3D Nanoscale Measurements of Electric and Magnetic Fields in Functional Materials with Electron Holography

Daniel Wolf, Felix Börrnert, Jonas Krehl, Andreas Lenk, Hannes Lichte, Axel Lubk, Falk Röder, Jan Sickmann, Sebastian Sturm, and Karin Vogel

Triebenberg Laboratory, Institute of Structure Physics, Technische Universität Dresden, 01062 Dresden, Germany

INTRODUCTION

In many functional materials such as semiconductors, atoms are arranged in a sophisticated way in order to modify the electronic structure generating fields controlling the specific function. Whereas the atomic structure can be analyzed, e.g., by means of highest performing Transmission Electron Microscopy (TEM), the resulting electric and magnetic fields cannot be easily measured, because they represent phase objects in terms of electron object interaction hence are normally invisible. However, the fields can be analyzed by means of electron interference in electron holography: in the TEM, the image wave is superimposed by a plane reference wave yielding the hologram, from which amplitude and phase modulation by the object are reconstructed quantitatively [1]. In the phase image, atomic resolution is achieved both laterally and in the signal [2,3].

ELECTRON HOLOGRAPHY AND HOLOGRAPHIC TOMOGRAPHY

Basics

The electron wave propagating through an object with electric potential $V(x, y, z)$ and magnetic vector potential $\vec{A}(x, y, z)$ experiences a phase shift. The phase difference with respect to the reference wave is given by

$$\varphi(x, y) = \sigma \int_{\text{object}} V(x, y, z) dz - 2\pi \frac{e}{h} \oint \vec{A}(x, y, z) d\vec{s}$$

where σ is the interaction coefficient, and the first integral is the “projected” electric potential; in the second integral, the loop goes from the illuminating electron source along the object wave to the image point (x, y) and back along the reference wave. Measuring the phase distribution from the holographically reconstructed wave, the integrals can be determined.

2D holography

For the simple case with $\vec{A} = \vec{0}$ and V independent from z , the phase simply reads as

$$\varphi(x, y) = \sigma V(x, y) t$$

at object thickness t . Then the 2D-potential V can easily be evaluated from the measured phase (Fig. 1a). More details about the method of 2D-holography and further examples, also from other groups, are shown in [4].

3D holography

Unfortunately, most object potentials vary also with z , but the resolution in z -direction is lost in the projected potential obtained. This means that the reconstructed potential data, which are averaged along z , do not present the local data. As a remedy, 3D-holography, i.e. electron holographic tomography (EHT), was developed: many 2D-holograms of the object are recorded in a tilt series with equidistant tilt increments. For each tilt, the 2D-phase image is reconstructed. Since the phase is given by the integral of V , it fulfills the projection requirement of tomography, and hence the series of 2D-phase images can be combined in a 3D-phase distribution. From this, the 3D-potential $V(x, y, z)$ of the object is calculated, e.g., determining the potential in a certain object slice [5]. For example, using EHT, the Fermi level pinning at semiconductor surfaces is revealed shown in Fig.1b [6]. Moreover, not only the internal potentials and fields are accessible with EHT, but also external magnetic and electric stray fields as reported in [7].

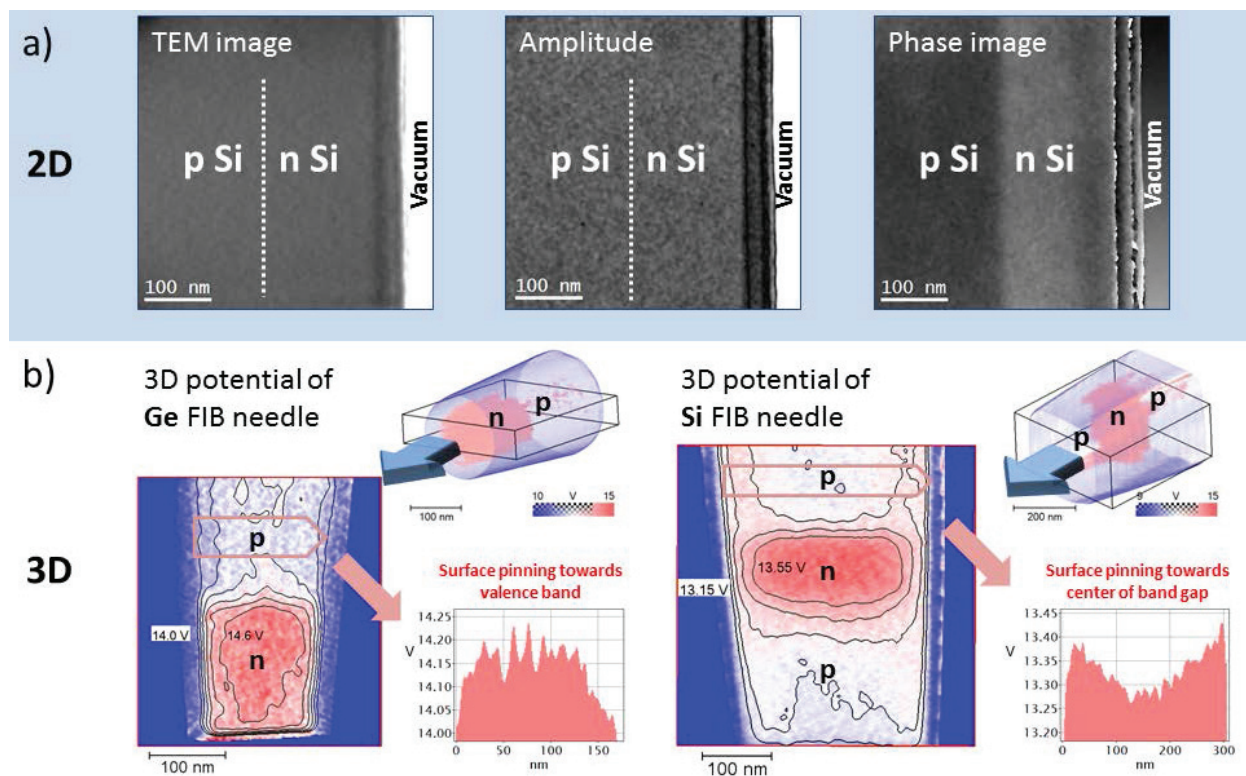


FIGURE 1. 2D and 3D potential mapping with electron holography. a) Electron holography on a planar sample of a p-n-doped silicon wafer. The doped regions exhibit no amplitude contrast as shown in the TEM image and the reconstructed amplitude as well. However, since the built-in potential in the depletion region provides phase contrast, p and n region can clearly be distinguished in the phase image. b) Electron holographic tomography on a FIB prepared needle-shaped sample of a p-n doped germanium and a p-n-p doped silicon wafer. In the 3D potential, the n-doped region is visible due to its higher potential compared to the p-doped substrate. By the iso-lines in the longitudinal section, the built-in voltage can be quantified. The line profiles through the p region visualize the potential pinning at the surface downwards in the Ge case and upwards in the Si case.

3D-holography: application to magnetic nanomaterials

For 3D analysis of the complete magnetic vector field $\vec{B} = (B_x, B_y, B_z) = \text{curl } \vec{A}$, two tilt series with mutually inclined tilt axes have to be taken for two components of \vec{B} , respectively; from these, the third component can be determined using Maxwell's equation. Often, already only one component gives very valuable insight into a magnetic structure. In FIG. 2, the 3D reconstruction of a magnetic Co nanopillar (NP) is shown; the determination of the electric potential and the B_y -component along its axis is depicted [8]. Interestingly, the 3D map of the magnetic induction reveals that the nanocrystalline Co NP forms a small inversion domain (red region in FIG. 2), which is not expected

from the shape anisotropy of the pillar. Micromagnetic simulations confirm this behavior and provide also the other two components of the B-field.

The research leading to these results has received funding from the European Union Seventh Framework Programme under Grant Agreement 312483 – ESTEEM2 (Integrated Infrastructure Initiative – I3).

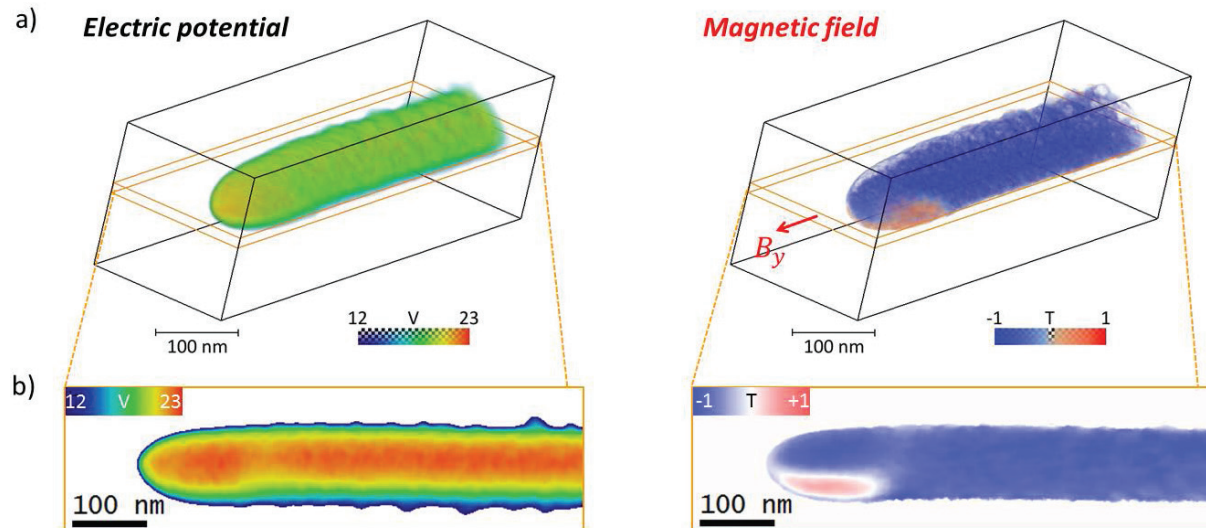


FIGURE 2. Electric potential and axial magnetic B-field component of a Co nanopillar reconstructed with electron holographic tomography. (a) Volume rendering, i.e. the colors correspond to the internal potential/B-field values. (b) 15 nm thick 2D slices through the 3D data as indicated by the orange boxes in (a).

REFERENCES

1. H. Lichte et al., *Ultramicroscopy* **134**, 136-134 (2013).
2. H. Lichte, *Ultramicroscopy* **108**, 256-262 (2008).
3. F. Röder et al., *Ultramicroscopy* **144**, 32-42 (2014).
4. H. Lichte and M. Lehmann, *Rep. Prog. Phys.* **71**, 016102-46 (2008).
5. D. Wolf et al., *Current Opinion in Solid State & Materials Science* **17**, 126-134 (2013).
6. D. Wolf et al., *Applied Physics Letters* **103**, 264104-4 (2013).
7. A. Lubk et al., *Applied Physics Letters* **105**, 173101-5 (2014).
8. D. Wolf et al., to be submitted (2015).

KEYWORDS

holography, tomography, electric, magnetic, potential, field, semiconductor, doping, nanoscale, domain

Barrier Modification of Metal-contact on Silicon by Sub-2 nm Platinum Nanoparticle

H. Zheng^a, S. C. Su^a, S. Mukherjee^a, K. Gangopadhyay^{a, b}, and S. Gangopadhyay^a

^a*Department of Electrical and Computer Engineering, University of Missouri Columbia, Missouri 65201, U.S.A.*

^b*Nanos Technologies LLC, Columbia, Missouri 65203*

INTRODUCTION

A longstanding issue in fabrication of semiconductor devices is Fermi level pinning of semiconductor at the metal-semiconductor interface. Selecting metals with different work functions provides only limited control over Ohmic contact or Schottky contact barrier height. Extensive studies have demonstrated reduced metal-semiconductor contact resistance using thin insulating tunnel barriers with fixed charges.^{1,2} However, the optimal insulating layer thickness (e.g. ~1 nm for Al₂O₃) is difficult to fabricate and thicker insulator layers increase the contact resistance due to reduction in tunneling probability. Dielectric layers below this thickness are generally unreliable due to surface discontinuities. In this study, we control the metal-semiconductor contact barrier through the introduction of sub-2 nm platinum nanoparticles (Pt NPs) deposited by tilted target sputtering (TTS). We show the size-dependent Pt NP properties and their role in Fermi level depinning at the metal-silicon interface with a 0.98 nm Al₂O₃ or 1.6 nm SiO₂ dielectric layer. Our initial study demonstrates that 0.74 nm Pt NPs modified samples show >100-fold higher current density compared to a Ti-thin oxide-Si contact (control). We further show that the contact can be modulated to be either Schottky or Ohmic using the same contact metal by varying only Pt NP size and areal density.

RESULTS AND DISCUSSION

FIGURE 1 a-f illustrates device schematics for the six device architectures used in this study. Metal/organic contaminants were removed from low-doped p-type Si (p-Si) using a modified Shiraki cleaning process. A ~1.6 nm chemically grown SiO₂ can be preserved after the HCl:H₂O soak by removing the final HF:CH₃OH soak. TTS was used to deposit Pt NPs onto the substrate with the deposition time and target angle tuned to obtain different Pt NP sizes and areal densities (**FIGURE 1 g**). Deposition times of 5, 10, 20, and 45 s at 23° incidence angle correspond to Pt NP sizes of 0.5, 0.7, 0.9, and 1.3 nm, respectively. With higher target angle (38°) and deposition time (20 s), Pt NP size is reduced to 0.7 nm, but with higher density (see ref 3–6 for details). A 0.98 nm Al₂O₃ layer was then deposited by Atomic Layer Deposition (ALD).^{3,4} Ti and/or Au metal contact was then electron beam deposited atop the samples. The backside of the substrate was then coated with Cr/Au to insure an Ohmic back contact. Samples were then H₂ annealed at 250 °C for 1 hr.

FIGURE 2 a-f show the current-voltage (IV) characteristics of the six device architectures used in this study. The role of 0.7 nm TTS Pt NPs deposited directly on p-Si was studied using **Structure 1** [Ti/Al₂O₃/Pt NPs/p-Si] (**FIGURE 2 a**). Significantly higher current level was observed on both forward and reverse bias region on introduction of the Pt NPs. While **Structure 1** without Pt NP showed Schottky-like contact behavior with imbalanced current injection in the two polarities, **Structure 1** with Pt NP showed Ohmic contact behavior with balanced current injection. Similar results were obtained for **Structure 2** [Ti/Pt NPs/SiO₂/p-Si] (**FIGURE 2 b**) and **Structure 3** [Au/Pt NPs/SiO₂/p-Si] (**FIGURE 2 c**). We attribute this improvement to the effective Fermi level depinning and barrier lowering in the presence of the Pt NPs. When the high work function Pt NP is placed in close proximity to the metal-semiconductor interface at thermal equilibrium, an electric dipole can be formed at the surface of the Pt NPs (**FIGURE 3**). This dipole-induced electric field can modify the contact barrier profile. Adding both SiO₂ and Al₂O₃ between the Ti and p-Si contacts (**Structures 4 and 5**) causes the tunneling dielectric to become too thick, resulting in an increase in tunneling resistance (**FIGURE 2 d-e**). Adding Pt NPs in **Structure 6** [Ti/Al₂O₃/Pt NPs/SiO₂/p-Si], the barrier and

contact properties can be effectively modulated between Schottky and Ohmic depending on the size and density of the Pt NPs (**FIGURE 2 f**). Devices with 0.74 nm Pt NP size and $5.2 \times 10^{12} / \text{cm}^2$ density displayed increased barrier height and Schottky type behavior while devices with 0.72 nm Pt NP size and $1.1 \times 10^{13} / \text{cm}^2$ density showed significant reduction in barrier height and Ohmic behavior. Pt NP size plays an important role in this barrier modification, which is presumably due to the size-dependent electron addition energy of Pt NPs in the dielectric. Pt NPs with larger size and smaller interparticle distance have smaller electron addition energy and, hence, the carriers can tunnel through the NPs more easily.

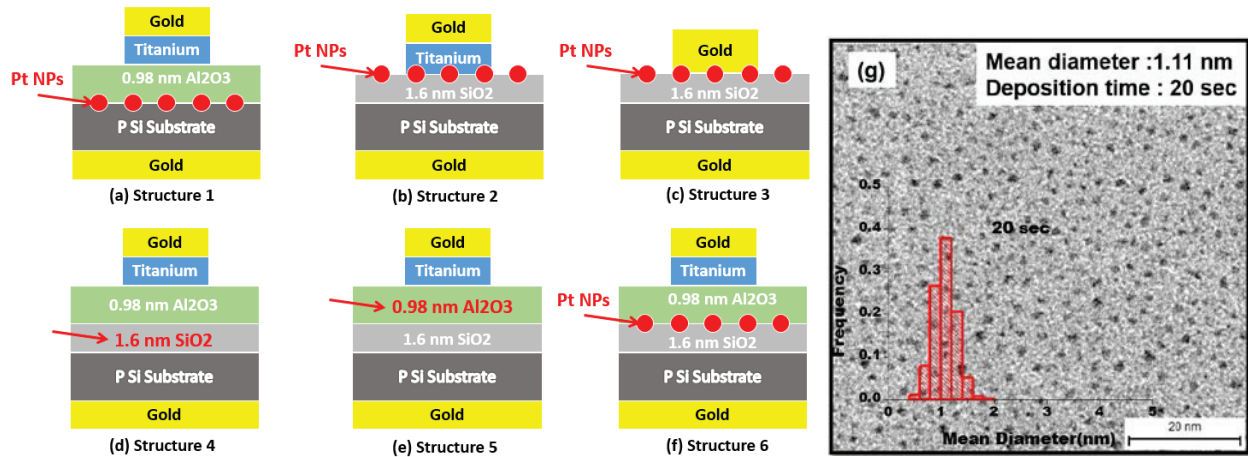


FIGURE 1. Schematics of six device architectures (Items in red are optional): (a) **Structure 1**, [Ti/Al₂O₃/Pt NPs/p-Si]; (b) **Structure 2**, [Ti/Pt NPs/SiO₂/p-Si]; (c) **Structure 3**, [Au/Pt NPs/SiO₂/p-Si]; (d) **Structure 4**, [Ti/Al₂O₃/SiO₂/p-Si]; (e) **Structure 5**, [Ti/Al₂O₃/SiO₂/p-Si]; (f) **Structure 6**, [Ti/Al₂O₃/Pt NPs/SiO₂/p-Si]; and (g) TEM image of 1.11 nm TTS-deposited Pt NPs.

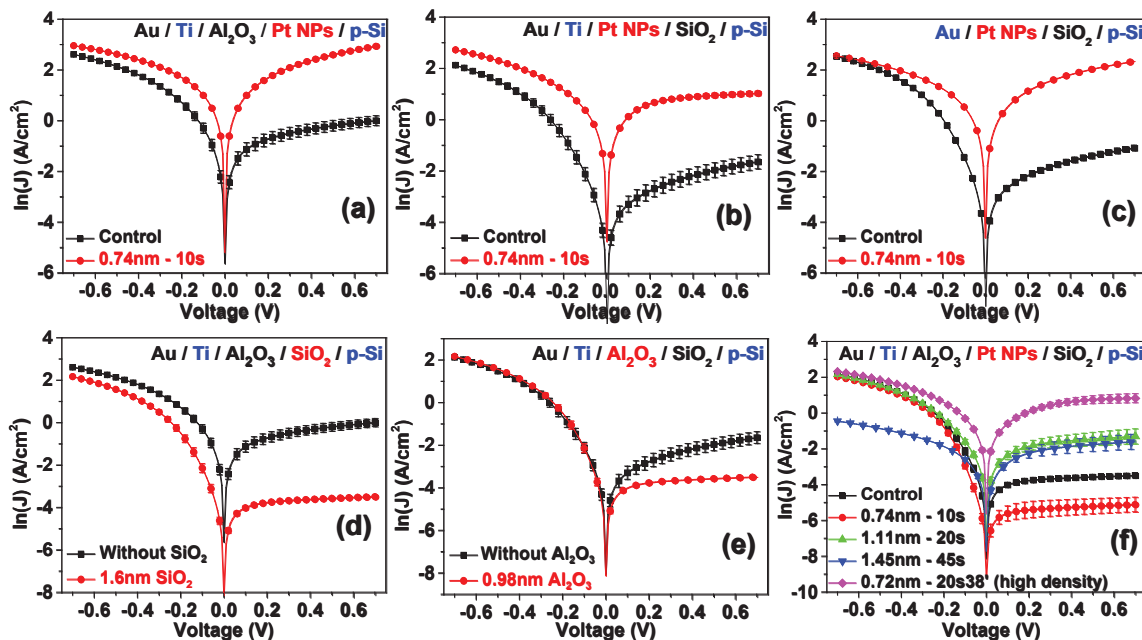
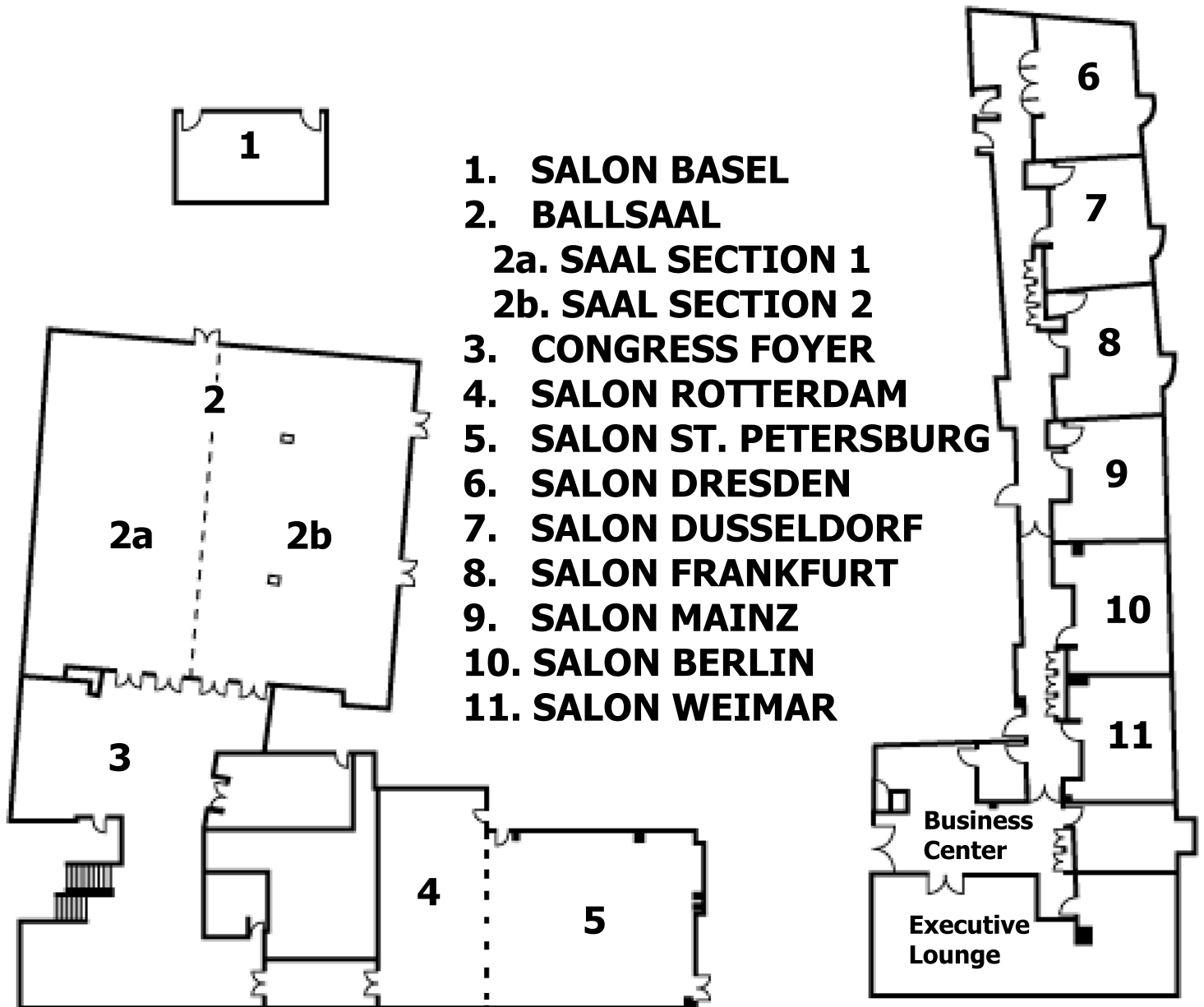


FIGURE 2. I-V characteristics of six different device architectures: (a) **Structure 1**; (b) **Structure 2**; (c) **Structure 3**; (d) **Structure 4**; (e) **Structure 5**; (f) **Structure 6**. Error bars are calculated from the I-V measurement of 7-8 different devices.

HILTON DRESDEN - FIRST FLOOR



FCMN EVENTS

Rooms 2a and 2b: Invited Talks

Rooms 4 and 5: Posters and Coffee Breaks

Room 3: Exhibits and Lunches

Program at a Glance

	Morning	AM Sessions	PM Sessions	Evening
Tuesday Apr. 14 th	7:30 Registration / Attendee Check-in	8:30 Conference Opening 9:00 Keynote Talks 11:45 General	13:45 Microscopy Metrology 15:45 Elec. Char. Metrology for New Memories	16:45 Poster Session
Wednesday Apr. 15 th	8:00 Registration / Attendee Check-in	8:30 Advanced and Novel Characterization Techniques 11:00 Next Generation Defect Inspection	13:30 Characterization for 1D and 2D Electronics 15:30 Metrology for Patterning	19:00 Banquet
Thursday Apr. 16 th	8:30 Registration / Attendee Check-in	9:00 Metrology for CMOS and Beyond 11:00 Nanoscale Thermal and Mechanical Characterization	12:00 3D IC Analysis / Metrology	

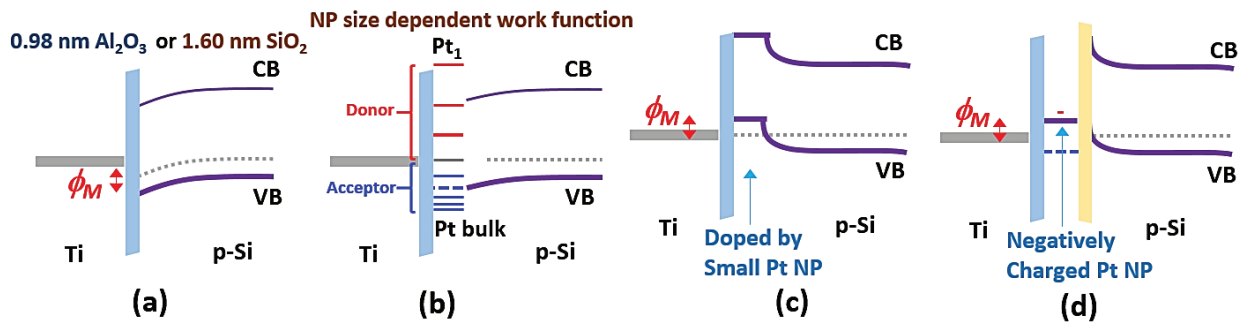


FIGURE 3. Energy band diagrams of the devices with thin dielectric layers: (a) without embedded Pt NPs; (b) with Pt NPs on Si, before contact; and (c) with Pt NPs on Si, after contact; (d) with Pt NPs embedded between thin dielectrics, after contact.

REFERENCES

1. A. Roy, J. Lin, and K. Saraswat, *Electron Device Lett. IEEE* **33**, 761–763 (2012).
2. D. Connelly, C. Faulkner, P. A. Clifton, and D. E. Grupp, *Appl. Phys. Lett.* **88**, 012105 (2006).
3. B. Ramalingam, S. Mukherjee, C. J. Mathai, K. Gangopadhyay, and S. Gangopadhyay, *Nanotechnology* **24**, 205602 (2013).
4. H. Zheng, B. Ramalingam, V. Korampally, and S. Gangopadhyay, *Appl. Phys. Lett.* **103**, 193305 (2013).
5. B. Ramalingam, H. Zheng, and S. Gangopadhyay, *Appl. Phys. Lett.* **104**, 143103 (2014).
6. M. Yun, B. Ramalingam, and S. Gangopadhyay, *J. Electrochem. Soc.* **159**, H393 (2012).

KEYWORDS

Fermi Level Depining, Barrier Modification, Metal-semiconductor Contact, Platinum nanoparticles, Sub-2 nm